September 1998 • NREL/TP-520-25101

NCPV Preprints for the 2nd World Conference on Photovoltaic Solar Energy Conversion

6–10 July 1998
Vienna, Austria

National Renewable Energy Laboratory
1617 Cole Boulevard
Golden, Colorado 80401-3393
A national laboratory of
the U.S. Department of Energy
Managed by Midwest Research Institute
for the U.S. Department of Energy
under Contract No. DE-AC36-83CH10093

NREL/TP-520-25101

NCPV Preprints for the 2nd World Conference on Photovoltaic Solar Energy Conversion

6–10 July 1998
Vienna, Austria

National Renewable Energy Laboratory
1617 Cole Boulevard
Golden, Colorado 80401-3393
A national laboratory of
the U.S. Department of Energy
Managed by Midwest Research Institute
for the U.S. Department of Energy
under Contract No. DE-AC36-83CH10093

Prepared under Task No. PV801702
September 1998

Available to DOE and DOE contractors from:
Office of Scientific and Technical Information (OSTI)
P.O. Box 62
Oak Ridge, TN 37831
Prices available by calling (423) 576-8401

Available to the public from:
National Technical Information Service (NTIS)
U.S. Department of Commerce
5285 Port Royal Road
Springfield, VA 22161
(703) 487-4650

TABLE OF CONTENTS

Page

I. Silicon

D.S. Ruby, P. Yang, S. Zaidi, S. Brueck, M. Roy, and S. Narayanan,
Improved Performance of Self-Aligned, Selective-Emitter Silicon Solar Cells 3

B.L. Sopori, W. Chen, J. Gee, and K. Jones,
On the Performance Limiting Behavior of Defect Clusters in Commercial Silicon Solar Cells 7

Y.S. Tsuo, J.M. Gee, P. Menna, D.S. Strebkov, A. Pinov, and V. Zadde,
Environmentally Benign Silicon Solar Cell Manufacturing 11

II. Thin-Film PV Technologies

S.K. Deb, R. Ellingson, S. Ferrere, A.J. Frank, B.A. Gregg, A.J. Nozik, N. Park, and G. Schlichthörl,
Photochemical Solar Cells Based on Dye-Sensitization of Nanocrystalline TiO_2 19

Amorphous Silicon

W. Gao, S.H. Lee, Y. Xu, D.K. Benson, S.K. Deb, and H.M. Branz,
A Wide-Gap a-SiC:H PV-Powered Electrochromic Window Coating 23

Q. Wang, B.P. Nelson, E. Iwaniczko, A.H. Mahan, R.S. Crandall, and J. Benner,
The Influence of Charge Effect on the Growth of Hydrogenated Amorphous Silicon by the Hot-Wire Chemical Vapor Deposition Technique 27

Cadmium Telluride

M.M. Al-Jassim, R.G. Dhere, K.M. Jones, F.S. Hasoon, and P. Sheldon,
The Morphology, Microstructure, and Luminescent Properties of CdS/CdTe Films 31

T.J. Coutts, X. Wu, P. Sheldon, and D.H. Rose,
Development of High-Performance Transparent Conducting Oxides and Their Impact on the Performance of CdS/CdTe Solar Cells 35

D.H. Levi, L.M. Woods, D.S. Albin, T.A. Gessert, R.C. Reedy, and R.K. Ahrenkiel,
The Influence of Grain Boundary Diffusion on the Electro-Optical Properties of CdTe/CdS Solar Cells 39

D.M. Waters, D. Niles, T.A. Gessert, D. Albin, D.H. Rose, and P. Sheldon,
Surface Analysis of CdTe after Various Pre-Contact Treatments 43

L.M. Woods, D.H. Levi, V. Kaydanov, G.Y. Robinson, and R.K. Ahrenkiel,
Electrical Characterization of CdTe Grain-Boundary Properties from As Processed CdTe/CdS Solar Cells 47

Copper Indium Diselenide

K. Ramanathan, H. Wiesner, S. Asher, D. Niles, R.N. Bhattacharya, J. Keane, M.A. Contreras, and R. Noufi,
High-Efficiency Cu(In,Ga)Se_2 Thin Film Solar Cells Without Intermediate Buffer Layers 51

III-V/High Efficiency Devices

D.J. Friedman, J.F. Geisz, S.R. Kurtz, and J.M. Olson,
1-eV GaInNAs Solar Cells for Ultrahigh-Efficiency Multijunction Devices 57

J.M. Olson and W.E. McMahon,
Structure of Ge(100) Surfaces for High-Efficiency Photovoltaic Applications 63

III. Module and BOS Manufacturing

H.P. Thomas, B. Kroposki, P. McNutt, C.E. Witt, W. Bower, R. Bonn, and T.D. Hund,
Progress in Photovoltaic System and Component Improvements 71

C.E. Witt, R.L. Mitchell, H.P. Thomas, M.I. Symko, R. King, and D.S. Ruby,
Manufacturing Improvements in the Photovoltaic Manufacturing Technology (PVMaT) Project 77

IV. Cell, Module, and System Testing

Cell

K. Emery, D. Dunlavy, H. Field, and T. Moriarty,
Photovoltaic Spectral Responsivity Measurements 85

B.L. Sopori, J. Madjdpour, and W. Chen,
Applications of "PV Optics" for Solar Cell and Module Design 89

Module

D.L. King , W.E. Boyson, and B.R. Hansen,
Improved Accuracy for Low-Cost Solar Irradiance Sensors 93

System

G.A. Kern, R.H. Bonn, J. Ginn, and S. Gonzalez,
Results of Sandia National Laboratories Grid-Tied Inverter Testing 97

D.L. King, J.A. Kratochvil, and W.E. Boyson,
Field Experience with a New Performance Characterization Procedure for Photovoltaic Arrays 103

P. McNutt, B. Kroposki, R. Hansen, K. Algra, and R. DeBlasio,
Development of Interim Test Methods and Procedures for Determining the Performance of Small Photovoltaic Systems 111

J.S. Ward, A. Duda, K. Zweibel, and T.J. Coutts,
Large-Area, High-Intensity PV Arrays for Systems Using Dish Concentrating Optics 115

V. Market Development

J.L. Stone, H.S. Ullal, and C. Sherring,
The Ramakrishna Mission Economic PV Development Initiative 123

R.W. Taylor,
Lessons Learned from the NREL Village Power Program 127

W.L. Wallace, L. Jingming, and G. Shangbin,
The Use of Photovoltaics for Rural Electrification in Northwestern China 131

I. Silicon

IMPROVED PERFORMANCE OF SELF-ALIGNED, SELECTIVE-EMITTER SILICON SOLAR CELLS

D. S. Ruby[1], P. Yang[1], S. Zaidi[2], S. Brueck[2], M. Roy[3] and S. Narayanan[3]
[1]Sandia National Laboratories, Albuquerque, NM 87185-0752 USA
[2]University of New Mexico, Albuquerque, NM 87106 USA
[3]Solarex (a business unit of Amoco/Enron Solar), Frederick, MD 21701 USA
Tel.: 505-844-0317, Fax: 505-844-6541, email: dsruby@sandia.gov

ABSTRACT: We improved a self-aligned emitter etchback technique that requires only a single emitter diffusion and no alignments to form self-aligned, patterned-emitter profiles. Standard commercial screen-printed gridlines mask a plasma-etchback of the emitter. A subsequent PECVD-nitride deposition provides good surface and bulk passivation and an antireflection coating. We used full-size multicrystalline silicon (mc-Si) cells processed in a commercial production line and performed a statistically designed multiparameter experiment to optimize the use of a hydrogenation treatment to increase performance. We obtained an improvement of almost a full percentage point in cell efficiency when the self-aligned emitter etchback was combined with an optimized 3-step PECVD-nitride surface passivation and hydrogenation treatment. We also investigated the inclusion of a plasma-etching process that results in a low-reflectance, textured surface on multicrystalline silicon cells. Preliminary results indicate reflectance can be significantly reduced without etching away the emitter diffusion.
Keywords: Passivation – 1: Silicon-Nitride – 2: Texturisation - 3

1. INTRODUCTION

The purpose of our work is to improve the performance of standard commercial screen-printed solar cells by incorporating high-efficiency design features without incurring a disproportionate increase in process complexity or cost. Our approach uses plasma processing to replace the heavily doped homogenous emitter and non-passivating antireflection coating (ARC) with a high-performance selectively patterned diffusion covered with a passivating ARC. A slight variation of the plasma step can effectively texture even multicrystalline silicon (mc-Si) surfaces to significantly reduce front surface reflectance.

1.1 Passivated, Patterned Emitter

Plasma-enhanced chemical vapor deposition (PECVD) is now recognized as a performance-enhancing technique that can provide both surface passivation and an effective ARC layer [1]. For some solar-grade silicon materials, it has been observed that the PECVD process results in the improvement of bulk minority-carrier diffusion lengths as well, presumably due to bulk defect passivation [2].

In order to gain the full benefit from improved emitter surface passivation on cell performance, it is necessary to tailor the emitter doping profile so that the emitter is lightly doped between the gridlines, but heavily doped under them [3]. This is especially true for screen-printed gridlines, which require very heavy doping beneath them for acceptably low contact resistance. This selectively patterned emitter doping profile has historically been obtained by using expensive photolithographic or screen-printed alignment techniques and multiple high-temperature diffusion steps [3,4].

We have attempted to build on a self-aligned emitter etchback technique described by Spectrolab that requires only a single emitter diffusion and no alignments [5].

Sandia is a multiprogram laboratory operated by Sandia Corporation, a Lockheed Martin Company, for the U.S. Department of Energy under Contract DE-AC04-94AL85000.

Reactive ion etching (RIE) using SF_6 etches back the emitter but leaves the gridlines and emitter regions beneath them unetched. This removes the heavily diffused region and any gettered impurities between gridlines while leaving the heavily doped regions under the metal for reduced contact resistance and recombination. This leaves a low-recombination emitter between gridlines that requires good surface passivation for improved cell performance. Therefore, we follow the etchback with a surface-passivating PECVD-nitride layer. The nitride also provides a good ARC and can be combined with plasma-hydrogenation treatments for bulk defect passivation.

1.2 Textured, Low-Reflectance Emitter

Several groups have reported interest in plasma-etching techniques to texture mc-Si cells, because mc-Si cannot benefit sufficiently from the anisotropic etches typically used for single-crystal Si. In contrast to laser or mechanical texturing, plasma-etching textures the entire cell at once, which is necessary for high-throughput. Inomata et al. used Cl_2-based RIE on mc-Si to fabricate a 17.1% efficient cell, showing that plasma-texturing does not result in performance-limiting surface damage [6].

We developed a variation of the SF_6 emitter etchback process, which results in good surface texturing. Use of SF_6 keeps the process compatible with the metal gridlines. This allows the texturing to be done after the metallization step as part of the emitter-etchback process.

2. EXPERIMENTAL PROCEDURE

The textured, self-aligned selective-emitter (SASE) plasma-etchback and passivation process is shown in Figure 1. The SASE concept uses cells that have received standard production-line processing through the printing and firing of the gridlines. Then the cells undergo reactive ion etching (RIE) to first texture and etch away the most heavily-doped part of the emitters in the regions between

the gridlines, increasing the sheet resistance in these areas to 100 ohms/square.

For emitter etchback, we used a new PlasmaTherm 790 reactor. This is a commercial RF dual parallel-plate reactor operating at 13.56 MHz. This equipment is IC industry-standard, programmable, and capable of being configured in a cluster-tool arrangement for high-throughput. Wafers were etched in pure SF_6 at a powers between 15 and 45 W and pressures ranging from 100 to 150 mTorr. Gas flow rates were between 14 and 26 sccm.

For texturization, we performed room-temperature RIE in a Technics, PEII-A parallel-plate reactor. We used mixtures of SF_6 with varying amounts of O_2. RF power ranged from 50 to 300 W.

Wafers received a silicon-nitride deposition (PECVD-nitride), using conditions similar to those found to be effective for bulk and surface passivation in String Ribbon™ mc-Si [2]. The plasma-nitride depositions were performed using the PECVD chamber of the PlasmaTherm reactor. Reaction gases for nitride deposition were a 5% mixture of silane in helium, nitrogen, and anhydrous ammonia. The optional H-passivation treatment consists of an exposure to a pure ammonia plasma between 300-400C in the PECVD reactor. We found that less power is required to generate a NH_3-plasma than a H_2-plasma, resulting in less surface damage. Nitride-coated cells then receive a forming gas anneal (FGA) at 300C for 30 minutes. The cells at this point are returned to the production-line for final cell processing, if any.

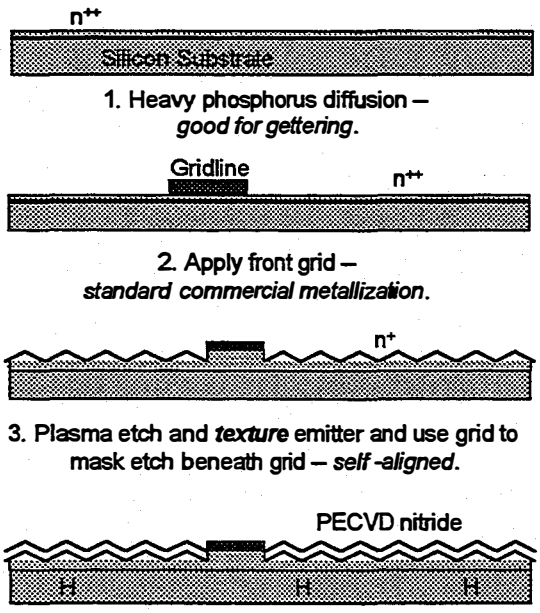

Figure 1. Process sequence for textured, self-aligned selective-emitter cells. The emitter etchback can be done after texturization to remove any surface damage the texturing may cause.

3. EXPERIMENTAL RESULTS

3.1 Emitter-Etchback Studies

The key to the success of the SASE process lies in finding an etching technique that results in uniform emitter etchback while avoiding both gridline and silicon surface damage. We investigated Si etch rates and uniformity for various RIE parameters using the PlasmaTherm reactor and compared them with those obtained using an older but similar Vacutec reactor, which produced SASE cells with half a percent higher efficiency than control cells [7]. Uniformity was monitored by measuring emitter sheet resistance over the full 130-cm^2 area of commercial wafers after the etchback. Surface damage was monitored by measuring the emitter saturation current density (J_{oe}) on high-resistivity float-zone wafers after passivation with a PECVD-nitride film [8].

We succeeded in finding a set of parameters for rf-power, flow rate, and pressure for the PlasmaTherm, which resulted in better uniformity and less surface damage than obtained with the Vacutec. The best result reduced uniformity variation from 10% to 2% and reduced J_{oe} from 270 to 225 fA/cm^2 on 100 Ω/sq. emitters.

3.2 Emitter-Passivation Studies

Our previous work with the Vacutec showed that we were able to obtain lower J_{oe} values and better surface passivation using a 3-step nitride deposition process compared to a single continuous deposition [7]. The 3-step process starts with deposition of a thin layer of nitride to protect the Si surface, followed by exposure to a NH_3-plasma, and finally the deposition of the remaining nitride required to attain the correct thickness for ARC purposes.

Comparison using the PlasmaTherm also showed better passivation using the 3-step process. We conducted a statistically designed multifactor experiment to find the 3-step parameters that would minimize J_{oe} on float zone wafers using our previous response surface methodology [7,8]. The results of a quadratic interaction experiment are shown in Fig. 2.

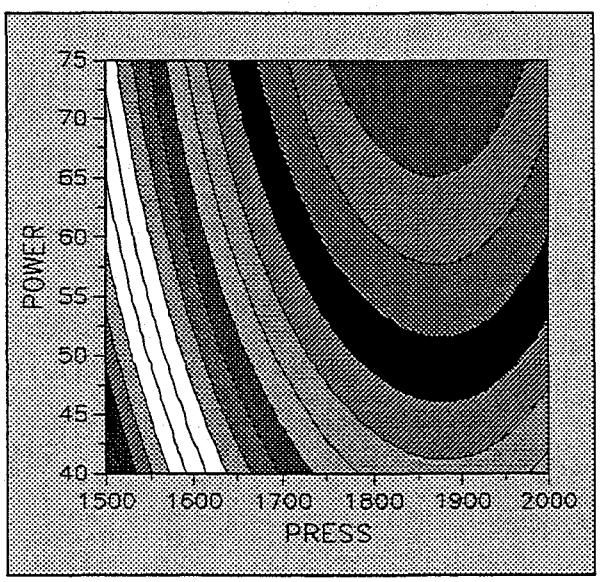

Figure 2. Contour plot showing response of J_{oe} to the power (W) and pressure (mT) during NH_3-treatment with a protective-nitride thickness of 10 nm. J_{oe} ranges from 216 in the lower left corner to a minimum of 161 fA/cm^2 near the upper right corner. The duration of the NH_3 hydrogenation was 20 minutes.

3.3 SASE cell processing

We used the parameters that produced minimum J_{oe} on 130-cm^2 cells processed up through gridline firing on the Solarex production line. We investigated whether shorter NH_3-treatments would retain the benefits of surface passivation. Results of IV testing are shown in Table. I.

Table. I: Six SASE sequences were applied to 12 Solarex mc-Si cells (2 cells/sequence) using matched material from the same ingot as the controls. Illuminated cell IV data ± standard deviation are shown normalized to a constant transmittance to account for the additional 1.1% spectral-weighted absorbtance in the nitride [11].

Eff. (%)	J_{SC} (mA/cm^2)	V_{OC} (mV)	FF (%)
90 sec. RIE, **1-step** SiN, FGA			
12.3±0.4	30.5±0.0	565±4	71.6±1.6
90 sec. RIE, **3-step** SiN, **5 min NH_3**, FGA			
12.9±0.1	30.6±0.1	573±1	73.5±0.4
90 sec RIE, **3-step** SiN, **10 min NH_3**, FGA			
12.4±0.0	30.3±0.0	570±0	72.0±0.0
150 sec RIE, **1-step** SiN, FGA			
12.1±0.5	30.1±0.0	562±7	71.3±2.2
150 sec RIE, **3-step** SiN, **5 min NH_3**, FGA			
12.9±0.2	30.4±0.3	576±4	73.5±1.4
150 sec RIE, **3-step** SiN, **10 min NH_3**, FGA			
13.0±0.2	30.4±0.0	577±2	74.0±0.9
Control Cells: No emitter etchback, TiO_2 ARC			
12.6±0.0	30.2±0.1	569±0	73.5±0.0

The first three groups of cells were not etched back sufficiently, because the etch duration did not account for etching through a thermal oxide that grew on the cells during gridline firing. These cells do not show consistent improvement over the controls.

The second three groups used a longer 150-second RIE-etch that removed the thermal oxide and then etched the emitters from their starting sheet resistance of 50 Ω/sq. to 100 Ω/sq.. The 1-step cells show a drop in performance compared to the controls, in agreement with our J_{oe} results that showed poorer passivation by a 1-step nitride. Once the emitter is etched back to 100 Ω/sq., it requires excellent surface passivation to avoid excess surface recombination.

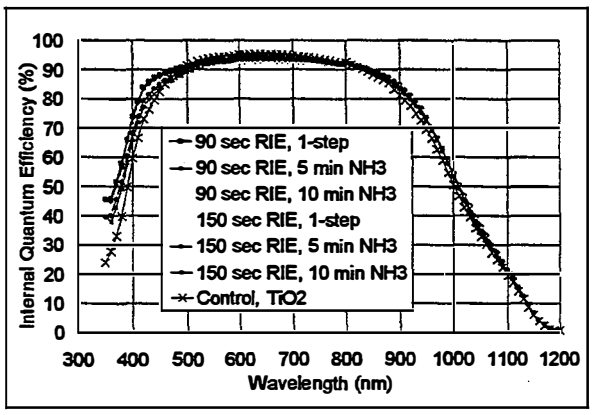

Figure 3. IQE for cells described in Table I.

The 3-step cells show significant improvements, especially in V_{OC}, suggesting longer diffusion lengths from bulk defect passivation. Internal quantum efficiency (IQE) of these cells, showing both improved red and blue response is shown in Figure 3.

All the nitride passivated cells show similar red and blue response, consistent with their similar J_{SC} values. The J_{SC} is no greater than that of the control cell because the increase in IQE is compensated by parasitic absorbtion in the nitride. This is due to the high refractive index of 2.2 used to minimize reflectance. Another series of SASE cells were processed using a lower refractive index of 2.12 to reduce the spectrally weighted absorbtance to 0.5%. Normalized IV data for these cells are shown in Table II.

Table. II: Three SASE sequences were applied to seven Solarex mc-Si cells using matched material from the same ingot as before. IV data are shown below normalized to the transmittance of the control cells.

Eff. (%)	J_{SC} (mA/cm^2)	V_{OC} (mV)	FF (%)
140 sec RIE, **3-step** SiN, **5 min NH_3**, FGA			
12.9±0.2	31.1±0.1	572±3	72.7±0.3
140 sec RIE, **3-step** SiN, **10 min NH_3**, FGA			
13.1±0.0	31.4±0.1	574±0	73.0±0.1
140 sec RIE, **3-step** SiN, **20 min NH_3**, FGA			
12.2±0.4	31.2±0.1	563±5	69.5±1.5
Control Cells: No emitter etchback, TiO_2 ARC			
12.3±0.1	30.8±0.0	558±2	71.4±0.4

The SASE cells have consistently higher J_{SC} than the controls, because now the increased IQE due to passivation is not lost due to excessive parasitic absorbtion. The cells that received 10 minutes of NH_3-hydrogenation performed the best, exceeding the controls by almost a full percentage point due to the large improvement in V_{OC}. However, improvement in V_{OC} is reduced for the cells that received a 20-minute NH_3-exposure. These cells also suffered a loss in fill factor due to an increase in diode ideality factor.

3.4 RIE-textured cells

We developed an RIE process that uses SF_6/O_2 mixtures to produce a randomly textured surface on c-Si. Figure 4 shows an SEM of an RIE-textured sample with less than 0.5% spectral reflectance at all wavelengths.

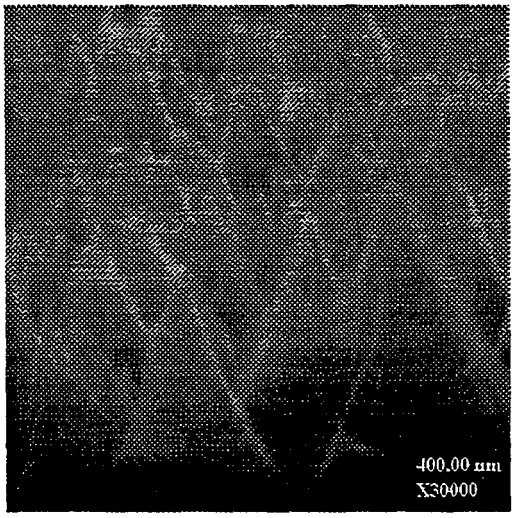

Figure 4. SEM of Si surface textured for 30 minutes.

About 6.0 μm of Si was removed from the surface shown in Fig. 4. This process could be applied to the wafers before emitter diffusion, when removal of a few micrometers of Si would not be an issue. The SASE process could then be applied after gridline firing as usual.

We developed a second process that could be applied after emitter diffusion since it removes only 0.1 μm from the surface, increasing the emitter sheet resistance to about 60 Ω/sq. This process requires the Si surface to be prepared in a simple manner using low-cost, low-temperature techniques. An SEM of such a textured surface prepared in this manner near a cleaved wafer edge is shown in Figure 5.

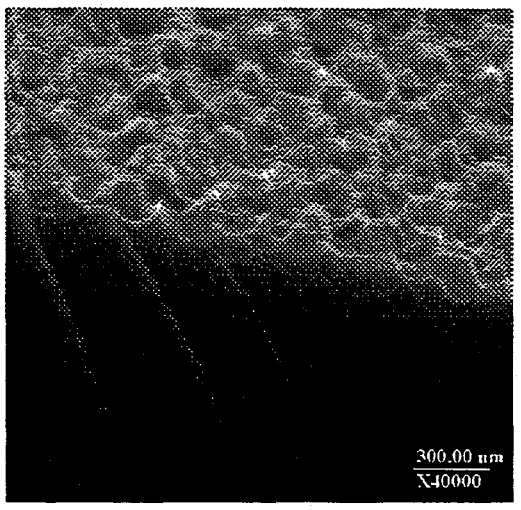

Figure 5: Textured Si surface with 0.1 μm feature sizes.

This second process was applied to single-crystal wafers with three different surface preparation conditions. Specular reflectance curves of the three resulting textures are compared to that of bare Si in Fig. 6.

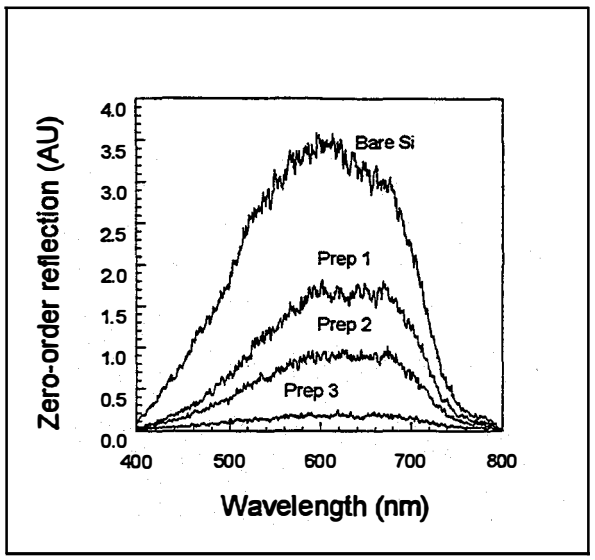

Figure 6: Specular reflectance of samples with three different surface preparation conditions. The reflectance of the textured samples has been reduced by a factor of 2.2, 4.4, and 24, respectively.

We applied this second process to full-size mc-Si wafers with gridlines using preparation conditions 1 and 2. These cells are currently in process at Solarex and could provide an increase of up to a full percentage point in efficiency due to reflectance reduction alone.

4. CONCLUSIONS

The SASE process has been improved using statistical experiments, more complete emitter etchback, and lower absorbtance nitride films to achieve nearly a full percentage point efficiency increase over the standard production line process. The use of an optimum-duration, ammonia-plasma hydrogenation treatment is crucial to the increased performance. In addition, plasma texturing has been shown to reduce reflectance significantly while removing only the heavily diffused portion of the emitter region. As a result, texturing could be included as part of the emitter etchback process.

5. ACKNOWLEDGMENTS

The authors would like to thank B.L. Silva and R.N. Stokes for much of the cell processing, and gratefully acknowledge B.R. Hansen for the cell measurements.

REFERENCES

[1] Z. Chen, P. Sana, J. Salami, and A. Rohatgi, IEEE Trans. Elect. Dev., 40, June 1993, pp. 1161-1165.

[2] D.S. Ruby, W.L. Wilbanks, C.B. Fleddermann, and J.I. Hanoka, Proc. 13th EPSEC, Nice, October 1995, pp. 1412-1414.

[3] R. Einhaus et al., Proc, 14th EPSEC, Barcelona, Spain, July; 1997.

[4] J. Horzel, J. Szlufcik, J. Nijs, R. Mertens, Proc. 26th IEEE PVSC, Anaheim, CA, September 1997

[5] N. Mardesich, Proc. 15th IEEE PVSC, May 1981, pp. 446-449.

[6] Y. Inomata, K. Fukui, K. Shirasawa, Solar Energy Mat. Solar Cells, 48, (1997), pp 237-242.

[7] D. S. Ruby, P. Yang, M. Roy and S. Narayanan, Proc. 26th IEEE PVSC, Anaheim, CA, September 1997, pp. 39-42.

[8] D. S. Ruby, W. L. Wilbanks, and C. B. Fleddermann. Proc. First WCPEC, Dec. 1994, pp. 1335-1338.

[9] P. Doshi, G.E. Jellison, Jr., and A. Rohatgi, "Characterization and optimization of absorbing plasma-enhanced chemical vapor deposited antireflection coatings for silicon photovoltaics," Appl. Opt., 36, Oct. 20, 1997.

ON THE PERFORMANCE LIMITING BEHAVIOR OF DEFECT CLUSTERS IN COMMERCIAL SILICON SOLAR CELLS

Bhushan L. Sopori, Wei Chen, James Gee* and Kim Jones
National Renewable Energy Laboratory
1617 Cole Boulevard, Golden, Colorado 80401, U. S. A.
*Sandia National Laboratory, Albuquerque, NM, U. S. A.

ABSTRACT: We report the observation of defect clusters in high-quality, commercial silicon solar cell substrates. The nature of the defect clusters, their mechanism of formation, and precipitation of metallic impurites at the defect clusters are discussed. This defect configuration influences the device performance in a unique way – by primarily degrading the voltage-related parameters. Network modeling is used to show that, in an N/P junction device, these regions act as shunts that dissipate power generated within the cell.
Keywords: Multicrystalline Silicon - 1: Defect Clusters - 2: Impurity Precipitation - 3

1. INTRODUCTION

The low-cost substrates used for commercial Si solar cell fabrication have high concentrations of impurities and defects. A variety of measures such as higher quality feedstock and better crucible quality have resulted in reduced metallic impurity content to the levels approaching 10^{14} cm^{-3}. Likewise, improvements in the thermal conditions during the crystal growth processes have yielded substrates with very low average defect density – typically $<10^5/cm^2$. However, this reduction in the defect density is accompanied by an agglomeration of defects to form local defect clusters. These defect clusters can have a strong influence on the device characteristics by primarily lowering the voltage-related cell parameters without significantly lowering the photocurrent [1]. These characteristics of defect clusters appear to control performance of the high-efficiency, large-area solar cells. This paper briefly describes the nature of the defect clusters in the photovoltaic (PV) silicon substrates and explains the mechanism(s) by which these defects control the device performance.

2. NATURE OF DEFECT CLUSTERS

Defect clusters consist of agglomerations of extended defects like dislocations, stacking faults, and (in some cases) grain boundaries, in otherwise very low defect density wafer. Figure 1 is a map showing the distribution of defects in a 5-cm x 5-cm section of a commercial, multicrystalline silicon (mc-Si) wafer. The darker regions indicate higher defect densities. This figure shows that a majority of the wafer has a low or zero dislocation density, while other regions have high concentrations of defects that are clustered together. The average value of the dislocation density in the entire wafer is about $10^5/cm^2$. The structure of a defect cluster can be seen in Figure 2. The defects were delineated by etching the sample in Sopori etch [2]. Detailed analyses show that a defect cluster involves a series of long, intertwined dislocation loops. Because these loops and networks are high-energy defect configurations, they are thermally unstable and can change during device processing. Furthermore, the defect clusters can be efficient nucleation sites that can become decorated with impurity precipitates during crystal growth. This propensity for impurity decoration of a defect cluster has a strong bearing on how it affects the device performance.

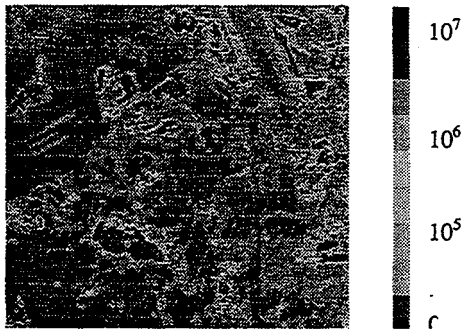

Figure 1. A defect map of a 5-cm x 5-cm section of a commercial mc-Si wafer. The scale is in defects/cm^2

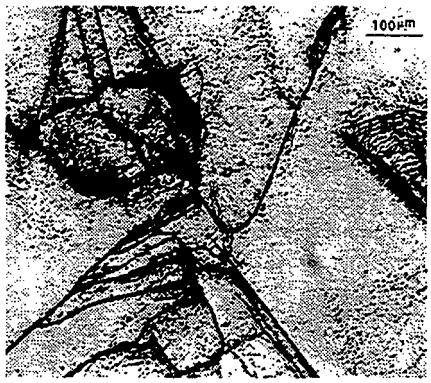

Figure 2. Photograph showing chemically delineated structure of a defect cluster.

3. FORMATION OF DEFECT CLUSTERS

Accumulation of point defects to form either vacancy or interstitial defects is well known in silicon technology. The local temperature gradients and the point-defect supersaturation drive such a process. Defect clusters are formed during the cool-down

portion of an ingot. The following explanation appears to be the most likely reason for the formation of defect clusters. During the crystal growth, the defects are formed in the regions of the ingot where the stress levels exceed the plastic yield stress. Because the yield stress depends on the crystal orientation, a given stress can exceed the yield stress of some grains. This stress can lead to the generation of extended defects, like dislocations and stacking faults, in a selective manner. Thus, during the growth of a multicrystalline ingot (or a ribbon) a few "easy" grains can effectively relieve the stress by becoming heavily decorated with defects. If the magnitude of the stress is only slightly larger than the minimum yield stress, the generation of defects will be limited to the grains of such preferred orientations. However, a large thermal stress would result in the generation of defects in all grains. Consequently, the clustering would occur only when the material quality is quite high. Thus, one can expect a high-quality, multicrystalline silicon wafer to have localized regions of heavy dislocations.

4. PRECIPITATION OF METALS AT DEFECT CLUSTERS

Because a defect cluster is an agglomeration of extended defects, its behavior will be similar in many ways to that of a grain boundary. Thus, one may expect defect clusters to act as internal gettering sites and trap impurities. A decoration of these defects by the metallic impurities can further increase their carrier recombination and lead to profound effects on the cell performance. In addition, precipitates can begin to dissolve at temperatures required for solar cell processing, creating internal sources for impurities. This behavior is further discussed in the conclusion section of this paper.

An indirect evidence of impurity precipitation came from earlier work on mapping of metallic impurities (like Fe and Cr), defects, and minority carrier diffusion length (MCDL) in commercial PV-Si wafers [3]. It was observed that the regions having low values of the MCDL corresponded to lower concentrations of the metals, as well as to higher concentrations of defects. Because Fe and Cr are fast diffusers, they are expected to be uniformly distributed in the entire sample. These aparent inconsistencies can be reconciled by assuming impurity precipitation occurs in the defected regions, which causes the dissolved impurity concentration to go down in that region. Thus, previous analysis concluded, on an indirect basis, that heavily defected regions would have precipitated impurities. Extensions of similar analyses that show high recombination associated with the defect clusters can be observed directly by methods such as the photoluminescence and the minority carrier diffusion length (MCDL) mapping. Figure 3 illustrates these results. Figure 3a is a map of the room temperature photoluminescence (PL) of a 5-cm x 5-cm sample showing strong local variations in the PL signal (in arbitrary units). Figure 3a was done with a beam size of about 20 μm; the dark regions correspond to higher PL signal. The defect map of the region, corresponding to the PL map in Figure 3a, is shown in Figure 3b. This figure was made by PVSCAN5000 with a beam size of about 300 μm; here the darker regions have lower defect density. An excellent correlation is observed between the two images. Figure 3c shows a MCDL map of the same sample, measured by the SPV technique, using a beam size of 3 mm. A correlation between the PL emission and the MCDL is seen. In addition, one can observe the inverse correlation of PL and MCDL with the defect clusters.

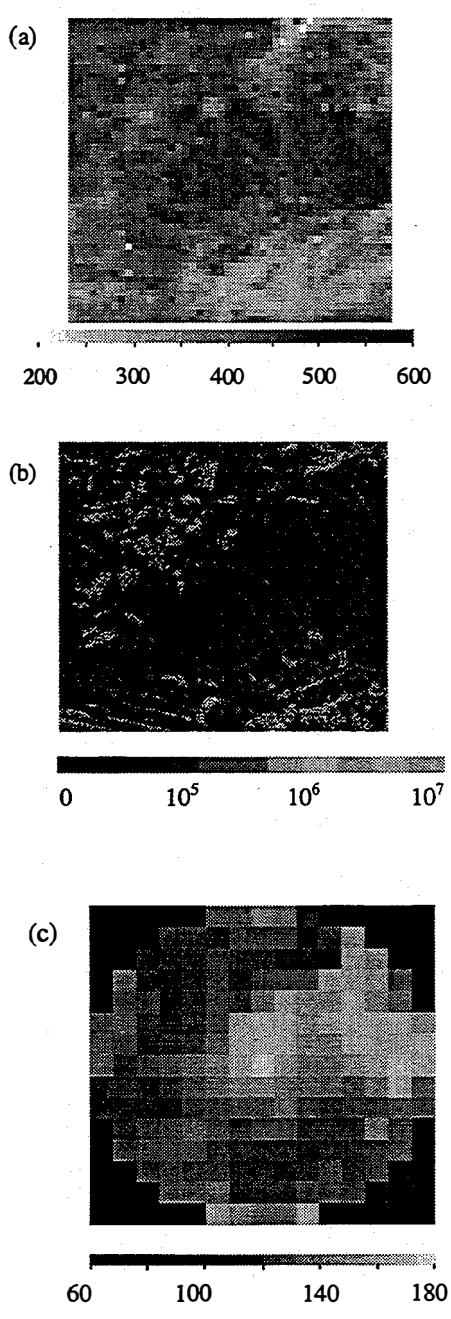

Figure 3: (a) PL in arbitrary units, (b) defect density in defects/cm^2, and (c) MCDL in μm maps of a 2-in x 2-in silicon sample showing correlation between them {the circular shape of the map in (c) is because the instrument is designed for the measurement of circular wafers}.

A direct evidence of precipitation comes from the TEM analyses made on different regions of mc-Si samples. Figure 4 is a micrograph of the precipitates observed in a region of a defect cluster. It was also determined that such precipitates occur only within the defect clusters.

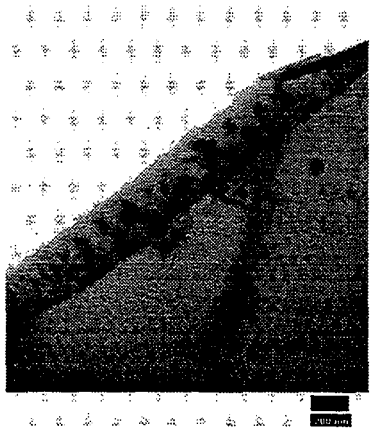

Figure 4. A TEM photo of a defect cluster showing direct evidence of impurity precipitation

5. INFLUENCE OF THE DEFECT CLUSTERS ON THE DEVICE PERFORMANCE

Defect clusters are localized regions of high carrier recombination in the as-grown substrate. This behavior is seen from Figure 3 as lower local values of the MCDL associated with the defected regions in an as-grown substrate. However, in spite of this reduction, the MCDL of the defected regions is above 50 μm – a value that can lead to a significant generation of photocurrent. It is because of this reason that the photogenerated current of a cell is not greatly impacted by defect clusters.

Defect clusters can affect the device performance in a number of other ways. A quantitative investigation of the effect of defect clusters on the performance of a large-area cell can be performed using a phenomenological approach that involves determination of :

1. The characteristics of the cell in the regions with no defect clusters
2. The characteristics of the defected region in the cell, and
3. A method of combining 1 and 2 to determine the effect of distributed defects on the device.

Item 1 above is well known – it can be expressed in terms of the J_{ph} and two exponential components of the dark current in a standard form as:

$$J_{dark}(V)=J_{01}.\exp\{(-eV/kT) - 1\} + J_{02}.\{\exp(-eV/2kT)-1\}. \quad (1)$$

The saturation currents J_{01}.and J_{02} can be written in standard forms of a P/N junction.

$$J = J_{ph} - J_{dark}(V). \quad (2)$$

where J_{ph} and $J_{dark}(V)$ are the photogenerated and the dark current densities, respectively.

A similar formalism can be applied to the cell corresponding to the defected region [4]. We have shown that the defected region can also be represented by equations similar to eq. (1) and (2) above. However, in this case, the values of various parameters will be different.

We have developed a computer model for an N/P junction device that calculates these parameters and uses a distributed network model to combine various regions of the device.

6. NETWORK MODEL FOR TOTAL CELL CHARACTERISTICS

The device is divided into an array of diodes, with each diode is small enough to assume a uniform distribution of defects. Each node in the matrix depicts a local cell, connected to other cells by a resistor representing the series resistance. The series resistance arises from a number of sources that include the sheet resistivity of the junction in an N/P device. Each local region, having a known defect density, is described by dark current given by:

$$I_{dark}= I_{01} \{ \exp(eV/kT-1)\} + I_{02} \{ \exp(eV/2kT-1)\} + I_{01} \{ \exp(eVn-1)\}.$$

(The last term in the above equation is added to represent tunneling current that occur in heavily defected regions due to hopping mechanism.) Hence, a local cell element (n,m) in the matrix is represented by a current source comprised of I_{01nm}, and I_{02nm}, and a corresponding light-induced current density $J_{ph,nm}$. One can represent

$J_{01nm}= I_{01}x\ F_{nm}x\ \exp(eV/kT-1)$, and

$J_{02nm}= I_{02}x\ F'_{nm}x\ \exp(eV/2kT-1)$,

where I_{01} and I_{02} represent dark saturation currents in the "defect-free" device element. F_{nm}, and F'_{nm} are the factors representing the ratio of dark current normalized by the "defect-free" current, for each component. A finite-element computer code, written in Microsoft Excel, is used to analyze the network.

Our network modeling results show that:

1. Defect clusters in a large-area cell act as shunts that preferentially lower Voc and FF without significantly lowering Jsc.
2. Such shunts act as " internal sinks" by dissipating the power within the cell.
3. Cell performance is sensitive to the spatial distribution of the defects.
4. Clustering of defects can cause significantly more degradation in the device performance compared to a situation where the total number of defects are uniformly distributed over the entire device.

We consider an example of a cell in which 20% of the device area is covered by defect clusters, and 80%

of the area is defect-free. The parameters for the defect-free region are:

J_{ph}= 0.035A/cm^2, J_{01}= 3.6 x 10^{-9} A/cm^2 , J_{02}= 4.5 x 10^{-13} A/cm^2.

From the experimental data, the parameters for the "defected" cell are:

J_{ph}= 0.0245 A/cm^2 , J_{01}= 3.6 x 10^{-8} A/cm^2 , J_{02}= 4.5x 10^{-11} A/cm^2.

Figure 5 shows the calculated I-V characteristics of these two cells. Their cell parameters are: Voc= 650 mV, Jsc= 34.45 mA/cm^2, FF= 81.01, and the efficiency=18.4 for defect-free; and Voc= 62 mV, Jsc=32.7 mA/cm^2, FF= 75.76 and Eff = 16.7 for defected cells, respectively. It is seen that all the parameters of the "defected" cell are lower than for the "defect-free" cell. However, the major reduction is in the V_{oc} and the FF. It should be pointed out that in an "undefected" cell, a reduction of 30 mV would be accompanied by a large reduction in Jsc in accordance with the cell equation; shunting produces a disproportionate reduction in the voltage.

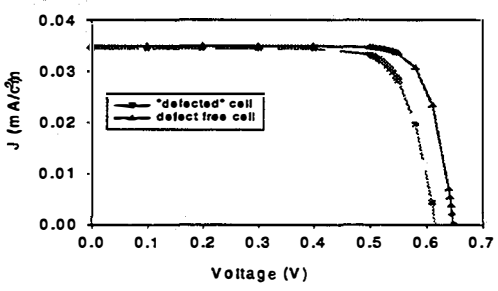

Figure 5. Calculated I-V characteristics showing a significant decrease in Voc by introducing defect clusters in a solar cell.

7. EFFECT ON SOLAR CELL PROCESSING

Because defect clusters are decorated with impurities, they are likely to make device performance very sensitive to the process conditions. This effect can happen via two mechanisms: (i) the inability to getter precipitated impurities, and (ii) processing mc-Si wafers at high temperature (>900°C) can causes partial dissolution of the precipitated impurities leading to increased impurity concentrations in the device.

8. CONCLUSION

We have shown that the clustering of defects can occur in high-quality, multicrystalline Si solar cell substrates. A mechanism for the formation of such defects is proposed. Defect clusters can contain precipitated impurities; as a result, impurity gettering cannot work well in such regions [5]. If device fabrication is done at high temperatures, typically exceeding 900 °C, some of the precipitates can start dissolving which, in turn, can increase the concentration of soluble impurities in the bulk of the device. This behavior can make cell performance very sensitive to the processing conditions. Defect clusters act as shunts, degrading primarily the voltage-related parameters of the device. By introducing device-processing conditions that can rapidly dissolve the precipitates and allow them to be gettered, one can ameliorate the effect of defect clusters by processes such as phosphorus diffusion and Al alloying. Such a high-temperature process may also unpin the defects to acquire a lower energy configuration and a lower density.

Detailed analyses have shown that the net reduction in the photogenerated current is much smaller than the fractional area of the defect clusters. This is because the photocurrent can be quite high even for short MCDL values. Consequently, the dominant effect of the defect clusters is not via the reduction in the photocurrent, but by affecting the voltage-related parameters.

In addition, as described in this paper, because defect cluster propagates through the entire thickness of the substrate, it is a "filamentary" junction shunt. The shunting effect is further enhanced by the impurity decoration during the crystal growth.

ACKNOWLEDGMENT

This work was supported by the US Department of Energy under Contract # DE-AC36-83CH10093. The authors are very grateful to Prof. Teh Tan of Duke University and Prof. Sergei Ostapenko of University of South Florida for many valuable discussions on the formation and characterization of cluster defects.

REFERENCES

[1] Bhushan Sopori, Procd. ICDS-19, Trans Tech Pub., Edited by Gordon Davies and Maria Helena Nazare, 527 (1997).

[2] B. L. Sopori, J. Electrochem. Soc., 131, 667 (1984).

[3] B. L. Sopori, L. Jastrzebski, T. Y. Tan, and S. Narayanan, Procd. 12th PVSEC, 1003(1994).

[4] J. G. Fossum and F. A. Lindholm., IEEE Trans. ED-27, 692(1980).

[5] B. L. Sopori, W. Chen, K. Nemire, J. Gee, S. Ostapenko, Procd. MRS '98 Spring Meeting, Symposium on Defect and Impurity Engineered Semiconductors and Devices II, to be published.

ENVIRONMENTALLY BENIGN SILICON SOLAR CELL MANUFACTURING

Y.S. Tsuo
National Renewable Energy Laboratory, Golden, CO 80401, USA
Phone: 303-384-6433, Fax: 303-384-6531, E-mail: simon_tsuo@nrel.gov

J.M. Gee
Sandia National Laboratories, Albuquerque, NM 87185, USA
Phone: 505-844-7812, Fax: 505-844-6541, E-mail: jmgee@sandia.gov

P. Menna
National Agency for New Technologies Energy & Environment, I-80055 Portici, Italy
Phone: 39-81-772-3205, Fax: 772-3299, E-mail: menna@epocal.portici.enea.it

D.S. Strebkov, A. Pinov, and V. Zadde
Intersolarcenter, Moscow 109456, Russia
Phone: 7-095-171-1920, Fax: 7-095-170-5101, E-mail: intersolar@glas.apc.org

ABSTRACT: The manufacturing of silicon devices - from polysilicon production, crystal growth, ingot slicing, wafer cleaning, device processing, to encapsulation - requires many steps that are energy intensive and use large amounts of water and toxic chemicals. In the past two years, the silicon integrated-circuit (IC) industry has initiated several programs to promote environmentally benign manufacturing, i.e., *manufacturing practices that recover, recycle, and reuse materials resources with a minimal consumption of energy.* Crystalline-silicon solar photovoltaic (PV) modules, which accounted for 87% of the worldwide module shipments in 1997, are large-area devices with many manufacturing steps similar to those used in the IC industry. Obviously, there are significant opportunities for the PV industry to implement more environmentally benign manufacturing approaches. Such approaches often have the potential for significant cost reduction by reducing energy use and/or the purchase volume of new chemicals and by cutting the amount of used chemicals that must be discarded. This paper will review recent accomplishments of the IC industry initiatives and discuss new processes for environmentally benign silicon solar-cell manufacturing.
Keywords: c-Si - 1: Manufacturing and Processing - 2: Environmental Effect - 3

1. INTRODUCTION

With the worldwide photovoltaic (PV) solar energy market expanding rapidly and the demand outpacing supply, the crystalline-silicon solar PV module is finally becoming a commercially viable product. Most of the newcomers and the capacity expansions of existing producers are based on either single-crystal silicon grown by the Czochralski (Cz) method or polycrystalline silicon by casting. There are also increasing numbers of suppliers who are developing production equipment for the industry based on best-known practices (BKPs) of silicon solar cell and module processing. Because solar electricity generation is a large-area application, it is likely the PV industry will eventually use more silicon than even the integrated-circuits (IC) industry. It is important at this stage to review the environmental impact of the rapidly growing silicon PV industry and to find opportunities for improving energy efficiency and productivity and reducing environmental impact.

The manufacturing of semiconductor silicon devices - from polysilicon production, crystal growth, ingot slicing, wafer cleaning, device processing, to encapsulation - requires many steps that are energy intensive and use large amounts of water and toxic chemicals. In the past two years, the IC industry has initiated several programs to promote environmentally benign manufacturing, i.e., manufacturing practices that recover, recycle, and reuse materials resources with a minimal consumption of energy. One of the programs is the establishment of the *Engineering Research Center for Environmentally Benign Semiconductor Manufacturing* on April 15, 1996, with an initial funding of US$10 million from the United States National Science Foundation (NSF) and Semiconductor Research Corporation (SRC). Crystalline-silicon modules accounted for 87% of the worldwide PV module shipments in 1997 and 93% of those modules shipped for outdoor applications [1]. Silicon PV module manufacturing has many steps similar to those used in the IC industry. Although the annual sales of the worldwide silicon PV module industry is about 400 times smaller than that of the IC industry, the PV industry consumes about 10% of the worldwide polysilicon production. Obviously, there are significant opportunities for the silicon PV industry to learn from new developments in the IC industry and to implement more environmentally benign manufacturing approaches. Such approaches often have the potential for significant cost reduction by reducing the purchase volume of new chemicals and by cutting the amount of used chemicals that must be discarded. Because PV manufacturing has lower semiconductor material-quality requirements than IC manufacturing, some lower cost and

more environmentally sound processes may be acceptable for PV manufacturing even though they don't meet the stricter requirements of IC manufacturing.

It is not possible to review here in detail all the steps involved in the manufacturing of silicon PV modules. We will simply highlight some areas where we think opportunities exist to make the module manufacturing process more environmentally benign.

2. INDUSTRY INITIATIVES AND RESOURCES

Three recent initiatives by the semiconductor industry in the environmentally benign manufacturing area could produce results that also benefit the PV industry: (1) The National Science Foundation and the Semiconductor Research Corporation jointly established the *NSF-SRC Engineering Research Center for Environmentally Benign Semiconductor Manufacturing* on April 15, 1996 [2]. SRC is a consortium of 65 corporations and government agencies that plans, directs, and funds the semiconductor industry's pre-competitive, long-term research [3]. (2) In April 1997, the international trade association for the semiconductor industry, Semiconductor Equipment and Materials International (SEMI), created a new *Environmental Health and Safety Division* that will explore worldwide environmental priorities for the industry [4]. (3) In October 1997, the Electric Power Research Institute (EPRI) and SEMATECH Corp. formed a new center, the *EPRI Center for Electronics Manufacturing*, to address productivity, environmental, and energy issues in the electronics industry [5]. SEMATECH is a non-profit R&D consortium of U.S. semiconductor manufacturers.

The NSF-SRC Center carries out research in six areas of semiconductor manufacturing: water conservation, plasma processes, wet chemicals, chemical-mechanical polishing, emission of organics, and risk-assessment studies. Some of these research results are presented in a weekly teleconference seminar series hosted by the four participating universities: University of Arizona, Massachusetts Institute of Technology, Stanford University, and University of California-Berkeley [6]. A good source of information on the Environmental, Safety, and Health (ES&H) goals of the semiconductor industry is the ES&H Section of the United States National Roadmap for Semiconductors [7]. In addition to these semiconductor industry organizations, the United States National Photovoltaic Environmental, Health and Safety Information Center [8] regularly publishes information on PV ES&H-related issues [9].

3. POLYSILICON PRODUCTION

For the feedstock material used in crystal growth, the silicon PV industry has been relying on rejected materials from the IC industry. These rejected materials, about 2,100 metric tons in 1997, amount to about 10% of the semiconductor-grade polysilicon used by the IC industry. This arrangement worked well until 1995 when a shortage of polysilicon feedstock began to drive up the cost and limit the growth of the silicon PV industry. If the PV industry continues to grow at the present rate, which in recent years has been higher than the growth rate of the IC industry, and if crystalline silicon continues to be the dominant technology of the PV industry, then we must develop new sources of solar-grade polysilicon. There are two possibilities: (1) build new factories dedicated to the production of low-cost (< US$10/kg), solar-grade polysilicon, and (2) find new ways to use the rejected silicon that is not currently being used, for example, purifying the about 30% of silicon lost from wafer-cutting operations (kerf loss) of semiconductor-grade polysilicon into solar-grade polysilicon. The purity requirements for solar-grade polysilicon, according to the Solar-Grade Silicon Stakeholders Group, are the following: it is preferred that polysilicon have either B or P doping, with no compensation; resistivity at 25°C should be greater than 1 ohm-cm; oxygen and carbon should not exceed the saturation limits in the melt; and the total non-dopant impurity concentration should be less than 1 ppma [10].

More than 98% of semiconductor-grade polysilicon is produced by the trichlorosilane ($SiHCl_3$) distillation and reduction method [11,12]. The trichlorosilane is manufactured by fluidizing a bed of fine pulverized metallurgical-grade silicon (MG-Si), which is more than 98% silicon, with hydrogen chloride in the presence of a copper-containing catalyst. The MG-Si, which costs about US$1/kg, is produced by the reduction of natural quartzite (silica) with coke (carbon) in an electric arc furnace. This method of polysilicon production is very energy intensive [13], and it produces large amounts of wastes, including a mix of environmentally damaging chlorinated compounds. About 80% of the initial metallurgical-grade silicon material is wasted during the process. In addition, the semiconductor-grade polysilicon material produced by this method far exceeds the purity requirement of the PV industry, and the cost (over US$50/kg, with most of it attributable to the $SiHCl_3$ processes) is several times higher than what the PV industry can afford [14]. Every watt of crystalline silicon PV module generating capacity requires roughly 20 g of polysilicon. Thus, if the cost of solar-grade polysilicon is US$20/kg, the cost of polysilicon per watt of a crystalline-silicon PV module is US$0.40. It is obvious that less complicated, less energy intensive, more efficient, and more environmentally benign methods need to be developed to meet the cost and quality requirements of the PV industry. New methods of producing solar-grade polysilicon should either be chlorine free or recycle chlorine internally to reduce cost and avoid damage to the environment.

3.1 Low-Temperature, Chlorine-free Processes for Polysilicon Feedstock Production

The National Renewable Energy Laboratory (NREL) and Sandia National Laboratories (SNL), with funding from the Initiative for Proliferation Prevention (IPP) Program, has initiated a joint research program with the Intersolarcenter to study new chlorine-free methods of producing solar-grade polysilicon. So far, the most promising method developed by this project is one that uses MG-Si and absolute alcohol as the starting materials. This new process requires only 15 to 30 kWh of energy per kg of polysilicon produced vs. about 250 kWh/kg of the trichlorosilane method. The silicon yield (polysilicon and the main by-product, silica sol) is in the 80% to 95% range

vs. 6% to 20% for the trichlorosilane method. The eventual cost goal is US$10 per kg of solar-grade polysilicon.

The basic processing stages of this chlorine-free polysilicon production process are the following:

1. The reaction of metallurgical-grade silicon with alcohol proceeds at 280°C in the presence of a catalyst:

$$Si + 3\,C_2H_5OH \xrightarrow{catalyst} Si(OC_2H_5)_3H + H_2 . \quad (1)$$

2. The disproportion (i.e., simultaneous oxidation and reduction) of triethoxysilane in the presence of a catalyst will lead to the production of silane and tetraethoxysilane:

$$4\,Si(OC_2H_5)_3H \xrightarrow{catalyst} SiH_4 + 3\,Si(OC_2H_5)_4 . \quad (2)$$

3. Dry ethanol and such secondary products as high-purity SiO_2 or silica sol can be extracted by hydrolysis of tetraethoxysilane. The alcohol will be returned to Stage 1.

$$Si(OC_2H_5)_4 + 2\,H_2O \longrightarrow SiO_2 + 4\,C_2H_5OH . \quad (3)$$

4. Silane is decomposed pyrolytically to pure silicon and hydrogen at a temperature of about 900°C:

$$SiH_4 \xrightarrow{850°\text{-}900°C} Si + 2\,H_2 . \quad (4)$$

The purity requirements for solar-grade silicon are not as high as those for electronic applications. Thus, the silane will undergo a simplified cycle of purification, and at Stage 4 the less expensive and less energy-consuming process of a fluidized bed reactor can be used, instead of the well-known Siemens Process [11].

3.2 Purification of Metallurgical Silicon

NREL and ENEA (National Agency for New Technologies Energy & Environment) have proposed a novel method of producing solar-grade polysilicon by directly purifying MG-Si pellets. The process uses the very large surface areas, produced by porous silicon etch on the surfaces of the silicon wafer, as sites for gettering impurities in the subsequent high-temperature annealing. The details of this process will be presented seperately at this conference [15].

3.3 New Sources of Silicon Waste from the Electronic Industry

When wafers are sliced from silicon ingots using a multiple-wire saw, a layer of silicon about 250 micrometers thick is lost per wafer. This kerf loss is higher for inner-diameter (ID) saws. Depending on the wafer thickness, this kerf loss represents from 25% to 50% of the ingot material, several times the quantity of the material that is presently used by the PV industry. Presently, the solar industry uses mainly Cz ingot top and tails, pot scrap, and rejected wafers from the IC industry [14]. If a method can be developed to produce solar-grade polysilicon by purifying the kerf remains of semiconductor-grade ingots, enough polysilicon would be generated for over 300 MW/year of crystalline-silicon solar cells, i.e., more than two times the size of the current silicon solar-cell production.

4. CRYSTAL GROWTH

There are four types of crystalline-silicon solar cells: single-crystal, polycrystalline, ribbon, and silicon film deposited on low-cost substrates. In 1997, market share of the worldwide PV cell and module shipment for the four types of crystalline-silicon solar cells were 49.6% for single-crystal, 34.0% for polycrystalline, 3.2% for ribbon, and 0.4% for silicon film [1]. Crystal growth from a silicon melt generates relatively little waste. The main concern is the energy required and the amount of argon gas used during crystal growth. Electricity and argon needed for Cz growth are the highest among the four types of silicon materials [13]. Recently, however, the world's largest manufacturer of Cz silicon solar cells, Siemens Solar, Industries, announced a joint project with the Northwest Energy Efficiency Alliance to cut the amount of electricity used to grow crystals and yield savings of 40% to 50% [16].

5. WAFER SLICING AND CLEANING

5.1 Wafer Slicing

In the last six years or so, the PV industry has made the transition from using ID saws for wafer slicing to using multiple-wire saws. Multiple-wire saws can improve wafer yield per unit length of ingots by over 50% because of lower kerf loss and thinner wafers. However, wafer slicing is still one of the most expensive processes in silicon solar-cell manufacturing because of the large quantities of consumables (stainless-steel wire and abrasive slurry) and the kerf loss. During wafer slicing, ingots are bonded to a ceramic submount with hot-melt adhesive and sliced into wafers using multiple steel wires to which an abrasive slurry is fed. The slurry is composed of silicon carbide (SiC) and mineral-oil-based or glycol-based slurry vehicle. Oil-based slurry is commonly used by the PV industry. Compared to the water-soluble, glycol-based slurries more commonly used by the IC industry, oil-based slurries produce more environmentally damaging wastes and require more extensive wafer cleaning. The added cost and the process changes needed for the PV industry to switch over to glycol-based slurry need to be investigated. Methods of proper disposal or recycling of the stainless-steel cutting wire also need be studied, as does the effective recovery of the SiC in the slurry. The development of water-base slurries will also help reduce cost and environmental damage.

5.2 Wafer Cleaning and Etching

The cost of chemical waste disposal is high. It is important for the PV industry to find ways to reduce chemical consumption and waste generation through *source reduction, recovery, recycle, reuse, and substitution.* Because wafer cleanliness for PV is not as critical as for IC manufacturing, a safe choice, in terms of making sure the highest quality and most extensive cleaning procedures are used, is not necessarily the right

choice in terms of cost reduction and environmental safety. Certain methods, such as dry cleaning processes, although not adequate for the IC industry standards, may be sufficient for the PV industry. For example, centrifugal shear carbon dioxide cleaning [17] is worth considering as an alternative to organic solvent and/or hot detergent cleaning methods for wafer degreasing and cleaning after slicing. This process uses carbon dioxide in three coexisting phases: liquid, supercritical, and dense-gas. Operating temperature ranges from 298 K to 310 K, and pressure ranges from 56 ATM to 100 ATM. CO_2 gas is non-flammable, non-combustible, and non-corrosive, and is abundant, inexpensive, and reusable. Compressing CO_2 at about 70 ATM and at temperatures below its critical temperature (305 K) liquefies the gas. Compressing CO_2 above its critical temperature and pressure (72.9 ATM) does not cause a phase change, yet the density of the gas may be liquid-like. Static and dynamic cleaning processes employing the multi-phase CO_2 system have been developed. The excellent cleaning abilities derive from a combination of solvent cleaning power and, in the dynamic processes, by physical cleaning action. Although CO_2 at these pressure and temperature conditions presents densities comparable to other cleaning agents (about 500 g/L), it has a viscosity comparable to gases. For instance, it is from 10 to 30 times smaller than 1,1,1-trichloroethane (TCA).

For texture etching and/or surface damage removal, most of the PV industry has been using sodium hydroxide etchant. NaOH etchant is considerably cheaper and easier to dispose of than the conventional hydrofluoric-nitric-acetic acid etchant. In an NREL-funded program, Siemens Solar Industries found that the caustic waste per wafer generated by the saw-damage-removal etching process was reduced by about 20% after the switch from ID saws for wafer slicing to multiple-wire saws [18]. This is because the wire-sawn wafers require less etching to remove saw damage.

The Photovoltaic Device Fabrication Laboratory (PDFL) at Sandia National Laboratories has had a program to continuously monitor and reduce chemical usage since the laboratory began operations in 1989. The chemical waste generation has been reduced by nearly 75% since 1990 by using three procedures: (1) eliminate and/or replace hazardous chemicals, (2) recycle chemicals, and (3) reduce usage of remaining hazardous chemicals. A key feature of this effort was the use of statistical experimental designs to screen chemicals for their effectiveness in wafer cleaning and statistical process control to ensure that chemical-reduction changes did not impact the manufacturing process. An experiment was performed that used statistical designs to examine the effect of 22 different parameters associated with chemical cleaning of wafers. The experiment was able to eliminate a popular, but expensive, chemical (hydrogen peroxide) that is widely used in the IC industry for cleaning silicon wafers. Subsequent experiments and changes in procedure have eliminated sulfuric and phosphoric acids from PDFL.

Hydrofluoric (HF) acid solution is used for wafer cleaning, dopant oxide removal, and diffusion tube and quartzare cleaning. It accounts for a very large percentage of the total hazardous waste generated by silicon solar-cell manufacturing. It is possible to reprocess used HF solutions using reverse osmosis [19]. A cost-benefit analysis indicates that, for a system with a capacity of 1000 gal/day, about one US dollar is the net savings for every gallon of HF solution reprocessed [20].

5.3 Optimizing Water Use and Reuse

The semiconductor industry worldwide spends as much on ultrapure water as on wet chemicals for wafer processing, about US$700 million each in 1996 [21]. The net-feed water use by the IC industry averages about 30 gallons per square inch of wafer processed in 1997. The current United States National Roadmap for Semiconductors recommends decreasing the net-feed water use to 10 gallons/in^2 in 2000 and 2 gallons/in^2 in 2012 [22]. The NSF/SRC Center is studying methods to decrease water usage by more efficient rinse processes, water conservation in cooling, scrubbing and washing, and by lowering idle flows [23].

The silicon PV industry, of course, uses significantly less water per wafer than the IC industry. However, the value of the final product per wafer of the PV industry is orders of magnitude less than that of the IC industry. Obviously, water use by the PV industry is a significant cost factor that needs to be carefully studied. It is also not clear whether the PV industry really needs to use the same high-purity deionized water as that used by the IC industry. Water purity in the semiconductor process is typically measured in a bath with a resistivity monitor. The resistivity is inversely proportional to the ionic concentration of chemicals. At 25°C, water can exhibit a resistivity of 18.2 megaohm-cm if no impurities are present. The American Society for Testing and Materials (ASTM) has set four types of requirements for electronic water [24]. The resistivity (in megaohm-cm) at 25°C for the highest-grade electronic water, Type E-1, should be above 18.0 for 95% of the time and never less than 17.0. Type E-2 should be above 17.5 for 90% of the time and not less than 16.0. Type E-3 should be above 12.0. Type E-4 should be above 0.5. Type E-1 water, which costs 1 to 2 US dollars per 100 gallons, is intended for use in the production of devices having line widths below 1.0 micrometer. Type E-2 water is for line widths below 5 micrometers and is probably more than adequate for even the most critical wafer-cleaning needs of the PV industry. Even Type E-3 may be adequate in most cases.

Reclaiming water is also an important issue to be investigated by the PV industry. For every dollar spent to generate and process ultra-purity water by the IC industry, about $0.60 is spent treating the industrial wastewater. According to SEMATECH, 70% of its members are reclaiming at least some of their water. Careful design of the methods of recycling used water back to the feed makeup for the water purification plant and the methods of reclaiming water for use in support processes, such as cooling and gas scrubbing, is important for reducing the cost of PV manufacturing.

6. SOLAR CELL PROCESSING

For junction diffusion, either a belt furnace or a tube furnace is typically used. Tube furnaces traditionally use a

$POCl_3$ liquid source dopant, which generates toxic P_2O_5 and Cl_2 effluents and requires frequent cleaning of diffusion tubes using HF solutions. Belt furnaces are more environmentally benign because they can use water-soluble, non-toxic, spin-on or spray-on dopants or vapor dopants and do not require HF cleaning. Optically enhanced doping methods, such as the solar furnace doping proposed by NREL [25], are also environmentally benign alternatives.

Edge trimming to remove electrical shorts between the front and back junction can be done either by laser cutting or plasma etching. Because of its very high throughput, $CF_4 + O_2$ plasma etching is commonly used by the PV industry. However, CF_4 is one of the perfluorinated compounds (PFCs) that has no known natural destruction mechanisms, and thus, has a large global-warming potential [26]. The PV industry needs to either find an alternative to the CF_4 and O_2 plasma etch or improve the effluent treatment to include PFC capture and recycling.

Antireflection coatings can be deposited by vacuum evaporation, plasma deposition, atmospheric-pressure chemical vapor deposition, and spin-on liquids. Silane, which is pyrophoric, is commonly used in depositing silicon nitride antireflection coatings [27]. A safer alternative, chlorosilane, which is non-pyrophoric, has been used successfully by the IC industry for silicon nitride depositions [9].

For metal electrodes on the solar cells, it is not desirable to use silver-tin-lead solder baths after screen printing to enhance the conductivity of the metal grids because of the added lead content to the cells.

7. MODULE ASSEMBLY

7.1 No-Clean Flux

Flux, typically a derivative of pine resin, is applied to cell interconnection strips before soldering to act as a deoxidizer and to ensure better adhesion between the solder and solar cells. Conventional flux leaves residues on the cell surfaces that need to be cleaned with a chlorofluorocarbon (CFC) compound. CFCs are known to cause ozone depletion in the atmosphere [28]. Recently, water-soluble fluxes and no-clean fluxes, low-residue fluxes that could be left on the solar cell after soldering have become widely available [29]. In an NREL-funded program, Siemens Solar was able to eliminate the CFC usage in the manufacturing facility by switching from conventional solder paste to a "no-clean" solder paste [18]. The no-clean process both eliminates the environmental damaging CFC emissions and reduces costs. Siemens Solar also found that, by using a water-soluble flux, the CFC usage can be reduced by about 60% over a conventional flux. However, it appeared that water rinse of the cells retained moisture during the lamination sequence and caused module reliability problems.

7.2 Lead-Free Solder

Lead is a well-known hazard to human health. When disposed of in landfills, it can leach into soils and pollute ground water. It is important for the PV industry to remove or minimize the use of lead in modules so that proper disposal at the end of module life will not become a problem [30]. For example, some European countries have proposed a ban on the landfill disposal of electronic products containing lead. There are two sources of lead in a crystalline-silicon PV module: solder-dipped electrodes and solder-coated copper ribbons. The practice of dip-coating solar-cell contact electrodes is no longer necessary with modern screen-printed electrodes, but it is still used by a significant number of module manufacturers. The lead-tin solder that coats the surfaces of copper ribbons for tabbing strips is needed to prevent the oxidation of the copper and to improve the solderability of the ribbons. However, lead-free alternatives to lead-tin solder have been investigated extensively by the printed-circuit-board industry [31]. For example, the National Center for Manufacturing Sciences in Ann Arbor, Michigan, has recently completed a US$10-million project that evaluated 79 lead-free solder alloys and found seven promising replacement candidates [32]. The International Tin Research Institute (ITRI) in Middlesex, England, has also done extensive studies on lead-free solder alloys [33].

A very promising alternative for the tin-36% lead-2% silver ribbon coatings commonly used by the PV industry is the tin-3.5% silver alloy. It is identified as a promising alternative for the standard tin-37% lead alloy by both NCMS and ITRI. The silver in the alloy is needed to increase the pull strength of the ribbon. The 221°C melting temperature, although higher than the 183°C for the standard lead-tin alloy, is acceptable. Because it is a binary alloy, it should have excellent stability. Its resistance to high-temperature fatigue is also good. The present cost of the alloy, at US$0.10 per cubic centimeter, is about twice the standard lead-tin alloy, which is the cheapest of the tin alloys. The cost difference between the silver-tin alloy and the lead-tin-silver alloy is small.

8. CONCLUSIONS

As the silicon PV industry continues to rapidly expand, the environmental impact of its manufacturing processes and products will receive increasing attention. It is particularly important for a renewable energy technology to address its environmental impact during manufacturing because one of the primary benefits of renewable energy generation is its low environmental impact. We have discussed several alternative approaches in this paper that are both cost effective and environmentally benign. However, the manufacturability and reliability of most of these alternative approaches need further investigation. We propose that the silicon PV industry form an association of government laboratories, equipment suppliers, and cell and module manufacturers to promote more environmentally benign manufacturing approaches. This association can also coordinate the PV industry's interactions with the environmental associations of the integrated-circuits and printed-circuit-board industries mentioned in this paper.

REFERENCES

[1] P.D. Maycock, PV News, Feb. 1998.

[2] C.R. Helms, Solid State Technology, March 1997, p.52.

[3] Technical reports on ES&H studies funded by SRC can be found at the Web site www.src.org/resrch/pubs/pubs97/toc/sa_esh.dgw.

[4] A. Bordeaux, Solid State Technology, Dec. 1997, pp.109-112.

[5] SEMATECH's recent reports on ES&H can be found at the Web site www.sematech.org/public/docubase/abstract/tech-5.htm.

[6] The NSF-SRC Seminar Series archive and announcements can be found at the Web site www.erc.arizona.edu. The Web site, ESH Subway – Semiconductors & The Environment at www-mtl.mit.edu/semisubway/esh_subway.html, is also a good starting point for finding information and news about semiconductor manufacturing and the environment.

[7] The ES&H Section of the The United States National Roadmap for Semiconductors is available online at www.sematech.org/public/roadmap/doc/esh_toc.html.

[8] National Photovoltaic Environmental, Health and Safety Project, Biomedical and Environmental Assessment Group, Brookhaven National Laboratory, Upton, New York 11973, USA; Principal Investigators: P.D. Moskowitz (516-282-2017) and V.M. Fthenakis (516-282-2830).

[9] See, for example, V.M. Fthenakis, Prog. Photovolt. Res. Appl. 6 (1998) 91.

[10] Summary of the Panel Discussions of the Sixth Workshop on the Role of Impurities and Defects in Silicon Device Processing, September 1996, NREL/SP-413-21640.

[11] L.C. Rogers, *Handbook of Semiconductor Silicon Technology*, W.C. O'Mara, R.B. Herring, and L.P. Hunt, editors, Noyes Publications, New Jersey, USA, 1990.

[12] P. Frankl, H. Lee, and N. Wolfgnag, *Industrial Ecology*, R.U. Ayres and L.W. Ayres, editors, Edward Elgar Publishing Co., Cheltenham, UK, 1996.

[13] K. Kato, A. Murata, and K. Sakuta, Prog. Photovolt. Res. Appl. 6 (1998) 105.

[14] M.G. Mauk, P.E. Sims, and R.B. Hall, American Inst. of Physics Proceedings, CP404 (1997) 21.

[15] P. Menna, Y.S. Tsuo, M.M. Al-Jassim, S.E. Asher, and T.F. Ciszek, these proceedings.

[16] Solar & Renewable Energy Outlook, April 1998.

[17] D.R. Jackson, Deflex Co. Technical Paper, pp.1-9, 1997.

[18] T. Jester, Final Subcontract Report, 1 April 1992 to 31 May 1995, Report #NREL/TP-411-20016.

[19] D. Mukherjee, A. Kulkarni, A. Chawla, and W.N. Gill, Chem. Engr. Commun. **130** (1995) 127.

[20] A. Kulkarni, D. Mukherjee, and W.N. Gill, Semiconductor International, July 1995, pp.207-212.

[21] M.C. Lancaster, Solid State Technology, Sept. 1996, pp. 70-75.

[22] The United States National Roadmap for Semiconductors is available online at www.sematech.org/public/roadmap.

[23] Annual Report, NSF/SRC Engineering Research Center for Environmentally Benign Semiconductor Manufacturing, April 1997.

[24] American Society for Testing and Materials designation D5127-90, Standard Guide for Electronic Grade Water.

[25] Y.S. Tsuo, J.R. Pitts, M.D. Landry, C.E. Bingham, A. Lewandowski, and T.F. Ciszek, Proceedings First World Conf. on PV Energy Conversion, (1994) 1307.

[26] J. Langan, P. Maroulis, and R. Ridgeway, Solid State Technology, July 1996, pp.115-122.

[27] F. Duerinckx, R. Einhaus, E. Van Kerschaver, J. Szlufcik, J. Nijs, R. Mertens, M. Roy, and S. Narayanan, 26th PV Spcialists Conf. Proc. (1997) pp. 259-262.

[28] T.S. Perry, IEEE Spectrum, Feb. 1993, pp.20-26.

[29] G. Evans and N. Lee, Electronic Packaging & Production, May 1998, p.42.

[30] C. Eberspacher and V.M. Fthenakis, 26th PV Specialists Conf. Proc. 919970 pp. 1067-1072.

[31] B. Trumble, IEEE Spectrum, May 1998, pp.55-60.

[32] National Center for Manufacturing Sciences, "*Lead-Free Solder Project Final Report*," NCMS Project No. 170502. Web site of NCMS is www.ncms.org.

[33] Web site of the International Tin Research Institute is www.itri.co.uk.

II. Thin-Film PV Technologies

PHOTOCHEMICAL SOLAR CELLS BASED ON DYE-SENSITIZATION OF NANOCRYSTALLINE TiO_2

S. K. Deb, R. Ellingson, S. Ferrere, A. J. Frank, B. A. Gregg, A. J. Nozik, N. Park, and G. Schlichthörl
National Renewable Energy Laboratory (NREL), 1617 Cole Boulevard, Golden, CO 80401-3393 USA

ABSTRACT: A photoelectrochemical solar cell that is based on the dye-sensitization of thin nanocrystalline films of TiO_2 (anatase) nanoparticles in contact with a non-aqueous liquid electrolyte is described. The cell, fabricated at NREL, shows a conversion efficiency of ~9.2% at AM1.5, which approaches the best reported value of 10%-11% by Grätzel at EPFL in Lausanne, Switzerland. The femtosecond (fs) pump-probe spectroscopy has been used to time resolve the injection of electrons into the conduction band of nanocrystalline TiO_2 films under ambient conditions following photoexcitation of the adsorbed Ru(11)-complex dye. The measurement indicates an instrument-limited ~50 fs upper limit on the electron injection time. We also report the sensitization of nanocrystalline TiO_2 by a novel iron-based dye, CIS-[Fe^{II}(2,2'-bipyridine-4,4'-dicarboxylic acid)$_2$(CN)$_2$], a chromophore with an extremely short-lived, nonemissive excited state. The dye also exhibits a unique "band selective" sensitization through one of its two absorption bands. The operational principle of the device has been studied through the measurement of electric field distribution within the device structure and studies on the pH dependence of dye-redox potential. The incorporation of WO_3-based electrochromic layer into this device has led to a novel photoelectrochromic device structure for "smart window" application.
Keywords: Dye-sensitized photoelectrochemical solar cel -1: Photoelectrochromic window-2

1. INTRODUCTION

The idea of dye-sensitization of inorganic materials goes back several decades, and a vast body of literature exists on the dye-sensitization of AgBr for photographic applications. The first use of dye-sensitized TiO_2 for solar energy conversion was reported in a U.S. patent issued in 1978, in which a photoelectrochemical cell based on dye-sensitization of TiO_2 particles, particularly in anatase form, was reported [1]. The dye used was N-methylphenazinium ion which extended the spectral response of TiO_2 to the 500-nm region. However, the conversion efficiency of such a device was relatively low and the stability of dye was an issue. A breakthrough occurred in recent years when M. Grätzel and B. O'Regan reported a photochemical solar cell using nanoparticle TiO_2 sensitized by a more efficient and stable Ru(11)-complex dye [2]. The standard dye used in present cells [3] is Ru(11)(4,4'-dicarboxy-2,2'-bipyridine)$_2$(NCS)$_2$ (absorption peak at 550 nm); this system shows conversion efficiencies of 7%-10% under standard solar conditions. A recent new "black" dye (4,9,14-tricarboxy 2,2'-6,6'-terpyridyl ruthenium(11)trithiocyanate) has recently been reported by Grätzel that produces an efficiency of nearly 11% [4].

The photoelectrode of a dye-sensitized PV cell consists of a 10-20-μm film of nanocrystalline TiO_2 particles (10-30 nm in diameter) that contain a monolayer of adsorbed dye molecules; the dye-coated particles are supported on a transparent conducting glass substrate (e.g., tin oxide) (see Fig. 1). The pores of the nanocrystalline TiO_2 film are filled with a liquid electrolyte containing the iodide/triiodide redox couple in a non-aqueous electrolyte, such as acetonitrile. A transparent counter electrode is placed over the nanocrystalline TiO_2, and the edges of the cell are sealed. Upon photoexcitation of the cell, the excited dye molecules inject electrons efficiently into the TiO_2 conduction band, effecting charge separation. The injected electrons traverse the nanocrystalline film with little loss and are collected at the conducting glass substrate. After passing through the external circuit and delivering power to a load, the electrons re-enter the cell at the counter electrode and reduce triiodide to iodide, which then diffuses into the pores of the TiO_2 film to reduce the photo-oxidized dye back to its original state.

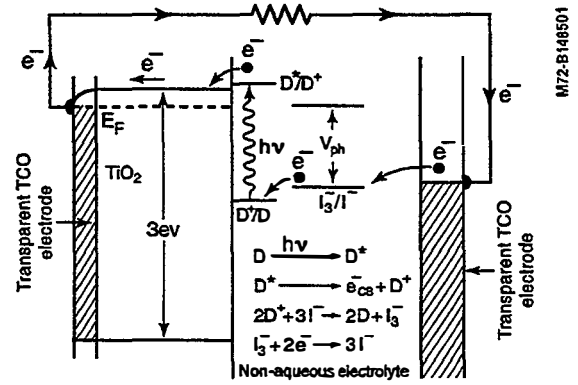

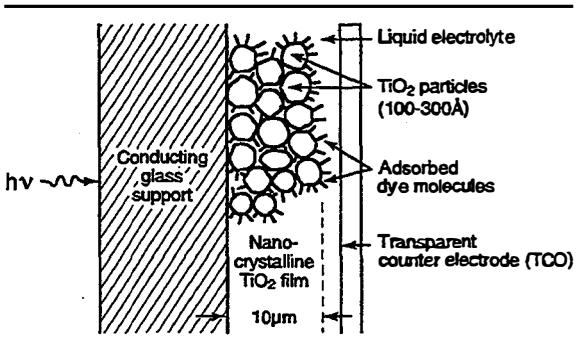

Figure 1: Band diagram and structure of photochemical solar cell

In this paper we report the fabrication of an ~9.2% -efficient cell using an essentially similar technology. Dynamics of electron injection into nanocrystalline TiO_2 films sensitized with Ru-based dye has been studied by transient infrared absorption spectroscopy. We also report the sensitization of TiO_2 by an iron bipyridyl complex, a chromophore with an extremely short-lived, nonemissive excited state.

2. THE NREL PHOTOELECTROCHEMICAL SOLAR CELL PROJECT

The Photoelectrochemical Solar Cell project at NREL is an integrated program of basic and applied research that is jointly planned and funded by the U.S. Department of Energy's Office of Energy Research and Office of Energy Efficiency and Renewable Energy. In this section we discuss our research on the development of dye-sensitized photovoltaic cells and elucidate the operating principle of these devices.

2.1 NREL Cell Preparation and Efficiency

We have fabricated a dye-sensitized TiO_2 solar cell (with no antireflection coating) with a conversion efficiency of 9.2%. This value approaches the best achieved, to date, by the group of Grätzel at EPFL (10%-11%) and is substantially higher than efficiencies reported by other laboratories. The ~9.2% cell displayed a short-circuit photocurrent J_{sc} of 17.899 mA/cm^2, an open-circuit photovoltage V_{oc} of 756 mV, and a fill factor of 68%.

The preparation of TiO_2 film was adapted from the literature [5-6]. A conducting glass plate (Asahi Glass; F-doped SnO_2 overlayer, 80 % transmittance in the visible, 14% haze, 7Ω/sq) was used as the substrate for depositing TiO_2 films. To control the thickness of the TiO_2 film and to mask electrical contact strips, 0.5-cm width of the conducting glass plate was covered along the length of each edge with adhesive tape. A mixture of TiO_2 colloids and TiO_2 powder were deposited on the surface of the conducting glass. After removing the adhesive tapes, the assemblage was heated in air for 30 min at 450°C and then allowed to cool. The TiO_2-covered plate was cut into a 1.25 x 1.2 cm electrode. The film was then immersed in an aqueous 0.3 M $TiCl_4$ solution for 2 days in a closed chamber, washed with distilled water, and annealed again at 450 °C for 30 min. The thickness of the resulting film was about 12 μm.

The TiO_2 electrodes were coated with $[RuLL'(NCS)_2]$ (L = 2,2'-bypyridyl-4,4'-dicarboxylic acid, L' = 2,2'-bipyridyl-4,4-ditetrabutylammoniumcarboxylate). The dye-coated nanocrystalline TiO_2 electrode was soaked in 4-*tert*-butylpyridine for 15 min and then dried under a N_2 stream. Pt counter electrodes with a mirror finish were prepared by electron beam, depositing a 60 nm layer of Pt on top of a 40 nm layer of Ti on a glass plate. The Pt electrode and the dye-coated TiO_2 electrode were sealed together with 25-μm thick strip of Surlyn (Dupont), sandwiched along the length of each edge. Sealing was accomplished by pressing the two electrodes together at a pressure of 900 psi and a temperature of 120 °C. A small quantity of a redox electrolyte, consisting of an alkyl methylimidazolium iodide and I_2 in acetonitrile, was introduced into the porous structure of the dye-covered TiO_2 film by capillary action. The dye-coated TiO_2 film was illuminated through the transparent conducting glass support.

2.2 Improving the Photovoltage Through Surface Modification

A major factor limiting the conversion efficiency of present dye-sensitized TiO_2 solar cells is the low photovoltage [7], which is substantially below the theoretical maximum [8-10]. Charge recombination at the nanocrystallite/redox electrolyte interface is expected to play a significant role in limiting the photovoltage. There are two likely recombination pathways occurring at the interface. The injected conduction-band electrons may recombine with oxidized dye molecules or react with redox species in the electrolyte. Owing to the rapid rate of reduction of the oxidized dye molecules by I^- ions, which are present at high concentration, the contribution of this latter energy-loss channel to the recombination current can usually be ignored [11]. The net recombination process, controlling the photovoltage, is represented by the reaction [6]:

$$2e^- + I_3^- \rightarrow 3I^-$$

Some suppression of back electron transfer in TiO_2, as manifested by a higher open-circuit photovoltage V_{oc}, has been reported [12,13] as a result of chemically treating the surface with 4-tert-butylpyridine.

In this paper, we report on the effect of various surface modifying reagents on V_{oc} and the underlying mechanism [14,15] for their action. An unexpected result is the discovery that the reaction rate for recombination is second order in triiodide ion concentration. The mass-transport theory is also applied to determine whether the nanoporous TiO_2 film impedes the diffusion of triiodide ions in the cell.

The fill factor is also not significantly changed by surface treatment. The major effect of surface treatment is to increase V_{oc} and consequently the cell efficiency. The improved V_{oc} with respect to the untreated surface (V_{oc} = 0.57 V) ranges from 0.64 V for vinylpyridine-treated electrodes to 0.73 V for polyvinylpyridine-treated electrodes, corresponding to respective increases of 70 and 160 mV. The largest improvement was for an NH_3-treated electrode, which yielded a V_{oc} of 0.81 V, corresponding to an increase of 240 mV, and a conversion efficiency of 7.8 %.

To determine whether the nanoporous TiO_2 film impedes the diffusion of I_3^- ions in the liquid phase, the dependence of V_{oc} on the radiant power at low I_3^- concentration was studied, and mass transport theory was applied to the experimental data to obtain the diffusion coefficient of I_3^-. The calculated curve coincides closely with the experimental data for an optimized diffusion coefficient of 7.55 10^{-6} cm^2/s for I_3^- ions in CH_3CN/NMO (50:50 wt%)/TiO_2. After correcting for the TiO_2 porosity (0.3) [16], the diffusion coefficient of I_3^- ions in the solution phase was determined to be 2.5 10^{-5} cm^2/s, which is in good agreement with values obtained for I_3^- ions in CH_3CN [(8.5-30) 10^{-6} cm^2/s] and NMO (2.8 10^{-6} cm^2/s) [17-19]. The similarity of our measured value of the diffusion coefficient with those reported in the literature implies that, in the I_3^- concentration range investigated, most of the I_3^- remains in solution and is not adsorbed to the TiO_2 surface. In other words, the porous structure of the TiO_2 films does not significantly retard the diffusion of I_3^- ions in the solution phase.

2.3 Mechanisms

2.3.1 Time-Resolved Infrared Spectroscopic Studies of Electron Injection in Dye-Sensitized TiO_2

We have used femtosecond pump-probe spectroscopy [20] to time resolve the injection of electrons into nanocrystalline TiO_2 film electrodes under ambient conditions following photoexcitation of the adsorbed dye [Ru(4,4=-dicarboxy-2,2=-bipyridine)$_2$(NCS)$_2$] (N3). Pumping at one of the metal-to-ligand charge transfer absorption peaks and probing the absorption by injected electrons in the TiO_2 at 1.52 μm and in the range of 4.1 to 7.0 μm, we have directly observed the arrival of electrons injected into the TiO_2 film. Our measurements indicate an instrument-limited ~50-fs upper limit on the electron

injection time. We have compared the infrared transient absorption for noninjecting systems consisting of N3 in ethanol and N3 adsorbed to films of nanocrystalline Al_2O_3 and ZrO_2,

Several groups studying the transient absorption of the excited and oxidized states of the dye in the visible and near-IR have reported evidence for ultrafast (<1 ps) charge separation and electron injection. Tachibana *et al.* [21] reported transient absorption measurements at 750 nm which were ascribed to the formation of oxidized N_3 (pumped at 605 nm); analysis of the rise time of the 750-nm absorption indicated biphasic electron injection with injection times of 150 fs (instrument limited) and 1.2 ps. Hannappel *et al.* [22] measured the rise of the near-infrared absorption of injected electrons at 1100 nm following photoexcitation of N3 at the lower-energy metal-to-ligand charge transfer (MLCT) absorption peak (550 nm). However, to obtain unambiguous results, it was necessary for these experiments to be conducted under ultrahigh vacuum (UHV) conditions. Based on time-resolved infrared (TRIR) absorption measurements, our measurements provide further evidence of ultrafast electron injection times (50 fs) for the N3-TiO_2 electrode under ambient conditions. By measuring the time-resolved absorption in the mid-IR, we are able to obtain unambiguous conclusions without the need for UHV. Probing in the mid-IR allows us to bypass the issue of the correct absorption spectrum for oxidized N3 and eliminate the possibility of any signal contributions from the cationic or excited states of the dye.

2.3.2 Induced pH-Sensitivity in Sensitizing Dyes

It was recently reported [23] that the rate of recombination between the electron in the TiO_2 and the oxidized dye was dependent on pH. Because the conduction-band potential of the TiO_2 is known to have a Nernstian dependence on pH, whereas the potentials of the usual family of ruthenium-based sensitizing dyes show little or no pH dependence in solution, it was assumed that varying the pH would vary the driving force for the recombination reaction. Surprisingly, the rate of the electron transfer reaction was independent of pH over a range where it was expected to change by many orders of magnitude.

Here we report measurements on a similar dye and show that, although its oxidation potential is independent of pH when the dye is dissolved in solution, its potential becomes pH-dependent when it is adsorbed on the TiO_2. The pH dependence is close to the 59-mV/unit pH expected theoretically for the flatband potential of an oxide semiconductor. Therefore, in this system, there is little or no change in the difference between the TiO_2 flatband potential and the Ru(II)/Ru(III) potential of the adsorbed dye over the range from pH 2.5 to pH 8. This may explain the lack of pH dependence of the recombination rate observed in reference 23. Therefore, it is not necessary to invoke unusual models of electron transfer to explain the behavior of the dye-sensitized cells. Such a change in pH-dependent behavior of a sensitizing dye upon adsorption has not been previously reported.

We have extended our experiments to include several types of dyes on both semiconducting and insulating surfaces and see similar behavior in all cases. We believe the effect is caused by the dye being inside the Helmholtz plane of the semiconductor; thus, it experiences a substantial fraction of the potential experienced by the semiconductor upon adsorption or desorption of ions such as H^+ and OH^-. The induced pH-dependence of the oxidation potential has implications for the design and optimization of dye-sensitized solar cells. Specifically, it is not possible to independently adjust the potentials of the semiconductor and the dye by the use of potential-determining ions. Although our experiments were in aqueous systems, the same effect should occur in the non-aqueous solvents used in the standard PV cell configuration that contains the potential-determining Li^+ ions.

and found no indication of electron injection at probe wavelengths in the mid-IR (4.1 to 7.0 μm).

2.3.3 PotentialDistribution in Dye-Sensitized Cells

One important factor that has never been clearly understood about the dye-sensitized cells is the distribution of electrical potential through the cell under working conditions. The individual TiO_2 particles are too small to support a space-charge layer, but they are sintered together to form an electrically conducting, porous film. Is there then a space-charge layer across the film at short-circuit and/or at open-circuit? We have investigated this problem by impedance spectroscopy measurements and electrochemical-dye desorption measurements. The results are unambiguous: because of the porous nature of the TiO_2 film, ions can migrate through the film to neutralize any applied fields over very short distances. Therefore, under normal operating conditions, there are essentially no electric fields of range longer than about 10 nm in the cell. It is clear from these considerations that charge motion through the TiO_2 films occurs entirely by diffusion, rather than by drift.

This understanding has important consequences for the design of solid-state analogues of the dye-sensitized cells. Because there are essentially no electric fields present in the dark, an electric field is created by the photoinjection process upon illumination, and this electric field must oppose charge separation. In the standard, solvent-containing configuration, this induced electric field is quickly neutralized by the motion of electrolyte ions, and thus, the electrons can be separated from the holes (oxidized ions). However, in the solid-state analogues proposed and studied so far, there have been no mobile electrolyte ions. The conversion efficiency in such systems has been uniformly low. We now believe this was caused by the induced, uncompensated electric field in such cells that opposed charge separation. It should be possible, however, to design a solid-state version of these cells that contains mobile electrolyte ions that will eliminate this problem.

3. PHOTOSENSITIZATION OF TiO_2 BY IRON-BASED DYE

Herein we report the sensitization of nanocrystalline TiO_2 by CIS-[Fe^{II}(2,2'-bipyridine-4,4'dicarboxylic acid)$_2$(CN)$_2$], a chromophore with an extremely short-lived, nonemissive excited state. The complex was prepared via a modified procedure of Schilt [24]. Its absorbance spectrum exhibits one bipyridyl based π-π^* transition (318 nm) and two MLCT bands (430 nm, 635 nm, with a shoulder at ~550 nm). The complex adsorbs out of a 10^{-3} M methanolic solution containing 20 mM chenodeoxycholic acid [25] onto nanocrystalline films of TiO_2 [26], rendering the films a dark blue. Under white-light illumination of approximately "one sun" (75 mW/cm^2, $\lambda > 400$ nm) in a regenerative cell configuration, a short-circuit photocurrent of 290 μA/cm^2 and an open-circuit photovoltage of -360 mV are obtained. No attempt was made to optimize the cell performance.

This is the first report of a substantial photosensitization effect by an iron(II) bipyridyl complex. Like those of bipyridyl complexes of ruthenium(II), their intense visible absorptions are due to excitation into initially singlet MLCT states via $t_{2g} \rightarrow \pi^*$ electronic transitions.

The photocurrent action spectrum for [Fe^{II}(2,2'-bipyridine-4,4'-dicarboxylic acid)$_2$(CN)$_2$] on TiO_2 is superimposed upon the absorption spectrum of the adsorbed dye. It can be seen that the photocurrent action spectra qualitatively trace the dyes' absorbance features. To our knowledge, this is the first observation of a "band selective" sensitization phenomenon. A precise explanation for why injection is more efficient from one of two absorption transitions is not yet possible without detailed knowledge of the excited-state configuration of [Fe^{II}(2,2-bipyridine-4,4'-dicarboxylic acid)$_2$(CN)$_2$][27].

4. PHOTOELECTROCHROMIC CELLS

A dye-sensitized solar cell electrode was recently combined with an electrochromic film to produce what we called a "photoelectrochromic" window [28]. Because of the complementary nature of the two technologies, we were able to combine just one half of a typical dye-sensitized solar cell with one half of a typical electrochromic cell. The electrochromic film was deposited on the counterelectrode of a dye-sensitized solar cell and lithium ions were added to the electrolyte solution. The I_2 required in the electrolyte for high-power solar cells was eliminated in order to maximize the photovoltage, and a low concentration of a more transparent dye was employed as the sensitizer. In this configuration, the photovoltage produced by the dye-sensitized electrode drives electrons and compensating Li^+ cations into the WO_3 film, resulting in a colored electrochromic film. When illumination ceases, the potential of the charged WO_3 film causes the coloration process to reverse, expelling Li^+ from the WO_3 film and transferring electrons, via the external circuit, back to the oxidized iodine species in solution.

5. ACKNOWLEDGMENTS

This work was supported by the Office of Basic Energy Sciences, Division of Chemical Sciences (B.A.G., A.J.N., G.S., and A.J.F.) and the Office of Utility Technologies, Division of Photovoltaics (S.K.D., N.P., S.F.), U.S. Department of Energy.

REFERENCES

[1] S. Chen, S. K. Deb, H. Witzke, U.S. Patent 4,080,488, March 21, 1978.
[2] B. O'Regan, M. Grätzel, Nature **353** (1991) 737.
[3] M.K. Nazeeruddin, A. Kay, I. Rodicio, R. H. Backer, E. Mueller, P. Liska, N. Viachopoulos, M. Grätzel, J. Am. Chem. Soc. **115** (1993) 6382.
[4] M. Grätzel, AIP Conf. Proc. **404** (1997) 119
[5] M. Grätzel, K. Kalyanasundaram, Curr. Sci **66** (1994) 706.
[6] G. Smestad, C. Bignozzi, R. Argazzi, Sol. Energy Mater. Sol. Cells **32** (1994) 259.
[7] A. Stanley and D. Matthews, Aust. J. Chem. **48** (1995) 1294.
[8] A. Matthews, P. Infelta, M. Grätzel, Aust. J. Chem., in press.
[9] G. Smestad, Sol. Energy Mater. Sol. Cells **32** (1994) 273.

while injection is relatively efficient (10%-11%) from the higher energy MLCT (~420 nm), injection is much less efficient (~2%) from the lower energy MLCT transition (~600 nm). For all dyes heretofore reported in the literature,

[10] P. Liska, Ph.D. Thesis of Swiss Federal Institute of Technology, No. 1264 (1994).
[11] A. Hagfeldt, S. E. Lindquist, M. Grätzel, Sol. Energy Mater. Sol. Cells **32** (1994) 245.
[12] M. Grätzel, K. Kalyanasundaram, Current Science **66** (1994) 706.
[13] M. Grätzel, Platinum Metals Rev. **38** (1994) 151.
[14] S.Y. Huang, G. Schlichthörl, A.J. Nozik, M. Grätzel, A.J. Frank, J. Phys. Chem. **101** (1997) 2576.
[15] G. Schlichthörl, S.Y. Huang, J. Sprague, A.J. Frank, submitted.
[16] N. Papageorgiou, M. Grätzel, P. P. Infelta, Sol. Energy Mater. Sol. Cells, in press.
[17] V.A. Macagno, M.C. Giordano, and A.J. Arvia, Electrochimica Acta **14** (1969) 335.
[18] P. G. Desideri, L. Lepri, D. Heimler, Encyclopedia of Electrochemistry of the Elements; Bard, A. J Ed.; Marcel Dekker, Inc., New York **1** (1973) 91.
[19] N. Papageorgiou, Y. Athanassov, P. Bonhôte, H. Pettersson, M. Grätzel, J. Electrochem. Soc., in press.
[20] R. J. Ellingson, J. B. Asbury, S. Ferrere, H. N. Ghosh, J. Sprague, T. Lian, A. J. Nozik, J. Phys. Chem. (1998) in press.
[21] Y. Tachibana, J. E. Moser, M. Graetzel, D. R. Klug, J. R. Durrant, J. Phys. Chem. **100** (1996) 20056.
[22] T. Hannappel, B. Burfeindt, W. Storck, F. Willig, J. Phys. Chem. B **101** (1997) 6799.
[23] S.G. Yan, J. Hupp, J. Phys. Chem. **100** (1996) 6867.
[24] A. A. Schilt, J. Am. Chem. Soc. **82** (1960) 3000.
[25] A. Kay, M. Grätzel, J. Phys. Chem. **97** (1993) 6272.
[26] A. Zaban, S. Ferrere, J. Sprague, B. A. Gregg, J. Phys.Chem. B **101** (1997) 55.
[27] S. Ferrere, B. A. Gregg, J. Am. Chem. **120** (1998) 843.
[28] C. Bechinger, S. Ferrere, A. Zaban, J. Sprague, B. A. Gregg, Nature **383** (1996) 608.

A WIDE-GAP A-SiC:H PV-POWERED ELECTROCHROMIC WINDOW COATING

W. Gao, S.H. Lee, Y. Xu, D.K. Benson, S.K. Deb and H.M. Branz
National Renewable Energy Laboratory,
1617 Cole Blvd., Golden, CO 80401, USA

ABSTRACT: We report on the first monolithic, amorphous-silicon-based, photovoltaic-powered electrochromic window coating. The coating employs a wide bandgap a-$Si_{1-x}C_x$:H n-i-p photovoltaic (PV) cell as a semitransparent power supply, and a $Li_yWO_3/LiAlF_4/V_2O_5$ electrochromic (EC) device as an optical-transmittance modulator. The EC device is deposited directly on top of a PV cell that coats a glass substrate. The a-$Si_{1-x}C_x$:H PV cell has a Tauc gap of 2.2 eV and a transmittance of 60% to 80% over a large portion of the visible light spectrum. We reduced the thickness of the device to about 600 Å while maintaining a 1-sun open-circuit voltage of 0.9 V and short-circuit current of 2 mA/cm^2. Our prototype 16 cm^2 PV/EC device modulates the transmittance by more than 60% over a large portion of the visible spectrum. The coloring and bleaching times of the EC device are approximately 1 minute under normal operating conditions (±1 volt). A brief description of photoelectrochromic windows study is also given.
Keywords: a-Si – 1: Wide gap – 2: Electrochromic window – 3

1. INTRODUCTION

A variable-transmittance coating, based on reversibly coloring electrochromic (EC) material, has significant potential applications in architectural windows, the automobile industry, sunglasses, and toys[1,2]. With their ability to modulate solar energy transmittance, EC-coated windows could provide substantial total energy savings considering the worldwide production of flat glass is ~1 billion m^2 per year, and new windows installed in the United States are ~60 million m^2 per year [1,3].

Computer models predict that applications could be highly cost effective when a building's energy management system is constructed from independent, smart components[4]. This system would replace centralized controls with distributed smart components, each reacting to the local environment and energy management requirements. However, the technology presently requires costly low-voltage wiring throughout the building. A monolithic, self-powered tandem PV-EC device would eliminate the need for wiring to each window and should reduce costs[4]. The challenge is to create a window that is easy to manufacture and install, and has sufficient contrast between the bleached and colored states. A semitransparent PV power source distributed over the entire window is a good candidate system.

Electrochromism in transition-metal oxides has been studied extensively since its discovery in 1969[5]. The fundamental mechanism of the change in optical properties remains controversial[6,7]. However, for device engineering a simple phenomenological model suffices. The features of an EC material (e.g., WO_3) that are important for EC-device operation are that (a) a reversible insertion-phase compound is formed with small, mobile ions (e.g., Li^+), and (b) each ion inserted induces an optical absorption center[8,9]. Thus, by inserting and extracting Li^+, the optical absorption of a WO_3 film can be continuously and reversibly varied. Transport of Li^+ in and out of a WO_3 film is balanced by an equal but opposite electron current as given by the reversible reaction:

$$WO_3 + yLi^+ + ye^- \leftrightarrow Li_yWO_3 \quad (1)$$

which converts transparent WO_3 into optically absorbing Li_yWO_3 and back again. The concentration of Li^+, y, determines the absorption coefficient of the Li_yWO_3 film and thus the optical properties of the darkened EC device. In most EC devices, an ion storage layer (e.g., V_2O_5) undergoes a complementary reaction similar to Equation (1), but there is no corresponding color change. An ion conductor layer (e.g., $LiAlF_4$) ensures that all current flow through the device must be carried by Li^+ ions instead of electrons. The color-state of the complete device is determined by the applied electrostatic potential[10].

The monolithic, tandem PV/EC device (see Fig. 1) requires a transparent PV coating that still outputs enough voltage to drive the EC device and enough current to operate the device at a reasonable speed. For the EC device currently employed, a 25-mC/cm^2 charge is required to finish a darkening or bleaching process. To darken the window in 5 minutes requires only about 0.1 mA/ cm^2 current density from the PV device. This gives room to increase the bandgap and reduce the thickness of a standard terrestrial PV device in order to reach a reasonable bleached-state transparency.

Although there is a considerable body of research on wide-bandgap silicon-carbon alloys, we believe this is the first project to utilize a semitransparent solar cell made entirely of a-SiC:H material[11]. The main technical challenge lies in reducing the thickness to less than 100 nm for semitransparency. When semitransparent PV devices become very thin, the PV device may develop shorts more easily and render the PV/EC stack useless. This problem has made the fabrication of monolithic PV/EC devices challenging.

To realize a monolithic PV/EC structure, each of the nine layers of the tandem device as shown in Fig. 1 (left), our target design, must be optimized to obtain good device performance. In Fig. 1 (left), transparent conducting oxide (TCO) is used for each conducting layer to maximize the device transmittance. By connecting three conducting layers to a battery and controlling circuitry, the device could be fully controlled by the user in the manual mode or automatically controlled by external circuitry. The device can be colored under the light by connecting the top and bottom TCO. When the coloration processes

finish, extra energy generated by the PV device could be stored in a rechargeable battery via the middle contact. This energy could be used to bleach the EC device when necessary.

Earlier, we reported side-by-side testing of prototype PV and EC devices[12,13], however, this approach hid some problems we encountered when constructing the monolithic, stacked PV/EC device. Fig. 1 (right) shows the device structure reported here. We used thin gold as the top electrode to save time and improve reproducibility during our preliminary fabrication processes. The middle contact was removed to avoid the PV-shorting problem temporarily. In this way, we are able to stack the PV-EC device together and study the other opto-electronic characteristics of the device.

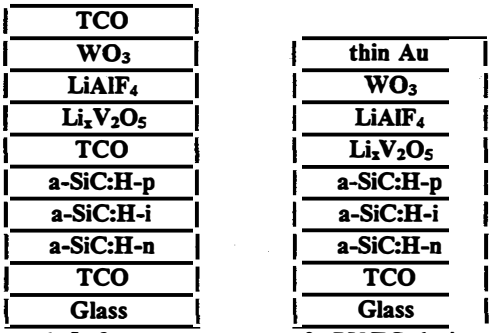

Figure 1: Left, target structure of a PV/EC device. The upper half is EC and the lower half is PV. The middle contact permits battery charging and user control. Right, present device structure. When the top and the bottom conductors are connected, the device darkens. An external power is used to bleach the device.

When the device is short-circuited under illumination, the light generates photovoltaic voltage in the PV part, which raises the potential applied to the EC part. This potential difference drives a coloration current through the EC device equal to the current flow through the PV device. To bleach the device, an external voltage is applied between top and bottom electrodes. The bleaching current flows through both the EC and PV portions. In this situation, the PV device is forward biased and presents a small potential barrier that the external power source has to overcome. The size of the barrier is related to the current. At a high bleaching current, this barrier is about same as the open-circuit voltage of the PV device.

In this paper, we report our studies of wide-bandgap semitransparent a-$Si_{1-x}C_x$:H and its incorporation in PV cells, briefly review the EC device characteristics, and describe integration of these devices into a monolithic PV/EC stack. Details of EC device optimization are reported elsewhere[14]. A brief discussion of photoelectrochromic (PEC) device is also given for comparison.

2. EXPERIMENTAL

The PV part of the electrochromic window is fabricated by plasma-enhanced chemical vapor deposition (PECVD) on a smooth SnO_2:F-coated glass substrate, in a single-chamber deposition system. The three layers of the n-i-p solar cell are all made of a-$Si_{1-x}C_x$:H materials. The radio frequency power is between 3 and 6 watts for a 5x5 cm^2 substrate. At approximately 200°C to 220°C substrate temperature and a working pressure of 0.5 to 3 torr, the deposition rate is 1-2 Å/s. Optimized thicknesses of the n, i, and p layers are roughly 10, 40, and 10 nm, respectively. Thicknesses were measured with a Tencor alpha-step 200-step profilometer. Light and dark conductivities were measured using a Keithley 6517A electrometer and an ELH light at 100 mW/cm^2. Following our previous work[12], we define the semitransparency gap, E_{st}, as the photon energy at which the absorption coefficient is $5x10^4$ cm^{-1} (at this energy, approximately half of the photons is absorbed through a 1000-Å film). We calculated E_{st} from optical transmission spectra measured on a Cary 2300 spectrophotometer. The Tauc gap is roughly 0.3 eV below E_{st} in our a-$Si_{1-x}C_x$:H.

The EC part of the electrochromic window is composed of thin-film WO_3 (the electrochromic layer); $LiAlF_4$ (the ion conductor); and V_2O_5 (the ion-storage layer). They are deposited in a thermal-evaporation system by using pure WO_3 powder, a mixture of LiF and AlF_3 powder, and pure V_2O_5 powder, respectively. Their thicknesses are WO_3, 120 nm; $LiAlF_4$, 1000 nm; and V_2O_5, 500 nm. A 55-nm layer of lithium is deposited after V_2O_5 (equivalent to $Li_{1.2}V_2O_5$), and 8.5 nm of gold are used as a semitransparent top contact. The current deposition sequence shown in the Fig. 1 (right) is based on the consideration of preventing the hygroscopic-lithiated $Li_{1.2}V_2O_5$ layer from absorbing water vapor from the air. By properly controlling the layer thickness, the coloring and bleaching voltages are adjusted for compatibility with the underlying PV device. Improvements in transparency would be expected if the Au layer were replaced by a transparent conducting oxide layer. The coloration-cycling measurement were done using a 670-nm laser detected by a photodiode. The hermetic sealing is performed by covering the device with a second glass layer, filling the space with dry nitrogen, and sealing the edges with epoxy.

3. RESULTS AND DISCUSSIONS

3.1 a-SiC:H Material Properties

Extensive research has been reported on amorphous silicon-based wide-bandgap materials, especially on a-$Si_{1-x}C_x$:H[11]. It is well known that the bandgap increases as more carbon is incorporated. Although the amount of carbon incorporated into the film depends on the deposition condition, the relation between optical bandgap and carbon content of a-Si:H material is relatively universal. This had led to the observation that the optical bandgap, E_g, depends linearly on carbon context, x[11],

$$E_g(x)=E_g(x=0)+1.68x, \qquad (2)$$

for x between 0 to 0.4. However, as C is added, photoelectronic properties always deteriorate. By hydrogen dilution of the precursor gases, it is possible to make a material that has a bandgap about 0.4 eV greater than a-Si:H while preserving reasonable photoelectronic properties[15].

Fig. 2 shows the optical absorption spectra of films grown with varying C content. E_{st} is successfully adjusted by varying the methane-to-silane ratio in the gas phase during the PECVD deposition. By changing this ratio from 0.67 to 2, E_{st} is increased from 2.25 eV to

2.5 eV (Tauc bandgap from 1.94 to 2.19 eV), equivalent to 10% to 26% of carbon incorporated into the film according to Eqn. (2). Absorption within the spectral region of maximum human eye sensitivity is significantly reduced. If the bandgap were pushed to a higher value, the photoconductivity would be decreased dramatically[11]. In order to keep a reasonable output from this a-$Si_{1-x}C_x$:H solar cell, the material with 2.5-eV semitransparency gap is used as the i-layer material during our solar cell fabrication. The deposition parameters and measurement results of our chosen material are listed in Table 1.

Table 1: Deposition parameters and properties of the a-$Si_{1-x}C_x$:H intrinsic layer.

SiH_4 (sccm)	CH_4 (sccm)	H_2 (sccm)	Power (mW/cm^2)	P (Torr)	E_{at} (eV)	σ_{ph} (ns/cm)	σ_{ph}/σ_d ($x10^4$)
5	10	75	73	3	2.5	77	18

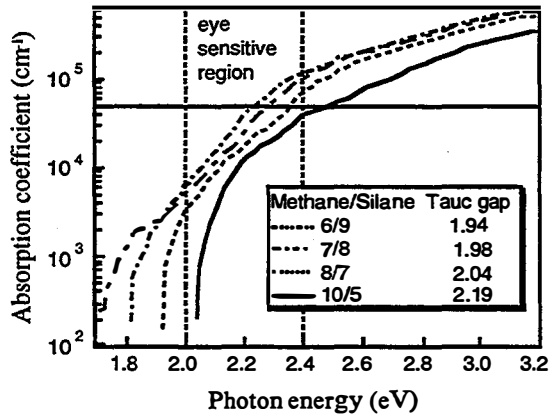

Figure 2: Absorption coefficient curves for the films deposited at different methane/silane ratios.

3.2 PV Device Optimization

To reduce the absorption from the PV portion of the device, one must minimize the thickness of each layer while maintaining a high output voltage to drive the EC device. It is clear that there is a lower limit on device thickness—the best combination of the layer thickness and properties is a compromise between different factors.

A series of thickness-optimization experiments were therefore carried out. The open-circuit voltage (V_{oc}) falls when the p and n layers are thinned beyond a critical thickness. This is due to the weakening of the built-in potential. Our optimized n- and p-layer thicknesses were about 100 Å. The most critical optimization is that of the i-layer. Fig. 3 shows the change of V_{oc}, short-circuit current density (J_{sc}), fill factor (FF), and conversion efficiency of an a-SiC:H solar cell when the i-layer deposition time is reduced from 20 min to 5 min. When the i-layer is less than 40-nm thick, pinholes dramatically degrade the performance of the device. The best results for a PV device at the i-layer thickness of 40 nm are V_{oc}, 0.9 V; J_{sc}, 2 mA/cm^2; FF, 0.5; and efficiency, 1%. This is measured under a Xenon lamp solar simulator

Clearly, I_{sc} and the conversion efficiency are reduced dramatically with the i-layer thickness. However, it is noticeable that the I_{sc} does not change proportionally to the i-layer thickness (I_{sc} is roughly halved when the i-layer thickness changes to 1/4). This shows the effect of improved collection efficiency at higher field intensity inside the i-layer. Another noticeable fact is that V_{oc} decreases from 865 mV at 1600 Å to 741 mV at 400 Å. This phenomenon has previously been reported in crystalline-Si solar cell studies[16,17]. The general trend of V_{oc} change when the device thickness is decreased is determined by the competition of surface and volume recombination. When surface recombination is dominating, V_{oc} will drop with decreasing device thickness, but when volume recombination is dominating, V_{oc} will increase. From this point of view, our device is in a surface-recombination controlled regime even though special attention has been paid to graded buffer layer doping and to interface cleaning during fabrication.

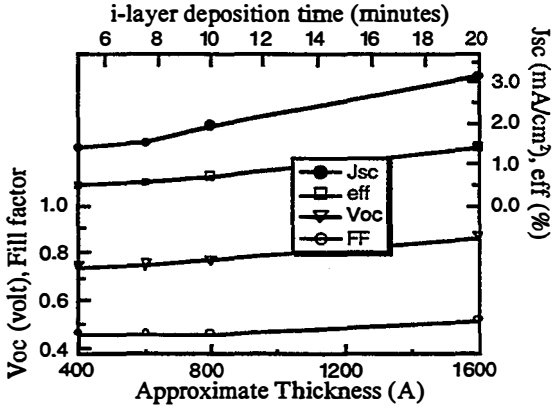

Figure 3: I-V curve parameters of a-SiC:H solar cells versus i-layer thickness.

3.3 EC Device Characterization

Fig. 4 shows transmittance and current density change of an EC test device as a function of time. The device was alternately colored at -1.0 volt and bleached at +1.0 volt. Its transmittance changes between 63% and 20% at 670 nm between the bleached and colored states. At -1 volt (negative bias to the WO_3), the transmittance of the device decreases and approaches its saturation value after 2 min. When the voltage is reversed, the bleaching process finishes in about 1 min. The much shorter bleaching time compared to the coloring process is due to a different Li driving potential. The bleaching-saturation current density is less than 10 $\mu A/cm^2$ due to the low parasitic electronic conductivity of the $LiAlF_4$ ion electrolyte. This device exhibits a good open-circuit optical memory, which is desirable for the present application.

3.4 PV and EC Integration

Fig. 5 shows the transmittance spectra of a 16 cm^2 monolithic PV/EC device with the structure shown in Fig. 1 (right). It is colored by short-circuiting the top and bottom transparent electrodes under 1-sun illumination, and is bleached by applying 2 volts with a polarity that forward biases the PV device. These spectra are shown in the two upper curves of Fig. 5. The bottom curve shows a more deeply colored state obtained by applying 0.6 volt of external coloring voltage to augment the 1-sun PV voltage. Our PV/EC device shows a relative transmittance change of more than 60% at 670 nm under 1-sun illumination, and a 80% change when the small external voltage is applied. The deeper coloration with the external voltage indicates potential to improve the device contrast either by designing for higher PV voltage or by improving the EC device. The absence of a middle

conductor in this device required that both coloring and bleaching current flow through the PV and EC device all the time. Therefore, the 2-volt bleaching voltage includes the part required to overcome a built-in potential from the PV device (about 0.8 volt). In the final retrofit electrochromic window structure, a middle contact layer will be inserted for user control and the option of PV battery charging. This effort is ongoing.

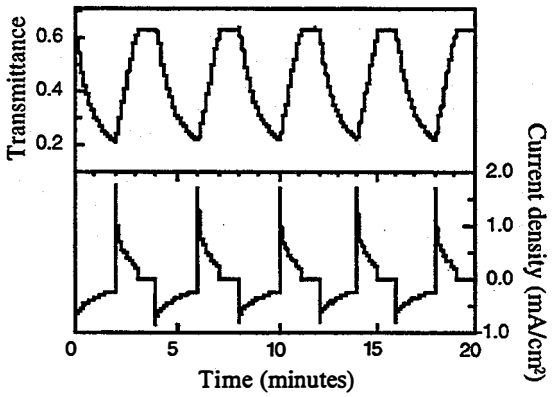

Figure 4: Potentiostatic cycling test measured with a 670-nm laser. Each polarity (±1 volt) is applied for 2 min.

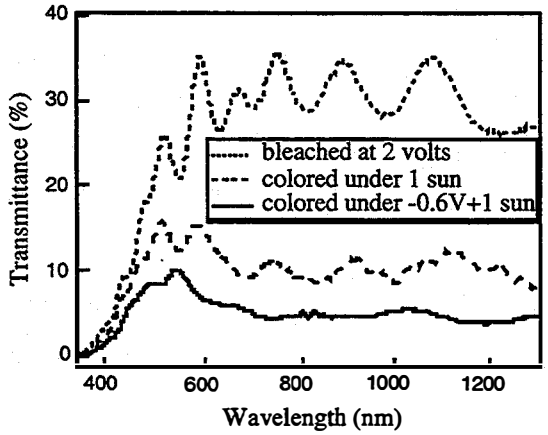

Figure 5: The transmittance spectra of PV/EC device at colored and bleached states under different conditions.

3.5 PEC Windows

NREL has developed an alternative photoelectrochromic device for the self-powered smart window application[18]. The light-absorbing function in the PEC cell is performed by a dye-sensitized semiconductor electrode that produces a photo-voltage sufficient to color the EC film deposited on the counter electrode. A high-surface-area transparent TiO_2 film, consisting of ~30nm-diameter TiO_2 particles sintered at 450°C, is coated with an adsorbed sensitizing dye. Light absorption by the dye leads to electron injection into the TiO_2 followed by re-reduction of the oxidized dye via electron transfer from I^- in solution. The injected electrons move through the TiO_2 film to the contacting SnO_2 electrode and then into the external circuit. The dye coverage was kept low to make the cells almost transparent in the "off" state; The counter electrode was prepared by thermal evaporation of a 500-nm-thick layer of WO_3 onto an indium-tin-oxide coated glass substrate. Cells were fabricated ranging in size from 1 to 25 cm^2.[18].

Self-powered PEC cells have several advantages over the use of conventional photovoltaics for large-area window or display applications. It is a simple device that is easily assembled without electrical shortcircuits. The light-absorbing dye layer can be made optically thin by either reducing the thickness of the TiO_2 layer or by decreasing the concentration of the adsorbed dye. However, because there are only two terminals, there would be less user control compared with the electrochromic window device reported here.

4. CONCLUSIONS

We have made the first monolithic, amorphous-silicon-based, photovoltaic-powered electrochromic window coating. The thickness of the PV device has been reduced to about 600 Å while maintaining 1-sun open-circuit voltage of 0.9 V and short-circuit current of 2 mA/cm^2. The current preliminary design demonstrates most of the features required for a practical, self-powered electrochromic window coating. Design improvements have been identified that could enhance the performance and operational flexibility of the PV/EC coating.

ACKNOWLEDGEMENT

We thank A. Madan and A. Catalano from MVSystems, Inc., for their help in providing a-Si:H deposition facilities and for helpful discussion. This work was supported by OER/BES Advanced Energy Projects of DOE under contract No. DE-AC 36-83CH1009.

REFERENCES

[1] Carl M. Lampert. Solar Energy Materials and Solar Cells **32** (1994) 307.
[2] C.G. Granqvist. Solid State Ionics **53-56** (1992) 479.
[3] S.P. Sapers, et al. 1996 Society of Vacuum Coaters, 39th Annual Technical Conference Proceedings (1996) p 248-255.
[4] D.K. Benson and H.M. Branz. Solar Energy Materials and Solar Cells **39** (1995) 203.
[5] S.K. Deb. Appl. Opt. Suppl. **3** (1969) 193.
[6] S.K. Deb. Philos. Mag. **27** (1973) 801.
[7] R.S. Crandall and B.W. Faughnan. Phys. Rev. Lett. **39** (1977) 232.
[8] B.W. Faughnan, R.S. Crandall and P. Heyman. RCA Review **36** (1975) 177.
[9] R.D. Rauh and S.F. Cogan. J. Electrochem. Soc. **140** (1993) 378.
[10] J.N. Bullock and H.M. Branz. SPIE: Optical Materials Technology for Energy Efficiency and Solar Energy Conversion **2531** (1995) 152.
[11] J. Bullot and M. P. Schmidt. Phys. Stat. Sol. (b) **143** (1987) 345.
[12] J.N. Bullock, C. Bechinger, D.K. Benson, H.M. Branz. J. Non-Cryst. Solids **198-200** (1996) 1163.
[13] C. Bechinger, et al. J. Appl. Phys. **80** (1996) 1226.
[14] S.H. Lee, et al. to be published.
[15] A. Matsuda, et al. J. Appl. Phys. **60** (1986) 4025.
[16] H. Kiess, et al. 11th E.C. Photovoltaic Solar Energy Conference 1992 p. 241.
[17] M.A. Green, et al. 13th E.C. Photovoltaic Solar Energy Conference 1995 p. 13.
[18] C. Bechinger, et al. Nature **383** (1996) 608.

THE INFLUENCE OF CHARGE EFFECT ON THE GROWTH OF HYDROGENATED AMORPHOUS SILICON BY THE HOT-WIRE CHEMICAL VAPOR DEPOSITION TECHNIQUE

Qi Wang, Brent P. Nelson, E. Iwaniczko, A. H. Mahan, R. S. Crandall, and J. Benner
National Renewable Energy Laboratory, 1617 Cole Blvd., Golden, CO 80401 USA

ABSTRACT: We observe at lower substrate temperatures that the scatter in the dark conductivity on hydrogenated amorphous silicon (a-Si:H) films grown on insulating substrates (e.g., Corning 7059 glass) by the hot-wire chemical vapor deposition technique (HWCVD) can be five orders of magnitude or more. This is especially true at deposition temperatures below 350°C. However, when we grow the same materials on substrates with a conductive grid, virtually all of our films have acceptable dark conductivity (< 5 x 10^{-10} S/cm) at all deposition temperatures below 425°C. This is in contrast to only about 20% of the materials grown in this same temperature range on insulating substrates having an acceptable dark conductivity. We estimated an average energy of 5 eV electrons reaching the growing surface in vacuum, and did additional experiments to see the influence of both the electron flux and the energy of the electrons on the film growth. Although these effects do not seem to be important for growing a-Si:H by HWCVD on conductive substrates, they help us better understand the important parameters for a-Si:H growth, and thus, to optimize these parameters in other applications of HWCVD technology.
Keywords: Vienna Conference - 1: HWCVD - 2: Conductivity - 3: Electron emission.

1. INTRODUCTION

Hydrogenated amorphous silicon (a-Si:H) grown by the traditional plasma-enhanced chemical vapor deposition (PECVD) technique is now used in numerous commercial electronic applications. After more than 20 years of research, this technique is mature relative to other growth methods. It fabricates device quality a-Si:H materials and devices, and is a controllable process that can be scaled up. A major drawback is the slow deposition rate for producing the high quality material, which limits the throughput for device manufacturing. Increased deposition rate can bring the cost down. Clearly there is a demand for alternative deposition to grow high-quality material at higher deposition rates. A recent report of achieving 9.8% [1] initial solar cell efficiency at 17 Å/sec deposition rate in the small scale using HWCVD suggests that this could be a good candidate. The advantages of the HWCVD relative to PECVD include: 1. The growth rate for high-quality a-Si:H can be much higher [2] (more than 10 times); 2. The a-Si:H produced by HWCVD is more stable [3]; and 3. The structure of the high-quality a-Si:H is different and more dense [4]. While the process of HWCVD is very easy to operate, the technique is not as well understood. HWCVD materials can be superior to PECVD materials, but the variation in material properties from laboratory to laboratory and over the course of a batch of depositions is much greater. In this paper, we report the observation of non-uniform electronic properties of a-Si:H material grown at certain conditions [5], present an overview of the HWCVD process, speculate on the role of the electrons emitted from the filament on the material quality, and propose ways to grow films with uniform electronic properties.

2. EXPERIMENTAL

We deposit a-Si:H films on 1 in x 1 in glass (Corning 7059 glass) in a HWCVD reactor. The standard conditions for growing a-Si:H film use 20-50 sccm of SiH_4 and 10 mT pressure. All the films are about 1 μm thick. Here we give a brief description of the HWCVD deposition technique. We use a straight or spiral tungsten filament with a diameter of 0.5 mm and place it 4-5 cm below the substrate. A spiral shaped filament has proven to better accommodate to the thermal stress due to the heating and cooling of the filament, enabling an increase in the filament lifetime. A typical lifetime of the filament varies from 5 to 9 hours depending on deposition conditions. Tungsten reacts with SiH_4 at lower filament temperatures, which forms alloy and ultimately causes the filament to break. The filament itself is a research subject, and we do not discuss it in this paper. The filament is heated by an AC or DC current (14 A) to about 1900 °C. A process gas, such as silane, passes by the hot-filament, dissociates, and leads to a-Si:H deposition on the substrate.

We use two different methods to heat the substrate, this leads to two different HWCVD reactors. Fig. 1 shows the schematic diagram of the two HWCVD reactors. Our first reactor utilized a six-way cross (we name it the cross reactor, see Fig 1a.). The substrate is mounted on the bottom of the sample holder and an external heater heats the sample holder and the substrate. The temperature of the substrate is monitored using a thermocouple attached to the outside of the top flange. In this design the top part of the cross is hot and the rest is cold. The filament is placed below the substrate, and the direction of gas flow is perpendicular to the filament. The details of this HWCVD reactor are reported elsewhere [6]. Our new reactor design places a stainless-steel tube inside the vacuum chamber (we name it the tube reactor, see Fig. 1b.), and the tube is heated using a resistive heating wire wrapped around the outer tube. Substrates are placed in the middle of the tube and can be transported to the load lock. This design produces an isothermal region in the middle of the tube and ensures the uniformity of the substrate temperature. The filament is placed inside the tube and below the substrate, and parallel to the gas flow.

We measure dark conductivity vs. spatial position on an a-Si:H film using a Keithley electrometer model 619 or 6517a. The thickness of the film is measured using a Tencor Instrument Alpha-Step 200 profilometer. For charge-collection measurement, we use an electrically isolated stainless-steel plate as a collector, position it next

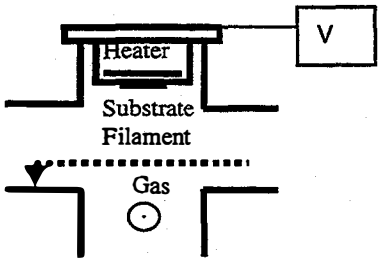

Figure 1a: The HWCVD cross reactor

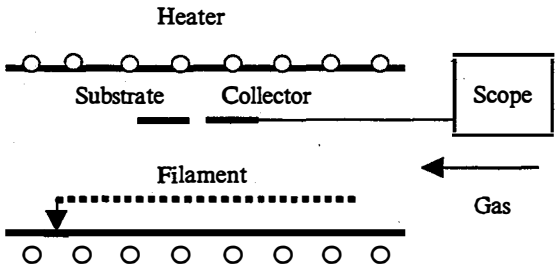

Figure 1b: The HWCVD tube reactor. Tube is side the vacuum chamber which is not shown.

to the substrate in the tube reactor, and use an oscilloscope to monitor the charge collected by the plate during the time the filament is on as shown in Fig. 1b.

3. RESULTS AND DISCUSSION

We originally observe at a lower substrate temperature (220°C), that the scatter in the dark conductivity on films grown on insulating substrates (e.g., Corning 7059 glass), by the HWCVD in the cross reactor can be as much as five or more orders of magnitude. Fig. 2 shows the mapping of the dark conductivity across a 1 in x 1 in substrate. This effect is enormous: the film at the edge of the substrate has a typical low dark conductivity while the value in the middle is almost 5 orders of magnitude higher, even on such a small scale as a 1 in x 1 in substrate. To understand this behavior we have concentrated on two ideas. The first one is the non-uniformity of the temperature distribution across the substrate, where the temperature in the center differs from that on the edge. It is well known that substrate temperature does affect the quality of the film. The results of this research have been published elsewhere [5]. The idea investigated in this paper deals with the charging of the insulting substrate by electrons emitted from filament. As we shall show that the charge on the edge is likely to discharge while the charge in the center which remains will affect the film quality. We will describe and demonstrate how electrons are released from the hot filament, how the electrons interact with process gas in the gas phase, and how the electrons contribute to reactions at the substrate surface.

The filament is directly heated by passing a current. The hot filament provides a heat source and also a source of electrons. Without the presence of process gas, the HWCVD reactor is just like a vacuum tube. Based on the vacuum-tube theory, the emission current density J_c follows

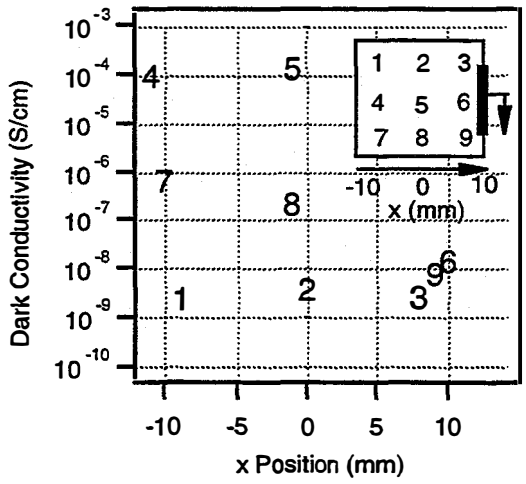

Figure 2: The mapping of dark conductivity of a-Si:H on glass substrate at 220°C substrate temperature. Inserted figure is the glass substrate and the numbers indicate the positions on the film that conductivity be measured. The dark strip on the side is grounded metal clips to hold substrate.

Richardson's law:

$$J_c = A_c T^2 \exp(-E_w/kT), \qquad (1)$$

where A_c is a constant which is a function of the material, E_w is the work function of the material, and T is the emission temperature. J_c increases with increasing filament temperature.

We use tungsten as the filament material. There is a report using Tantalum as the filament material [7]. The advantages of tungsten are low cost and high filament temperature. For tungsten, A_c equals 60 A/cm^{2}K^2 and E_w equals 4.5 eV. At 2200 K, J_c equals 14.4 mA/cm^2, corresponding to 9 x 10^{16} electrons/sec cm^2.

We measure the electrons coming out of the hot filament in the tube reactor. The setup is described in Fig. 1b. Electrons emitted from the filament pass through the vacuum region, hit the isolated collector, and cause a current flow to the ground. The signal is monitored using an oscilloscope. Fig. 3a shows the voltage applied to the filament as a function of time, and Fig. 3b shows the monitored charge signal. For a DC current (DC+) with the filament voltage positive relative to the collector, there is no signal. Electrons are suppressed by the high potential at the filament relative to the collector and no electrons pass through the vacuum region. For a DC current (DC-) with the filament voltage negative to the collector, there is a constant negative signal. Electrons accelerate in the vacuum region and reach the collector. For an AC current, the collected signal becomes more complicated: the signal varies with time. As previously mentioned, there are no signals for every positive voltage cycle. For every negative voltage cycle, there is a negative signal, but with two humps. These two humps are due to magnetic field changes

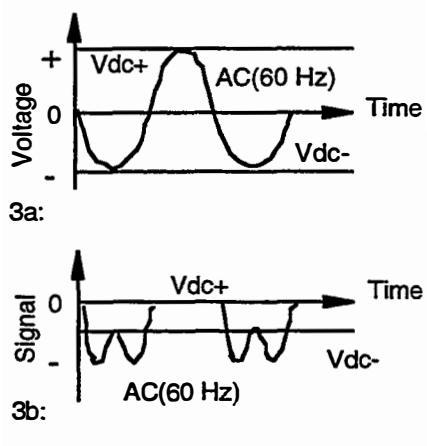

Figure 3: Results of charge-collection experiment. The voltage arrow applies to the filament and the signal arrow represents the oscilloscope monitoring.

in response to the electric field varying with time. The magnetic field influences the emission of electrons from the filament and also the trajectory of the electrons entering in the vacuum. An additional complication is that the electron distribution in the vacuum is not uniform because of the voltage drop across the filament. In our system, a typical voltage drop on the filament is about 8-10 V. We estimate that the average energy which electrons reach the substrate is about 4-5 eV in vacuum.

We feel there is a need to better understand the mechanism of the HWCVD technique. HWCVD is a complicated process, illuminating the substrate with heat, light, and electrons. A simplified model could be that HWCVD is composed of thermal CVD, photo-CVD, and PECVD.

The principal mechanism of HWCVD deposition is that SiH_4 molecules hit the hot filament and decompose into one Si and four H, and are evaporated into the reaction region. These atoms collide with other SiH_4 that does not hit the hot filament. The reactions can be described as:

$$Si+SiH_4 \rightarrow SiH_3+SiH \quad (2)$$

and

$$H+SiH_4 \rightarrow SiH_3+H_2 . \quad (3)$$

It is these Si containing radicals which reach the substrate and make a deposition. The interested reader can find more information in E. Molenbroek's thesis [8].

We measure the light intensity at the substrate surface is about 3-4 Suns (300-400 mW/cm^2) using a crystal Si photodiode in our reactor configuration. Most photons are in infrared region because the filament temperature is about 2200 K. We do not discuss how the light interact with gases and at the substrate surface in this paper.

The electrons interaction with process gases is unavoidable, because there are high electron densities at the surface of the filament. The electron reaction with SiH_4 is well-known, for example:

$$e^- + SiH_4 \rightarrow SiH^+_3 + H + 2e^- . \quad (4)$$

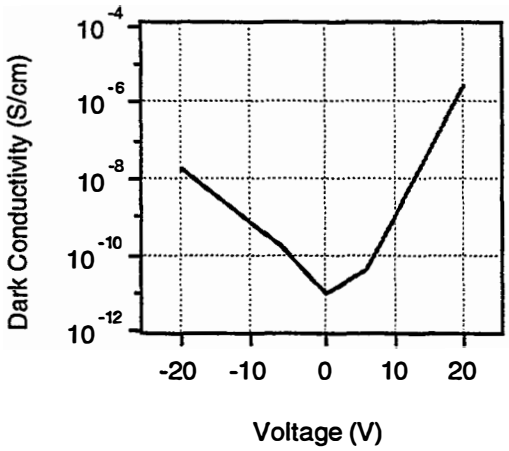

Figure 4: The effect of bias on the a-Si:H film quality. The represents the value of many sample data.

We did a preliminary study of the effect of voltage bias on the substrate on the film quality in the cross reactor. We float the substrate by isolating the top flange with a Viton O-ring instead of the copper gasket and use nylon bolts instead of stainless-steel bolts. We apply the DC voltage directly to the top flange relative to the ground (see Fig. 1a.). The substrate is attached to the flange. The drawback of this arrangement is that base pressure is higher than our conventional configuration.

It is worthy to note that electrons even without any voltage bias have an average energy of 5 eV. Hence, applying a bias will increase or decrease the electron energy. Fig. 4 shows the film dark conductivity as a function of bias in a range from –20 to 20 V. It shows that bias does affect the film quality. It seems that the best-quality material is near zero bias, while high bias increases the dark conductivity. Certainly a better bias experiment design, such as a diode or a triode electrode is needed to re-confirm this effect.

Finally, we report on our observations of how electrons react at the substrate surface. We design two experiments to test if it is the electrons coming from the filament that influence the electronic properties of growing a-Si:H films. One uses a metal grid on an insulating substrate. The idea is to have electrons discharge through the grid. The other experiment involved increasing the substrate temperature. The conductivity of the film increases with the temperature, and electrons can be discharged more easily [5].

We put two different substrates into the tube reactor. One is a plane, 25 mm x 25 mm Corning 7059 glass and the other is a 7059 glass, with an Ag grid put on the surface using a silver epoxy. The grid divides the substrate into nine areas of open glass, approximately 7 mm x 7 mm, with a conductive border around all four outside edges of the open area. After growing a film simultaneously on both substrates, we measure the conductivity on both substrates at similar locations (nine positions on each). Fig. 5 shows the dark conductivity in the grid sample made at 220°C substrate temperature as a function of its position. The scatter of the dark conductivity is much suppressed compared with the data presented in Fig. 2. The variation is

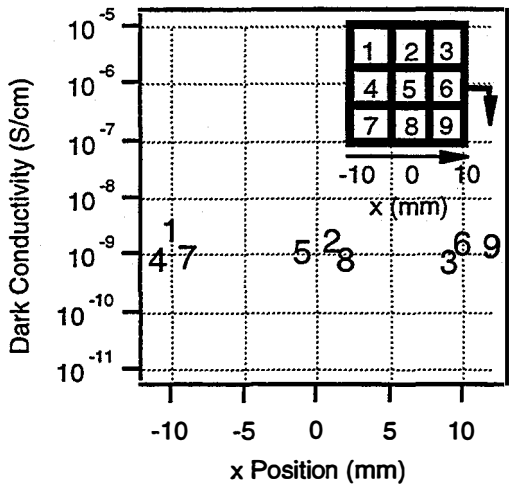

Figure 5: The effect of Ag grid on the dark conductivity. Sample is made at 220°C substrate temperature.

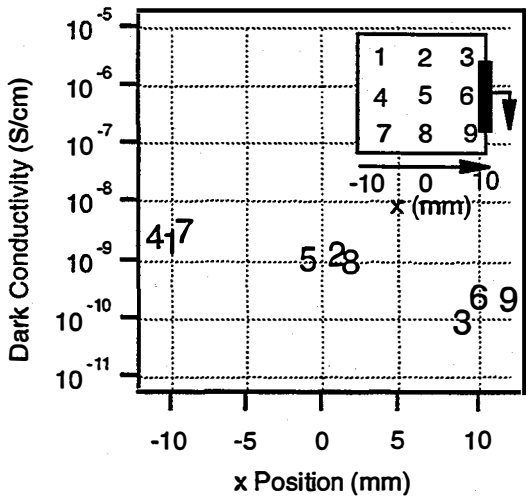

Figure 6: The effect of higher substrate temperature (350°C) on the dark conductivity of a-Si:H material. The dark strip on the side is grounded metal clips to hold substrate.

limited to one order of magnitude. This indicates that the grid does help to discharge the substrate.

We also find that our samples made at above 350°C substrate temperature have much less scatter in the dark conductivity. Fig. 6 shows the results of dark conductivity of a sample made at 350°C. The results are consistent with our premise that electrons charge the insulating substrate. At higher substrate temperature, the conductivity of the film increases enough to enable the electrons to be discharged from the film.

While the effects we report do not seem to be important for growing a-Si:H by HWCVD on conductive substrates or at higher substrate temperatures, it helps us better understand the important parameters for a-Si:H growth and thus to optimize these parameters for other applications of the HWCD technology.

ACKNOWLEDGMENTS

We gratefully acknowledge helpful discussions with Howard Branz and Yueqin Xu. This work is supported by the U.S. Department of Energy under contract No. DE-AC36-83CH10093.

REFERENCES

[1]. A.H. Mahan, R.C. Reedy Jr, E. Iwaniczko, Q. Wang, B.P. Nelson, Y. Xu, A. C. Gallager, H. M. Branz, R. S. Crandall, J, Yang, and S. Guha, in Amorphous and Microcrystalline Silicon Technology -1998, MRS Proc. 1998, in press.

[2]. A.H. Mahan, J. Carapella, B.P. Nelson, R.S. Crandall, and I. Balberg, Jour. of Appl. Phy. 69, 6728 (1991).

[3]. A.H. Mahan and M. Vanecek, Amer. Inst. of Phy. Conf. Proc. 234, 195 (1991).

[4]. Y, Wu, J.T. Stephen, D.X. Han, J.M. Rutland, R.S. Crandall, and A.H. Mahan, Phys. Rev. Lett. 77, 2049 (1996).

[5]. B. P. Nelson, Qi Wang, E. Iwaniczko, A.H. Mahan, and R.S. Crandall, in Amorphous and Microcrystalline Silicon Technology -1998, MRS Proc. 1998, in press.

[6]. M. Vanecek, A.H. Mahan, B.P. Nelson, and R.S. Crandall, Proc. 11th European PV Solar Energy Conf. Edited by L. Guimaraes, W. Palz, C. Dereyff, H. Kiess, and P. Helm (Harwood Acad. Publ., Switzerland, 1993), p. 96.

[7]. S. Bauer, W. Herst, B. Schroder, and H. Oechsner, in 26th PVSC IEEE 1997, p. 719.

[8]. E.C. Molenbroek, PhD Thesis, University of Colorado, Department of Chemistry, 1995.

THE MORPHOLOGY, MICROSTRUCTURE, AND LUMINESCENT PROPERTIES OF CdS/CdTe FILMS

M.M. Al-Jassim, R.G. Dhere, K.M. Jones, F.S. Hasoon, and P. Sheldon
National Renewable Energy Laboratory, 1617 Cole Blvd., Golden, CO 80401, USA
Phone: (303) 384-6602, Fax: (303) 384-6446, E-mail: mo@nrel.gov

ABSTRACT: This paper is concerned with the characterization of CdS/CdTe polycrystalline thin films for solar cells. The morphology, microstructure, and luminescent properties are studied by a powerful array of characterization techniques. The presence of pinholes in 100-nm thick CdS is observed. The microstructure of CdS and CdTe films is shown to be heavily faulted polycrystalline. The effect of deposition temperature on the grain size and the microstructure is investigated. The interdiffusion of sulfur and tellurium at the CdS/CdTe interface is studied for the first time by a nanoprobe technique. Considerable amount of sulfur is detected in CdTe in the vicinity of the interface of samples deposited at 625°C. The recombination behavior of grain boundaries and intragrain defects is investigated in as-deposited and heat-treated samples.
Keywords: CdTe - 1: Defects - 2: Interface - 3

1. INTRODUCTION

Considerable amount of work has been done on the development of CdS/CdTe solar cells over the last 10 years. However, little has been reported on the microstructure of these films or the recombination behavior of structural defects in them. Further, the interdiffusion issue at the CdS/CdTe interface has so far been studied only by low spatial resolution techniques such as secondary ion mass spectrometry (SIMS) and Auger depth profiling. Preliminary transmission electron microscopy (TEM) investigation [1] showed that CdTe films are heavily faulted with a high density of structural defects. Atomic force microscopy (AFM) examinations proved to be a very powerful approach to study the morphology of as-deposited and heat-treated CdTe films [2]. The CdS/CdTe interface has been a subject of many studies. SIMS was used to study the interdiffusion of sulfur and tellurium [3, 4]. However, SIMS probes relatively large areas and the depth resolution is very sensitive to the surface roughness of the CdTe film. Similarly, X-ray diffraction was extensively used to study the CdS/CdTe interface [5, 6]. Again, this probes relatively large areas and the results can be ambiguous.

In this work, the morphology, microstructure, interface chemistry, and the luminescent properties of the CdS/CdTe system were investigated. The aim in CdS is to optimize the film thickness, grain size, and defect density. In CdTe, the objective is to achieve a better understanding of the nature, generation, three-dimensional distribution, and recombination behavior of structural defects. Further, a direct and unambiguous measurement of interdiffusion at the interface was sought.

2. EXPERIMENTAL

The substrates used in this study were either SnO_2-coated Corning 7059 borosilicate glass, or (100) Si wafers. The latter were used to facilitate TEM cross-sectional sample preparation. The CdS films were grown on these substrates by chemical bath deposition (CBD) using a solution of ammonium acetate, cadmium acetate, thiourea, and ammonium hydroxide in deionized water [7]. The film thickness was varied from 15 to 100 nm by varying the deposition time from 10 to 40 min. Prior to CdTe deposition, the CdS films were heat-treated in a hydrogen ambient for 15 min at 400°C. The CdTe films were deposited by close space sublimation (CSS) in a He/O_2 mixture with a total reactor pressure of 15-30 torr [3]. The substrate temperature varied from 425°-625°C. The source temperature was adjusted to obtain a deposition rate of about 1.5-2 μm/min. CdTe films with a nominal thickness of 3-4 μm were used. The heat treatment was carried out by dipping the CdTe films in $CdCl_2$/methanol solution (25% to 75% of saturated solutions) for 15 minutes at 55°C, followed by heat treatment at 400°C in a 4:1 volume ratio He/O_2 ambient for 30 min. The film morphology was studied by high resolution, field-emission scanning electron microscopy (FESEM). The structural characterization was carried out by conventional and high resolution TEM. The chemical analysis of the CdS/CdTe interface region was performed in a field-emission analytical TEM using energy-dispersive X-ray spectroscopy (EDS) analysis. The probe size used was in the 1-2 nm range. The recombination behavior of structural defects, such as grain boundaries, was probed using room-temperature cathodoluminescence imaging in a conventional SEM.

3. CdS

The CdS grain size was studied as a function of film thickness. Fig. 1 shows a CdS film deposited for 15 min, resulting in a film thickness of approximately 40 nm. The average grain size in

this film is approximately 30 nm which corresponds to the film thickness. However, increasing the film thickness to 100 nm did not give rise to a linear increase in grain size. This is illustrated in Fig. 2, which is a FESEM micrograph of a 100 nm thick film, exhibiting an average grain size of 60 nm.

One of the main objectives of this study is to establish the minimum CdS film thickness at which a continuous film is achieved. Examining the thinnest sample (10-min deposition, 20-nm film) indicated that large areas of the SnO_2 film are covered by CdS. However, the coverage is not complete. Increasing the deposition time to 15 min resulted in a higher surface coverage. Nonetheless, two undesirable features were clearly revealed by FESEM. The first is gross discontinuities in the CdS film, and the second is a high density of pinholes (Fig. 1). The size of the gross discontinuities observed was up to 10 μm. What we refer to as pinholes here, however, are features on the order of a micron or less. As the deposition time increased, both the size of the discontinuities and their density decreased. At 30 min of deposition, the large discontinuities shrunk in size to the 1-2 μm range, and the density of the pinholes decreased significantly. At 35 min of deposition, the film thickness is ~100 nm. The gross film discontinuities are virtually absent, but pinholes are still clearly evident. Increasing the deposition time to 40 min or more resulted in undesirable film properties, such as the deposition of fine-grain material on the film's surface and the incorporation of particles in the film. These particles are believed to be caused by homogeneous nucleation of CdS in the solution.

The chemical properties of the gross discontinuities were investigated by Auger electron spectroscopy (AES). Such analysis revealed that many of these discontinuities are bare SnO_2 film. This is indicative of a lack of CdS nucleation in these areas. Such a nucleation could have been inhibited by the contamination of these areas on the SnO_2 film surface. Other AES analyses showed that some of these areas comprise a thinner CdS film than the matrix. This was clearly shown in AES surveys taken within and adjacent to one of these regions. Both analyses revealed CdS; However, after a short 1-min sputter, only SnO_2 signal was detected from the defective region. This is clearly indicative of the low CdS film thickness in these regions. Furthermore, AES analyses revealed the presence of oxygen and carbon in many of these regions. This supports the hypothesis that this type of defects is caused by contamination. The latter is likely to originate from impurity species in the chemical bath itself [8].

4. CdTe

TEM cross-sectional examination was performed on CdTe films deposited at different temperatures [Fig. 3]. The grain size in as-deposited CdTe increased significantly with increasing substrate temperature. However, no correlation was observed between the grain size of the CdTe and that of the underlying CdS. This is contrary to our previous findings on CdTe deposited by physical vapor deposition [1]. We believe this results from the CSS deposition being a higher temperature process, with a higher surface mobility during growth.

Figure 1: SEM micrograph of a 40-nm thick CdS Film, showing gross discontinuities and pinholes.

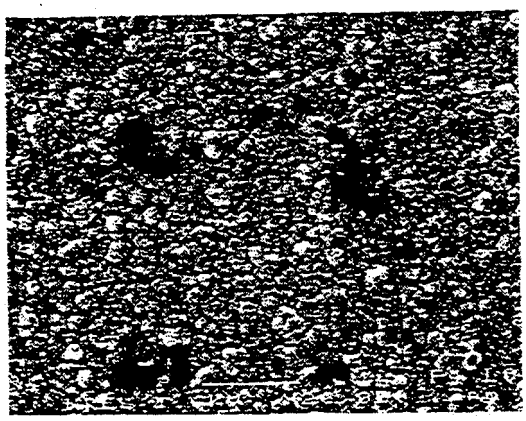

Figure 2: SEM micrograph of a 100-nm thick CdS Film, showing pinholes.

As-deposited CdTe films were found to be heavily faulted with a high density of planar defects and threading dislocations. Fig. 3 shows TEM cross-sections of CdTe films deposited at 425, 525 and 625°C. This figure clearly shows the high density and the three-dimensional distribution of planar defects. These defects are primarily stacking faults and micro-twins on {111} planes. Their density, however, varies from one grain to another. Additionally, cross-sectional examination revealed that the defect density decreases as the film thickness increases. We believe this is largely due to the annihilation of stacking faults as a result of interaction on intersecting {111} planes.

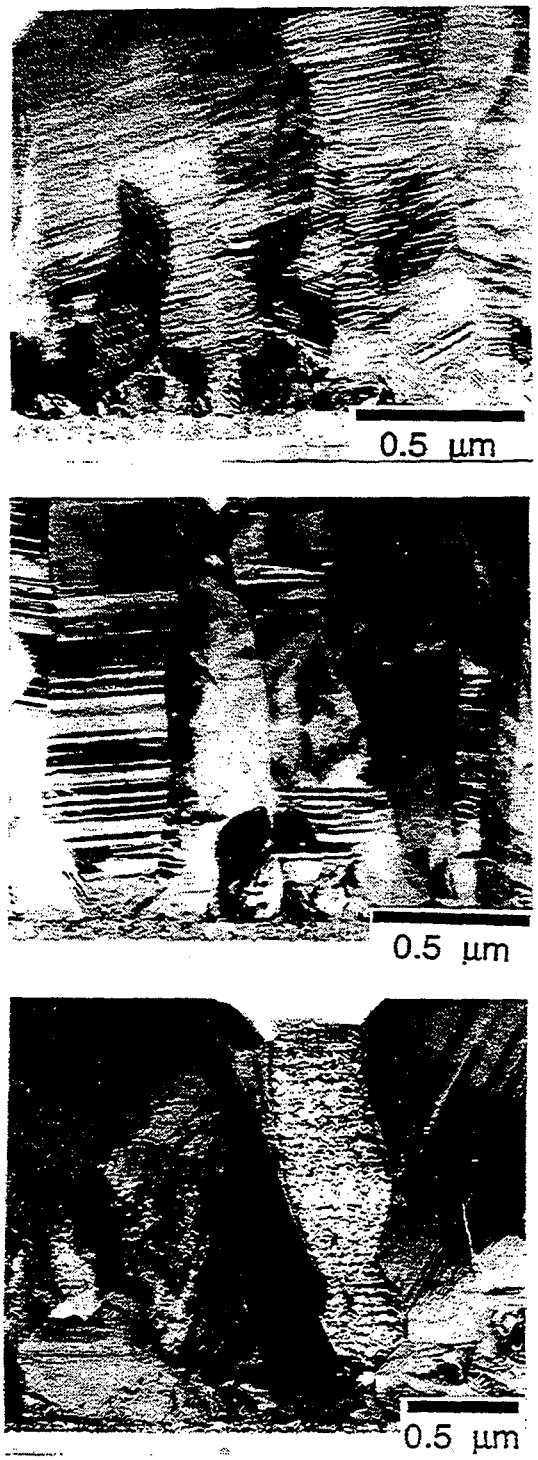

Figure 3: TEM cross-sections of CdTe films deposited at: top, 425°C; middle, 525°C; and bottom, 625°C.

However, the defect density is not affected by substrate temperature. Furthermore, high-resolution investigation of the CdS/CdTe interface region in $CdCl_2$-treated samples revealed a very complex defect structure. An extremely high density of stacking faults was observed in the vicinity of the interface. This is believed to be caused by the sulfur diffusion into CdTe and the alloying of the interface region. We observed that the composition of this CdS_XTe_{1-X} interface alloy is very non-uniform. Therefore, it is conceivable that the boundary between the cubic tellurium rich CdS_XTe_{1-X} and the hexagonal sulfur rich CdS_XTe_{1-X} is a stacking fault.

EDS elemental analysis was performed on samples deposited at 425° and 625°C with no heat treatment. The analyses were carried out using line scans and stationary probe. In the linescan analysis mode, a 2-nm probe was moved across the interface region in 2-nm increments. The dwell time on each point was set at 100 s to achieve good counting statistics. Cd, Te, and S were analyzed and plotted as a function of position. Fig. 4 shows such analysis for the sample deposited at 425°C. Clearly, the interface is fairly abrupt with an interface width on the order of 25 nm. EDS analysis of the sample with a CdTe film deposited at 625°C revealed startlingly different results (Table I). Stationary probe analysis was performed at 20nm from the interface, and 1.5 µm away. Clearly, a considerable amount of sulfur is diffusing into CdTe giving rise to what is believed to be an alloyed CdS_XTe_{1-X} region. The extent of this region and how that is affected by deposition and post-deposition treatment is currently being investigated.

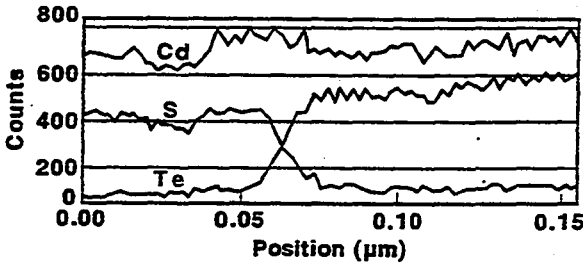

Figure: 4: High resolution EDS elemental line-scans across the interface of a 425°C sample.

Table I: EDS chemical analysis of CdTe.

	Near Interface	1.5 µm away
Cd	51.45%	52.29%
Te	38.31%	46.65%
S	10.24%	1.05%

Cathodoluminescence (CL) was performed on as-deposited and $CdCl_2$-treated samples in both

plan-view and cross-sectional configuration. To minimize the error in estimating the carrier recombination efficiency at defect sites, linescan measurements were performed. However, it must be cautioned here that the effect of surface topography could not be eliminated. Fig. 5 shows a CL linescan across an as-deposited CdTe film revealing a very high degree of non-radiative recombination at grain boundaries and at intragrain defects. Fig. 6 is a similar CL linescan on the same sample after $CdCl_2$ treatment. This indicates a factor of two reduction in the recombination efficiency at grain boundaries and at intragrain defects. This is clearly indicative of the passivating effect of the $CdCl_2$ treatment.

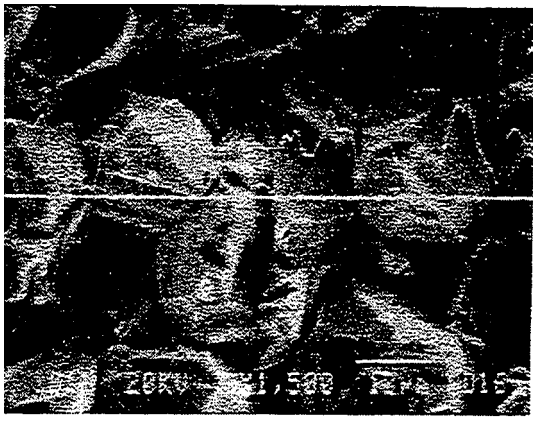

Figure 5: CL linescan superimposed on an SEM image of an as-deposited CdTe film.

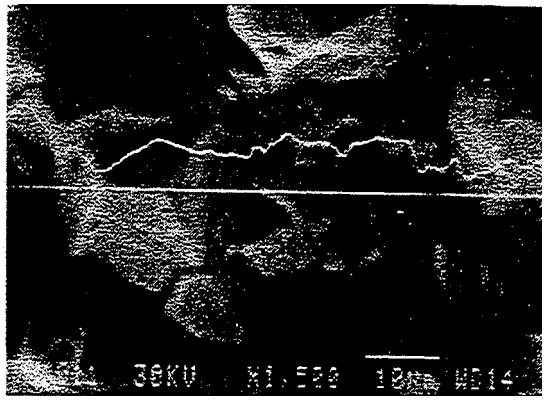

Figure 6: CL linescan superimposed on an SEM image of the CdTe film shown in Fig. 5 after $CdCl_2$ treatment.

5. SUMMARY

All CdS films examined in this study exhibited pinholes and discontinuities varying in size and density. This could have a significant impact on cell performance, as these pinholes could provide shunting paths between the CdTe and the SnO_2. The CdS grains are heavily faulted, with a high density of stacking faults. This will have a deleterious effect on the CdS/CdTe interface region, as we have shown in a previous study that planar defects in CdS tend to propagate into the CdTe films. Most CdTe grains are heavily faulted, with a high density of dislocations, stacking faults and twins. The defect density varied from one grain to another. However, the density is not significantly affected by substrate temperature. Hence, the widely observed improvement in device performance with increasing substrate temperature is not caused by a reduction in structural defect density.

This study clearly revealed that grain boundaries and intragrain defects in CdTe act as active non-radiative recombination sites. CL examination showed that $CdCl_2$ treatment markedly lowers the recombination efficiency of grain boundaries, and intragrain defects in CdTe.

At deposition temperatures below 450°C, only small amounts (~1%) of sulfur were detected in the CdTe films in the vicinity of the interface. In CdTe films deposited at 625°C, on the other hand, sulfur levels exceeding 10% were detected. This clearly indicates that CdTe devices deposited at high temperatures have an alloyed (CdS_xTe_{1-x}) active region.

ACKNOWLEDGMENT

This work was performed for the U.S. Department of Energy under contract No. DE-AC36-83CH10093.

REFERENCES

[1] M.M. Al-Jassim, F.S. Hasoon, K.M. Jones, B.M. Keyes, R.J. Matson, H.R. Moutinho, Proceedings 23rd IEEE PVSC conf. (1993) 459.
[2] H.R. Moutinho, M.M. Al-Jassim, D.H. Levi, P.C. Dippo, L.L. Kazmerski, J. Vac. Sci. Technol. A 16 (1998) 1251.
[3] R.G. Dhere, D.S. Albin, D.H. Rose, S.E. Asher, K.M. Jones, M.M. Al-Jassim, Material Res. Soc. Proc. 426 (1996) 361.
[4] S.E. Asher, Proceedings Microbeam Analysis (1990) 97.
[5] B.E. McCandless, R.W. Birkmire, Proceedings of the 14th Photovoltaic Program Review, Denver, CO, 1996, AIP Conference Proceedings 394 (1996) 647.
[6] I. Clemminck, M. Burgelman, M. Casteleyn, J. De Poorter, A. Vervaet, Proceedings 22nd IEEE PVSC conf. (1991) 1114.
[7] F.S. Hasoon, M.M. Al-Jassim, A. Swartzlander, P. Sheldon, Proceedings 26rd IEEE PVSC conf. (1997) 459.
[8] J.D. Webb, D.H. Rose, D.W. Niles, A. Swartzlander, M.M. Al-Jassim, Proceedings 26th IEEE PVSC conf. (1997) 399.

DEVELOPMENT OF HIGH-PERFORMANCE TRANSPARENT CONDUCTING OXIDES AND THEIR IMPACT ON THE PERFORMANCE OF CDS/CDTE SOLAR CELLS

T. J. Coutts, X. Wu, P. Sheldon, and D. H. Rose
National Renewable Energy Laboratory, 1617 Cole Blvd., Golden, CO 80401, USA
Telephone: (303)-384-6561
FAX: (303)-384-6430
e-mail: tim_coutts@nrel.gov

ABSTRACT: This paper begins with a review of the modeled performance of transparent conducting oxides (TCOs) as a function of their free-carrier concentration, mobility, and film thickness. It is shown that it is vital to make a film with high mobility to minimize the width and height of the free-carrier absorption band, and to optimize the optical properties. The free-carrier concentration must be kept sufficiently small that the absorption band does not extend into that part of the spectrum to which the solar cell responds. Despite this consideration, a high electrical conductivity is essential to minimize series resistance losses. Hence, a high mobility is vital for these materials. The fabrication of thin-films of cadmium stannate is then discussed, and their performance is compared with that of tin oxide, both optically and as these materials influence the performance of CdTe solar cells.

Keywords: CdTe - 1: Transparent conducting oxides - 2: Sputtering - 3

1 . INTRODUCTION

In recent years we have undertaken both fundamental and applied work on novel transparent conducting oxides (TCOs). The key motivations are that i) almost no new materials have been developed for at least 30 years, and ii) almost all optimized conventional TCOs (virtually irrespective of the method of deposition) give essentially identical optical and electrical properties. We therefore modeled the materials to establish the key parameters influencing their optical and electrical performance, developed high-performance films of cadmium stannate (CTO), and successfully applied these films to CdS/CdTe solar cells. This paper deals with each of these aspects.

2 . MODELING

TCOs obey the Drude free-electron model surprisingly well, and our approach was to calculate the optical constants of arbitrary TCOs in terms of their free-carrier concentration, effective mass, and high frequency permittivity. The mobility is also required as an input, and this was calculated as a function of their carrier concentration, using the model of ionized impurity scattering of free- charge developed by Conwell et al. [1]. With this approach, once the effective mass and high-frequency permittivity were specified, the carrier concentration was the only adjustable parameter. This permitted us to calculate the complex permittivity and optical constants. Having calculated the values of refractive index and extinction coefficient, (N and k) we then calculated the transmittance, reflectance and
absorbance of a 500 nm film on glass. The key point to emerge from our modeling was that it is vital to fabricate films with high electron mobility to obtain high optical transmittance the visible part of the spectrum, as well as high electrical conductivity. As we shall show, CTO has a much higher mobility than conventional TCOs.

Figure 1 shows the modeled variation of absorbance with wavelength, the carrier concentration being treated parametrically. The effective mass and high-frequency permittivity were assumed to be 0.35 m_e, and 5, respectively, in accordance with previous observations reported by Dhere et al. [2]. Figure 2 shows the modeled transmittance for the same set of parameters as used in Figure 1. Figure 3 shows the variation of resistivity and mobility, the latter being based on the model of ionized impurity scattering of carriers. The resistivity approaches an asymptotic value of approximately 10^{-4} Ω cm, which, for a 500-nm thick film, is equivalent to 2 Ω/□.

As discussed in the next section, the optical and electrical properties of actual films are very similar to the values predicted by the modeling. It is important to minimize the free-carrier absorbance and simultaneously achieve low resistivity and it is therefore essential to maximize carrier mobility.

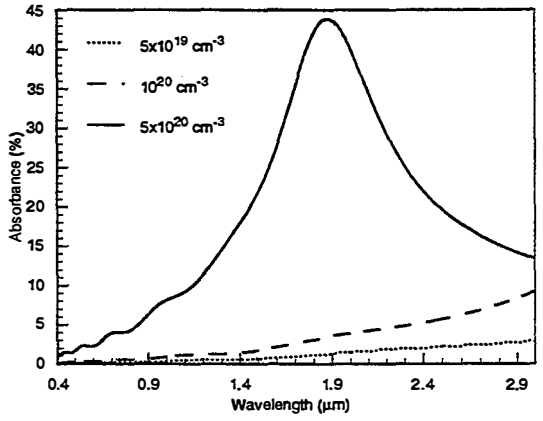

Figure 1: Modeled variation of the free-carrier absorbance of TCO films, the carrier concentration being treated parametrically.

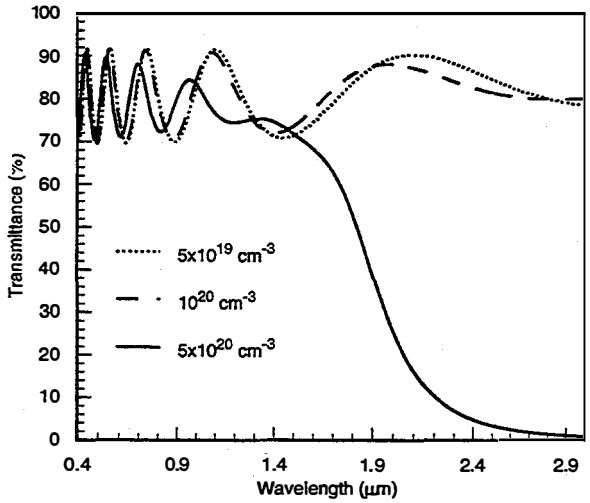

Figure 2: Modeled transmittance of a TCO film: the parameters being the same as in Figure 1.

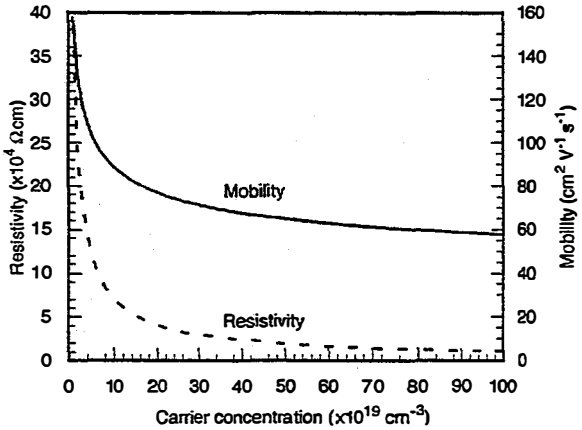

Figure 3: Modeled resistivity and mobility of TCO films.

A previous report by Nozik [3] indicated that high mobility could be achieved in this material, possibly because of a low free-carrier effective mass. There are only two ways to obtain a higher mobility: improve the carrier relaxation time, or use a material with a lower effective mass. The lower limit of resistivity is very similar to values obtained in practice.

Many investigators have published data on TCOs and the most striking feature is the similarity of the optimized electrical and optical properties. This appears to apply to films made from many materials, different deposition techniques, different deposition parameters.

Thus, we originally concluded (a conclusion that was later shown by Mulligan [4] to be incorrect) that the option of improving the relaxation time was probably not realistic. This was the primary motivation for searching for materials with lower effective masses. Careful analysis [5], later showed that the improvement in the properties in general, and the mobility in particular, was in fact due to an improvement in the relaxation time of CTO films, beyond that typically obtained for more traditional materials [2].

Notice that the increasing carrier concentrations in Figure 1 lead to the absorption band gradually extending further into the part of the spectrum to which the solar cells respond. This leads to a reduction of the short-circuit-current density and also causes the TCO film to appear brown. Excessive free-carrier concentration is responsible for the well-known brown appearance of non-optimal TCO films.

3 . TCO DEPOSITION AND PERFORMANCE

Films of CTO were deposited by radio-frequency sputtering, in pure oxygen, on room-temperature substrates of soda-lime glass (although higher-quality substrates have also been used). They were then annealed in pure argon, or argon/CdS, at a temperature of up to 680°C. This sequence has previously been shown to give the highest performance films. It has been shown that the structure of films prepared in this way is single-phase spinel but if other processing sequences were used, then multiple phases resulted, which never performed as well as single phase materials. These comments apply to both the conductivity and optical transmittance of the films. When optimized, single-phase films had a resistivity as low as 1.1×10^{-4} Ω cm. A comparison of the optical absorbance of a typical research-quality CTO film and a sample of commercially-available SnO_2, deposited onto a soda-lime substrate, using chemical vapor deposition from a $SnCl_4$ precursor, is shown in Figure 4. The carrier concentrations for the SnO_2 and the CTO were 5×10^{20} cm^{-3} and 3.2×10^{20} cm^{-3}, respectively, and the film thicknesses were about 500 nm for both materials. The mobilities of the films were 15 and 54 cm^2 V^{-1} s^{-1} for the tin oxide and CTO, respectively.

Clearly, the performance of the CTO is considerably superior to that of the tin oxide. The reason for this, in accordance with the modeling data reported above, is the extraordinarily high electron mobility, which was more than 60 cm^2 V^{-1} s^{-1} in some cases.

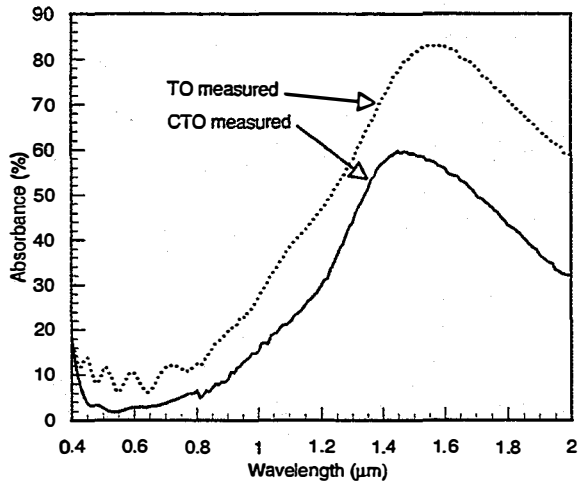

Figure 4: Measured free-carrier absorbance of films of tin oxide and CTO.

Films of CTO were deposited by radio-frequency sputtering, in pure oxygen, on room-temperature substrates of soda glass (although other higher quality substrates have also been used). They were then annealed in pure argon, or argon/CdS, at a temperature of up to 680°C. This sequence has previously been shown to give the highest performance films. It has been shown that the structure of films prepared in this way is single phase spinel but, if other processing sequences were used, the multiple phases resulted. These never performed as well as the single phase materials. These comments apply to both the conductivity and optical transmittance of the films. When optimized, these films had a resistivity as low as 1.1×10^{-4} Ω cm. A comparison of the optical absorbance of a typical research-quality CTO film and a sample of commercially-available SnO_2 is shown in Figure 4. The carrier concentrations for the SnO_2 and the CTO were 5×10^{20} cm^{-3} and 3.2×10^{20} cm^{-3}, respectively, and the film thicknesses were about 0.5 μm for both materials. The mobilities of the films were 15 and 54 cm^2 V^{-1} s^{-1} for the tin oxide and CTO, respectively. Clearly, the performance of the CTO is considerably superior to that of the tin oxide. The reason for this, in accordance with the modeling data reported above, is the extraordinarily high electron mobility, which was more than 60 cm^2 V^{-1} s^{-1} in some cases.

4. APPLICATION OF CADMIUM STANNATE TO CDS/CDTE SOLAR CELLS

The improved material properties of CTO films provide a strong impetus to incorporate them in a superstrate structure. Reduced film resistivity and improved transmittance provide significant device/module design flexibility that did not previously exist. For example, the reduced CTO resistivity permits a thinner front-contact to be used (~200 nm at <10 Ω/sq.), yielding improved transmission and ultimately improved device performance (by increasing the short-circuit current density, Jsc). Alternatively, a thicker CTO film (~650 nm at ~3 Ω/sq.) could be used that would have the advantage of reducing the number of interconnects required in module production, thereby improving throughput, reducing interconnect losses, and reducing manufacturing costs. Figure 5 shows the relationship between the TCO film transmission and the resulting Jsc for devices deposited on both CTO and SnO_2 superstrates. For example, replacing the 1,000-nm SnO_2 film with a 250-nm CTO film yielded an increase in J_{sc} of more than 1.5 mA/cm^2. It is important to note that devices fabricated on the thicker CTO films always gave the highest fill factors. Fill factors of 75% have been achieved using 600-nm-thick CTO films in ~1-cm^2 square devices. These films have resulted in devices with efficiencies of up to 14.5% (V_{oc}=0.834 V, J_{sc}=23.9 mA/cm^2, FF=72.8%), as measured under standard conditions. Therefore, thicker CTO films, with lower sheet resistivities, may be better suited for module applications. We also find that processing parameters that were optimum for SnO_2-coated glass are not suitable for CTO-coated glass. For example CTO-based devices exhibit optimum performance with significantly lower $CdCl_2$ concentrations than conventional SnO_2-based devices with much better adhesion. Figures 6 and 7 show the current/voltage and relative external quantum-efficiency characteristics of a

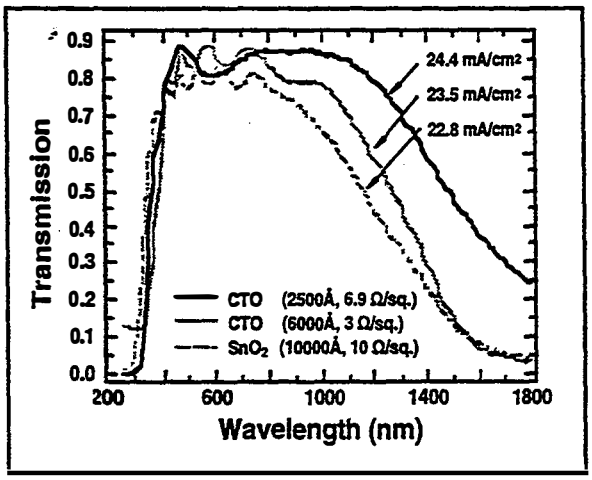

Figure 5: Relationship between J_{sc} and transmittance of tin oxide and CTO films [5].

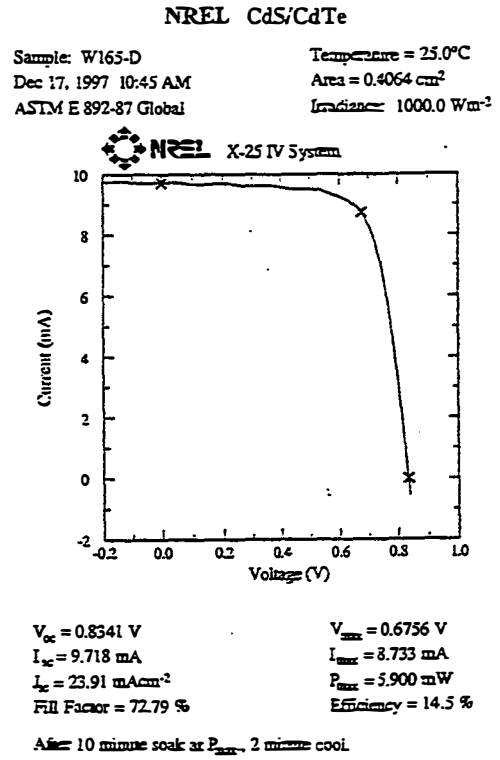

Figure 6: Current/voltage characteristic of a CdS/CdTe device using a CTO top contact.CdS/CdT solar cell with a CTO back-contact.

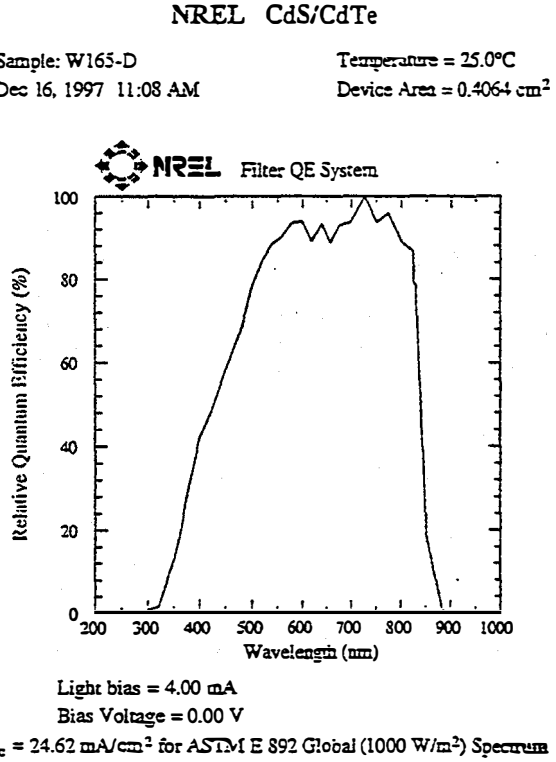

Figure 7: Relative external quantum efficiency of the cell shown in Figure 6.

5. DISCUSSION AND CONCLUSIONS

Modeling shows that a high electron mobility is necessary to obtain TCOs with high transmittance in the visible and high conductivity. Without high mobility, a high carrier concentration is needed to achieve high film conductivity. However, this leads to a severe deterioration of the optical properties of the films and causes browning, with an accompanying reduction in the short-circuit current of the device. In modeling the properties of the TCO films, the dominant scattering mechanism has been assumed to be due to ionized impurities. This is not unreasonable as a first step but has not yet been confirmed unambiguously. This mode of scattering leads to a decreasing mobility with carrier concentration, as shown in Figure 3. However, in previous work, Mulligan [5] and Coutts et al. [6], showed that the mobility actually increases, in some cases, with carrier concentration. This is more difficult to explain, but we suggested that in relatively low-carrier-concentration films, the dominant scattering centers are grain boundaries. As the carrier concentration increases, the material becomes progressively more degenerate, and the Fermi level moves above the peak in the grain-boundary scattering potential. The Fermi electrons (the only ones contributing to the conduction process) are thus unaffected by the grain boundaries. We suggested that at higher carrier concentrations, the dominant scattering centers may change from grain boundaries to ionized impurities and/or acoustic phonons. Hence, we expect to see the mobility of CTO films flatten and eventually decrease at even higher carrier concentrations, if these can be achieved. Hence, there appears to be the possibility that the mobility could be further increased with benefits to the electrical and optical properties.

Annealing of the CTO films in argon, and in close proximity to a CdS film leads to significant increases in both mobility and carrier concentration. The increase in the carrier concentration may cause the increase in the mobility, as suggested above, but the reason for the increase in carrier concentration is not yet understood. Early indications suggest that it may be due to the incorporation of excess cadmium in interstitial donor sites.

CTO is an ideal candidate for superstrate PV devices. Cd_2SnO_4-based CdS/CdTe polycrystalline thin-film solar cells with efficiencies of 14.5% have been prepared for the first time. Although we have not yet achieved a new record efficiency for CdTe cells [7] using CTO back contact window layers, we believe that the performance of these devices is far from optimized.

ACKNOWLEDGEMENTS

The authors wish to thank Keith Emery and his Team for their measurements of the J/V and quantum efficiency characteristics. This work was supported by the U.S Department of Energy under Contract No. DE-AC36-83CH10093.

REFERENCES

[1] E. Conwell and V. F. Weisskopf, Phys. Rev. **77** (1950) 388
[2] R. G. Dhere, T. A. Gessert, L. L. Schilling, A. J. Nelson, K. M. Jones, H. Aharoni, and T. J. Coutts, Solar Cells, **21** (1987) 281
[3] A. J. Nozik, Phys. Rev. **B-6** (1972) 453
[4] W. P. Mulligan, Ph.D. Thesis, Colorado School of Mines, (1996)
[5] X. Wu, P. Sheldon, T. J. Coutts, D. H. Rose, and H. R. Moutinho, Proceedings of the 26th. Photovoltaic Specialists Conference, Anaheim, (1997), 347
[6] T. J. Coutts, X. Wu, and W. P. Mulligan, J. Elec. Mats. **25** (1996) 935
[7] J. Britt and C. Ferekides, Appl. Phys. Lett. **62** (1993) 2851

THE INFLUENCE OF GRAIN BOUNDARY DIFFUSION ON THE ELECTRO-OPTICAL PROPERTIES OF CdTe/CdS SOLAR CELLS

D.H. Levi, L.M. Woods,* D.S. Albin, T.A. Gessert, R.C. Reedy, and R.K. Ahrenkiel
National Renewable Energy Laboratory (NREL)
1617 Cole Blvd., Golden, CO 80401 USA
* Colorado State University, Fort Collins, CO 80523, USA

ABSTRACT: We report on a study of the effects of diffusion of metals through polycyrstalline CdTe thin films. The metals Ni, Pd, Cu, Cr, and Te are deposited onto the back surface of 10-μm thick CdTe/CdS device structures using room-temperature evaporation. We found that four out of the five metals produce significant changes in the photoluminescence (PL) of the near-junction CdTe material. These changes are explained in terms of spatial variations of the photoexcited carrier distribution and spatial variations in the sulfur composition of the CdTeS alloy material near the CdTeS interface. The changes in carrier distribution appear to be associated with band bending and electric fields induced by diffusion of the metals to the CdTe/CdS interface. In addition to PL measurements, we have also utilized a technique for detaching the CdTe film from the CdS/TCO/glass superstrate to directly access the front surface of the CdTe absorber layer. We have used secondary ion mass spectroscopy to measure the metal diffusion profiles from this interface.
Keywords: CdTe - 1: Grain Boundary Diffusion - 2: Spectroscopy - 3

1. INTRODUCTION

It is widely recognized that grain boundaries exert significant influence on the electrical and optical properties of polycrystalline semiconductors used in thin-film solar cells. Grain boundaries tend to have a high concentration of lattice defects and impurities. This can make them a dominant factor in the electrical properties of a polycrystalline semiconductor. Diffusion of impurities along grain boundaries in polycrystalline thin-film CdTe/CdS solar cells is likely to be several orders of magnitude faster than diffusion through the bulk [1]. Rapid diffusion along grain boundaries will have a significant influence on the results of post-deposition processing such as $CdCl_2$ treatment and back contact application. Thus it is important to further our understanding of diffusion of impurities along grain boundaries and of how such diffusion processes affect the electronic and optical properties of CdTe/CdS solar cells.

2. EXPERIMENTAL CONDITIONS

2.1 Samples

Samples in this study consist of close-spaced sublimated CdTe on 800Å thick chemical-bath deposited CdS on SnO_2 / 7059 glass superstrates. The CdTe thickness is approximately 10 μm with a grain size which varies from approximately 1 μm at the front of the film to approximately 5 μm at the back surface. All samples have undergone a 400° C post-growth vapor-$CdCl_2$ treatment. Efficiencies for cells fabricated from these films are in the range of 12 - 14%. Evaporation at approximately 300 K is used to deposit 500 Å of the metals Ni, Pd, Cu, Cr, and Te onto the back surface. Half of each sample is then annealed for 30 minutes at 300° C in a flowing helium atmosphere. Ion-beam milling is then used to remove the metal layer from both annealed and unannealed pieces of each sample. Annealed and unannealed pieces are then halved again. One half of each undergoes ion-beam milling to remove 1 μm of CdTe from the back surface of the film. The other half of each of these pairs undergoes a "lift-off" procedure [2] which separates the film at the CdTe/CdS interface. Secondary Ion Mass Spectroscopy (SIMS) is then used to measure a depth profile of the metal concentration within the film.

2.2 Photoluminescence

Room-temperature, pulsed-excitation PL spectra are measured at each step of the above process. Typical room-temperature PL measurements on polycrystalline CdTe (px-CdTe) are dominated by recombination at defects because of the high density of defect states relative to the photoexcited carrier density. The PL spectra described in this study are unique in that a cavity-dumped dye laser is used as the excitation source. The laser provides pulses 5 picoseconds in duration at a repetition rate of 1 Mhz. Because of the extremely low duty cycle of the laser, we are able to inject much higher photoexcited carrier densities than are practical with a CW laser. Initial carrier densities immediately after the laser pulse are approximately $4x10^{16}$ cm^{-3}. At these high-injection conditions, the PL spectra are dominated by band-to-band recombination, which we have verified by studying the density-dependence of the spectra [3]. Photoexcitation is through the transparent CdS window layer at a wavelength of 600nm. The 1/e penetration depth for this wavelength in CdTe is 0.2 μm. Numerical modeling indicates that over 90% of the photoexcited carriers recombine within 3000 Å of the CdTe/CdS interface, hence the term junction photoluminescence. The measurement is conducted under open circuit conditions. Spectral resolution is 1 nm, which corresponds to approximately 2 meV in the wavelength range of interest.

2.3 Secondary Ion Mass Spectroscopy

The SIMS measurements were carried out using a Cameca IMS-5F instrument. A beam of O_2^+ purified by a mass filter was used as the source of the primary ions. The impact energy of the primary ion beam was 5.5 keV at a incident angle of 42° from the surface normal. The primary current was 250 nA. An area of 200x200 μm^2 was raster scanned. Positive secondary ions generated from the sample were accelerated normal to its surface and were detected at 4.5 keV. Secondary ions were collected from a 60-μm^2 area in the center of the raster scanned area to minimize effects from the crater walls. High-mass resolution techniques were utilized in the seperation of $63Cu^+$ from $126Te^{++}$. In the sample chamber, the working pressure was $2x10^{-10}$ Torr. Secondary ions were counted by an electron multiplier detector.

3. EXPERIMENTAL RESULTS

3.1 Photoluminescence Results

As discussed above, the conditions of our PL experiment measure band-to-band recombination spectra of an approximately 3000-Å thick layer on the CdTe-side of the CdTe/CdS interface. Fig. 1 illustrates the typical junction PL spectrum measured on NREL polycrystalline CdTe/CdS/TCO and CdTe/TCO device structures. All deposition and treatment conditions are identical for the two films. The only difference is the presence of the CdS layer in one film. The differences in the two spectra are striking. The CdTe/TCO film spectrum consists of a single gaussian peak at the 1.51-eV bandgap energy of CdTe. The CdTe/CdS/TCO film spectrum consists of two peaks that can be fit with a sum of two gaussians. The fitting functions are illustrated by the dashed lines in Fig.1.

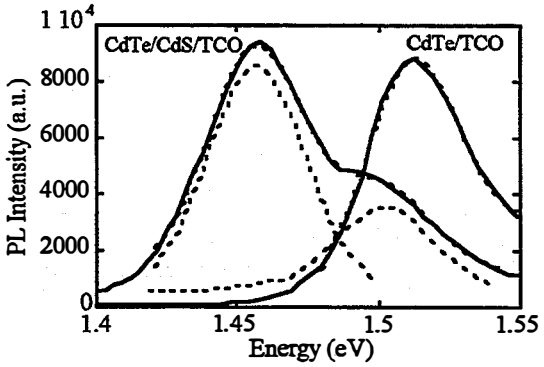

Figure 1: Junction PL spectra for pre-metallization devices illustrating effect of presence of CdS layer. Dashed lines demonstrate Gaussian fits.

The peak energies of the two peaks in the CdTe/CdS/TCO spectrum are 1.501 and 1.457 eV, respectively. The bandgap of a CdTeS alloy initially decreases as sulfur is added to CdTe up to a sulfur concentration of approximately 20% [4]. We have done a linear fit to the CdTeS alloy bandgap dependence on sulfur concentration for concentrations below 20%, and have come up with a reduction of 4.5 meV in bandgap for each 1% increase in sulfur concentration. We conclude that the two peaks in the CdTeS spectrum are due to regions of alloy with compositions of 2% and 12%, respectively. The 12% composition is consistent with grazing-incidence x-ray diffraction measurements of alloy composition on lift-off samples [5], which probe only the first 50 Å of the film. It is not clear at this time why the spectrum displays two distinct peaks rather than a single broad peak spanning the range of bandgap energies from 12% to 0% sulfur. Possible explanations are an electric field-induced segregation of photoexcited carriers, or a CdTeS alloy composition distribution which is bi-modal instead of changing smoothly with distance from the interface.

The effects of evaporation of 500 Å of Cr on the back surface of a CdTe/CdS/TCO film are illustrated in Fig. 2. The premetallization spectrum is shown for comparison.

The spectrum can still be fit with two gaussian peaks, but in this case both peaks have shifted in energy, and the relative intensity ratio between the two peaks has changed significantly. In this case, the peaks are at 1.494 and 1.462 eV. This corresponds to sulfur compositions of 4% and 11%, respectively. Similar changes have been observed with Ni, Pd, and Te. Copper is the only metal that failed to produce significant changes in the junction PL spectrum.

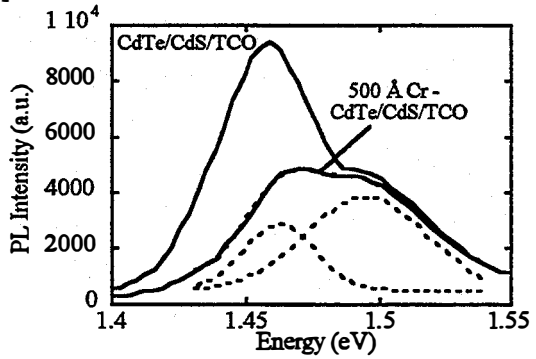

Figure 2: Junction PL spectra for non-metallized and 500 Å Cr sample illustrating the nature of the changes induced in the spectra by metallization.

The intensity ratio between low and high energy peaks in the PL spectrum is a useful method for quantifying the degree of perturbation in the spectrum. The value of this ratio for all samples prior to metallization is in the range 2.7 ± 0.2. After metallization, the ratio is reduced to less than one for some metals. We find that for some of the metals these effects are significantly enhanced by annealing. It is rather surprising that Cu produces little if any effect, as Cu is known to be an effective dopant and a fast diffuser in CdTe [6].

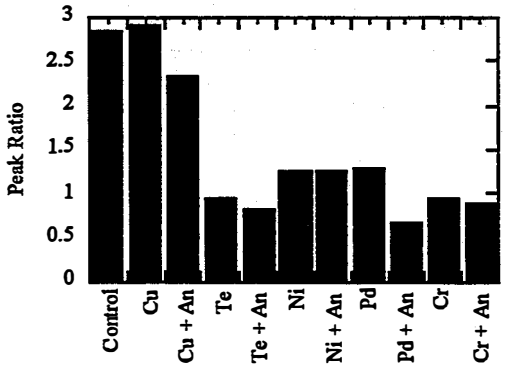

Figure 3: Peak ratio in PL spectrum vs. metallization and annealing. Ratio increases with intensity in lower energy peak.

PL spectra were measured after both the shallow and deep ion-beam milling of the back surface of metallized and metallized-and-annealed samples. The spectra reverted back to their pre-annealed character with shallow milling for all but the annealed Cr and annealed Pd samples. The deep ion-beam milling step reverted the PL spectra for the latter two samples. These results appear to suggest that the metallization-induced changes in the junction PL spectra are due to a back-surface field (BSF) effect.

To investigate the BSF hypothesis, we have measured junction PL under bias on a completed device. We find that the shape of the spectrum is unchanged for short-circuit, open-circuit, and 10-V reverse-bias conditions. If the observed changes in the PL spectra with metallization were due to a BSF effect, we would expect application of a 10 V-bias to produce large changes in the shape of the PL spectrum.

We have also used the numerical device modeling program SimWindows™ to simulate the effects of a large BSF on the electric fields and photoexcited carrier distributions at the CdTe/CdS interface. The results show no changes at all in fields or carrier distributions near the junction unless the bulk doping in the CdTe absorber layer is reduced to 10^{13} cm^{-3} or lower. Capacitance measurements have indicated that the carrier density in the p-type CdTe absorber layer of NREL CdTe/CdS devices is in the range of 10^{15} cm^{-3}. We conclude that it is not likely that the changes in junction PL with metallization are caused by a BSF.

3.2 SIMS Results

SIMS depth profiles on lift-off samples have been successfully carried out on the Cr, Pd, and Cu samples. For the Cu sample, Cu penetrates approximately 1 μm into the film prior to annealing. After annealing Cu is distributed throughout the film at a concentration between 0.01 and 0.1 %. This is an extremely high concentration, which verges on a Cu:CdTe alloy rather than a dopant or impurity. SIMS has a rather low sensitivity for Pd. Prior to annealing, Pd is detected only near the back surface of the device. After annealing, there is a significant SIMS-Pd signal throughout the device. We have been unable to quantify the concentration of Pd because of a lack of calibrated sensitivity factors for Pd in CdTe or HgCdTe.

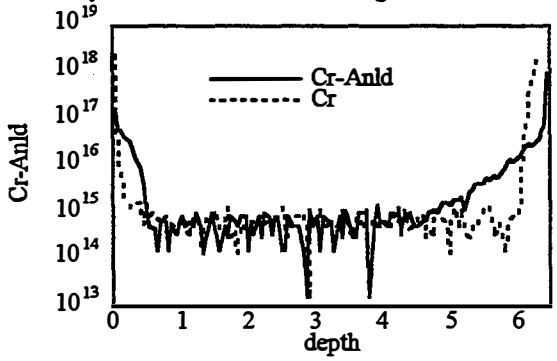

Figure 4: SIMS profile of Cr concentration in sample before and after annealing.

Fig. 4 presents the Cr diffusion profiles. Prior to annealing, the Cr signal is above background only near the front and back interfaces. The nonzero Cr signal at the front interface is inconclusive, as this could be due to environmental contamination. After annealing, Cr penetrates almost 2 μm into the back of the film, and roughly 0.5 μm into the front of the film. We note that the measured Cr distribution at the front of the film is nonhomogeneous, most likely caused by inhomogeneity in the film-diffusion properties. The SIMS concentration calibration was estimated due to the lack of CdTe SIMS standards. Relative sensitivity factors (RSFs) were calculated for Cu and Cr based on published HgCdTe RSFs [7].

Because SIMS measures many grains and grain boundaries at once we must also take into account the volume of grain boundaries relative to the total volume. This ratio will depend on the grain size and the width of the grain boundaries. For a rough estimate we have assumed rectangular grains with planar grain boundaries. For the films used in this study the grains are approximately 1 μm in diameter and we estimate 10 Å thick grain boundaries. In this case the grain boundaries make up 0.2 % of the total film volume. If we make the simplifying assumption that the metals are completely contained within the 10 Å thick grain boundaries this implies that concentrations measured by SIMS are a factor of $5x10^2$ lower than the concentration within the grain boundary. This means an impurity can be present in the grain boundaries at relatively high doping levels (e.g. 10^{18} cm^{-3}) and still be below the SIMS baseline.

4. DISCUSSION

4.1 Model for Junction Photoluminescence

The key to understanding the changes observed in the junction PL spectra is the relationship between the spatial extent of sulfur diffusion into the CdTe absorber layer and the spatial distribution of photoexcited carriers under our experimental conditions. Figure 5 illustrates this relationship. This double-y plot shows a model calculation [8] of the spatial extent of recombination under the experimental conditions described in Section 2. The radiative recombination distribution is shown by dashed lines for two different surface recombination velocities (SRV). Superimposed is a SIMS profile of the sulfur distribution as a function of distance from the CdTe/CdS interface. The CdTeS alloy bandgap will shift 4.5 meV for each 1% change in the sulfur composition of the alloy. Thus, a spatial shift in the recombination distribution will produce a shift in the peak energy of the junction PL.

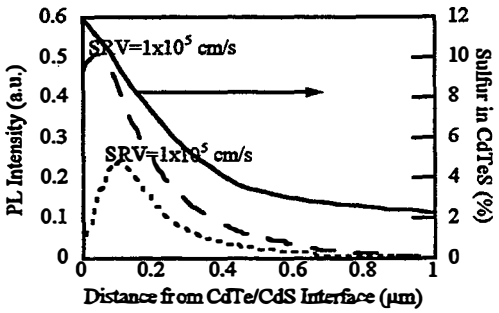

Figure 5: Spatial distribution of recombination vs. sulfur alloy composition in CdTe layer. Dashed lines show recombination for two different values of SRV.

In the model calculation of Fig. 5 we have used variations in SRV to produce changes in the recombination distribution. Band-bending, electric fields, and changes in doping can produce similar or more complex redistributions of the carrier and recombination distributions. It should also be noted that the SIMS profile of sulfur distribution is an average over many grains and grain boundaries. It is likely that the actual alloy composition has abrupt local variations which are averaged out by the "macroscopic" SIMS measurement. Such abrupt variations could produce the two-peaked structure observed in junction PL measurements.

4.2 Grain-Boundary Diffusion

Grain-boundary (GB) diffusion processes in thin films can be significantly different than GB diffusion in bulk material. Grain-boundary diffusion lengths can equal or exceed the film thickness. In this case the back surface of the film can significantly affect the diffusion profiles. Gilmer and Farrell [9] have studied the problem of GB diffusion in thin films for various boundary conditions. Figure 6 presents their numerical modeling results for

conditions where GB diffusion is coupled with bulk diffusion. The film thickness is D, and there is an infinite reservior of diffusant at the surface labeled 0. Two boundary conditions are considered; 1) the surface at D is a barrier for further diffusion, or 2) there is rapid diffusion parallel to the surface at D.

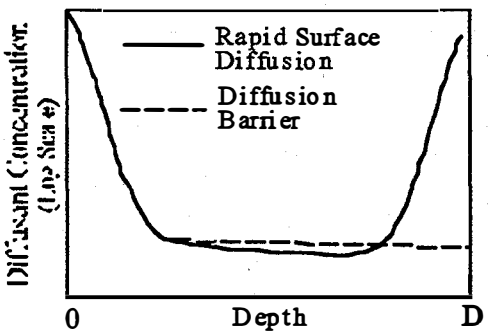

Figure 6: Numerical modeling results for grain boundary diffusion showing the effect of rapid surface diffusion at the buried interface D.

The latter case is the solid line in Fig. 6. Impurity atoms diffuse through the grain boundaries and spread out at the surface D. This surface then acts as a new source of impurities for diffusion back into the bulk. The profile for case number two is quite similar to the SIMS profile for the annealed Cr sample as shown in Fig. 4. Note that the two figures are right-to-left mirror images of each other.

The model of Fig. 6 together with the SIMS profile of Fig. 4 provides a possible scenario for the distribution of metals under the conditions in this study. If GB diffusion is significantly faster than bulk diffusion the metals will be located primarily within in the GB's and at the front surface. The concentrations of metallic impurities in the GB's will be roughly 500 times higher than the values measured by SIMS. For the SIMS results of Fig.4 this corresponds to an upper limit on concentration for GB's in the middle of the film of approximately $5x10^{17}$ cm^{-3}, and somewhere between $1x10^{17}$ and $5x10^{19}$ cm^{-3} at the CdTe/CdS interface. If the metallic impurities are active as dopants these concentrations would make the GB's channels of high conductivity within the relatively low-doped p-type CdTe matrix.

4.3 Implications for PL Spectra

It was noted in section 3.1 that removal of the metallic layer from the back surface using ion-beam milling caused the junction PL spectrum to revert to its pre-metallization character. The two exceptions, annealed Pd and annealed Cr, did not revert until an additional 1 μm of CdTe was removed. SIMS profiles revealed that these two metals penetrated several microns at the back surface with annealing.

We are lead to postulate the following model of the effect of GB diffusion on junction PL. From electrostatics we know that a metal will not support an electric field, all of the metal remains at a single electrical potential. When the metallic layer is present on the back surface it provides a "grounding layer" which connects all of the grain boundaries, and through the GB's, the front surface. This effect produces the band bending at the front surface which perturbs the junction PL spectra. When the metallic layer is removed from the back surface the GB's are no longer connected together and essentially "float" at the potential of the bulk material surrounding them. This eliminates the band bending at the front surface and the PL spectrum reverts to its pre-metallization character. The samples with annealed Cr and Pd required further ion-beam milling because of the deep penetration of the metals at the back surface. Copper failed to produce a shift in the PL spectrum because it is highly mobile in the bulk of CdTe and dopes grains and GB's equally. This is consistent with the high Cu concentrations measured by SIMS.

CONCLUSIONS

Device modeling and bias-dependent PL measurements imply that the changes in junction PL spectra produced by metal deposition are not due to a back-surface field effect. SIMS depth profiles and theoretical modeling of diffusion in polycrystalline thin films indicate that metals deposited on the back surface rapidly diffuse along the grain boundaries and may accumulate at the CdTe/CdS interface. Highly-doped GB's act as conduction pathways to connect the front and back surfaces, maintaining both surfaces at the same potential. These perturbations will alter the spatial distribution of radiative recombination, producing the observed changes in the junction PL spectra. The exact nature of the shifts in peak energy and relative intensity is difficult to explain without detailed knowledge of the spatial composition of the CdTeS alloy near the interface. The two-peak structure of the junction-PL implies some type of metastable miscibility gap in the alloy composition not predicted by equilibrium phase diagrams.

ACKNOWLEDGEMENTS

The authors wish to thank Anna Duda for extensive assistance with metals deposition. We also thank Falah Hasoon, Alice Mason, and David King for evaporation of copper, EPMA, and XPS, respectively. This project was funded by the U.S. Department of Energy under contract DE-AC36-83CH10093.

REFERENCES

[1] I. Kaur et.al. in Fundamentals of Grain and Interphase Boundary Diffusion, p.2, (J. Wiley and Sons, Chichester), 1995.

[2] see Woods, et.al. in these proceedings.

[3] D.H. Levi, et.al, Proceedings of the 26th IEEE PVSC, Anaheim, CA, 1997, p351.

[4] ibid, [3].

[5] D. Albin, et.al., Fall 1997 Materials Research Society Symposium G, Boston, MA."

[6] H.C. Chou, et.al., J. Elect. Mat., **25**, p.1093,(1996).

[7] R. G. Wilson, et.al., Secondary Ion Mass Sectrometry: A Practical Handbook for Depth Profiling and Bulk Impurity Analysis (Wiley, New York, 1987)

[8] based on analytical solution in J. Vaitkus, Phys. Stat. Sol., **34**, p.769 (1976).

[9] G.H. Gilmer and H.H. Farrell, J. Appl. Phys. **47** (1976), p.4373.

SURFACE ANALYSIS OF CdTe AFTER VARIOUS PRE-CONTACT TREATMENTS

D.M. Waters*, D. Niles, T.A. Gessert, D. Albin, D.H. Rose, P. Sheldon
1617 Cole Blvd.
National Renewable Energy Laboratory
Golden, CO 80401, USA

ABSTRACT: We present surface analysis of close-spaced sublimated (CSS) CdTe after various pre-contact treatments. Our methods include Auger electron spectroscopy (AES), x-ray photoelectron spectroscopy (XPS), and grazing-incidence x-ray diffraction (GI-XRD). XPS and GI-XRD analyses of the surface residue left by our solution-based $CdCl_2$ treatment do not indicate the presence of a significant amount of $CdCl_2$. In addition, the solubility properties and relatively high thermal stability of the residue suggest the presence of the oxychloride $Cd_3Cl_2O_2$ rather than $CdCl_2$ as the major chlorine-containing component. Of the methods tested for their effectiveness in removing the residue, only HNO_3 etches removed all detectable traces of chlorine from the surface.
Keywords: CdTe - 1: PV Materials - 2: Characterization - 3

1. INTRODUCTION

CdTe is a good choice of absorber material for photovoltaic devices due to its near-ideal bandgap (1.5 eV) and high absorption coefficient ($6x10^4$/cm at 0.6 μm). Solar cell efficiencies as high as 15.8% have been achieved with CSS CdTe as the absorber layer and a CdS window layer [1].

Treating CdTe with chlorine prior to making the back contact is known to dramatically improve the performance of CdTe/CdS solar cells. However, the mechanisms of this treatment are not fully understood and are likely functions of the CdTe microstructure. The promotion of CdTe recrystallization (resulting in larger grains) [2, 3], enhanced CdS/CdTe interdiffusion [3], a reduction in the number of defect states throughout the CdTe layer [2], and low resistance p-type conductivity [4] have been attributed to the action of chlorine in CdTe.

Chlorine can be introduced either during the formation of the CdTe layer or after by diffusion through the exposed CdTe surface. Our solution-based $CdCl_2$ treatment, which employs the latter method, leaves a significant amount of chlorine-rich residue on the CdTe surface.

An etch with nitric and phosphoric acids (n-p etch) after the $CdCl_2$ treatment is commonly used to form a Te-rich layer at the CdTe surface by preferentially removing chlorine, cadmium, and oxides. This layer is thought to be beneficial because excess Te can promote p-type conductivity in CdTe [5, 6]. The results of Valdna et al. suggest that the removal of excess chlorine by the n-p etch may also play an important role in establishing p-type conductivity at the CdTe surface [7].

In light of the availability of techniques that can be used to form a Te-rich surface layer in lieu of n-p etching (e.g., evaporating or sputtering Te), it seems reasonable to seek out complementary means for removing the chlorine-rich surface residue. We used AES to study the effects of various treatments intended to remove the residue and found that it was surprisingly resistant to our methods. Further investigation into the matter using XPS and GI-XRD revealed some interesting compositional characteristics of the residue.

2. EXPERIMENTAL

The CdTe material used for this study was deposited by CSS on CdS in an ambient of 0.5-torr O_2 and 14.5-torr He at 620°C. The CdTe layer is 8-9 μm thick and has a surface roughness of approximately 120 nm. The CdS layer (80 nm) was deposited on SnO_2-coated glass by chemical bath deposition.

The solution $CdCl_2$ treatment begins with soaking the samples for 15 min in a boiling bath of 11.3-g/L anhydrous $CdCl_2$ in methanol. The samples are then quickly dried with N_2 (g) and annealed at atmospheric pressure in a flow-through furnace at 400°C for 40 min. A continuous gas flow of 100 sccm He and 25 sccm O_2 is used for the duration of the anneal. An additional 5-slm flow of He is used until the temperature rises to 100°C. It takes 5 to 10 min for the sample temperature to rise from room temperature to 400°C and approximately 30 min to cool down to 100°C.

For the solubility tests, samples were taken directly from the $CdCl_2$-treatment annealing furnace and were rinsed either for 1 min with deionized water or for 20 sec with methanol, and then dried with nitrogen.

Two etching solutions were used for the acid-etch experiment. For the standard treatment, samples were taken directly from the $CdCl_2$-treatment annealing furnace and etched with a solution mixture of 350 mL 85% H_3PO_4, 140 mL H_2O, and 4.4 mL 70% HNO_3. They were removed from the etching solution when bubbles appeared across the entire sample surface (approximately 35 sec). The samples were then rinsed thoroughly in deionized water and dried with nitrogen. The other etchant is a dilute solution of nitric acid (0.03 N). The sample was etched for one minute and then rinsed thoroughly with deionized water and dried with nitrogen.

Vacuum anneals were performed in a Phi AES system on samples taken directly from the $CdCl_2$-treatment annealing furnace. The chamber was evacuated to $5x10^{-8}$ torr, and the sample mount temperature was raised to 400°C in 2.5 min. This temperature was maintained for 45 min. Final spectra were taken once the sample mount had cooled to 100°C and did not differ substantially from spectra taken at 400°C. The AES technique provides an analysis depth of roughly 2 nm.

*e-mail: waters@physics.ucsc.edu; Dept. of Physics, University of California, Santa Cruz 95064

Our system has a spot size diameter on the order of 0.1 mm.

Because over-exposure to an electron beam can decompose chlorine-containing compounds such as $CdCl_2$ [8], care was taken to minimize beam exposure. A low electron beam energy (3 KeV) was used and the total electron beam exposure time for each sample was limited to 2 min. We confirmed that the decomposition reaction progress was not significant by comparing the chlorine signal from other areas of the sample.

For our XPS experiments, we used a Physical Electronics x-ray photoelectron spectrometer with an energy resolution of 0.2 eV. The XPS technique provides an analysis depth of roughly 3 nm. The system has a spot size diameter of 0.8 mm. Standard sensitivity factors were used to determine atomic concentrations [9].

We used a Scintag polycrystalline texture stress x-ray diffractometer with a thin film (parallel-beam) attachment for grazing incidence diffraction. In this configuration, x-ray penetration is fixed by the incident angle. With our setting of $\Omega = 2°$, the theoretical sampling depth (based on a perfectly smooth surface) is on the order of 500 nm. JCPDS files were used as standards for peak identification.

3. RESULTS AND DISCUSSION

3.1 Solubility Properties of the Residue

Prior to this analysis, we had assumed that a rinse with deionized water or methanol would remove the chlorine-containing component of our solution $CdCl_2$ treatment residue. This was based on our assumption that the residue is primarily $CdCl_2$, which is soluble in both water and methanol. However, we found that much of the residue is insoluble in both water and methanol (Fig. 1), which raised some questions regarding its composition. In addition, because chlorine residues left by vapor $CdCl_2$ treatments are reported to be soluble in both water and methanol [10, 11], we conclude that our solution $CdCl_2$ residue does not have the same composition as these vapor treatment residues.

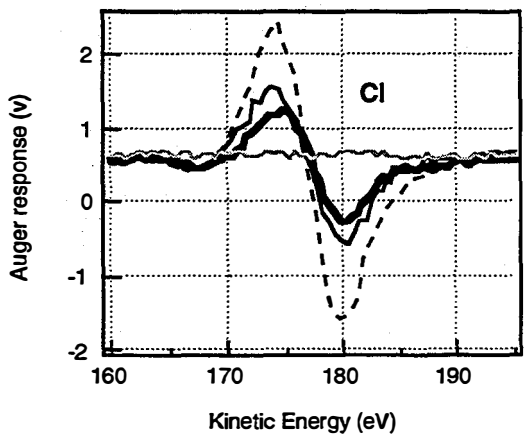

Figure 1: The chlorine signal after the solution $CdCl_2$ treatment (dashed line), subsequent water rinse (solid), methanol rinse (bold), and etch with dilute nitric acid (flat, grey line).

3.2 The Effect of a 400°C Vacuum Anneal on the Residue

Vacuum annealing is a proven method for removing chlorine residue from CdTe following some types of chlorine treatments [7, 10, 11]. However, as can be seen from Fig. 2, a 45-min anneal at 400°C and 10^{-8} torr removes very little chlorine from the solution $CdCl_2$-treated surface. Even after a 17-hour vacuum anneal, a substantial amount of chlorine remains. The relatively high vapor pressure of $CdCl_2$ (10^{-3} torr at 400°C, which is five orders of magnitude higher than the vacuum chamber pressure) suggests that if the residue contained a considerable amount of $CdCl_2$, we would observe a corresponding decrease in the chlorine concentration with vacuum annealing.

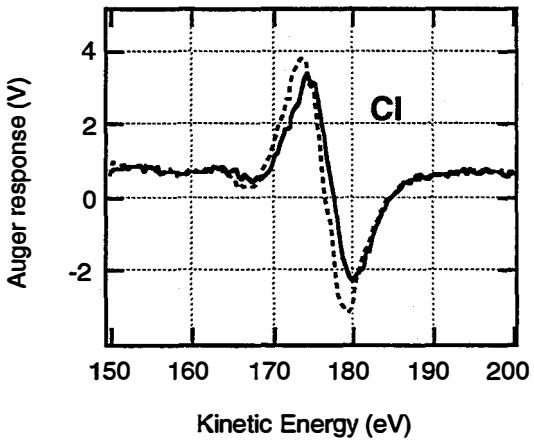

Figure 2: AES spectra of chlorine before (dashed line) and after (solid line) a 45-min anneal at 10^{-8} torr.

It is difficult to find a chorine-containing compound with properties that match those of the residue. The presence of a significant amount of $CdCl_2$ at the surface is unlikely because of its expected volatility under our vacuum anneal conditions and its high solubility in water and methanol. Cadmium chlorates are also soluble in water and alcohol. The tellurium chlorides $TeCl_2$ and $TeCl_4$ are too volatile to remain at the sample surface during the $CdCl_2$ treatment anneal or the vacuum anneal. However, the oxychloride $Cd_3Cl_2O_2$ has thermal properties consistent with those of the residue and is insoluble in methanol. Perhaps the characteristics of the residue can be explained by the presence of this compound.

If the limited solubility and relatively high thermal stability are due to the formation of oxychlorides, it seems reasonable to assume that vacuum annealing is most effective in removing residue from $CdCl_2$ treatments when exposure to oxygen during the treatment is minimized. Interestingly, although we found that chlorine-bound oxides do not form until the $CdCl_2$ treatment anneal, the results of annealing in He (only) indicated that surface oxides form independent of whether oxygen is provided by the anneal ambient.

3.3 The Effects of Acid Etching on the Residue

Although we were unable to remove the chlorine residue with water, methanol, or a 400°C vacuum anneal, we found that all detectable traces of chlorine can be removed from the sample surface by etching the sample for one minute with dilute nitric acid (0.03 N) and then rinsing it thoroughly with deionized water. Because CdTe is known to decompose in nitric acid, we could not conclude that the chlorine compound also decomposed. Our final composition was slightly Te rich

relative to a polycrystalline CdTe standard, indicating that some CdTe decomposition had indeed occured.

The standard etching step used in our device fabrication employs a concentrated solution of nitric and phosphoric acids for the formation of a Te-rich region at the CdTe surface. It is very effective at removing oxides, chlorides, and cadmium (Fig. 3). As with the less concentrated nitric acid solution, all signs of chlorine are eliminated from the surface by the etch.

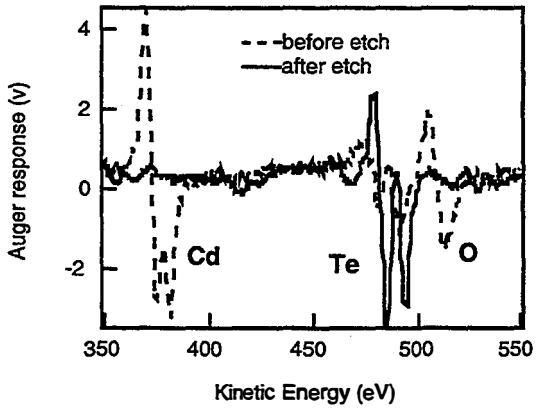

Figure 3: Auger analysis of solution $CdCl_2$-treated CdTe after an etch with a concentrated solution of nitric and phosphoric acids.

3.4 Grazing-angle X-ray Diffraction Analysis

We used GI-XRD to further characterize the surface of solution $CdCl_2$-treated CdTe. Two samples were treated in a $CdCl_2$/methanol solution, but only one was given a $CdCl_2$ treatment anneal (Fig. 4).

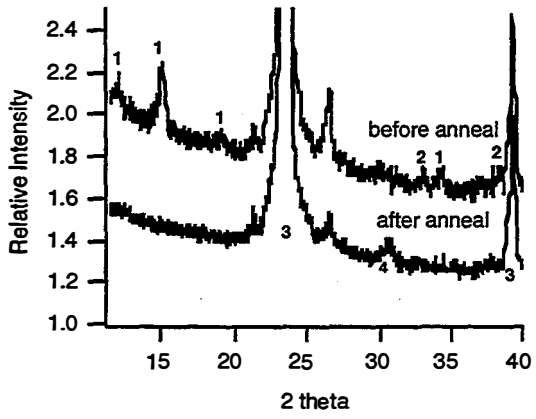

Figure 4: Preliminary GI-XRD results from samples before and after the $CdCl_2$-treatment anneal indicating the peak identification by number: 1- $CdCl_2$-H_2O; 2- CdO; 3- CdTe; 4- $Cd_3Cl_2O_2$.

The most prominent peaks are due to cubic CdTe (23.76° and 39.32°). $CdCl_2$ is present as orthorhombic $CdCl_2$-H_2O (2θ = 12.10°, 15.06°, and 34.10°). Monoclinic CdO is also observed (2θ = 32.96° and 38.24). After the $CdCl_2$-treatment anneal, the $CdCl_2$-H_2O and CdO peaks are no longer detectable. Anhydrous $CdCl_2$ is not observed either. Thermal desorption could account for the loss of $CdCl_2$, which has a vapor pressure on the order of 10^{-3} torr at 400°C [12], but certainly not the loss of CdO, which requires temperatures greater than 1000°C to build up an appreciable vapor pressure [13]. There is a new peak at 30.52°, which may be due to monoclinic $Cd_3Cl_2O_2$. We propose that the following reaction may have occured during the anneal: 2 CdO + $CdCl_2$ --> $Cd_3Cl_2O_2$. Although some weaker peaks support this assignment, their signal-to-noise ratio is poor. Since there is only one distinct peak that matches the standard diffraction spectrum for $Cd_3Cl_2O_2$, the identification of this compound by GI-XRD is uncertain.

3.5 Properties of Oxychlorides

As mentioned earlier in this paper, the chemical and thermal properties of the residue appear to be consistent with what is known about the oxychloride $Cd_3Cl_2O_2$. Further, the GI-XRD results seem to support this identification. For these reasons, we include some relevant information from the literature regarding this compound and also another oxychloride, tellurium oxychloride ($Te_6O_{11}Cl_2$).

A study of the system CdO-$CdCl_2$ by Walter-Levy and Groult [14] reports that CdO and $CdCl_2$ react to form $Cd_3Cl_2O_2$ at around 400°C. The dehydration of species that contain hydroxyl groups (e.g., $Cd[OH]_2$ and Cd[OH]Cl) also leads to the formation of $Cd_3Cl_2O_2$ around 400°C. In the referenced publication, the authors show that $Cd_3Cl_2O_2$ is stable up to 600°C and insoluble in alcohol, consistent with the compound in question.

$Te_6O_{11}Cl_2$ is also worth mentioning because it is formed at 400°C and is stable up to 650°C [15], which appears consistent with the thermal characteristics of the residue. However this compound is typically formed from $TeCl_4$(g) and TeO_2. As will be explained in the next section, we have reason to believe that $CdTeO_3$ is the primary surface oxide, rather than TeO_2. In addition, we are not aware of any free Te at the surface (needed to form $TeCl_4$). The Te-containing compounds that we have detected (CdTe and $CdTeO_3$) are probably too stable to form the tellurium chloride. Futher, if $TeCl_4$ was present during the anneal as a solid or gas, it probably would not remain at the surface long enough for $Te_6O_{11}Cl_2$ to form. Therefore, of the two oxychlorides we have discussed, $Cd_3Cl_2O_2$ appears the more likely constituent of the residue, not only based on the GI-XRD result, but also on the greater assumed availability of the reactants required to form it as compared to the assumed availability of reactants to form $Te_6O_{11}Cl_2$.

3.6 X-ray Photoelectron Spectroscopy of the Residue

When discussing XPS results, it is common to identify compounds by the characteristic electron binding energies of elements in those compounds. However, we present our data in terms of *differences* between characteristic binding energies for elements in a given compound. This lessens the contribution to energy shifts from sample charging.

The signal from chlorine persists 13 nm into the material and accounts for 10 atomic % of the surface composition (neglecting carbon). The difference in binding energies between cadmium and chlorine at the surface is 206.7 eV. The corresponding reference value for $CdCl_2$ is 207.1 eV. We would expect to observe an asymmetry in the Cd peak if $CdCl_2$ were present. However, the peak is relatively symmetrical and centered at an energy relative to Te that is consistent with the presence of CdTe (within 0.1 eV).

The oxygen peak (not shown) does not indicate the presence of Cl-O bonds. Oxychlorides such as $Cd_3Cl_2O_2$

have no Cl-O bonds, and may explain the presence of a Cl peak in the absence of $CdCl_2$ and chlorates.

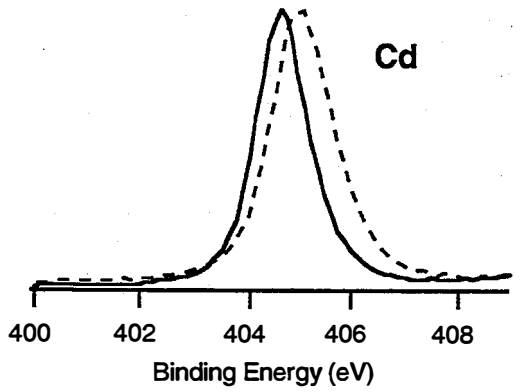

Figure 5: XPS spectra of Cd, at the surface (dashed line) and at 13 nm (solid line).

The difference in binding energies between the two Te peaks at the surface is 3.57 eV (Fig. 6), which more strongly suggests the presence of $CdTeO_3$ (3.5 eV) [16] than TeO_2 (3.2 eV) [16]. After removal of the first few nanometers of material the oxide signal is very small (the dotted line). At 13 nm, the Te-oxide is no longer present and the difference between the binding energies of Cd and Te is 167.4 eV, characteristic of CdTe [9].

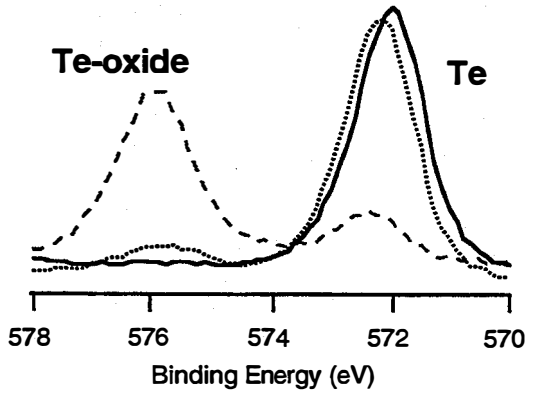

Figure 6: XPS spectra of Te, showing the presence of Te oxide(s) at the surface (dashed line), and its diminution deeper in the material: at 4 nm (dotted line) and at 13 nm (solid line).

Our XPS results seem to suggest the presence of oxychloride(s). However, because we have no $Cd_3Cl_2O_2$ and $Te_6O_{11}Cl_2$ standards, we cannot determine where the peaks would lie for these compounds and thus, cannot use our XPS results to confirm or disprove their presence.

4. CONCLUSIONS

We investigated the surface composition of CSS CdTe after a solution $CdCl_2$-treatment using AES, XPS, and GI-XRD. Our results indicate that residue remaining after the $CdCl_2$ treatment does not contain a significant amount of $CdCl_2$. Rather, it contains chlorine compound(s) much more chemically and thermally stable than $CdCl_2$. It appears likely that $Cd_3Cl_2O_2$ formed from $CdCl_2$ and CdO during the annealing step of the $CdCl_2$ treatment process and has a strong influence on the properties of the residue.

The relatively high stability of the residue makes it difficult to remove from the CdTe surface. Of the methods we investigated, only acid-etching removes the Cl-rich surface residue. Rinsing with deionized water, rinsing with methanol, and vacuum annealing, which have been reported as effective means for removing residue from samples treated by other $CdCl_2$ methods, are not effective in removing the thicker, more oxide rich layer that is left by the solution-$CdCl_2$ treatment.

5. ACKNOWLEDGMENTS

This work was supported by the U.S. Department of Energy under contract No. DE-AC36-83CH10093 and a GAANN grant from the Department of Education and UCSC. The authors would like to express their gratitude to A. Mason, Y. Mahathongdy, and R. Ribelin for their contributions to this project. D. Waters would also like to thank her academic advisor, D. Belanger, for his continued support and encouragement.

REFERENCES

[1] J. Britt, C. Ferekides, Appl. Phys. Lett. **62** (1993) 2851-2.
[2] S.A. Ringel, A.W. Smith, M.H. MacDougal, A. Rohatgi, J. Appl. Phys. **70** (1991) 881-889.
[3] B.E. McCandless, L.V. Moulton, R.W. Birkmire, Prog. Photovolt. Res. Appl., **5** (1997) 249-260.
[4] V. Valdna, Mat. Res. Soc. Symp. Proc. **442** (1997) 585-591.
[5] D.W. Niles, X. Li, P. Sheldon, J. Appl. Phys. 77 9 (1995) 4489-4493.
[6] A.J. Ricco, H.S. White, M.S. Wrighton, J. Vac. Sci. Technol., **A2** (1984) 910-915.
[7] V. Valdna, J. Crys. Growth, **161** (1996) 164-167.
[8] C.J. Aidinis, M. Green, J. Appl. Phys. **63** 9 (1988) 4397-4405.
[9] J.F. Moulder, W.F. Stickle, P.E. Sobol, K.D. Bomben, Handbook of X-ray Photoelectron Spectroscopy (Perkin-Elmer Corp., 1992).
[10] T.X. Zhou, N. Reiter, R.C. Powell, R. Sasala, P.V. Meyers, IEEE Proceedings of the 1st WCPEC (1994) 103-106.
[11] B.E. McCandless, H. Hichri, G. Hanket, R.W. Birkmire, IEEE Proceedings of the 25th PVSC, (1996) 781-784.
[12] D.R. Stull, Ind. Eng. Chem. **39** (1947) 517.
[13] R.C. Weast, M.J. Astle, CRC Handbook of Chemistry and Physics, 63rd ed. (CRC Press, 1982).
[14] L. Walter-Levy, D. Groult, Bull. Soc. Chim. Fr. **11** (1970) 3868-78.
[15] G.I. Novikov, V.V. Zvezdina, V.P. Bochin, Russian Journal of Physical Chemistry, 52 **4** (1978) 608-609.
[16] F. Wang, A. Schwartzman, A.L. Fahrenbruch, R. Sinclair, R.H. Bube, J. Appl. Phys. 62 **4** (1987) 1469-1476.

ELECTRICAL CHARACTERIZATION OF CdTe GRAIN-BOUNDARY PROPERTIES FROM AS PROCESSED CdTe/CdS SOLAR CELLS

L.M. Woods,* D.H. Levi, V. Kaydanov,** G.Y. Robinson,* and R.K. Ahrenkiel
National Renewable Energy Laboratory, 1617 Cole Blvd., Golden, Colorado 80401, USA
*Colorado State University, Ft. Collins, Colorado 80523, USA
**Colorado School of Mines, Golden, Colorado 80401, USA

ABSTRACT: An ability to liftoff or separate the thin-film polycrystalline CdTe from the CdS, without the use of chemical etches, has enabled direct electrical characterization of the *as-processed* CdTe near the CdTe/CdS heterointerface. We use this ability to understand how a back-contact, nitric-phosphoric (NP) etch affects the grain boundaries throughout the film. Quantitative determination of the grain-boundary barrier potentials and estimates of doping density near the grain perimeter are determined from theoretical fits to measurements of the current vs. temperature. Estimates of the bulk doping are determined from high-frequency resistivity measurements. The light and dark barrier potentials change after the NP etch, and the origin of this change is postulated. Also, a variable doping density within the grains of non-etched material has been determined. These results allow a semi-quantitative grain-boundary band diagram to be drawn that should aid in determining more-accurate two-dimensional models for polycrystalline CdTe solar cells.
Keywords: CdTe - 1: Grain Boundary Barrier - 2: Nitric - Phosphoric etch - 3

1. INTRODUCTION

It is generally believed that diffusion of impurities up grain boundaries from the underlying films and substrate greatly affect the electrical properties of the CdTe film during growth and subsequent high-temperature processing of a CdS/CdTe device. Herein, we will make use of an ability to liftoff or separate the post-processed thin-film polycrystalline CdTe from the CdS, SnO_2 and glass substrate, without the use of chemical etches. We use this ability to understand how a back-contact, nitric-phosphoric (NP) etch affects the grain boundaries of the front buried homojunction and postulate the subsequent effects on device operation. A connection was established between the NP etch and the electrical junction, 7.5 microns away, in a recent photoluminescence study [1].

In our study, we will present theory and quantitative determination of the grain boundary barrier potentials, and will estimate the bulk doping, as well as the doping density near the outside of the grain. These properties are determined from measurements of DC current versus temperature, and DC and AC electrical conductivity, and are found as a function of back-contact processing and depth into the film.

These findings will aid in determining more-accurate two-dimensional models of the polycrystalline devices for fully understanding device operation.

2. EXPERIMENTAL CONDITIONS

2.1 Sample Preparation

All samples described herein were processed at the National Renewable Energy Laboratory (NREL). The CdTe film is deposited by close-spaced sublimation (CSS) onto CdS, which is deposited by a chemical-bath solution. The substrate was a bilayer SnO_2-coated Corning 7059 glass. The as-grown CdTe film thickness is about 10 μm. The CdTe/CdS devices receive a high-temperature $CdCl_2$ vapor treatment. At this point, a 30-second NP etch (about 1% nitric acid, 70% phosphoric acid, and 29% water) dip is performed on some samples. All samples are then ion-beam-milled about 250 nm, which removes the conducting Te-rich surface from the samples that were NP etched. Further milling is performed to achieve the total film thickness of 10, 7.5, 5.0, 3.5, and 2.0 μm, to systematically study the effects of the NP etch on the grain boundaries versus depth. The remaining CdTe film is removed or lifted off from the device by using a technique similar to that of von Windheim et al. [2], but developed independently at the National Renewable Energy Lab. for CdTe on CdS. In this manner, smooth films of CdTe formerly in contact with CdS can be made as large as 1.5 cm in diameter. Several parallel strips of gold contacts are then applied by evaporation and by using metal masks. The contacts are 11 mm long and are spaced 0.4 mm apart.

2.2 Measurement Apparatus

Electrical measurements were made using a two-probe method, a heated copper block, temperature controller, and thermocouple for temperature monitoring and feedback. A Keithley 485 picoammeter was used for the DC current measurement that was fully automated with computer control. The AC resistance was measured using HP 4274 and 4275 LCR meters, which together provided a 100-Hz to 10-MHz frequency range. An HP 6825 external power supply provided bias control. A three-point probe method was used to confirm neglible contact resistance.

3. BACKGROUND AND THEORY

It has been shown that polycrystalline material can be modeled, as shown in Fig. 1 [3]. Typically, the grain-boundary resistance dominates the film resistivity, $R_1 >> R_2$. Thus, R_1 dictates the DC conductivity measurement and enables the grain-boundary properties to be studied. A high-frequency measurement of the conductivity

effectively shorts out R_1 via C and enables us to measure the intragrain resistance, R_2.

The primary deterrent for determining grain-boundary potentials is the lack of knowledge of the doping density near the grain boundaries. Without this knowledge, one can not easily predict whether the conduction mechanism over the grain boundary is due to drift-diffusion, thermionic, thermally assisted tunneling, or just tunneling. Thus, previous studies report only the conductivity activation energies [2], or assume thermionic emission based on bulk values of the doping density or measurements of *bi*crystal capacitance [4]. We have found that measurement of *poly*crystalline capacitance is unreliable at this point due to geometry considerations. In this report, the conduction mechanism will be determined by analyzing the conductivity temperature dependence. This approach has been used in the past on polycrystalline GaAs [5]. In this study, values of barrier height and doping density are taken from the conduction model that best fits the current temperature dependence.

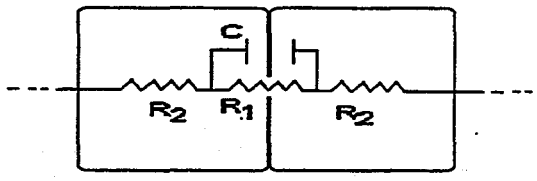

Figure 1: Grain-Boundary Electrical Model with intragrain resistance, R_2, in series with a grain-boundary impedance, R_1 in parallel with C. Typically, $R_1 >> R_2$.

The current-voltage relation for grain boundaries has been developed by Muller [6]. The following voltage dependence for grain boundaries has been determined for small-applied voltages or qV<<2kT, by equating currents into the grain boundary with those exiting the grain boundary:

$$J \cong (2-\gamma) J_0 \left(\frac{qV}{2kT} \right), \qquad (1)$$

where J_0 is the model-dependent portion of the saturation current, V is an estimate of the voltage applied per grain boundary, and γ is the grain-boundary capture coefficient and is a number between 0 and 1. In equation (1), the variation of the Fermi level in the boundary is neglected as it is predicted to be small. Thus, the small applied voltage result with γ=0 is the same current-voltage relation derived for small-applied voltages of a Schottky barrier. Because the current-voltage relation is independent of the conduction mechanism, erroneous estimates of γ and V are not expected to alter the results as to which model fits best.

Crowell and Sze developed a current model for Schottky barriers that combines drift-diffusion theory with thermionic emission theory [7]. The saturation current from this theory can be written as:

$$J_0 = \frac{qN_b}{\frac{1}{v_d} + \frac{1}{v_r}} \exp\left(-\frac{qV_b}{kT} \right), \qquad (2)$$

where V_b is the grain-boundary barrier height, N_b is the doping in the vicinity of the grain boundary, v_d is the effective diffusion velocity and is equal to μE_m. E_m is the value of the maximum electric field, which in this case is equal to $(2qN_bV_b/\varepsilon_s)^{1/2}$ for a double depletion region at barrier maximum. Also, v_r is the "recombination velocity" for carriers thermally emitted over the barrier and is a constant of the material equal to $(kT/2\pi m^*)^{1/2}$. Thus, if v_r is much lower than v_d, then the current flow is limited by thermionic emission. Conversely, if v_d is much lower than v_r, then the current flow is limited by drift-diffusion. In this equation quantum mechanical reflection of carriers is neglected as well as phonon backscattering and image force barrier lowering. These factors are not expected to appreciably alter V_b, or give order of magnitude differences in N_b, according to the authors.

Crowell and Rideout developed a current model for Schottky barriers that assumes thermally assisted tunneling [8]. This model covers the full range from pure thermionic emission to pure tunneling; however, the approximations used begin to break down at these limits. The saturation current for this model can be written generally as follows:

$$J_0 = \frac{A^* T}{k} \int_0^\infty f_1(E) T(E) f_2(E) dE, \qquad (3)$$

where A* is the Richardson constant, and f_1 and f_2 are the Fermi-Dirac occupancy functions of the left and right-hand side, respectively. T(E) is the transmission probability assuming the WKB approximation, a parabolic potential or uniform doping, a parabolic energy-momentum relationship, and a carrier with energy E. In equation (3), the density-of-states dependence on energy is removed from the integrand and contained within A*. This approximation only becomes non-negligible for carriers with low energy or when tunneling through the bottom of the barrier is dominant. Also, no mixing of valence and conduction band states was taken into account, which can lead to errors if the barrier height is greater than ½ E_g [9]. The validity of this approximation is to be determined.

Padovani and Stratton (P&S) estimated an analytical solution to equation (3) by expanding the transmission probability integral of equation (3) in a Taylor series around the energy, where the number of emitted carriers is maximum [10]. This gives the following saturation current equation for a reverse-biased Schottky barrier:

$$J_0 \cong \frac{A^* T}{k} \sqrt{\pi E_{00}} \sqrt{-qV - E_{vf} + \frac{qV_b + E_{vf} - qV}{\cosh\left[\left(E_{00}/kT \right)^2 \right]}} \; x \exp\left(-\frac{qV_b + E_{vf} - qV}{E_{00} \coth\left(E_{00}/kT \right)} \right), \qquad (4)$$

where V in this case is the applied voltage per grain boundary. and is usually negligible for small-applied voltages. With E_{00} being a constant that is proportional to the square root of N_b and is equal to:

$$E_{00} = \frac{q\hbar}{4\pi}\sqrt{\left(\frac{N_b}{m^* \varepsilon_s}\right)}, \qquad (5)$$

The energy separation between the Fermi level and valence bands, E_{vf}, near the grain boundary, but in the absence of a potential barrier, can be expressed in terms of E_{00}. The value of E_{00}, or doping density, determines how far up the barrier the peak in thermally assisted emission occurs, and the energy spread of this emission is related to the barrier energy.

4. RESULTS

To confirm the existence of a dominate grain-barrier resistance and the model as shown in Fig. 1, the resistance frequency response was performed on etched and non-etched samples. Fig. 2 shows an example of the resistivity dependence on frequency in the light, and thus, confirms the model. As can be seen from the figure, the resistance is reduced by several orders of magnitude at high frequencies and is indicative of the dominant barrier resistance. Also, the value of high-frequency resistance is nearly constant in all samples. This indicates that the intragrain resistance, or bulk doping, remains unchanged. However, there is a dependence on the low-frequency resistance, or barrier resistance, between etched and non-etched samples.

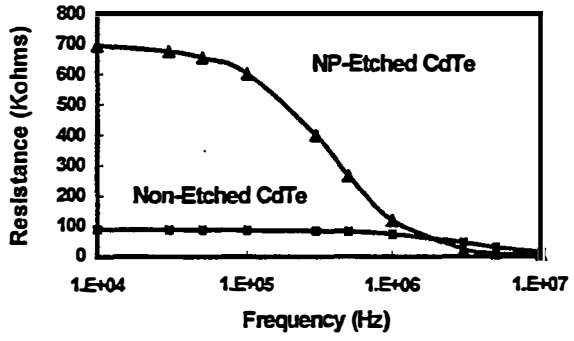

Figure 2: Resistance frequency response of non-etched and NP-etched CdTe under 1-sun illumination. Breakpoint is approx. equal to $(R_1C)^{-1}$.

The barrier potentials, V_b, were determined by measuring the current vs. temperature for each sample and fitting each sample to each conduction model as described earlier. The results of each fit for a typical non-etched sample are shown in Fig. 3. As can be seen from the figure, the thermally assisted tunneling model fits best. It should be noted that the maximum value of N_b was limited to 10^{15} cm^{-3} for drift-diffusion, as at this point $v_r \approx v_d$. A maximum value was also set for the thermionic emission case of $N_b = 10^{17}$ cm^{-3}, as at this point the effects of tunneling may be significant. If the best fit for thermionic emission went to this maximum, then the data should be fit with the thermally assisted tunneling model. This was the case for the samples herein. The barrier height, V_b, as determined by the thermally assisted tunneling model was 772 meV and E_{00} was 7.9 meV. This barrier height correlates well with values of about 0.8 eV for the valence band offset between an unreacted metal on a "pinned" Fermi level CdTe surface [11]. For comparison, V_b as determined from thermionic emission was 624 meV using the maximum value of N_b. N_b as determined from E_{00} is about $7x10^{17}$ cm^{-3}. Thus, previous studies, which used bulk values for N_b, would yield even lower and more erroneous values for V_b.

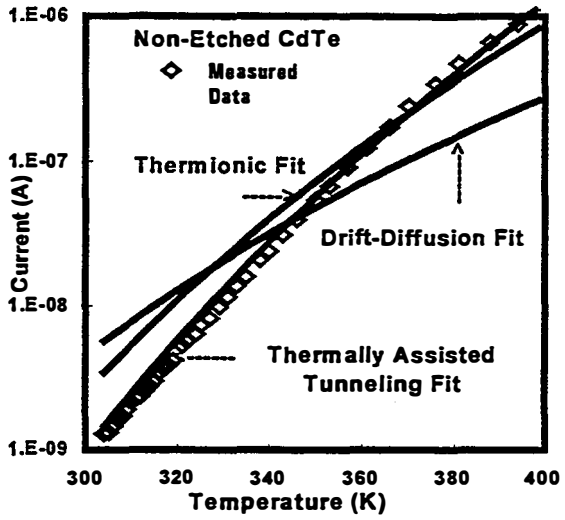

Figure 3: Comparison of fits to current vs. temperature data for different models of conduction.

Similar good fits can be obtained for the NP-etched samples. In this case, the thermionic model fits almost as well as the thermally assisted tunneling model. It was observed that varying the conduction thickness over a couple of orders of magnitude had little effect on the resultant barrier height of about 275 meV. For comparison, a V_b of 302 meV was obtained for the thermionic-only fit and using the maximum N_b value. The thermally assisted tunneling model value of V_b compares well with the value of 0.26 eV for the valence-band offset between evaporated Te on CdTe [11]. It was shown previously that the N-P etch preferentially etches grain boundaries and creates Te-rich grain boundaries [1].

The results of the fit and high-frequency resistance measurements for a non-etched sample allow us to calculate the shape of the band diagram, as seen in Fig. 4:

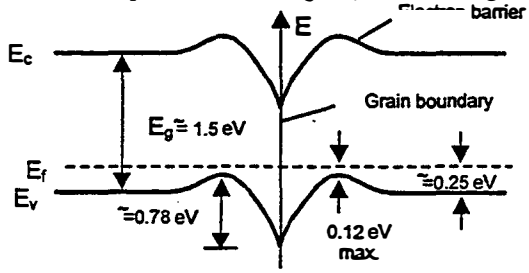

Figure 4: Grain-Boundary Band Diagram of non-etched CdTe. V_b and N_b as determined from thermally assisted tunneling theory fit to current vs. temperature data.

The bulk doping level was estimated to be about $7x10^{14}$ cm^{-3} and was determined from the value of the high-frequency intragrain resistance, device geometry, and a nominal value of 60 $cm^2/v\text{-}s$ as the bulk hole mobility in crystalline CdTe.

This doping level is about three orders of magnitude less than the doping in the vicinity of the grain boundary and gives rise to a minority-carrier barrier of about 0.12 eV near the potential barrier. However, the spatial extent of this barrier is unknown.

Because it was shown that the NP etch reduces the grain-boundary barrier height, the next step was to determine the extent of this effect with depth in the sample. Fig. 5 plots each of the NP-etched samples that have also been ion-beam milled to various depths in order to profile the effect. Non-etched, but ion-beam-milled samples were also measured for comparison. Four samples were processed at each film thickness, two non-etched and two NP-etched, and agreement between similarly processed samples was very good.

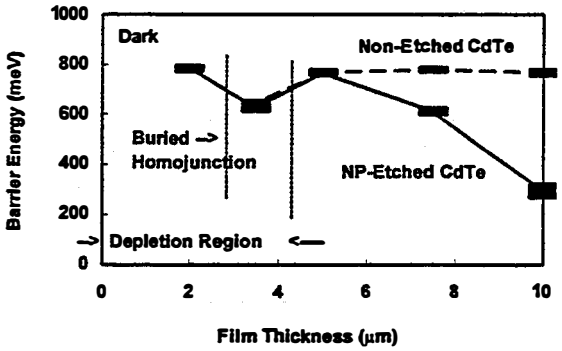

Figure 5: Effect of the NP etch on the CdTe grain-boundary barrier vs. depth. Possible extent of depletion region is shown due to buried homojunction.

From this plot we see that the N-P etch losses its effects after 5 μm of film have been removed. It was later shown that an NP-etched material had a buried homojunction that occurs about 2.5 μm into the film, (thickness = 2.5 μm), as deduced from electron-beam-induced-current (EBIC) measurements. This would deplete the adjacent 1-2 μm and thus possibly affect the result at a film thickness of 5 μm. The results below 5 μm are thus poorly understood at this point. It is also interesting to note that the barrier energy of about 0.6 eV for the film of thickness = 7.5 μm (2.5 μm of material removed) correlates well with the valence-band offset of about 0.59 eV between CdTe and a thin layer (t < 50 Å) of evaporated Te [11].

The 10-μm-thick, lightly milled samples were periodically remeasured over six months in room atmosphere to determine the stability of the barrier-reducing etch. The barrier heights asymptotically degraded (increased) quickly in the first couple of months, but then stabilized to an average value of 350 meV. This degradation is most likely due to oxidation of the tellurium in the grain boundaries. The oxidation of tellurium has been shown in a previous study using X-ray photoelectron spectroscopy [11], and results from that study indicate that it is likely that the NP-etched samples underwent a great deal of oxidation before the first samples were measured. A change in barrier height between 275 meV and 350 meV can increase the barrier resistance by an order of magnitude for devices relying on the NP etch to provide an interface layer for low-resistance back contacts. The non-etched, 10-μm samples were also remeasured for comparison, but their barrier heights were unchanged during the six months.

5. DISCUSSION AND CONCLUSIONS

Measurements of the grain-boundary barrier heights correlate with other measurements of valence-band offsets from a previous study. This previous study postulated that the N-P etch reduced the barrier height by creating a p-type tellurium layer to compensate the n-type defects at the grain boundary [11]. Also shown was a variable grain doping level, with increasing doping near the grain boundary of several orders of magnitude when compared to the bulk concentration. This information has allowed a detailed development of the grain-boundary band diagram, which predicts a minority-carrier or conduction-band barrier due to the variable doping. We postulate that if this layer is wider than electron mean free path length, then this layer could act to reflect the minority carriers before the grain boundary, and thus, temper the grain-boundary barrier effects on minority-carrier recombination. Lifetimes measured by time-resolved photoluminescence and solar cell J_{SC} measurements [12] corroborate this and appear to be unchanged by the NP etch. Finally, it was shown that the effects of the N-P etch are initially unstable and could result in severe increases in the back-contact series resistance of devices.

ACKNOWLEDGEMENTS

The authors would like to thank the following NREL employees: David Albin for growing the samples; Yoxa Mahathongdy for performing the $CdCl_2$ treatment; Anna Duda and Aaron Szalaj for aiding in the metal evaporation; and Tim Gessert for performing the ion-beam milling. This project was funded by the U.S. Department of Energy under contract DE-AC36-83CH10093.

REFERENCES

[1] D.H. Levi, et al., *Twenty-Sixth IEEE PVSC*, (1997).
[2] J. von Windheim, I. Renaud, and M. Cocivera, *J. Appl. Phys.*, 67,(9) 1990.
[3] D.P. Snowden and A. M. Portis, *Phys. Rev.*, 120,(6) 1960.
[4] T.P. Thorpe, Jr., A.L. Fahrenbruch, and R.H. Bube, *J. of Appl. Phys.*, 60(10), p. 3622, (1986).
[5] C.H. Seager and G.E. Pike, *Appl. Phys. Lett.*, 40(6), pg. 471, (1982).
[6] R.K. Muller, *J. of Appl. Phys.*, 32(4), p. 635, (1961).
[7] C.R. Crowell and S.M. Sze, *Solid-St. Electron.*, 9, p. 1035, (1966).
[8] C.R. Crowell and V.L. Rideout, *Solid-St. Electron.*, 12, p. 89, (1969).
[9] J.W. Conley and G.D. Mahan, *Phys. Rev.*, 161(3), p. 161, (1967).
[10] F.A. Padovani and R. Stratton, *Solid-St. Electron.*, 9, p. 695, (1966).
[11] D.W. Niles, X. Li, P. Sheldon, and H. Hochst, *J. of Appl. Phys.*, 77(9), p. 4489, (1995).
[12] Xiaonan Li, private communication, 1997.

HIGH EFFICIENCY $Cu(In,Ga)Se_2$ THIN FILM SOLAR CELLS WITHOUT INTERMEDIATE BUFFER LAYERS

K. Ramanathan, H. Wiesner, S. Asher, D. Niles, R. N. Bhattacharya, J. Keane, M. A. Contreras, and R. Noufi
Electronic Materials and Devices Division, National Renewable Energy Laboratory, 1617 Cole Boulevard, Golden CO 80401
Telephone: (303) 384-6454; Fax: (303) 384-6430; e-mail: kramanat@nrel.nrel.gov

ABSTRACT: The nature of the interface between $CuInGaSe_2$ (CIGS) and the chemical bath deposited CdS layer has been investigated. We show that heat-treating the absorbers in Cd- or Zn- containing solutions in the presence of ammonium hydroxide sets up an interfacial reaction with the possibility of an ion exchange occurring between Cd and Cu. The characteristics of devices made in this manner suggest that the reaction generates a thin, n-doped region in the absorber. We suggest that this aspect might be more important than the CdS layer in the formation of the junction. It is quite possible that the CdS/$CuInSe_2$ device is a buried, shallow junction with a CdS window layer, rather than a heterojunction between CdS and CIGS. We use these ideas to develop methods for fabricating diodes without CdS or Cd.

Keywords: Copper Indium Diselenide-1, Buried Junction-2, Cd Doping-3

1. INTRODUCTION

Thin films of ternary chalcopyrite semiconductor $CuInSe_2$ (CIS) and its solid solutions with $CuGaSe_2$ (CIGS) and $CuInS_2$ are one of the two principal options for realizing low-cost photovoltaic devices. Excellent device efficiencies have been demonstrated in small and large areas [1,2]. The devices are also known for their long-term stability in the field. All of these factors bode well for CIS photovoltaic technology becoming commercial in the near future. One of the critical elements of this technology is the junction formation step. The preferred approach is the deposition of a thin CdS layer produced by a chemical reaction in an aqueous bath, called the chemical bath deposition (CBD) process. No other semiconductor layer substituted for the CBD CdS has demonstrated devices comparable in efficiency or stability. Similarly, devices made by using CBD CdS exhibit better characteristics than those with CdS layers deposited by other methods such as vacuum evaporation or sputtering.

A set of explanations have been put forth to account for the fortuitous advantages of the CBD CdS. The commonly held beliefs are that the CBD process produces uniform, thin, covering films. The films are highly resistive, and this leads to the notion that the CdS layer in a device is fully depleted. The CdS/CIS junction has been treated as an abrupt heterojunction, and this assumption has never been put to rigorous experimental test. The existence of ordered vacancy phases (OVC) such as $CuIn_3Se_5$ and $CuIn_5Se_8$ at the surface region of the chalcopyrite is thought to yield a buried junction [3,4]. However, when these compounds are synthesized separately, they do not show sufficiently high conductivity or definite conductivity type to persuade us to believe they can create a junction with the (1 12) chalcopyrite phase [5]. It is not clear whether the OVC phases exist in all films or if they appear as segregated layers of finite thickness at the surface. The surface regions of the absorbers are also sinks for large amounts of alkali impurities such as Na diffusing out of the substrate. For a device engineer, this is a complicated picture to contend with. Given the fact that the OVC and the CdS layers are both low in carrier density, one must explain where the n-side of the device is, and where the electric field is developed.

Another interesting aspect of the junction formation by CBD CdS process is the inability to fabricate high efficiency devices for $CuIn_{1-x}Ga_xSe_2$ films when $x > 0.3$. EBIC scans show that for $x \leq 0.3$, the junction is buried, and for higher Ga contents it is found at the metallurgical plane [6]. The difficulty of obtaining higher efficiency devices with higher Ga levels has not been overcome.

Experience prior to the advent of CBD CdS was with evaporated CdS layers. Regardless of whether thin films or single crystals were used, buried junctions were observed. The first $CuInSe_2$ homojunctions were obtained by converting the surface of p-type single crystals by extrinsic doping to n-type with Cd or Zn [7]. The electrical activity of II_B elements in $CuInSe_2$ was established, and the experimental data up to this point showed that homojunctions or buried junctions actually resulted. The picture we have at present is different in many ways, and one must put this to experimental tests as much as possible.

From a practical viewpoint, it would be most desirable to replace the wet chemistry step with a vacuum process step. A second objective is the replacement of Cd to make the devices environmentally friendly. The ultimate goal is to make this the final step of the absorber preparation such that the entire processing can proceed in a seamless manner. To accomplish this, it would be helpful to know how the CBD process creates the junction, and use that knowledge to find alternative processes. At present, the alternatives consist of In_xSe_y and $ZnIn_2Se_4$ layers evaporated at the end of the absorber fabrication [8]; Zn (OSOH) complex grown by CBD [9]; and ZnO buffer layers by CVD [10]. A general comment that can be made of the first two approaches is that the devices made by these processes are sensitive to light and temperature, and they become fully efficient only after long heat treatments or light soaking. This is obviously a handicap.

2. EXPERIMENTAL

The CIGS thin films used in this study were grown by the three-stage process described elsewhere [11]. Soda

lime silicate glass was used as the substrate. A 1 μm thick molybdenum (Mo) layer was deposited by sputtering, and this serves as the back electrode. The $CuInGaSe_2$ films were grown by coevaporation of the elements in Se atmosphere. First, an $(InGa)_2Se_3$ layer was deposited at 300□C, and this is followed by evaporation of Cu and Se at 550□C to make the film composition slightly Cu rich. The composition was restored to a slightly Cu deficient one by the addition of $(InGa)_2Se_3$ again. Film composition was determined by electron probe microanalysis. P-type single crystals of $CuInSe_2$ were used for some studies, and these were grown by gradient freeze method. They were mechanically polished to a mirrorlike finish. To fabricate devices, a 50-nm thick CdS layer was deposited by CBD in about 4-5 minutes as the bath temperature was ramped from 40□C to 70□C . The bath composition was as follows: 0.0015 M $CdSO_4$, 1.5 M NH_4OH, and 0.15 M thiourea. A ZnO top electrode was deposited by r.f sputtering in two layers. First, a 50 nm ZnO film was deposited in Ar/O_2 ambient to yield a high resistivity layer. A 350-nm Al-doped ZnO was then deposited to serve as the conductive top electrode. Ni/Al metal grids were deposited on the ZnO for current collection. Current-voltage characteristics of the devices were measured under AM 1.5 Global spectrum adjusted for 1000 W/m^2 illumination. Secondary ion mass spectrometry (SIMS) was used to determine the distribution of the elements in the films and crystals. A low beam energy of 5 kV was chosen to minimize the effect of sputter mixing, and the sampling rate was high to ensure high depth resolution. The analyzed area was about 60 μm diameter. $(M+Cs)^+$ were used to matrix and surface ion yield variations. This also maximized the Cd signal.

We used partial electrolyte (PE) solutions to study the effect of the CBD reactants separately. For example, a Cd PE solution contains the cadmium salt and ammonium hydroxide in the same molar proportions as the CBD bath, described above, and is designated Cd PE. This allowed us to subject the absorbers to Cd and ammonium hydroxide only without the influence of thiourea. Absorbers were subjected to the Cd PE treatments for different times and temperatures. Similar baths were also constituted for the case of Zn. Following the solution treatments, a standard bilayer ZnO was sputter deposited to complete the devices.

We have also attempted to react Zn compounds in vapor or solid state. The idea is to diffuse Zn into the surface region and dope it n-type. $ZnCl_2$ dispersed in methanol was applied to the surface of the CIGS films, and they were baked at 200□C for 1-2 h in air. Following this step, the reaction products were etched in 10%-50% HCl. This ensured removal of residual chloride and hydroxide phases, and rendered the surfaces free of contaminants. Bilayer ZnO was again sputter deposited for device completion.

3. RESULTS

First, we describe the results from Cd or Zn PE treatments of $CuInSe_2$ films at 85□C for 10 min. The window layer is standard bilayer ZnO described above, and it has not been specially designed to optimize the performance of devices without CdS. Fig. 1 shows the current-voltage (I-V) curves for three devices made from the same $CuInSe_2$ film. The corresponding photovoltaic parameters are shown in Table 1.

The CdS device efficiency is 12.8%, which compares very favorably with the best devices reported to date. A comparison of its parameters with those of the Cd- and Zn-

Table 1: Light I-V parameters of $CuInSe_2$ devices with CdS, Cd PE and Zn PE treatments. Total area, 0.43 cm^2. After MgF_2 antireflection coating.

	ZnO/ CdS	ZnO/Zn PE	ZnO/Cd PE
V_{oc} (V)	0.485	0.444	0.443
J_{sc} ($mA.cm^{-2}$)	36.6	38.97	38.09
Fill factor	0.72	0.67	0.68
Efficiency (%)	12.78	11.56	11.46

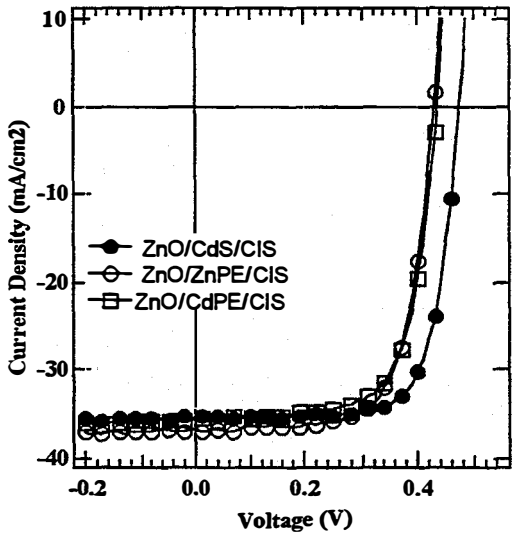

Fig. 1: Light I-V parameters of $CuInSe_2$ devices with CdS Cd PE and Zn PE treatments. All have two layer ZnO window. Total area, 0.43 cm^2. Before AR coating.

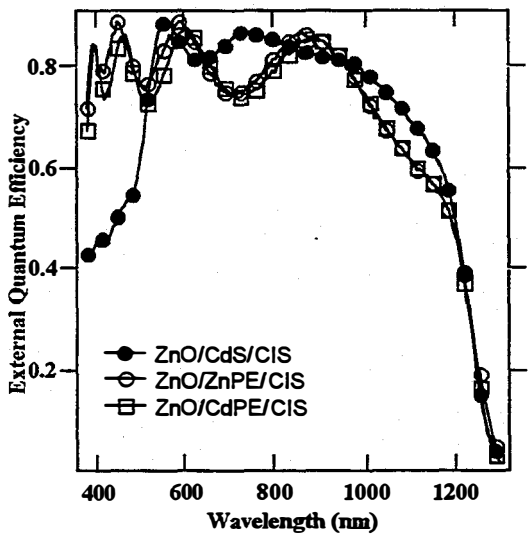

Fig. 2: Spectral response of the $CuInSe_2$ devices shown i Fig. 1. Measured before AR coating.

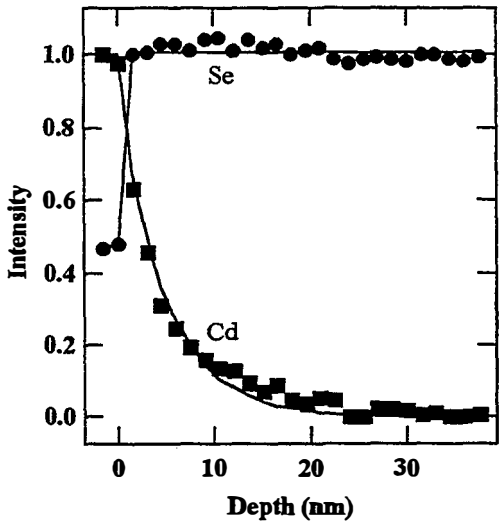

Fig. 3: XPS profile of Cd after Cd PE treatment. Th absorber is $CuInGaSe_2$ thin film.

treated devices shows that there is an increase in the current density (J_{sc}) and this is the expected gain when CdS-related absorption losses are eliminated. Reflectance losses of devices without CdS are considerably higher, and an antireflective coating increases the J_{sc} even further. The other interesting features are that the open circuit voltages (V_{oc}) of the Cd and Zn treated devices are within 50 mV of the CdS device, and the fill factors are close to 0.7. These losses are a consequence of a higher diode quality factor and a higher reverse saturation current density, and these are likely to arise from ZnO/CIS interface recombination. We must point out that devices made by directly sputtering ZnO on the CIS films result in poor diode characteristics. Typically, much lower voltages and fill factors are observed in comparison to the Cd-or Zn-treated devices. The spectral response of the above devices is depicted in Fig. 2, and the gain in the blue region is obvious.

Similar results have also been obtained for Ga containing absorbers where V_{oc}'s of 0.55 V have been observed as a result of Cd or Zn treatments. Trends in current densities and fill factors are the same as those described for $CuInSe_2$ devices. A comparison of the parameters for the direct ZnO, Cd PE treatment and the control devices is shown Table 2.

At this point, we must identify the possible mechanisms by which the PE treatments improve the diode properties. It is possible that Cd (Zn) species present in the alkaline solution interact with the absorber and induce some compositional and/or electronic changes. Group II elements are well known n-type dopants in $CuInSe_2$. To understand these potential effects, we have conducted X-ray Photoelectron Spectroscopy (XPS) and SIMS

Table 2: Light I-V parameters of $CuInGaSe_2$ devices with for direct ZnO, Cd PE/ZnO and CdS/ZnO. Total area, 0.43 cm^2. No AR coating.

	ZnO/CdS	ZnO/Cd PE	Direct ZnO
V_{oc} (V)	0.617	0.505	0.405
J_{sc} ($mA.cm^{-2}$)	30.18	33.54	25.5
Fill factor	0.73	0.67	0.51
Efficiency (%)	13.6	11.4	5.3

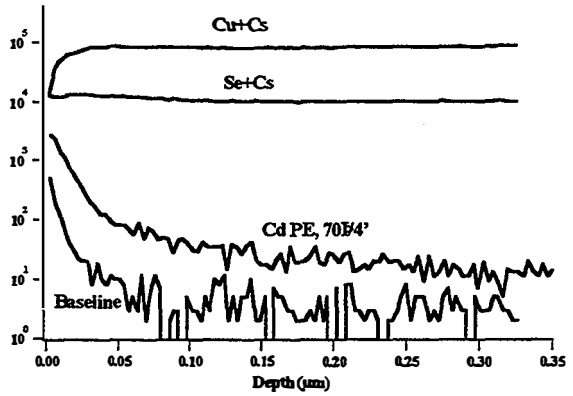

Fig. 4: SIMS profile of Cd, Cu and Se in $CuInSe_2$ thin films. Baseline refers to the as-grown film. The Cd PE treatment was done at 70□C for 4 min.

measurements of Cd PE treated thin films and single crystals, the results of which are described below.

3.1 XPS and SIMS Results

Fig. 3 shows the XPS profile of a Cd PE treated $CuInGaSe_2$ thin film. The Cd and Se signals are plotted as a function of depth. We find that appreciable levels of Cd are found in the surface region and possibly deeper. SIMS data show a similar effect, and an increase in the Cd concentration is observed in the Cd PE treated sample as compared to an as-grown $CuInSe_2$ film. This is shown in Fig. 4. The interpretation of SIMS data must take into account several factors specific to thin films such as surface roughness, and preferential sputtering. Because of these influences, it is difficult to make quantitative determinations of the concentrations. However, one can make the following observations about the trends. There appears to be an increase in the Cd concentration in the front region, possibly to a depth of 0.05-0.1 μm. The Cd level for longer depths is higher than the baseline, and it tends to approach the baseline in an asymptotic manner. This tail might be indicative of a faster diffusion through grain boundaries. The detection limit for Cd in the system is on the order of 10^{16} cm^{-3}, and this suggests that the measured Cd concentrations might be an order or two higher. Diffusion in polycrystalline thin films can be quite aggressive through the grain boundaries, and it is important

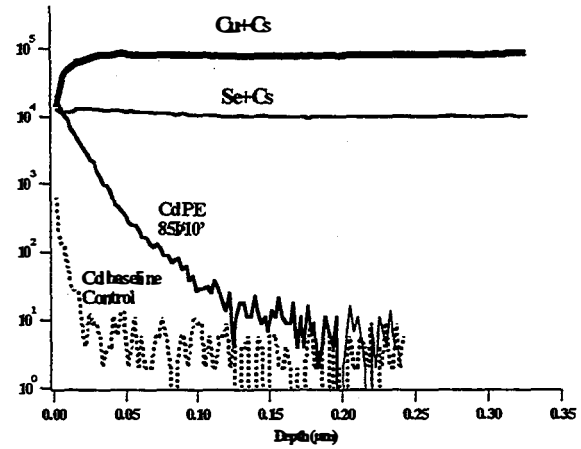

Fig. 5: SIMS profiles of Cd, Cu and Se in as- grown an Cd PE treated $CuInSe_2$ single crystals.

to sort out the contributions of intergrain and intragrain effects. Single crystals were chosen for this purpose.

The SIMS profile of a Cd PE treated single crystal sample is shown in Fig. 5. Here, the difference in Cd concentrations between the baseline (as grown crystal), and the Cd treated crystal is very clear, and the Cd signal reaches the baseline value. The in-diffusion of Cd coincides with a slight depletion of Cu level in the front region (not shown). We conclude from the above data that Cd is indeed incorporated in the absorber films. The mechanism of the reaction through which this occurs must be clarified. To explore this further, we soaked several large pieces of single crystals in a solution of 1.0 M $CdSO_4$ in 30% ammonium hydroxide at room temperature. The concentrations in this mixture are much greater than one would use in a CBD reaction, and the purpose here is to exaggerate the effects in a reasonable time. After 4 days, the solution was decanted and analyzed by inductively coupled plasma spectroscopy. The results were compared with a blank solution. The atomic concentrations, in ppm, were as follows, where the blank values are given in parentheses: Cu: 0.90 (0.02); In: 0.08 (0.01); and Se: 0.47 (0.09). We find that Cu is preferentially leached out, and some Se is also carried with it. The crystals were cleaned thoroughly in ultrasonic bath and then examined by XPS. The depth profile of Cd treated crystal shows the presence of Cd (see Fig. 6).

Further analysis of the shapes of the Cd 3d and Se 3d Auger lines demonstrates that the Cd is bound to Se, and the peak positions can be assigned to CdSe. The line shapes of the Cd and Se d levels are both altered by the Cd diffusion. These details will be published separately.

To summarize, our results suggest that the interaction of the absorber with the CBD solution results in an interfacial reaction. This might be the most important aspect of the CBD CdS process. The evidence for this is the fact that excellent devices are obtained simply by treating the absorbers in a combination of a Cd salt and ammonium hydroxide. The implication here is that the introduction of Cd can dope the absorber n-type and create a buried junction. This is consistent with the early observations on single crystals where Cd and Zn were found to dope the crystals n-type [7]. In studying the time dependence of this reaction, we found that the Cd profiles are established at low temperatures (40□C) and short times (1 min). One might envisage an ion-exchange reaction where the out-diffusion of Cu is driven by the in-diffusion of Cd; both facilitated by the ability of ammonia to complex the ions. The creation of a thin, heavily doped n-region can explain much of the observed phenomena. In a CdS device, the electric field will be supported entirely, or mostly, by this n-region, depending on the doping level. It is also quite possible that the Cu-deficient nature of the surfaces present natural sites for the occupation by Cd. In any case, we find that an enhanced n-doped region is more likely the heart of the device, rather than the CdS layer itself. The latter undoubtedly offers the benefits of a lattice-matched window layer, and it shields the absorber from ZnO and sputter damage. The foregoing discussion applies equally well to Zn as we have demonstrated with the Zn PE treatments.

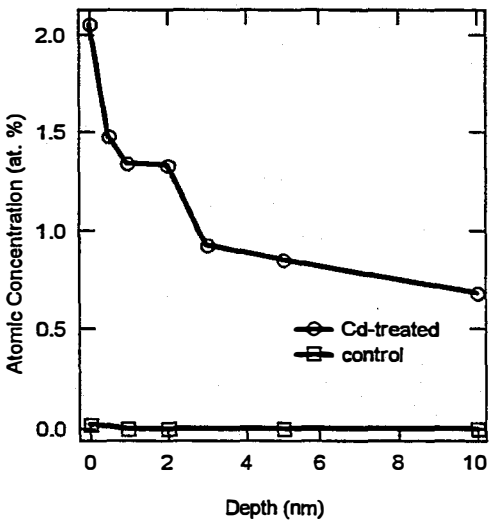

Fig. 6: XPS profile of Cd in $CuInSe_2$ single crystal after soaking for 4 days in 1.0 M $CdSO_4$, 30% NH_4OH.

3.2. Alternative Junction Strategies

The solutions to finding an alternative method for forming the junction follow from the previous section. Our approach is to develop methods for forming an n- type, emitter region by extrinsic doping. The most obvious candidates appear to be the II_B elements substituting for Cu; IV elements for the In or Ga; and the halogens for the Se atoms. The efficiency of the Cd "doping" suggests that Zn is the logical choice. Similarly, Cl or F could be effective on the Se sites. We have experimented with a variety of Zn sources, including elemental Zn. $ZnCl_2$ was chosen as the best candidate because of its low melting point and high vapor pressure at 200□C. The method of delivering the $ZnCl_2$ to the absorber surface has been varied. In one approach, the $ZnCl_2$ is dispersed in methanol and applied to the CIGS film. Following an annealing step at 200□C for 1 h, the reaction products are chemically removed by etching in HCl. The standard bilayer ZnO is sputtered to complete the device. The best result obtained by this method is a 13.5% efficiency device, and it did not require a light soak or heat treatment to realize the efficiency. The parameters of this device are: V_{oc}= 0.527 V, J_{sc}= 36.01 mA.cm^{-2}, and FF = 0.71. On

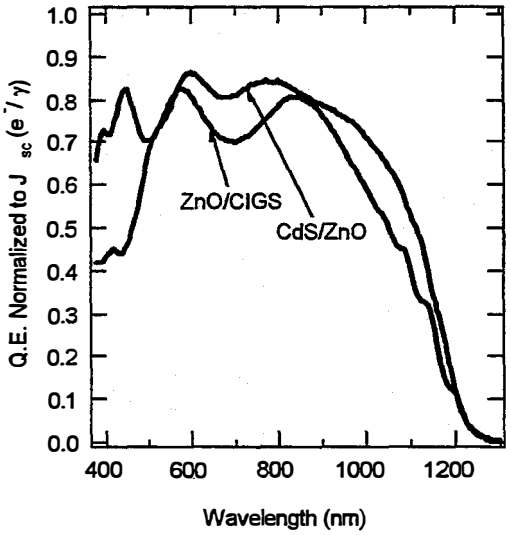

Fig. 7: Spectral response curves for CIGS devices with and without CdS.

another part of the absorber, a standard device (CdS/ZnO) was fabricated. A comparison of the spectral response curves is shown in Fig. 7. The gain in current density of the $ZnCl_2$ treated device is attributed to the elimination of the CdS related losses. Another interpretation is that the spectral response is indicative of a shallow n^+p junction with a thin, heavily doped emitter, and the ZnO serves as a conductive electrode.

At present, we are investigating completely "dry" methods such as close-spaced annealing to make the processing more suitable for manufacturing.

4. CONCLUSIONS

We have shown that the interfacial reaction that occurs in the chemical bath is instrumental in creating a buried junction in CIS-based absorbers. Ample evidence has been presented to show that Cd is introduced to such levels that it could form a thin, n-type emitter region. Devices made by wet chemical treatments in Cd or Zn solutions function like n^+p junctions with a ZnO window layer, and these offer the most compelling proof for this model. During the CBD CdS process, these changes could occur long before the CdS growth commences. The CdS layer provides a good lattice match to the absorber, a possible compositional grading at the interface region, and shielding from the sputter effects. It is unlikely that the junction is created solely by the OVC or the CdS, because neither component has demonstrated the carrier density to provide the electric field. The conductivity of the OVC layer is most likely enhanced by Cd doping, and this enables the formation of a more efficient junction. The inability to make efficient device from $CuGaSe_2$ or $CuIn_{0.5}Ga_{0.5}Se_2$ might stem from the fact that the former has not been made usefully n-type by extrinsic doping [12]. Finally, we show how the concept of extrinsic doping can be used to create a homojunction in the CIS based thin films.

ACKNOWLEDGMENTS

The authors wish to acknowledge the support of the National CIS Team of the Thin Film Partnership Program. We thank A. Mason, H. Field, D. Dunlavy and other members of the NREL Characterization Center for invaluable support. Contributions of Jim Dolan, Jeff Alleman and Jennifer Granata are acknowledged. This work is supported by the U. S. Department of Energy under Contract No. DE-AC36-83CH10093 to the National Renewable Energy Laboratory.

REFERENCES

[1]. J. R. Tuttle, J. S. Ward, A. Duda, T. A. Berens, M. A. Contreras, K. Ramanathan, A. L. Tennant, J. Keane, E. D. Cole, K. Emery and R. Noufi, Proc. Mat. Res. Soc. Symp., **426**, 143 (1996).

[2]. D. Pier, W. Chesarek, M. Dietrich, S. Kuriyabawa and R. Gay, Proc. 11th European PV Solar Energy Conference, 1992, pp 107-111.

[3]. D. Schmid, M. Ruckh, F. Grunwald, and H. W. Schock, J. Appl. Phys., **73**, 2902 (1993).

[4]. V. Nadenau, D. Braunger, D. Hariskos, M. Kaiser, Ch. Koble, A. Oberacker, M. Ruckh, U. Ruhle, R. Schaffler, D. Schmid, T. Walter, S. Zweigart and H. W. Schock, Prog. Photovoltaics, **3**, 363 (1995).

[5]. See: R. Herberholz, H. W. Schock, U. Rau, J. H. Werner, T. Haalboom, T. Godecke, F. Ernst, C. Beilharz, K. W. Benz and D. Cahen, Proc. **26th** IEEE PVSC, Anaheim CA, 1997, p. 323, and references therein.

[6]. R. J. Matson, M. A. Contreras, J. R. Tuttle, A. B. Awartzlander, P. A. Parilla and R. Noufi, Mat. Res. Soc. Symp. Proc., Vol. **426**, 183 (1996).

[7]. B. Tell and P. M. Bridenbaugh, J. Appl. Phys, **48**, 2477 (1977).

[8]. Y. Ohtake, M. Ichikawa, T. Okamoto, A. Yamada, M. Konagai, and K. Saito, Proc. **25th** IEEE PVSC, Washington, D. C., p. 793 (1996).

[9]. K. Kushiya, M. Tachiyuki, T. Kase, Y. Nagoya, T. Miura, D. Okumura, M. Satoh, I. Sugiyama, and O. Yamase, Proc. **25th** IEEE PVSC, Washington, D. C., p. 327 (1996).

[10]. L. C. Olsen, W. Lei, F. W. Addis, W. N. Shafarman, M. A. Contreras, and K. Ramanathan, Proc. **25th** IEEE PVSC, Washington, D. C., p. 363 (1996)

[11]. A. Gabor, J. R. Tuttle, D. S. Albin, M. A. Contreras and R. Noufi, Appl. Phys. Lett. **65**, 198 (1994).

[12]. J. H. Schon, O. Schenker, H. Riazi-Nejad, K. Friemelt, Ch. Kloc, and E. Bucher, Phys. Stat. Sol. (A), **161**, 301 (1997).

1-eV GaInNAs SOLAR CELLS FOR ULTRAHIGH-EFFICIENCY MULTIJUNCTION DEVICES

D. J. Friedman, J. F. Geisz, S. R. Kurtz, and J. M. Olson
National Renewable Energy Laboratory, 1617 Cole Blvd., Golden, CO 80401 USA

ABSTRACT: We demonstrate working prototypes of a GaInNAs-based solar cell lattice-matched to GaAs with photoresponse down to 1 eV. This device is intended for use as the third junction of future-generation ultrahigh-efficiency three- and four-junction devices. Under the AM1.5 direct spectrum with all the light higher in energy than the GaAs band gap filtered out, the prototypes have open-circuit voltages ranging from 0.35 to 0.44 V, short-circuit currents of 1.8 mA/cm^2, and fill factors from 61% to 66%. The short-circuit currents are of principal concern: the internal quantum efficiencies rise only to about 0.2. We discuss the short diffusion lengths which are the reason for this low photocurrent. As a partial workaround for the poor diffusion lengths, we demonstrate a depletion-width-enhanced variation of one of the prototype devices that trades off decreased voltage for increased photocurrent, with a short-circuit current of 6.5 mA/cm^2 and an open-circuit voltage of 0.29 V.
Keywords: GaInNAs - 1: Multijunction Solar Cells - 2: High-Efficiency - 3

1. INTRODUCTION

The $Ga_{0.5}In_{0.5}P$/GaAs tandem solar cell is in production for space photovoltaic applications and is a leading candidate for terrestrial high-concentration photovoltaics because of its record-setting efficiency [1-4]. The addition of an active Ge junction, yielding a three-junction device, has been demonstrated to boost efficiencies further [5]. However, the Ge band gap is not optimal for the third junction: significantly higher efficiencies would be obtained if the third junction could be fabricated from a 1-eV-band-gap material [6]. If this next generation of multijunction devices could be achieved, the Ge junction could be reintroduced under this three-junction stack for a resulting monolithic, two-terminal device with projected real-world efficiencies above 35% for air-mass 0 (AM0) and above 40% for 500-suns terrestrial [6]. This evolution of multijunction solar-cell structures from the existing two-junction device [1] to future-generation three- and four-junction devices is shown in Fig. 1. Projected idealized efficiencies [6] for these devices are summarized in Table I. (Practical efficiencies can be expected to be ~80% of the idealized values.) The crucial step in the evolution to these next generations of ultrahigh-efficiency devices is to develop the 1-eV third cell lattice-matched to GaAs (or Ge).

It has recently been shown that N induces a very large band-gap bowing for the $Ga_{1-x}In_xN_yAs_{1-y}$ alloy system. Concentrations of N as low as a few percent lower the band gap by a significant fraction of an eV [7]. Furthermore, with $y=0.35x$, the alloy is lattice-matched to GaAs (or Ge). For these reasons, Kondow proposed and demonstrated this material as the active layer for a 1-eV laser [8]. Here, we propose this material for a 1-eV GaAs-lattice-matched solar cell. We demonstrate several working prototype 1-eV solar cells based on GaInNAs active layers lattice-matched to GaAs which may be suitable for the third cell of the next generations of ultrahigh-efficiency devices, if problems with the quantum

Table I. Projected idealized solar photovoltaic conversion efficiencies at 300K for the device structures of Fig. 1 [6]. The AM0 numbers apply to use in space, and the AM1.5D 500 suns numbers apply to use in terrestrial concentrator systems.

Device	AM0 1 sun	AM1.5D 500 suns
2 junction	31%	36%
3 junction (with Ge)	35%	42%
3 junction (with 1-eV)	38%	47%
4 junction	41%	52%

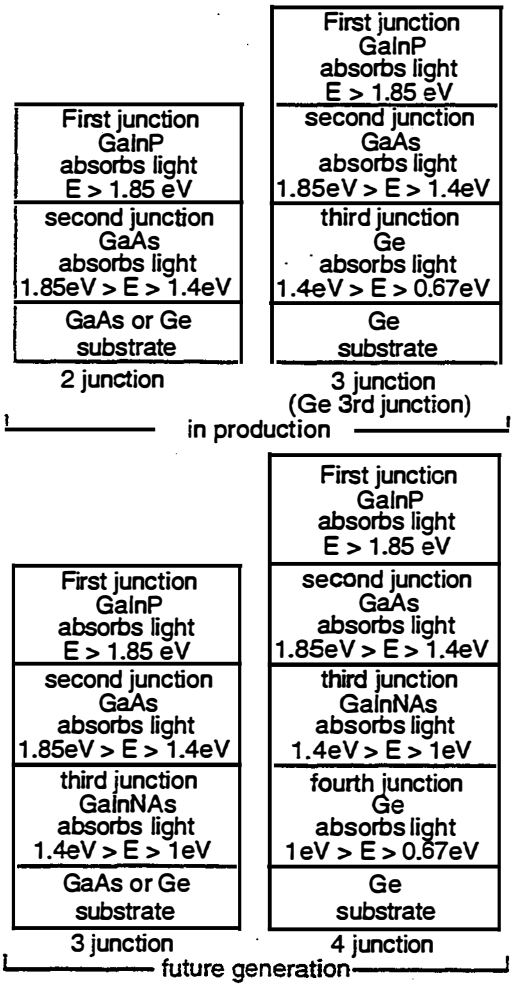

Figure 1. Evolution of multijunction solar-cell structures from the existing GaInP/GaAs two-junction device to three- and four-junction future-generation devices incorporating a 1-eV third junction. In each multijunction device, the individual cells are interconnected by tunnel junctions (not shown).

efficiency can be overcome.

2. DEVICE FABRICATION

The devices were grown by low-pressure metalorganic vapor-phase epitaxy on GaAs substrates oriented 2° to $(111)_B$ from (100), using trimethylgallium (TMGa), trimethylindium (TMIn), arsine (AsH_3), phosphine (PH_3), and dimethylhydrazine (DMHy) as the nitrogen source. For GaInNAs layers grown without any intentionally introduced dopant, the resulting background doping is *p*-type on the order of $10^{17}/cm^3$, probably largely from carbon introduced into the as-grown material from the dimethylhydrazine. Si (from disilane) and Se (from hydrogen selenide) were used as *n*-type dopants for the various layers, including the *n*-GaInNAs layers. Zn (from diethylzinc) was used as a *p*-type dopant for the GaAs and GaInP layers and for some of the GaInNAs layers. For other *p*-GaInNAs layers, the background *p*-type doping was used.

The nitrogen incorporation into GaInNAs is found to depend sensitively on the growth temperature and DMHy/AsH_3 flow ratio [9]; high temperatures lead to minimal incorporation, presumably because under these conditions growth proceeds near thermodynamic equilibrium, for which the N solubility is expected to be very small. For this reason, the GaInNAs layers of the devices presented here were grown at a relatively low temperature of ~580°–600°C, at a rate of 2.4 μm/hr and DMHy/AsH_3 flow ratio of 20. The compositions of the GaInNAs epilayers were determined by growing reference GaInNAs/GaAs structures under the same growth conditions as the GaInNAs layers in the devices, and then determining the compositions of the reference epilayers from x-ray diffraction measurements of the epilayer lattice constants [10]. The N concentrations were selectively cross-checked with secondary-ion mass spectroscopy (SIMS). The band gaps of the GaInNAs layers in the devices were determined from the device quantum efficiency (QE) curves, as discussed below.

The structures of the various prototype solar cells include both p/n and n/p GaInNAs homojunctions and a GaAs/GaInNAs heterojunction. The structures are shown schematically in Fig. 2. All the device structures include a GaInP window layer/stopetch layer and a GaAs contact layer. The heterojunction device includes a 3-μm-thick GaAs optical filter above the junction intended to minimize misleading photoresponse from the GaAs emitter layer. The structures were processed into solar cells with electroplated Au front grids and back contacts, with etched mesas defining an illuminated area of 0.10 cm^2. No antireflection coatings were applied. Several devices were fabricated on each wafer, and are designated, for example, as PA280#7.

3. DEVICE MEASUREMENT

To measure the current-voltage (IV) curves for the devices, the device currents were determined by integrating the measured external QEs of the devices against the ASTM standard AM1.5 Direct spectrum (1000 W/m^2) over the energy range below the GaAs band gap, since in the intended application in a multijunction device, the spectrum reaching the 1-eV cell will be filtered by the GaAs cell above it. The devices were then placed in the solar simulator and covered by a GaAs filter to remove light above the GaAs band edge. The simulator intensity was adjusted to set the short-circuit current of the device being measured in the simulator equal to its AM1.5D current calculated as described above. The IV curves were then measured at this simulator intensity. This approach assumes that the QE curves measured under low illumination accurately represent the QE under white light bias. We checked this assumption for device PA280#7 for light biases up to ~200mA/cm^2 and found that for photon energies below the GaAs band gap, the variation of QE with light bias is less than ±2%.

It should be emphasized that correctly measuring the IV curves for devices such as these, which are designed for operation under the spectral range of 1.0 to 1.4 eV, is not trivial. Before settling on the measurement technique described in the previous paragraph, we first tried measuring the IV curves by using a silicon reference cell calibrated while covered with a GaAs wafer to cut off the reference cell's photoresponse above the 1.4-eV GaAs band edge. One might at first expect such a reference cell setup to have a spectral response sufficiently similar to that of the GaInNAs devices under test to yield acceptably precise measurements of the photocurrents. However, this procedure generated spectral mismatch factors that differed from the ideal value of unity by almost a factor of

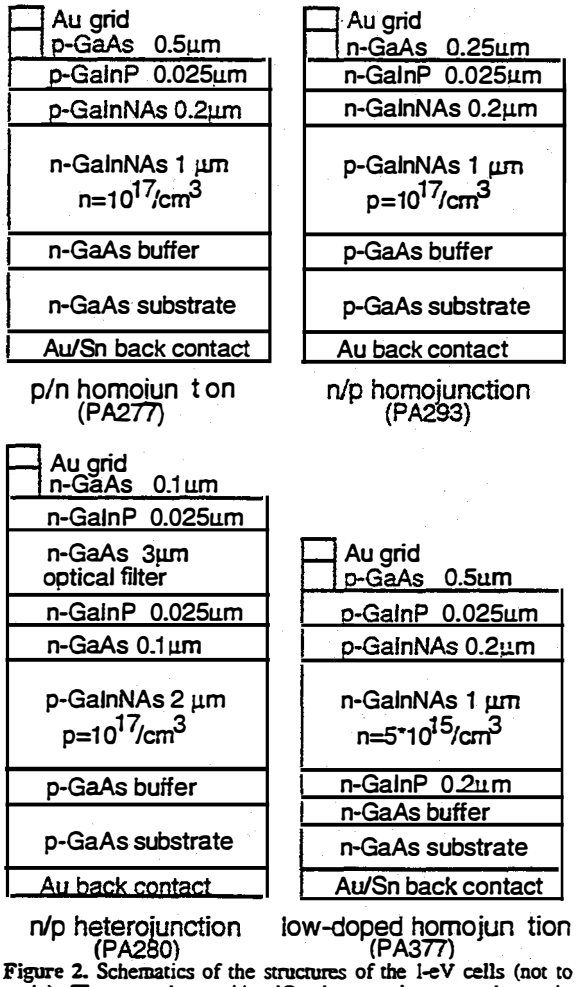

Figure 2. Schematics of the structures of the 1-eV cells (not to scale). The growth run identification numbers are shown in parentheses at the bottom of the figure. For each growth run, several devices were fabricated on the wafer, and are designated, for example, as PA280#7 in the tables and figures below.

two. There are at least three causes for this difficulty: (1) the spectral range of 1-1.4 eV is very narrow, (2) the spectrum of the simulator's xenon lamp has multiple spikes in this spectral region, and (3) for terrestrial spectra, there are two large atmospheric-absorption notches in the 1.0-1.4 eV spectral range. In addition, variations in the band gap of the GaInNAs alloy and drifts in the spectrum of the simulator can cause significant variation in the spectral correction factor, necessitating its measurement for every sample. We conclude that attempts to measure the currents for these devices by using the conventional expedient of a reference cell are likely to result in significant errors if a xenon arc lamp is the light source.

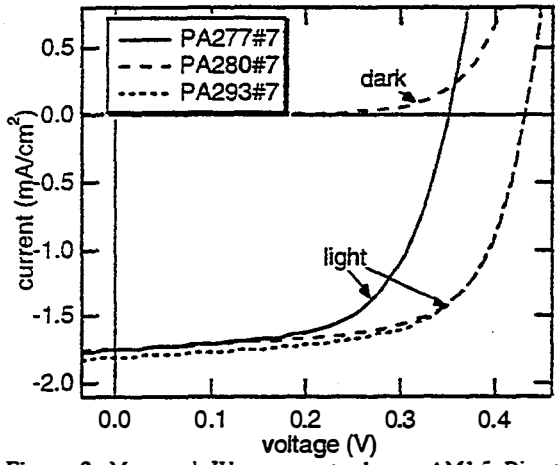

Figure 3. Measured IV curves at ~1 sun AM1.5 Direct illumination for several of the prototype devices of Fig. 2. The devices were covered by a GaAs filter and the currents were calibrated as described in the text. The corresponding dark IV curve for PA280#7 is shown also.

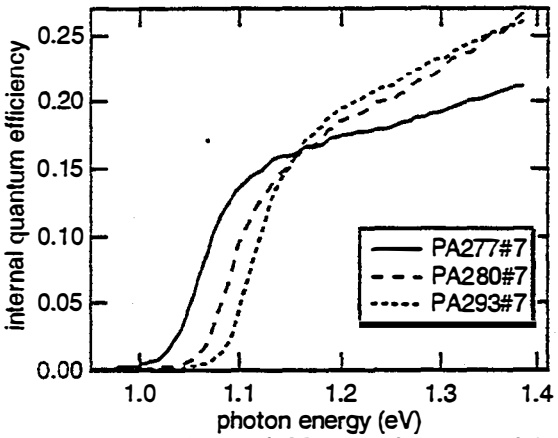

Figure 4. Measured internal QE curves for several of the prototype devices of Fig. 2.

Table II. GaAs-filtered AM1.5D device performance parameters V_{oc}, J_{sc}, and FF from the IV curves of Figs. 3 and 6(a); band gaps E_g from the QE curves of Figs. 4 and 6(b); and, in the last two columns, the currents calculated from the internal QE for the AM1.5D and AM0 solar spectra.

Device	V_{oc} (mV)	J_{sc} (mA/cm²) ext. QE AM1.5D	FF (%)	E_g (eV)	J_{sc} (mA/cm²) int.QE AM1.5D	J_{sc} (mA/cm²) int. QE AM0
PA277#7	353	1.8	61	1.052	2.5	2.7
PA280#7	435	1.8	66	1.078	2.6	2.7
PA293#7	435	1.8	64	1.095	2.6	2.7
PA377#3	294	6.5	59	1.025	9.2	10.2

4. CONVENTIONAL PROTOTYPES: RESULTS

The short-circuit current (J_{sc}), open-circuit voltage (V_{oc}), and fill factor (FF) from these IV curves are summarized in Table II (the parameters for device PA377#3 will be discussed below). The IV curves are shown in Fig. 3. The corresponding dark-IV curve for the n/p heterojunction device, PA280, is shown also. A comparison of the light and dark IV curves for this device shows that the apparent shunt resistance visible in the light IV curve can be attributed to field-aided collection, as the dark IV curve is not shunted. The V_{oc} expected for an ideal device in this band-gap range would be ~0.6-0.7 V, so that the V_{oc} of the prototypes are within ~0.2 V of the ideal. The nonideality of the FFs appears to result from various causes including field-aided collection and the low J_{sc}, which is at least a factor of three less than expected. The problems with J_{sc} will be discussed below.

The crucial test of whether the devices convert photons down to the desired energy of 1 eV is whether the devices show photoresponse down to these energies. Figure 4 shows the measured internal QE curves for the devices whose IV curves are shown in Fig. 3. All device QE data presented in this paper were taken at short circuit, i.e., zero applied voltage bias, at very low light levels of $< 10^{-2}$ suns. The band edges, tabulated in Table II, are roughly 1 eV, as desired for the third junction in the three- or four-junction ultrahigh-efficiency device designs of Fig. 1. However, while the QE curves confirm the devices' conversion of light down to ~1 eV, the curves also indicate a serious deficiency in these devices: the QEs are a factor of 3–5 lower than the near-unity QE for a good-quality GaAs cell, resulting in the low J_{sc} values measured from the IV curves for these devices.

5. CONVENTIONAL PROTOTYPES: DISCUSSION

In order to study the QE problem in more detail, a series of GaInNAs epilayers were grown on GaAs substrates under a wide range of growth conditions, at various thicknesses, both without and with back-surface

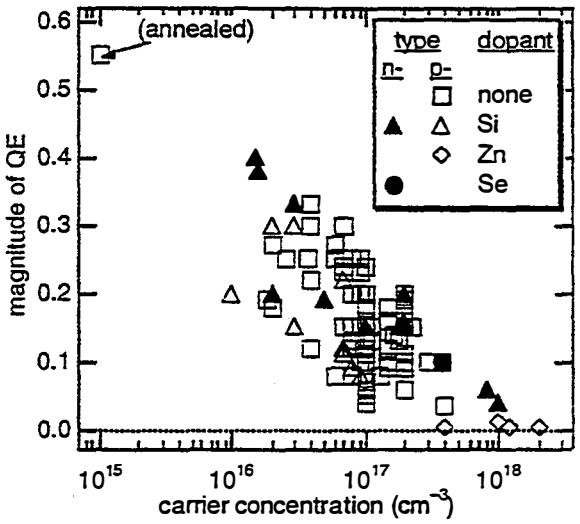

Figure 5. The QE of a variety of GaInNAs epilayers at 200 meV above the band edge, as a function of carrier concentration. All data shown are from layers with band gaps E_g<1.15 eV.

passivation layers, both without and with distillation purification of the DMHy source, and over a range of n- and p-type doping levels from $<10^{16}/cm^3$ to $>10^{18}/cm^3$. Growth temperatures from 550°C to 650°C, rates from 2.4μm/h to 7 μm/h, AsH_3/group-III ratios from 2 to 40, and DMHy/AsH_3 ratios from 7 to 100 were used. The as-grown epilayers were brought into contact with a liquid electrolyte, and the QEs of the resulting Schottky-barrier-like junctions were measured. The study is discussed in detail elsewhere [10]. The central finding is that the minority-carrier diffusion lengths are very short: shorter than the 0.04μm-0.4μm depletion widths. Thus there is carrier collection only from the depletion region. This is the cause of the field-aided collection behavior observable in the IV curves as noted above. Figure 5 shows the magnitude of the QE for a number of epilayers grown under a wide range of growth conditions as a function of the carrier concentration. The QE is seen to be determined by the carrier concentration, because of the dependence of the carrier concentration on the depletion width.

It remains to be determined whether the short diffusion lengths are due to extrinsic/ growth-related defects or instead to characteristics intrinsic to the GaInNAs material. A possible cause of extrinsic defects might be impurities introduced from an insufficiently pure DMHy source. Intrinsic causes of the short diffusion lengths might include localized energy states in the band structure [11], or spatially localized band fluctuations resulting from GaN clustering. If the cause of the short diffusion lengths is extrinsic, it should in principle be possible with further development to grow GaInNAs with a photoresponse comparable to that of good-quality GaAs. In this case, extension of the GaInP/GaAs two-junction device to three and four junctions by addition of a GaInNAs junction, as illustrated in Fig. 1, would result in the achievement of the efficiency boosts of Table I. If, however, the diffusion-length problem is an intrinsic one, the efficiency boosts of Table I will not be achievable with the GaInNAs device. Work on determining the cause of the low diffusion lengths is under way.

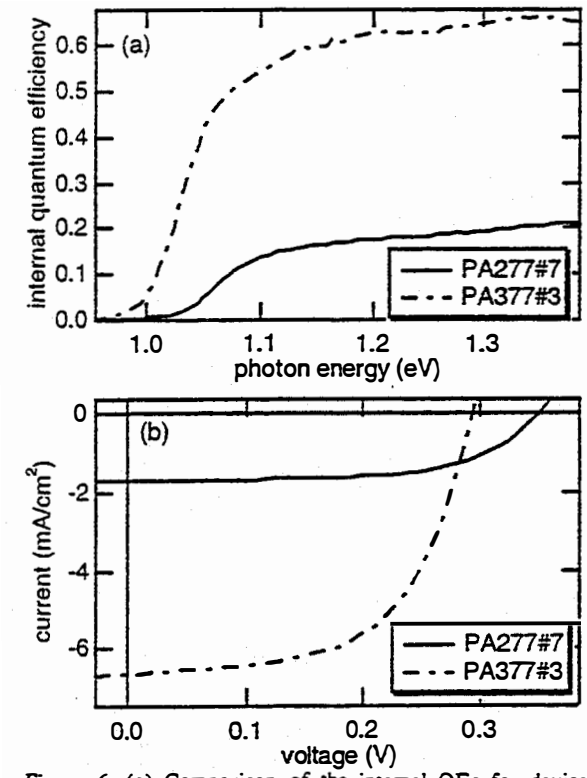

Figure 6. (a) Comparison of the internal QEs for device PA277#7, which has an $n=10^{17}/cm^3$ conventionally-doped base, and device PA377#3, which has an $n=5\times10^{15}/cm^3$ lightly-doped base. (b) Comparison of the IV curves for PA277#7 and PA377#3. Curves were measured as for Fig. 3.

6. ENHANCED-DEPLETION-WIDTH DEVICE: RESULTS AND DISCUSSION

In order to study the effect of the depletion width on the photocurrent in a full device structure, we fabricated a p/n homojunction device, PA377 in Fig. 2, whose main difference from the device PA277 is a much lower base doping of $n = 5\times10^{15}/cm^3$ than the $n = 1\times10^{17}/cm^3$ doping of PA277, as measured by capacitance-voltage (CV) measurement. The corresponding depletion width for PA377 as measured by CV is ~0.5 μm, a significant fraction of the 1-μm base layer thickness, and much greater than the 0.1-μm depletion width for the higher-doped PA277. The QEs for the two devices are compared in Fig. 6(a). The lower doping and consequent greater depletion width of PA377 give a significantly enhanced QE compared with PA277. Figure 6(b) compares the IV curves for these two devices. The enhanced QE for PA377 is reflected in a correspondingly enhanced J_{sc}. The overall efficiency of the device is not proportionally enhanced, because the V_{oc} is diminished, mostly because of the increased dark current. (Additionally, 30 to 70 mV of the decreased V_{oc}, and a small fraction of the increased J_{sc}, are due to the lower band gap for PA377 than for the other devices, as listed in Table II.) The dark currents for the devices discussed here are shown in Fig. 7, with lines corresponding to ideality factor n=1 and n=2 dark currents included for comparison. While PA293 has n=2, all the other devices have roughly n=1.5. The Sah-Noyce-Shockley treatment [12] of recombination/ generation currents in the depletion region gives n ranging from n=1 for shallow recombination centers to n=1.8 for deep centers. Therefore the n=1.5 ideality factors of Fig. 7 suggest that these devices may have trap levels intermediate between deep and shallow.

The tradeoff of increased current at the expense of decreased voltage may make it possible to meet the

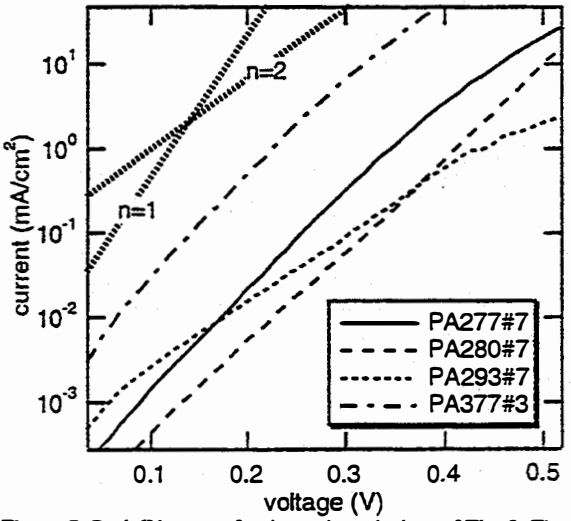

Figure 7. Dark IV curves for the various devices of Fig. 2. The slopes corresponding to idealit factors n=1 and 2 are indicated by the thick dotted lines labeled "n=1" and "n=2".

current-matching requirements for the third cell of the series-connected three- and four-junction devices of Fig. 1. A current of ~14 mA/cm^2 would be required from the GaInNAs device for current matching. Table II lists for each device the results of a calculation of the J_{sc} for the AM1.5D spectrum using the *internal* QEs of the devices, which is a reasonable projection of what the J_{sc} would be if high-quality antireflection coatings were applied to the devices. Device PA377#3 has a projected current of 9.2 mA/cm^2, which is within a factor of two of the current required for current-matching [1]. Bringing the current of future devices up to the current-matching value may be possible but will be challenging, because to achieve a sufficiently large depletion depth to bring the photocurrent up enough for current-matching would require a base doping density on the order of 1×10^{15}/cm^3. Achieving such a low doping density will not be easy given the $p\approx1\times10^{17}$/cm^3 background doping, requiring either a very delicate *n*-type counter-doping, a change in a growth condition (e.g., switching from dimethylhydrazine to an alternate source such as tertiarybutylhydrazine or plasma-cracked N_2) so as to reduce the background doping, or a treatment such as annealing [10] to lower the background doping level. The difficulty is illustrated by the variation in doping density which occurred across the PA377 wafer. Although only the #3 device from the wafer is discussed in this paper in detail, a total of a dozen devices were fabricated on the wafer. Doping densities on the various PA377 devices varied from the $n\approx5\times10^{15}$/cm^3 of #3 to an order of magnitude higher, with corresponding depletion widths and photocurrents lower by a factor of 2 or more. Thus, it may be possible to use this high-depletion-width low-voltage/enhanced-current version of the GaInNAs device as the third cell to gain an efficiency boost over the two-junction device, if the challenges associated with low base doping can be overcome. Alternatively to the low-doping approach, it might be possible to improve current collection by using a graded-band-gap or graded-doping base. It should be kept in mind that if it does prove possible to improve current collection enough to achieve current-matching and allow use of the GaInNAs device in the three- and four-junction devices of Fig. 1, the tradeoff of decreased V_{oc} for increased current means that the efficiency benefits of the GaInNAs third junction will be less than expected from the idealized calculations summarized in Table I. In order to model the device performance accurately enough to make a more precise statement about the effect of the decreased V_{oc}, it will be necessary to make measurements of GaInNAs materials parameters such as lifetimes and effective masses for which limited or no data exists for this new materials system.

7. CONCLUSIONS

Prototype solar cells with GaInNAs active layers have demonstrated photoresponse down to the 1-eV photon energy required for the third junction of future-generation multijunction devices. The internal QEs for devices with standard base dopings of 10^{17}/cm^3 are very low, on the order of 0.2, because of the low minority-carrier diffusion lengths in the GaInNAs layer. Efforts to understand and eliminate the cause of the low diffusion lengths are ongoing. Lowering the base doping greatly improves the photocurrent at the expense of the voltage and fill factor by increasing the depletion width. If challenges associated with the low doping can be met, it might be possible to use such a field-enhanced device in the multijunction structures of Fig. 1, although the efficiency benefits would be less than predicted in Table I.

ACKNOWLEDGMENTS

This work was supported by the U.S. Department of Energy contract number DE-AC36-83CH10093. We thank C. Kramer for help with the device fabrication, H. Field for help with device-measurement issues, and R. Reedy for SIMS measurements.

REFERENCES

[1] K.A. Bertness, S.R. Kurtz, D.J. Friedman, A.E. Kibbler, C. Kramer, and J.M. Olson, Appl. Phys. Lett. **65** (1994) 989.

[2] S.R. Kurtz, K.A. Bertness, D.J. Friedman, A.E. Kibbler, C. Kramer, and J.M. Olson, 1st World Conference on Photovoltaic Energy Conversion (1994) 2108.

[3] D.J. Friedman, S.R. Kurtz, K.A. Bertness, A.E. Kibbler, C. Kramer, and J.M. Olson, Progr. Photovolt. **3** (1995) 47.

[4] T. Takamoto, E. Ikeda, H. Kurita, and M. Ohmori, Appl. Phys. Lett. **70** (1997) 381.

[5] P.K. Chiang, J.H. Ermer, W.T. Nishikawa, D.D. Krut, D.E. Joslin, J.W. Eldredge, B.T. Cavicchi, and J.M. Olson, 25th IEEE Photovoltaic Specialists Conference (1996) 183.

[6] S.R. Kurtz, D. Myers, and J.M. Olson, 26th IEEE Photovoltaic Specialists Conference (1997) 875.

[7] M. Weyers, M. Sato, and H. Ando, Jpn. J. Appl. Phys. **31** (1992) 853.

[8] M. Kondow, K. Uomi, A. Niwa, T. Kitatani, S. Watahiki, and Y. Yazawa, Jpn. J. Appl. Phys. **35** (1996) 1273.

[9] M. Weyers and M. Sato, Appl. Phys. Lett **62** (1993) 1396.

[10] J.F. Geisz, D.J. Friedman, J.M. Olson, S.R. Kurtz, and B.M. Keyes, J. Cryst. Gr. (in press)

[11] L. Bellaiche, S.-H. Wei, and A. Zunger, Phys. Rev. B **56** (1997) 10233.

[12] C.T. Sah, R.N. Noyce, and W. Shockley, Proc. IRE **45** (1957) 1228.

STRUCTURE OF Ge(100) SURFACES FOR HIGH-EFFICIENCY PHOTOVOLTAIC APPLICATIONS

J.M. Olson and W.E. McMahon
National Renewable Energy Laboratory
Golden, CO 80401 USA

ABSTRACT: While much is known about the Ge(100) surface in a UHV/MBE environment, little has been published about this surface in an MOCVD environment. The main objective of this study is to determine the structure of the surface of Ge substrates in the typical MOCVD reactor immediately prior to and following the heteronucleation of GaAs and other lattice-matched III-V alloys, and to determine the conditions necessary for the growth of device-quality epilayers. In this paper we present the **first** STM images of the MOCVD-prepared Ge surfaces. Although many of the observed features are very similar to UHV- or MBE-prepared surfaces, there are distinct and important differences. For example, while the As-terminated surfaces for MBE-Ge and MOCVD-Ge are virtually identical, the AsH_3-treated surfaces in an MOCVD reactor are quite different. The terrace reconstruction is rotated by $\pi/2$, and significant step bunching or faceting is also observed. Time-dependent RD kinetic studies also reveal, for the first time, several interesting features: the transition rate from an As-terminated (1x2) terrace reconstruction to a stable AsH_3-annealed surface is a function of the substrate temperature, substrate miscut from (100) and AsH_3 partial pressure, and, for typical prenucleation conditions, is relatively slow. These results explain many of the empirically derived nucleation conditions that have been devised by numerous groups.

1. INTRODUCTION

Single-junction GaAs and GaInP/GaAs tandem solar cells are currently being produced using metal organic chemical vapor deposition (MOCVD) on a large scale for communication-satellite power applications. Virtually all of these devices are grown on Ge(100) substrates. Although there are a number of "recipes" for the growth of GaAs on Ge(100) with specular morphologies or low antiphase domain (APD) or low stacking-fault densities, many present contradictory results. For example, Pelosi et al. [1] find that the GaAs surface morphology is best for very low V/III ratio (on the order of 1), using a moderate growth rate (Rg~3.5 μm/hr) and low growth temperature (Tg=600°C). On the other hand, Li et al. [2] find the lowest APD density occurs for high V/III, low Rg and high Tg. Chen et al. [3] showed that "good" morphology could only be obtained for growth temperatures in a range of 600°C to 630°C.

Heretofore, most of the basic studies of the surface of Ge(100) were conducted on samples prepared under ultrahigh vacuum (UHV) or molecular beam epitaxy (MBE) conditions (see reference [4]). Virtually no attention has been paid to MOCVD-prepared surfaces due to the lack of tools required to determine the nature of these surfaces. And although double-stepped, single-domain vicinal (100) surfaces are, from MBE studies, considered important for APD-free growth, little attention is paid to this aspect of the problem in most of the MOCVD papers.

The objective of this study is to determine some of the basic properties of Ge(100) surface prepared in a typical MOCVD environment using reflectance difference (RD) spectroscopy, scanning tunneling microscopy (STM), low energy electron diffraction (LEED), and Auger electron spectroscopy (AES).

2. EXPERIMENTAL

The general experimental setup is shown in Fig. 1. The STM, LEED, and AES are housed in a UHV chamber that is attached to the MOCVD reactor via a UHV transfer line. An MOCVD-prepared sample can be quickly quenched and transferred to the analytical chamber without exposing the surface to air or any other reactive atmosphere. Attached to the same transfer line is a solid-source III-V MBE reactor.

The RD spectrometer is attached to the MOCVD reactor as shown in Fig. 2 and is used to determine *in situ* the state of the surface in real time. This spectrometer measures

$$\frac{\Delta R}{R} = \frac{R_{110} - R_{1\bar{1}0}}{\left(R_{110} + R_{1\bar{1}0}\right)/2}, \qquad (1)$$

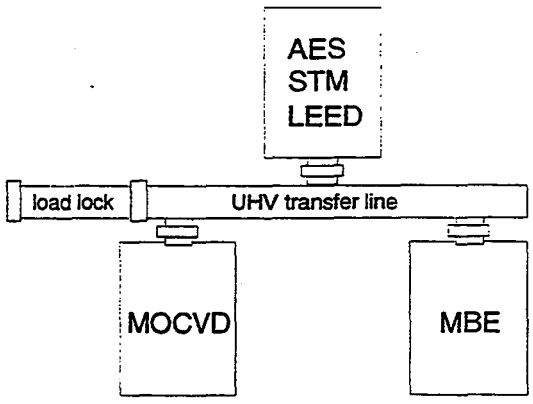

Figure 1. Schematic of MOCVD/MBE/Surface Analysis Cluster Tool.

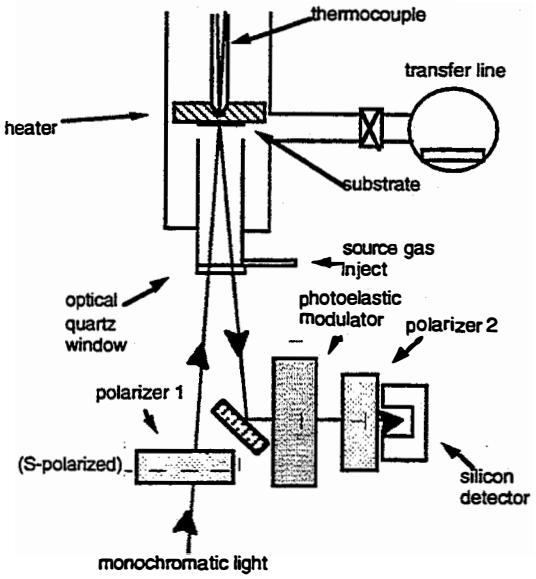

Figure 2. Schematic of RDS/MOCVD setup.

where $R_{[1\bar{1}0]}$ and $R_{[110]}$ are the reflectances for light polarized in the as-noted crystallographic direction. Further details are published elsewhere [5, 6].

The wafers were cleaned using a method similar to that described by Fitzgerald et al. [7]. The wafers were first etched in $1NH_4OH:1H_2O_2:10H_2O$ at room temperature for 1 min. This removes about 0.2 μm. The wafer is then rinsed in deionized H_2O for 2 min followed by 1 min in $1HCl:1H_2O_2:10H_2O$ and a 2-min rinse in flowing DI H_2O. The wafers are then blown dry with a stream of N_2 gas. The HCl-based solution also etches Ge at 0.2 μm/min. The samples are then spin-dried and mounted on molybdenum carriers. The carriers are heated radiatively with a low thermal mass resistance heater. The temperature of the sample is determined by optical pyrometry. The MOCVD reactor pressure was fixed at 70 torr with a H_2 carrier flow of 6 slm.

From a surface science point of view, the hot interior surfaces of a typical MOCVD reactor are an infinite source of impurities. Our reactors are used routinely to grow III-V compounds of Ga, In, Al, As, and P. Hence, if the last material grown in the reactor is, for example, GaInP, a subsequent anneal of Ge(100) in this reactor will contaminate the surface with, primarily, P and In. Therefore, the results in section 3.1. were achieved using a freshly cleaned reactor. For section 3.2., we used clean molybdenum susceptors in a GaAs-contaminated reactor. This contamination yields a finite partial pressure of As upstream of the substrate.

After annealing, the samples are quenched to room temperature and transferred quickly to the analytical chamber. The quench rate is between 200 and 300°C/min and the total transfer time is less than 10 min.

The STM images were recorded at a sample bias of –3V and a tunneling current of 1nA. With the exception of tilting and artificial illumination to enhance the contrast, the STM are as recorded.

3. RESULTS

All the Ge(100) surfaces examined in this study exhibited a 1x2 or 2x1 reconstruction to some degree. Schematics of these two reconstructions are presented in Fig. 3. The arsenic-free Ge(100) and As:Ge(100) results are very similar to those found for UHV- or MBE-prepared surfaces. The Ge dimer bonds form a 2x1 array with the bond axis parallel to the [011] step edge. With the addition of As to this surface, the surface symmetry becomes 1x2, comprised of As dimers with bond axes perpendicular to the step edges. In the following, we will briefly show the results for the clean Ge(100) and As:Ge(100) phases, then compare and contrast with the results for samples annealed in AsH_3.

3.1 Clean Ge(100)

The two principal contaminants of most Ge surfaces are carbon and oxygen. Exposing the surface to H_2 at elevated temperatures readily removes oxygen. The free energy for the reaction

$$GeO_2 + 2H_2 \Leftrightarrow Ge + 2H_2O \qquad (2)$$

goes through zero at about 500 K [8]. Hence at typical growth temperatures, there is virtually no germanium oxide on the surface of the growing crystal and indeed none is found with AES after annealing in H_2.

Prolonged annealing times in H_2 at elevated temperatures are required to remove C; the mechanism by which this occurs is not known. However, C is easily removed by annealing the sample in a partial pressure of AsH_3 or PH_3. Presumably, the atomic hydrogen from the dissociation reaction of the hydride molecule quickly reacts with the C contaminants to produce the stable, volatile species CH_4.

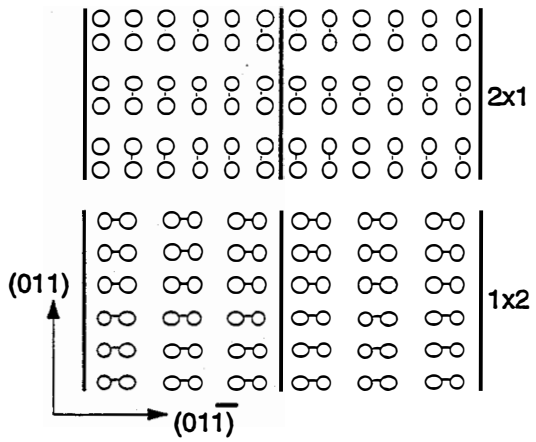

Figure 3. Summary of Ge(100) or As:Ge(100) surface phases. The Ge or As dimer bonds are represented by an array of dumbbells. For the 2x1 reconstruction, the dimer rows run perpendicular to the step edges (represented by thick vertical line segments). If the terrace reconstruction determines the GaAs sublattice orientation, then the 1x2 As:Ge(100) surface phase should produce GaAs with B-type (011) steps.

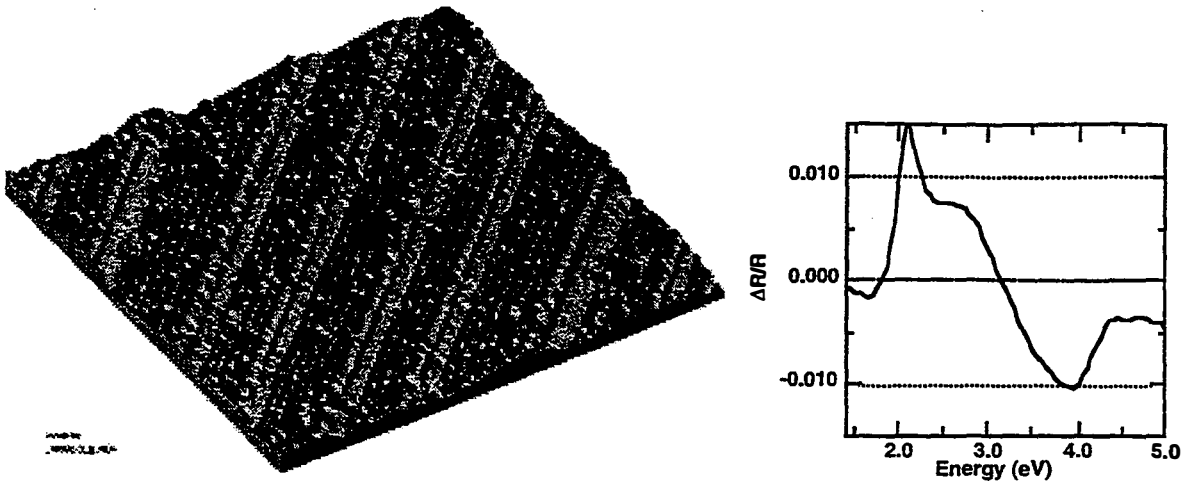

Figure 4. (a) STM image of As:Ge(100)6°(111). Dimer rows run parallel to step edges. (b) RD spectrum at room temperature for this surface.

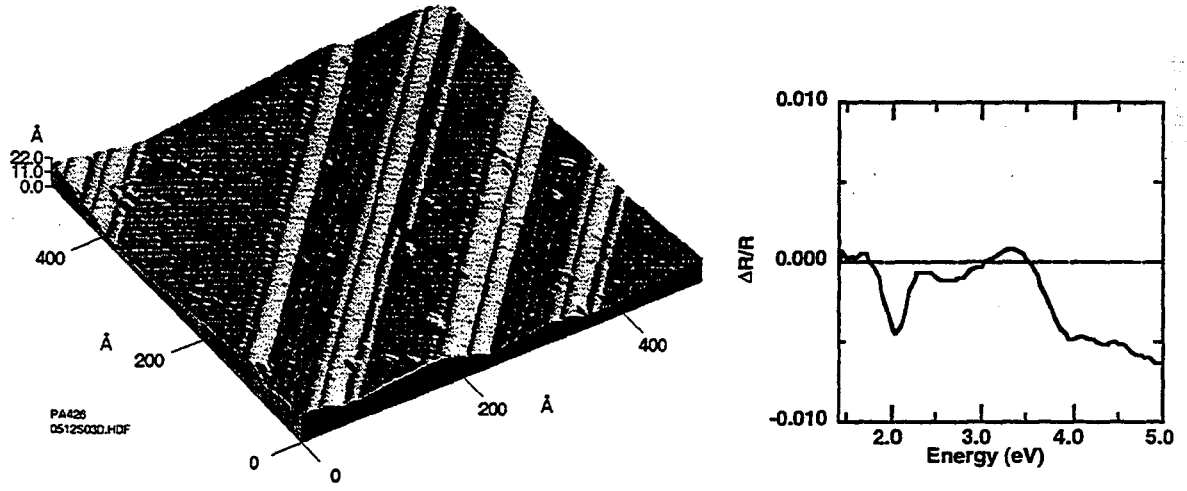

Figure 5. (a) STM image of a Ge(100)6°(111) surface annealed in AsH_3 at 640°C for 15 min. Surface is two-domain with dimer rows both parallel and perpendicular to the step edges. Steps are bunching to form facets. Step bunching process is facilitated by a slow AsH_3 etching of the Ge.

3.1.1. Low temperature Ge(100) phase

When clean, the surface of Ge(100) in UHV reconstructs, forming long rows of Ge-Ge dimers with a 2x1 surface reconstruction. Surfaces misoriented or tilted towards a [011] direction by a few degrees are composed of (100) terraces separated by steps that are $a_0/2$ high (where a_0=0.565 nm, the lattice constant of Ge) and the terrace width is $a_0/2/\tan\theta$ (where θ is the miscut angle from (100)). In a H_2 ambient, there is a tendency towards this state, but we find a higher surface concentration of the 1x2 surface reconstruction. This difference is probably not intrinsic to H_2, but is more likely due to the pinning of steps by impurities. We almost always see C on this surface with AES, and Gan et al. [9] have seen similar behavior.

The surface structure in real and reciprocal space was viewed with LEED and STM, respectively. The splitting of the [01] spots identifies the direction of the miscut and the average terrace width, and the half-order spots between the [11] and [01] normal spots indicate the direction of dimer-bond orientation.

The RD spectrum for this surface exhibits weak features around the critical points of bulk Ge, in particular, the critical point E_1 = 2.1 eV. This is indicative of a mixed 2x1/1x2 reconstructed surface and is consistent with the LEED and STM images.

3.1.2 High-temperature Ge(100) phase

At an annealing temperature greater than a critical temperature of about T_{cr} = 630°C, the RD spectrum is virtually featureless and samples quenched to room temperature exhibit a 1x1 LEED pattern with a high background. These results suggest that above 630°C, the Ge(100) surface becomes atomically rough.

3.2. As:Ge(100)

An STM image of the As:Ge(100) surface is shown in Fig. 4. Annealing the sample, in the absence of AsH_3, in an As-contaminated MOCVD reactor generates this surface. Arsenic, from warm reactor parts upstream of the substrate, reacts with the surface of Ge, breaking the Ge-Ge dimers and reforming an orthogonal array of As-As dimers. This STM image and a LEED pattern for this surface show a single domain, 1x2 reconstruction, and an ordered step array indicative of a step height of a_0. The RD spectrum for this surface (as shown in Fig. 4b) now exhibits a strong positive peak at or near E_1 and a negative peak around E_2.

At annealing temperatures less than T_{cr}, the intensity of the E_1 peak decreases with increasing temperature. Above T_{cr}, the RD spectrum is again featureless. However, in contrast to clean Ge(100), we were not able to quench this surface. As the temperature falls below T_{cr} during the quench, the 1x2 RD spectrum quickly re-emerges. The LEED for this sample is a poorly formed 1x2 pattern and AES shows the presence of As at the monolayer concentration.

3.3. AsH_3:Ge(100)

Arsine has a very unexpected effect on the surface of Ge. We first found that it slowly etches Ge. At an annealing temperature of 540°C and an AsH_3 partial pressure of 0.12 torr, the rate is ~0.5 ML/s. If Ge(100)6°(111) is annealed in AsH_3, the surface converts to a state characterized by the STM image shown in Fig. 5. This surface is two-domain with dimer rows running both parallel and perpendicular to the step edges. The terraces are wider and the steps higher than those in the STM micrograph of Fig. 4 for As:Ge(100), indicating the formation of step bunching and microfaceting. LEED images of the surface confirm the step bunching and show that the reconstruction is predominantly 2x1 with a minority 1x2 component.

The RD peak near E_1 has a flipped sign and is typically less intense than its As:Ge(100) counterpart. The rate of change of E_1 depends on AsH_3 partial pressure and temperature, as shown in Fig. 6. Note the long time constants associated with the AsH_3 annealing/etching. The steady state intensity of the E_1 peak decreases with increasing temperature, presumably because of changes in the relative populations of 2x1 and 1x2 domains on the surface. Also, in contrast to the clean Ge(100) and the As:Ge(100) phases, the RD spectrum is relatively stable above T_{cr}.

If the AsH_3 partial pressure in the reactor is reduced to zero, the surface converts reversibly to a state determined by the annealing temperature and the condition of the reactor and substrate holder. Above T_{cr}, the RD spectrum quickly approaches flat line. Below T_{cr}, with a GaAs-free substrate holder, the RD spectrum slowly evolves into the 1x2 spectrum; for a GaAs-coated substrate holder, the RD spectrum is close to flat line. This anomalous state is the focus of our current efforts.

We also examined a number of other (100) miscuts, and the results for the "verboten" miscut towards (110) is shown in Fig. 7. This surface is constructed of both 1x2 and 2x1 terraces with two orthogonal (11n)-like risers. The high quality image of Fig. 7 clearly portrays the complex step-riser reconstructions that can occur on miscut AsH_3:Ge(100) surfaces.

4. DISCUSSION

Ge(100) substrates annealed in AsH_3 exhibit surface phases that differ significantly from As:Ge(100) and clean Ge(100) annealed under UHV conditions. The main cause for this unexpected behavior is probably due to the fact that arsine etches Ge. At equilibrium, in the absence of growth or etching, it is expected that a single domain, 1x2 or 2x1 reconstruction, should prevail. This is driven mainly by the step-edge-terrace interaction energies. If a monolayer of Ge (or As) is added to or removed from this surface, the dimer orientation must rotate by 90°. If the AsH_3 etches the surface in monolayer increments, the local surface symmetry must alternately switch between 1x2 and 2x1 as etching proceeds. And if the surface is quenched at some instance, we would expect to see a mixed domain surface.

The development of microfacets is probably also the result of AsH_3 etching. In general, the fastest etching surfaces prevail (the opposite of growth). Step bunching can be caused by kinetic anisotropies associated with the etching process or can also be affected by step and terrace energies variations caused by reactions with other species such as AsH_3.

The net effect of etching is to yield a surface that is

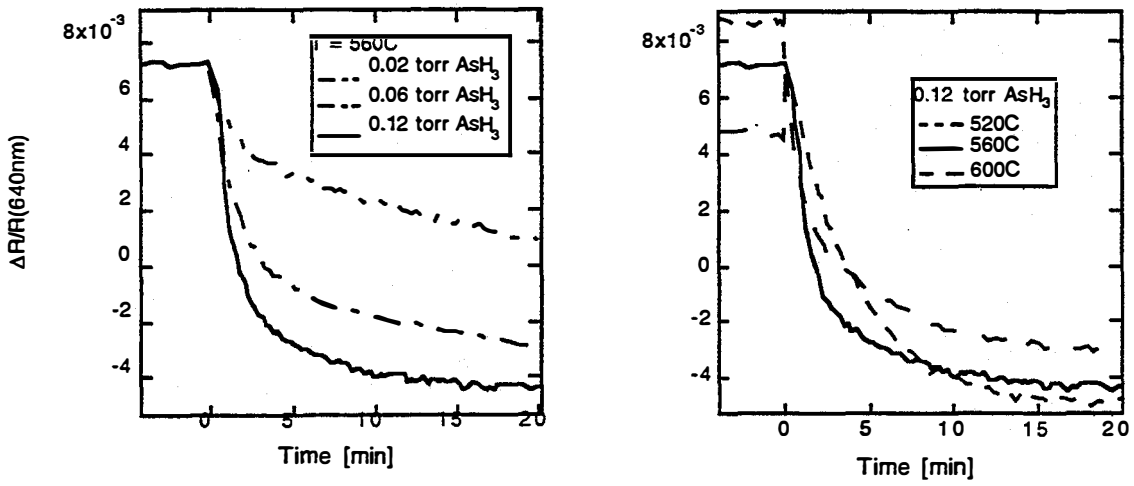

Figure 6. Transient RD signal at E_1 for a series of AsH_3 partial pressures and annealing temperature. The initial state is 1x2 As:Ge(100).

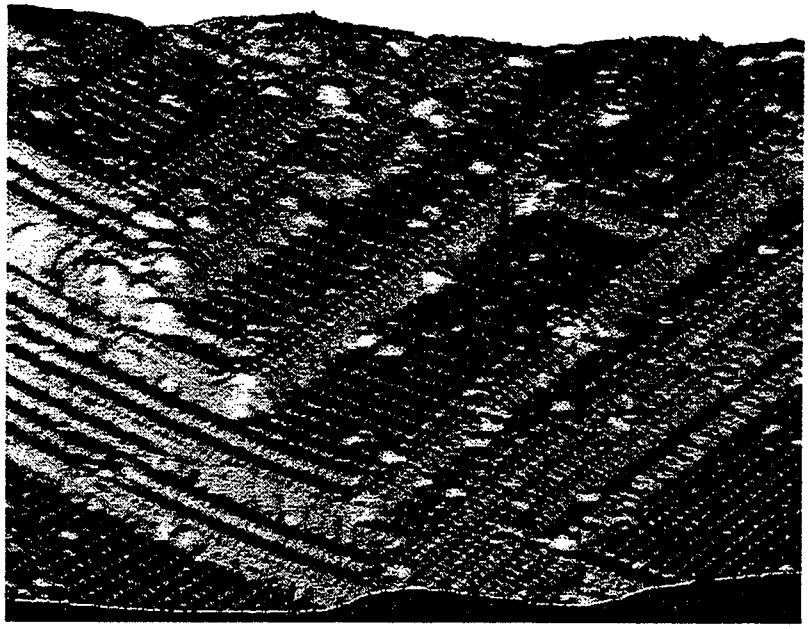

Figure 7. STM image of Ge(100)6°(110) annealed in AsH_3 at 640°C and an arsine partial pressure of 0.12 torr. Both 2x1 and 1x2 terraces are present. Individual terrace dimers and individual facet atoms are clearly visible. Microfacets show clear evidence of reconstruction.

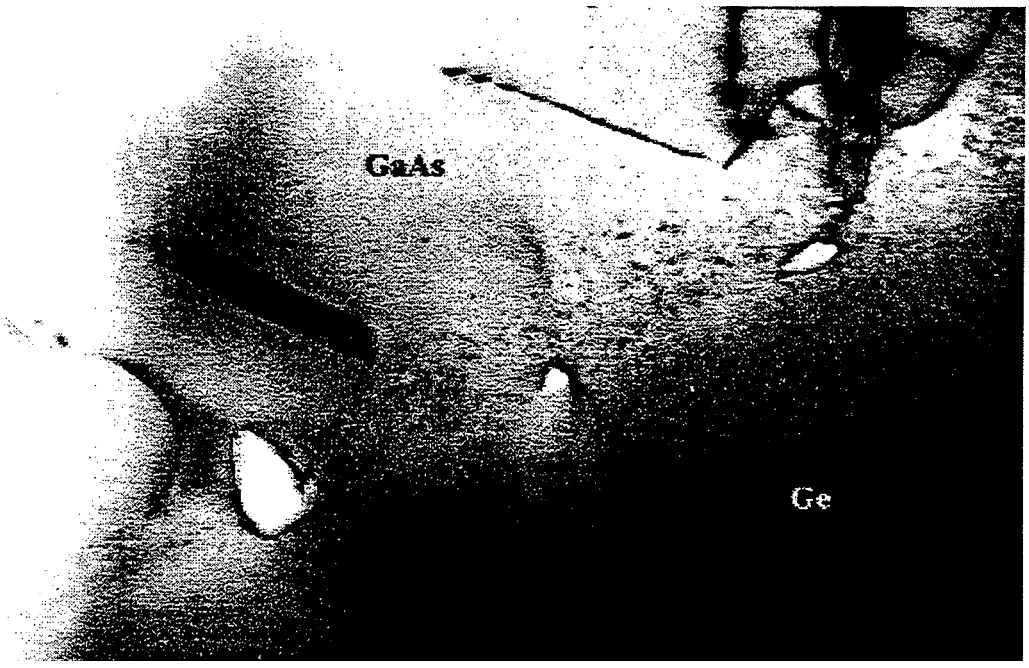

Figure 8. TEM micrograph showing antiphase domains (small truncated triangles) at the GaAs/Ge interface. The Ge(100)6°(111) substrate was annealed in AsH_3 under conditions similar to those use in Fig. 5.

probably less than ideal for the subsequent heteroepitaxy of GaAs. If the state of the surface just before growth is similar to Fig. 5, we might expect to see antiphase domains and a relatively rough interface. In Fig. 8, we show a transmission electron microscopy (TEM) micrograph of a GaAs layer grown on Ge(100)6°(111) similar to that in Fig. 5. It shows the presence of APDs as bright, rounded, or truncated triangular regions at the GaAs/Ge interface. These are eventually overgrown by the dominant domain. Although they do not extend far into the epilayer, they do appear to spawn other defects. A high-resolution TEM micrograph of the interface shows that the interface is indeed rough on an atomic level with a scale similar to that in Fig. 5.

These results also emphasize the importance of pregrowth conditions. It is quite clear that pregrowth parameters such as AsH_3 partial pressure, annealing

temperature and time, and reactor history and design may be more important than the particular reactor conditions during nucleation and growth. For example, it is customary to introduce arsine into the reactor at or near the beginning of a growth run. The time constant associated with the arsine/Ge etching reaction depends strongly on the arsine partial pressure. The prenucleation heatup and soak times relative to this etching time constant are now important parameters, because they probably determine the state of the surface immediately prior to nucleation.

5. SUMMARY AND CONCLUSIONS

Ge(100) substrates annealed in AsH_3 exhibit surface phases that differ significantly from As:Ge(100) and clean Ge(100) annealed under UHV conditions. We found that arsine etches Ge and precludes the development of a single-domain surface. It also causes step bunching and faceting.

Better devices and higher production yields may result from careful manipulation of the pregrowth conditions such as AsH_3 partial pressure, annealing temperature and time, and reactor history and design.

Contradictory results in the literature may be due to variations of the pregrowth conditions, which, in most cases, are not well documented.

ACKNOWLEDGMENTS

We wish to thank Sarah Kurtz, D.J. Friedman, and J. Geisz for useful discussions. We would also like to thank K. Jones and M.M. Al-Jassim for the TEM micrographs. The work was sponsored by the U. S. Department of Energy, Office of Energy Research, Basic Energy Sciences and by the U. S. Department of Energy under contract number DE-AC36-83CH10093.

REFERENCES

[1] C. Pelosi, G. Attolini, C. Bocchi, P. Franzosi, C. Frigeri, M. Berti, A. V. Drigo, and F. Romanato, "The role of the V/III ratio in the growth and structural properties of metalorganic vapor phase epitaxy GaAs/Ge heterostructures," *J Electron Mater*, **24**, 1723-1730 (1995).

[2] Y. Li, G. Salviati, M. M. G. Bongers, L. Lazzarini, L. Nasi, and L. J. Giling, "On the formation of antiphase domains in the system of GaAs on Ge," *J Cryst Growth*, **163**, 195-202 (1996).

[3] J. C. Chen, M. L. Ristow, J. I. Cubbage, and J. G. Werthen, "GaAs/Ge Heterojunction Grown by Metal-Organic Chemical Vapor Deposition and Its Application to High Efficiency Photovoltaic Devices," *J Electron Mater*, **21**, 347-353 (1992).

[4] T. Yasuda, L. Mantese, U. Rossow, and D. E. Aspnes, "Surface-induced optical anisotropies of single-domain (2 x 1) reconstructed (001) Si and Ge surfaces," *Phys Rev Lett*, **74**, 3431-3434 (1995).

[5] J. S. Luo, J. M. Olson, S. R. Kurtz, D. J. Arent, K. A. Bertness, M. E. Raikh, and E. V. Tsiper, "Optical anisotropy and spontaneous ordering in Ga0.5In0.5P: An investigation using reflectance-difference spectroscopy," *Phys Rev B-Condensed Matter*, **51**, 7603-7612 (1995).

[6] J. S. Luo, J. F. Geisz, J. M. Olson, and M. C. Wu, "Surface-related optical anisotropy of GaInP, InP, and GaP," *J Cryst Growth*, **174**, 558-563 (1997).

[7] E. A. Fitzgerald, J. M. Kuo, Y. H. Xie, and P. J. Silverman, "Necessity of Ga Prelayers in GaAs/Ge Growth Using Gas-Source Molecular Beam Epitaxy," *Appl Phys Lett*, **64**, 733-735 (1994).

[8] T. B. Reed, *Free Energy of Formation of Binary Compounds*. Cambridge: The MIT Press, 1971.

[9] S. Gan, L. Li, T. Nguyen, H. Qi, R. F. Hicks, and M. Yang, "Scanning tunneling microscopy of chemically cleaned germanium (100) surfaces," *Surface Sci*, **395**, 69-74 (1998).

III. Module and BOS Manufacturing

PROGRESS IN PHOTOVOLTAIC SYSTEM AND COMPONENT IMPROVEMENTS

Holly P. Thomas, Benjamin Kroposki, Peter McNutt, C. Edwin Witt
National Renewable Energy Laboratory
1617 Cole Boulevard
Golden, CO USA 80401

Ward Bower, Russell Bonn, Thomas D. Hund
Sandia National Laboratories
Albuquerque, NM USA 87185-0753

ABSTRACT: The Photovoltaic Manufacturing Technology (PVMaT) project is a partnership between the U.S. government (through the U.S. Department of Energy [DOE]) and the PV industry. Part of its purpose is to conduct manufacturing technology research and development to address the issues and opportunities identified by industry to advance photovoltaic (PV) systems and components. The project was initiated in 1990 and has been conducted in several phases to support the evolution of PV industrial manufacturing technology. Early phases of the project stressed PV module manufacturing. Starting with Phase 4A and continuing in Phase 5A, the goals were broadened to include improvement of component efficiency, energy storage and manufacturing and system or component integration to bring together all elements for a PV product. This paper summarizes PV manufacturers' accomplishments in components, system integration, and alternative manufacturing methods. Their approaches have resulted in improved hardware and PV system performance, better system compatibility, and new system capabilities. Results include new products such as Underwriters Laboratories (UL)-listed AC PV modules, modular inverters, and advanced inverter designs that use readily available and standard components. Work planned in Phase 5A1 includes integrated residential and commercial roof-top systems, PV systems with energy storage, and 300-Wac to 4-kWac inverters.
Keywords: Inverter- 1: Balance of Systems- 2: Components-3

1. INTRODUCTION

The DOE initiated the PVMaT project in 1990 to assist the U.S. PV industry to extend its world leadership role in PV manufacturing and the commercial development of PV modules and systems. The PVMaT project is a government/industry R&D partnership between the U.S. federal government (through the DOE) and members of the U.S. PV industry. PVMaT is designed to assist industry to improve manufacturing processes, accelerate manufacturing cost reductions for PV modules, improve commercial product performance, and lay the groundwork for a substantial scale-up in the capacity of U.S.-based PV manufacturing plants.

The PVMaT project is being conducted in Phases 1, 2, 3A, 4A, and 5A, designed to address selected R&D topics. A description of the focus and accomplishments for Phases 1-3A and an introduction to 4A have been detailed in previous papers [1-4]. Phase 4A, Product-Driven Manufacturing, is divided into two parts: 4A1 - Product-Driven System and Component Technology and 4A2 - Product Driven PV Module Manufacturing Technology. Phase 5A is also divided into two parts: 5A1- PV System and Component Technology and 5A2 - PV Module Manufacturing Technology. Phases 4A and 5A objectives include stimulating a broader interest in the production of PV products. In addition, these two phases are intended to encourage system and product integration, increase module production capacity, and reduce PV module production costs. Finally, Phases 4A and 5A are expected to stimulate advances in PV systems and components, and developments in design leading to overall reduced system life-cycle costs of the PV end-product. Manufacturing flexibility with the associated cost reduction, improved efficiency, and broader market applications for PV systems as a whole are also emphasized. All work in the PVMaT project is managed by a Technical Monitoring Team consisting of engineers and scientists from the National Renewable Energy Laboratory (NREL) and Sandia National Laboratories (SNL).

Progress in Phases 4A1 and 5A1 is summarized below. Progress in Phases 4A2 and 5A2 is reported at this conference in a paper by C. Edwin Witt et al.

2. PHASE 4A1 PRODUCT AND MANUFACTURING ADVANCEMENTS

Of the thirteen subcontracts awarded in Phase 4A, eight are in Phase 4A1. These eight are now completing their work, which deals with manufacturing generally related to PV system components, such as inverters, and system integration efficiency and design improvements. The companies and their related research and development topics are listed in Table I.

2.1 Phase 4A1 Developments in PV Systems and System Integration

Work completed by five of the Phase 4A1 companies can be grouped in the general category of manufacturing improvements for PV system integration. Descriptions of their progress follows, presented in alphabetical order.

Ascension Technology, Inc. (ATI) completed product enhancements and established the manufacturing capability for the fully integrated "SunSine™300 AC Module." This product, rated at 250 Wac at Standard Test Conditions (STC), consists of the SunSine™300 AC inverter attached to the back of the ASE Americas, Inc., large-area PV

laminate (260 to 300 Wdc) (Fig. 1). The AC Module can be configured for output into a 120/240 Vac split-phase or 120/208 Vac three-phase connection. The integrated unit is UL-listed, National Electrical Code (NEC) compliant and meets Federal Communications Commission (FCC) standards for electromagnetic interference. It is sold as a complete power unit, ready for utility interconnection, and is compatible with the Ascension RoofJack™ mounting system for rapid, low-cost installation. Features of the SunSine™300 inverter include a plug-in connector for rapid "AC Module" assembly and quick-connectors for rapid installation with no DC field-wiring needed [5]. The SunSine™300 AC inverter features include passive and active anti-islanding protection and maximum power-point tracking. ATI recently completed a pilot production run, to ISO 9001 standards, of 109 SunSine™300 AC Modules with 100% successful operation at start-up. Over 100 units have been installed and a production run of 200 AC Modules is now in progress.

Table 1: Subcontractors now completing work in PVMaT Phase 4A1 and topics of their work.

Company	Title
Ascension Technology, Inc.	Manufacture of an AC Photovoltaic Module
Advanced Energy Systems, Inc.	Next-Generation Three Phase Inverter
Evergreen Solar, Inc.	Advanced Polymer PV System
Omnion Power System Engineering Corp.	Three-Phase Power Conversion for Utility-Interconnected PV Applications
Solar Design Associates, Inc.	The Development of Standardized, Low-Cost AC PV Systems
Solar Electric Specialties	Design, Fabrication, and Certification of Advanced Modular PV Power Systems
Trace Engineering	Modular Bi-Directional DC- to AC- Power Inverter Module for PV Applications
Utility Power Group, Inc.	Development of a Low-Cost Integrated 20-kW AC Solar-Tracking Sub-Array for Grid-Connected PV Power System Applications

Evergreen Solar, Inc. combined several developments in module-related advancements. Based on their knowledge about the variety of polymeric materials on the market, Evergreen evaluated alternative materials to improve PV-panel manufacturing and PV-system installation.After testing and evaluation, the company identified two materials. The first is a transparent encapsulant laminated in air. This material permitted Evergreen to develop a continuous, non-vacuum

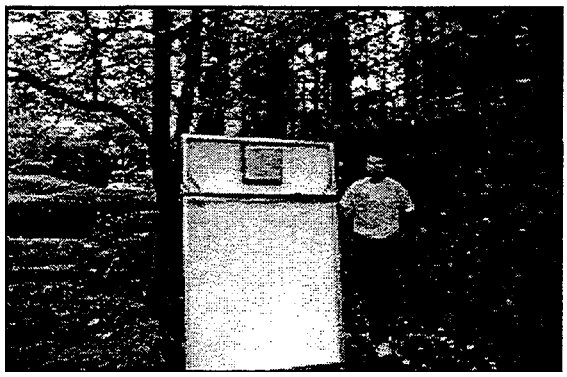

Figure 1: Back of Ascension Technology's "SunSune300™ AC Module " illustrating the AC inverter.

lamination process for PV panels using a heated-roll method. The encapsulant has reported material costs lower than EVA-based materials currently in use [12]. Evergreen also identified a PV-laminate backskin material. This material, used to replace Tedlar™, can also be applied as an edge sealant. This backskin material eliminates the need for a frame, as it is strong enough to protect the edges of the glass superstrate. The backskin is also highly puncture resistant, with low vapor permeability and high adhesion characteristics. The company capitalized on these multiple qualities to develop their Innovative Mounting System, where a mounting rail adheres to the back of the module for rapid, easy, panel installation in the field. Both these advancements are discussed in depth in papers by J. I. Hanoka at this conference.

Solar Design Associates, Inc. teamed with Solarex and Advanced Energy Systems, Inc. (AESI) to improve reliability and safety and to reduce costs through pre-engineered components for standardized, low-cost PV systems [6]. AESI completed product enhancements for their MI-250 MicroInverter, including software controls and power-line carrier monitoring. This AC inverter is UL-listed, FCC-compliant, and can be ordered in export voltage ranges. Solarex developed a low-cost, pre-engineered assembly for mounting a PV array. The standardized system combines framing and mounting the PV array and incorporates electrical interconnection, array wiring, grounding, and lightning protection into the frame. With features such as quick-connect wiring and approved, simplified grounding, PV systems can be rapidly installed at minimal cost. For example, a recent 1-kW Solarex system demonstration using thin-film modules was completely installed and operational, including the utility interconnection, in less than 4 hours.

Solar Electric Specialties (SES) completed manufacturing improvements as part of their effort to increase standardization and modularity in integrated, factory-packaged PV systems. The benefits to this approach are shorter lead times with lower materials costs, higher overall quality and system reliability, decreased management and engineering time, and lower installation labor. In addition, SES made a concerted effort to achieve safety and performance listings for two product lines, discussed below, including UL-listing and Factory Mutual (FM) approval. Their approach for standardized product lines simplifies the process for customers to specify

systems for particular needs. An important corollary to SES' standardized products and the products' compliance to standard safety measures is these factors give lending institutions greater confidence in the product, resulting in easier customer financing.

SES used two products, a 200 Wdc Modular Autonomous PV Power Supply (MAPPS) and a mobile 1-kW Photogenset, to establish this approach. The MAPPS product line is a stand-alone PV power system consisting of PV modules, solid-state power control systems, sealed batteries, and enclosures for the batteries and power control system. UL-listed and FM-approved products are available with outputs ranging from 12 - 24 Vdc[7]. The Photogenset product line combines a propane-powered generator (with an automatic oil-changer) integrated with a PV array and battery storage to provide off-grid AC power (Fig. 2). The 1-kW mobile system used to establish the processes for this SES product line includes a fully enclosed trailer containing a 4-kW inverter, a micro-processor-based power controller with full remote communications capabilities, a 2-channel PV combiner box, and wiring protection (disconnects and over-current protection) designed to meet UL safety standards. Although the system design and component selection were based on code requirements, this product is not UL-listed, as the company was unable to obtain a UL-listed generator.

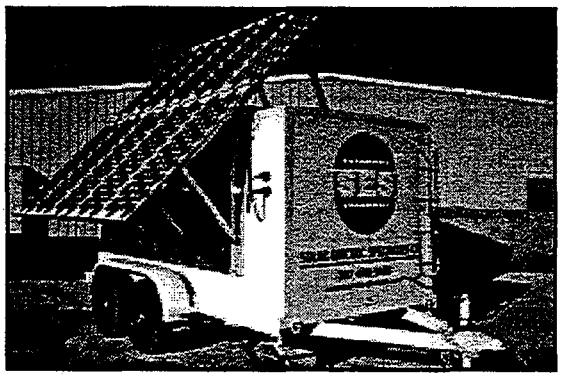

Figure 2: Solar Electric Specialties 1 kW Photogenset, shown in the trailer-mounted configuration.

Utility Power Group, Inc. (UPGI) completed manufacturing modifications and power processing improvements for larger utility interactive (U-I) systems. Based upon their utility-scale PV demonstration installations, UPGI determined that the most important factor to reduce costs and improve reliability was to bring as much of the field installation work as possible onto the factory floor, where labor is more efficient and assembly more consistent. UPGI's approach was to address the PV modules and power conversion and control separately, and to develop factory assembly methods for each. For PV modules, UPGI established a manufacturing process for integrating PV laminates into pre-assembled, field-deployable modular panels which can be assembled into 7- to 15- kW sub-arrays. UPGI assembles laminates into Modular Panels (MPs) consisting of several Siemens frameless laminates, either Model M-55 or SP7 (depending upon the size of the system that is ordered), adhesively attached to 'C'-shaped steel mounting rails. Laminate interconnection is also accomplished on the factory floor. The pre-assembled MPs are then mounted into recyclable shipping fixtures and delivered to the field ready for placement on the ground support structures [8].

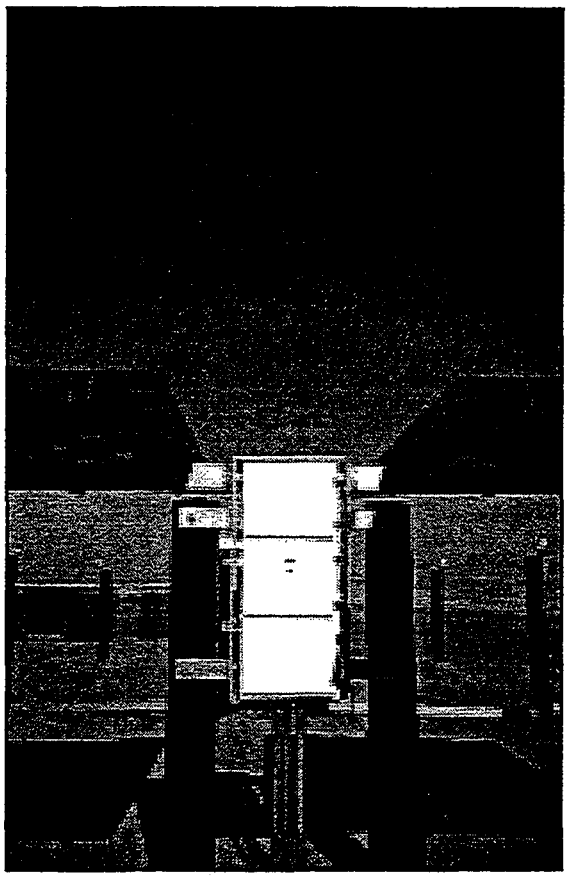

Figure 3: Photo by Utility Power Group, Inc. illustrating the Integrated Power Processing Unit and factory-assembled Modular Panels.

For their power conversion, UPGI streamlined assembly by integrating power conversion/control electronics, array-tracking control electronics, source-circuit protection hardware, and DC and AC switchgear into a single, pre-assembled unit termed an Integrated Power Processing Unit (IPPU) (Fig. 3). UPGI attaches the tracking mechanism for each sub-array to the back of the IPPU's enclosure prior to shipment to the site, so the unit arrives ready for connection at the center of each sub-array. The IPPU's 3-phase inverter is 96% efficient with less than 3% total harmonic distortion (THD) over a 25% to 100% output range. UPGI also refined the field installation methods for these systems. The company accomplished their objectives, achieving a 40% reduction in area-related balance-of-system costs and reducing net total costs of their single-axis-tracking PV systems by 23%. At the time of writing this paper, UPGI has deployed or contracted to place 10 systems totalling 2.5 MW.

2.2 Phase 4Al Inverters

Three Phase 4Al subcontractors are completing manufacturing and product improvements related to PV inverters, described below in alphabetical order.

Advanced Energy Systems, Inc. (AESI) improved product reliability and instituted design modifications to simplify manufacturing and maintenance, and consolidated subcomponents into compact, readily serviceable units [9]. For example, the digital inverter control and all inverter controllers (3-phase) are incorporated into a single printed circuit board. AESI also integrated power functions into a modular "PowerBlock," combining the Insulated Gate Bipolar Transistor (IGBT) power-switching subassembly, heat sink, fans, and capacitors. Another significant step was to incorporate communication, data-logging, and remote trouble-shooting capabilities into the product. AESI is demonstrating their results with a hybrid and a utility-interactive 60-kW inverter designed for fully automatic, unattended operation. The performance characteristics of the PV-wind hybrid unit include input voltages of 189 - 324 Vdc, output voltages of 3-phase 480 Vac, 60 Hz. Performance characteristics of the Utility-Interactive (U-I) unit include 95% peak efficiency, less than 5% THD, and internal circuit protection in the case of excess DC input voltages.

Omnion Power Engineering Corp. is developing a 100-kW U-I power-conversion system using a highly integrated power-switching assembly with the IGBTs laminated directly to the heat sink. The laminated power-switching assembly results in lower losses, smaller heat sinks, and reduced factory labor and assembly time. The unit's design was influenced by round-table discussions with system users, integrators, and utilities to define the most useful parameters for this product. Performance characteristics include a 93% peak inverter efficiency, a 300 - 600 Vdc input voltage window, with an operating voltage range of 252 - 308 Vac at 59-61 Hz [10]. Omnion has emphasized reliability in this product line and will use ISO9001 qualification procedures in their design process and in manufacturing. The unit is designed for a calculated mean-time-before-failure design goal of 40,000 hours. The product can be upgraded with optional features such as enhanced data acquisition suggested by the round-table advisors. The unit is designed to comply with applicable UL, IEEE, NEC, and FCC guidelines.

Trace Engineering streamlined their product manufacturing and improved reliability through a modular, versatile building-block inverter design for stand-alone, hybrid, or U-I applications [11]. The building block can operate in parallel or in series for single, split- and 3-phase applications. This universal "building block" design is intended to reduce Trace Engineering's manufacturing costs while maintaining sufficient versatility and compatibility with current inverter models. Trace Engineering used a 2.5-kW unit to demonstrate their approach, and elements of this design have already been incorporated into current Trace Engineering products. In addition, Trace developed a modular, UL-listed inverter and BOS packaging system, readily expandable for a variety of applications.

3. PHASE 5A1 PRODUCT AND MANUFACTURING ADVANCEMENTS

Four subcontracts are being negotiated under Phase 5A1. These address system integration or manufacturing enhancements generally related to PV system components and aspects other than modules, e.g., batteries, inverters, and/or system-integration efficiency and/or design improvements, and emphasize residential applications. The companies and their planned work are summarized in Table 2 and described below.

Table 2: Planned subcontractors and their research and development topics for Phase 5A1.

Company	Title
Ascension Technology, Inc.	Cost Reduction and Manufacture of the SunSine™325 AC Module
Omnion Power Engineering Corp.	Manufacturing and System Integration Improvements for One- and Two-Kilowatt Residential PV Inverters
PowerLight Corp.	PowerGuard® Advanced Manufacturing
Utility Power Group, Inc.	Development of a Fully-Integrated PV System for Residential Applications

ATI is refining the SunSine™300 inverter for improved manufacturabilty, lower cost, and enhanced performance. Their goals are to achieve a 40-50% cost reduction in the inverter, reduce the overall footprint of the unit, increase peak efficiency, achieve a minimum 270 Wac (STC) rating and establish a production capability of 5,000 units per year, with less than 0.1% failure at start-up. ATI plans to achieve improvements in the AC inverter performance and manufacturability by incorporating a soft-switching topology. With this modification, the inverter is expected to achieve higher efficiency through reduced switching losses when compared to the hard-switched approach in the current design. The enhanced product will be called the "SunSine™325 AC Module," and ATI plans to obtain UL-listing, FCC Class B verification, and other markings as needed for export products. Manufacture of the SunSine™325 AC Module will apply ISO9001 quality assurance procedures, and the new inverter design will undergo highly accelerated life tests (HALT) procedures to ensure long-term reliability.

The work with *Omnion* is now under negotiation. The company plans to complete design enhancements to produce Series 2500 1- and 2-kW inverters that are easily manufactured and suitable for use in residential applications. These inverters will be for U-I applications and meet design requirements for high-volume production (5,000 units/year). This product will use the transformerless, phase-leg topology of the Omnion Series 2200, but with enhancements for a larger input voltage range of 180 to 500 Vdc, making it easier to design systems using the broader array voltage windows presented by some thin-film PV arrays. Omnion expects this approach to result in lighter, more-efficient, lower-cost 1- and 2-kW inverters. This product line will also use the ISO9001 quality assurance during manufacture and the new design will undergo HALT procedures to ensure long-term reliability.

A third company in this group, *PowerLight Corporation*, plans a 3-year program to accomplish enhancements to their PowerGuard[R] product, a light weight, electrically active roof tile that can be mounted without roof penetrations in most applications. PowerLight plans advances in manufacturing to reduce cost, increase capabilities, and provide PV systems incorporating financing options. PowerLight expects to demonstrate system costs of $3.05/W and to complete improvements in PowerGuard[R] tile fabrication manufacturing to achieve a production capacity of 16 MW/yr. The products will be produced to meet UL and international requirements, and integrated warranties will be developed. Commercial demonstrations of the modified PowerGuard[R] systems will be evaluated each year. In addition, PowerLight is working with Trace Technologies (a sister company to Trace Engineering) to upgrade the control board for their grid-tied inverter. Advancements include redesigning the controller for PV-specific applications, adding an integrated data-acquisition system, and establishing communications for audit-worthy verification of PV system performance. The improvements will apply to a complete line of Trace Technologies' advanced inverter products from 25 to 300 kW.

UPGI plans to reduce the total installed cost and increase the reliability of residential roof-top-mounted PV systems and meet market requirements for a U-I PV system with storage. Through a range of integrating steps, UPGI plans to achieve a 30% reduction in total non-module-related system costs. The fully integrated system will incorporate roof-top PV modules, a 4- to 6-kW power unit and an optional battery storage unit. Power-conditioning components will be designed to support a variety of laminates, including the Siemens and Evergreen crystalline silicon, and Solarex amorphous-silicon products. The system will conform to applicable standards, building and seismic codes, and be adaptable to a wide range of roof materials for both new and retrofit applications. The results will be demonstrated through a pilot production run and beta-testing at a variety of locations.

4. SUMMARY

The system and component manufacturing advancements accomplished to date have resulted in improved reliability and greater variety of integrated U.S. PV products. Manufacturers report they are now producing more versatile products that are easier and less expensive to build, with demonstrated reliability, simplified commissioning and ready serviceability. Advanced systems range in size from 260 Wac to 15 kWac, and advanced inverter products range from 250 Wac to 100 kWac. Products and systems resulting from this project are now in use.

5. ACKNOWLEDGMENTS

This work is supported under DOE Contract Number AC36-83CH10093 with NREL, a national laboratory managed by Midwest Research Institute and Contract DE-AC04-94AL8500 with SNL, managed by Lockheed Martin Company. The authors wish to thank Paul Schissel for serving on the contract monitoring team for the Evergreen subcontract. Many people have contributed to developing and implementing the Photovoltaic Manufacturing Technology project and to the R&D efforts carried out in this program. The authors acknowledge that this paper represents their work.

REFERENCES

[1] C.E. Witt, L.O. Herwig, R. Mitchell, and G.D. Mooney, "Status of the Photovoltaic Manufacturing Technology (PVMaT) Project," Proceedings of the 22nd IEEE Photovoltaics Specialists Conference, Las Vegas, Nevada, October, 1991.

[2] C.E. Witt, L.O. Herwig, R.L. Mitchell, H.P. Thomas, R. Sellers, and D.S. Ruby, "Recent Progress in the Photovoltaic Manufacturing Technology Project (PVMaT)," Proceedings of the 1st World Conference on Photovoltaics, Waikoloa, Hawaii, December, 1994.

[3] R.L. Mitchell, C.E. Witt, H.P. Thomas, D.S. Ruby, R. King, and C.C. Aldrich, "Progress Update on the U.S. Photovoltaic Manufacturing Technology Project," Proceedings of the 26th IEEE Photovoltaics Specialists Conference, Anaheim, CA, September, 1997.

[4] W. I. Bower, H. P. Thomas, B. Kroposki, R. Bonn, and T. Hund, "Balance-of-System Improvements for Photovoltaic Applications Resulting from the PVMaT Phase 4A1 Program," Proceedings of the 26th IEEE Photovoltaics Specialists Conference, Anaheim, CA, September, 1997.

[5] M. Russell, C. Handleman, and G. Kern, "Manufacture of an AC Photovoltaic Module, PVMaT Annual Technical Report, August, 1995 - August 1996," NREL, Golden, CO, NREL/SR-520-23002, August, 1997.*

[6] S. Strong, J. Wohlgemuth, and M. Kaelin, "Development of Standardized, Low-Cost AC PV Systems, PVMaT Annual Report, September 1995-November 1996," NREL, Golden, CO, NREL/SR-520-23432, June, 1997.*

[7] T. Lambarski and G. Minyard, "Design, Fabrication, and Certification of Advanced Modular PV Power Systems, Final Report," NREL, Golden, CO, NREL/SR-520-24921, June, 1998.*

[8] M. Stern, R. West, G. Fourer, W. Whalen, M. Loo, and G. Duran, "Development of a Low Cost Integrated 20 kW AC Solar Tracking Sub-Array for Grid-Connected PV Power System Applications, PVMaT Final Report," NREL, Golden, CO, NREL/SR-520-24759, June 1998.*

[9] A. Wesley, and R. Wills, "Next-Generation Three-Phase Inverters, PVMaT Phase I Annual Report," NREL, Golden, CO, NREL/SR-520-23330, July 1997.*

[10] D. Porter, H. Meyer, and W. Leang, "Three-Phase Power Conversion for Utility Interconnected PV Applications, PVMaT Annual Technical Report, October 1995 - April 1997," NREL, Golden, CO, NREL/SR-520-24095, February 1998.*

[11] C. Freitas,"Development of a Modular, Bi-Directional Power Inverter for Photovoltaic Applications, PVMaT Annual Technical Report, August 1995-August 1996," NREL, Golden, CO, NREL/SR-520-23401, August 1997.*

[12] J. Hanoka, R. Chleboski, M. Farber, J. Fava, P. Kane, and J. Martz, "Advanced Polymer PV System, Final Report," NREL, Golden, CO, NREL/SR-520-24911, July, 1998.*

* Available from: National Technical Information Service, U.S. Department of Commerce, 5285 Port Royal Road, Springfield VA 22161 USA. Telephone: (703)487-4650.

MANUFACTURING IMPROVEMENTS IN THE PHOTOVOLTAIC MANUFACTURING TECHNOLOGY (PVMAT) PROJECT

C. Edwin Witt, Richard L. Mitchell, Holly P. Thomas, Martha I. Symko
National Renewable Energy Laboratory
MS-3221, 1617 Cole Blvd., Golden, CO, 80401, USA
Telephone: 303/384-6402; Fax: 303/384-6481

Richard King, U.S. Department of Energy, EE-131
1000 Independence Avenue SW, Washington DC, 20585, USA

Douglas S. Ruby, Sandia National Laboratories
Albuquerque, New Mexico, 87185-0752, USA

ABSTRACT: The Photovoltaic Manufacturing Technology Project (PVMaT) is a government/industry research and development (R&D) partnership between the U.S. federal government (through the U.S. Department of Energy [DOE]) and members of the U.S. PV industry. The goals of PVMaT are to help the U.S. PV industry improve module manufacturing processes and equipment; accelerate manufacturing cost reductions for PV modules, balance-of-systems components, and integrated systems; increase commercial product performance and reliability; and enhance the investment opportunities for substantial scale-ups of U.S.-based PV manufacturing plant capacities. The approach for PVMaT has been to cost-share risk taking by industry as it explores new manufacturing options and ideas for improved PV modules and other components, advances system and product integration, and develops new system designs, all of which will lead to overall reduced system life-cycle costs for reliable PV end products.
The PVMaT Phase 4A module manufacturing R&D projects are just being completed, and initial results for the work directed primarily to module manufacture are reported in this paper. Fourteen new Phase 5A subcontracts have also just been awarded, and planned R&D areas for the ten focussed on module manufacture are described. Finally, government funding, subcontractor cost-sharing, and a comparison of the relative efforts by PV technology throughout the PVMaT project are presented.
Keywords: Manufacturing and Processing - 1: Module Manufacturing - 2: PV Module -3

1. INTRODUCTION

The Photovoltaic Manufacturing Technology Project (PVMaT) is a government/industry research and development (R&D) partnership between the U.S. federal government (through the U.S. Department of Energy [DOE]) and members of the U.S. PV industry. Its goals are to help the U.S. PV industry improve module manufacturing processes and equipment; accelerate manufacturing cost reductions for PV modules, balance-of-systems components, and integrated systems; increase commercial product performance and reliability; and enhance the investment opportunities for substantial scale-ups of U.S.-based PV manufacturing plant capacities.

PVMaT was initiated in 1990. Its concept, general management, and procurement approaches were developed by a team consisting of representatives from industry, government, and national laboratories. Multi-year projects are being carried out through cost-shared awards resulting from competitive solicitations. Each proposal is evaluated by a panel of experts selected from technology, manufacturing, business planning, and applications (including utility) areas. To date, there have been five phases: Phase 1, identifying the industry's problems on a company-by-company basis; Phase 2 (in two parts, A and B), supporting research and development (R&D) to resolve module manufacturing problems and reduce manufacturing costs; Phase 3, supporting R&D to resolve generic issues in module manufacturing; Phase 4A, supporting R&D to facilitate product-driven manufacturing advances involving balance-of-systems components as well as modules; and Phase 5A, continuing efforts similar to those addressed Phase 4.

This paper describes activities primarily related to module manufacture and includes Phase 4A2 R&D results and newly awarded Phase 5A subcontract plans. Phase 4A1 and 5A1 subcontracts, addressing systems and system components other than modules, are described in a separate paper in these proceedings. The paper is by H. P. Thomas et al., from the National Renewable Energy Laboratory. Phases 1, 2, and 3 of PVMaT have been described in detail in earlier papers [1-3]. Finally, in this paper, we present some summary information on government funding, subcontractor cost-sharing, and a comparison of the relative efforts by PV technology throughout the PVMaT project.

2. PHASE 4A2

R&D results from the five PVMaT 4A2 projects are presented below.

ASE Americas, Inc. is advancing its technology through manufacturing line improvements that consist of (1) a further decrease in the edge-defined film-fed growth (EFG) wafer thickness to 250 micrometers in mass production and

an increase in the number of wafers produced from one crucible, (2) an increase in the electronic quality of as-grown EFG material to meet the demands for higher-efficiency solar cells, (3) an improved solar-cell fabrication technology, (4) developing a diffusion glass removal process that is environmentally safe and reduced in cost, and (5) developing an integrated interconnect, lamination, and fabrication method. Recent accomplishments include construction and demonstration of prototype equipment for removing phosphorous glass from diffused wafers that can reduce acid consumption and fluoride emissions by 95%, implementation of the first phase of a Statistical Process Control program and the development of a new module diode housing.

AstroPower, Inc. has completed its 4A subcontract that addressed the development of a low-cost manufacturing capability for Silicon-Film™ solar cells and panels by using the continuous-processing capability of the Silicon-Film™ technology. Their efforts have been to (1) eliminate wafer-sawing steps, (2) develop a high-yield, continuous manufacturing technology, and (3) increase solar-cell size. The AP225 Silicon-Film™ cell is in production, and efficiencies exceeding 12% have been measured on this 240-cm^2 cell. Small-scale devices have demonstrated efficiencies of 16.6%. Processing advances include the development of a continuous diffusion process and a continuous antireflection-coating process.

Iowa Thin Film Technologies Inc. is increasing the throughput of their metallization, a-Si deposition, laser-scribing, and welding processes, with the goal of reducing the overall module manufacturing costs on the ITF production line by 68%. They have improved laser registration and substrate throughput by 30% through the development of a new position detector and alignment system and the installation of a new laser scriber, increased throughput in the printer by 70% with an active screen alignment that allows a 10-micron reproducibility, identified a water-based ink that withstands the subsequent processing temperatures, and improved the throughput of the ZnO deposition process step by 50%.

Photovoltaics International, LLC is establishing a low-cost manufacturing capability for linear concentrator modules by using their continuous-processing capability. Under this manufacturing effort, they will take advantage of the continuous-processing capability of their lens and side-panel extrusion technology. They have completed the tooling and testing of the new 20-inch lens extrusion process equipment, completed the design and initial fabrication of the receiver assembly station, completed design and prototyping of the roll-formed frame process, and completed development of the self-jigging, low V_{oc} linear concentrator module.

Siemens Solar Industries is addressing improvements in their Czochralski (Cz) silicon module manufacturing technology to reduce module cost per watt by 18%. These goals are being addressed by identifying alternative Cz module designs, material sources, and processes that lower module component costs, and by improving manufacturing process yields, reducing labor costs in Cz module manufacturing, and increasing productivity. They have implemented production of the 150-mm cell and module product line, which leverages the use of silicon by over 30% in the production of Cz solar cells; continued to improve manufacturing productivity and yield by over 10%; implemented Statistical Process Control in their diffusion and cell printing lines to improve capability and electrical yields; and implemented polysilicon preparation techniques to mitigate silicon supply variation on yields.

3. PHASE 5A

Eleven subcontracts have been awarded in the PVMaT 5A competition and three more are in the final stages of negotiations. The 14 subcontracts are expected to total about $60 million over a 3-year period with a 48% subcontractor cost-sharing. (Thirty-one offerors responded to the PVMaT 5A Request for Proposals. They proposed activities totaling more than $97 million. Of that amount, about 49% was offered as subcontractors' cost-share.)

Table 1 presents the 5A winners and their respective areas of manufacturing R&D. Subcontractors addressing primarily their own process-specific module manufacturing problems are designated 5A2. Subcontractors addressing primarily generic R&D of interest to broad portions of the industry or system and other non-module component manufacturing problems are designated 5A1.

TABLE 1. PVMaT PHASE 5A MANUFACTURING AREAS

Type	Company	Manufacturing R&D Area
5A1	Ascension Technology, Inc.	Manufacture of the Advanced SunSine™ 325 AC Module
5A2	ASE Americas Inc.	The EFG High Volume PV Manufacturing Line
5A2	AstroPower	Silicon-Film™ Solar Cells by a Flexible Manufacturing System
5A1	Crystal Systems, Inc.	Production of Solar Grade Silicon by Refining of Liquid Metallurgical Grade Silicon
5A2	Energy Conversion Devices, Inc.	Efficiency and Throughput Advances in Continuous Roll-to-Roll a-Si Alloy PV Manufacturing Technology
5A2	Evergreen Solar, Inc.	Continuous, Automated Manufacturing of String Ribbon Si PV Modules
5A2	Global Solar Energy, L.L.C.	Throughput Improvements for Thin-Film Based CIGS Modules
5A1	Omnion Power Engineering Corporation	Manufacturing and System Improvements for One and Two kW Inverters

5A1	PowerLight Corporation	Advanced Powerguard® Manufacturing
5A2	Siemens Solar, Inc.	R&D on Siemens Cz Silicon Product Manufacturing
5A2	Solar Cells, Inc.	R&D on CdTe Product Manufacturing
5A2	Solarex	Improvements in Polycrystalline Silicon PV Module Manufacturing
5A2	Spire	Post-Lamination Manufacturing Process Automation for Photovoltaic Modules
5A1	Utility Power Group	Development of a Fully-Integrated PV System for Residential Applications

As mentioned above, Phase 5A subcontracts, addressing systems and system components other than modules, are described in a separate paper by H. P. Thomas et al., from the National Renewable Energy Laboratory. The other 5A awards are described below.

ASE Americas Inc. will work on improvements in process integration, Statistical Process Control implementation, data systems implementation, and ISO9000 and ISO14000 implementation. The improvements will be directed at reducing yield losses in areas of electrical and mechanical performance and reducing chemical waste. ASE will also develop processes that can be scaled to high volumes in the growth of thin EFG cylinders with improved productivity, as well as the production of solar cells from much thinner wafers. This effort includes work in laser-cutting technology to increase speed for cutting wafers and R&D to ensure a stronger EFG wafer and improve cell processing to achieve 15% solar cell efficiencies.

AstroPower, Inc. is improving their flexible manufacturing system for their Silicon-Film™ solar cells. Their research during this three-year effort will address several areas of the Silicon-Film™ production line, including the development of a continuous, in-line processing technology for large-area (30-cm wide by 1.2-m long) planks with higher throughputs, reduced material cost, and increased safety. As part of this subcontract, AstroPower will develop a continuous, high-speed, large-area contact metallization process for large-area Silicon-Film™. This will significantly increase their throughput, improve front-contact line width and contact resistance, and reduce cost. Achieving the expected improvements in the Silicon-Film™ sheet-growth processes would result in large-area (900-cm^2), 12%-efficient (10.8-W) solar cells.

Crystal Systems, Inc. is working on the production of solar-grade silicon by refining liquid metallugical-grade (MG) silicon at low cost, in abundant supply to meet the PV industry's rapidly expanding needs. The approach proposed is based on thermo-chemical refining techniques and the Heat Exchanger Method (HEM)™. The goal of this work will be equipment and processes adequate for use in an MG-silicon production plant using 500-kg charges, as well as demonstrating the removal of impurities, including boron and phosphorous, to less than 1 ppma after refinement at the 500-kg charge level. The development and implementation of this upgraded solar-grade silicon feedstock is expected to result in significant labor cost savings and increased throughput, with the production cost goal of solar-grade silicon to be less than $20/kg.

Energy Conversion Devices, Inc. (ECD) is performing manufacturing R&D to: develop a new substrate-heating system and temperature-sensor system designed to achieve more accurate temperature controlling and monitoring for the production of high-efficiency solar cells; develop a set of in-line, real-time, material-quality monitoring systems for production machines; demonstrate the feasibility of using Zn metal targets in the DC sputtering process to prepare ZnO layers for high-performance back-reflectors; and redesign the internal hardware for a-Si intrinsic layer (i-layer) deposition chambers.

Evergreen Solar, Inc. is improving their string ribbon crystal-growth process through reductions in labor and material costs, and capital costs of additional furnaces, through increased automation and increased efficiency. They will also develop high-throughput automated cell and module manufacturing line processes such as: a continuous glass etch; high-speed drying and application of decals; automation in diffusion, glass etch, high-speed drying, printing and application of contact decals; and molecular hydrogen passivation. Additionally, Evergreen will increase their manufacturing automation and throughput and decrease their labor costs by deploying a patterned backskin, an in-line tester, and an automated stringing operation.

Global Solar Energy, L.L.C. will perform R&D as follows: refining an all-laser, multiple-beam, high-speed scribing method for all copper indium gallium diselenide (CIGS) PV layers; developing a process for ink-jet printing as a replacement to screen printing for insulating scribed areas, and integration of this process, along with the laser-scribing methods, into the manufacturing production line; developing and integrating a high-rate CIGS deposition process for a moving flexible substrate onto their manufacturing line; designing, assembling, and optimizing a Parallel Detector Spectroscopic Ellipsometer (PDSE) for transfer onto the thin-film CIGS production line; and developing an alternative back-contact material that is compatible with CIGS processing on a flexible substrate.

Siemens Solar Industries is concentrating their research on the development and integration of new optimized cell fabrication processes into their manufacturing line for the production of 17%-efficient, 125-μm thick cells. Also, they will develop large-area cell production capability for 200-mm-diameter, 4.5-watt prototype solar cells and low-cost prototype modules. Siemens environmental, safety, and health activities will be directed toward reducing their hazardous waste by over 50% through recycling and re-use of slurry materials in their wire-saw process and a more than 70% reduction in caustic waste.

Solar Cells, Inc. (SCI) is developing, designing, and implementing an improved ethylene vinyl acetate (EVA)

lamination process, an improved potting procedure, and an improved scribing technique for the SCI cadmium telluride (CdTe) module production line. They will also complete qualification testing of their frameless, 60-cm x 120-cm module with pigtails, as well as other advanced module designs such as: (1) investigating a junction box instead of pigtails; (2) evaluating module sizes other than 60 cm x 120 cm; (3) developing alternative module voltage configurations; (4) and developing alternative encapsulation materials or processes. Additionally, SCI will work toward refining and improving their environmental, safety, and health programs throughout their facilities and initiating activities related to obtaining ISO14000 certification.

Solarex is performing R&D in several parallel areas. The first area involves Solarex working with a lower-tier subcontractor to develop a process to produce silicon feedstock from commercial-grade H_2SiF_6. Also, Solarex will refine production-line process areas for improved product and materials handling to increase production line yield and reduce labor costs. They will improve process measurement and control in their production line and reduce rework by implementing an improved information system. Solarex will also make improvements in their casting and wafer-sawing processes, while developing manufacturing techniques that are environmentally more benign. Solarex will demonstrate and implement a cost-effective, robust, cell process that produces a minimum average cell efficiency of 15% and improves their cell-line electrical yield. Finally, they will develop an encapsulation system that meets their technical and reliability requirements and can be laminated and cured more quickly in the present Solarex laminators.

Spire Corporation is addressing automated photovoltaic module assembly. They will develop a series of automated, flexible systems, including (1) an integrated module-edge processing system, combining automated edge trimming, edge sealing, and framing processes, (2) an automated junction-box installation system, (3) a final module test system combining high-voltage isolation testing and performance testing in a SPI-SUN SIMULATOR™, and (4) an automated buffer storage system. Solar-cell laminates and other module materials provided by the industry will be used by Spire to evaluate the automated processes developed in the program. The systems will be capable of assembling modules made with either crystalline-silicon solar cells or thin-film solar-cell laminates.

4. PVMAT - TECHNOLOGIES AND RESOURCES TO DATE

Table 2 shows, by technology area, the total funding for PVMaT for Phases 2 through 4 (the problem solution phases). The more mature crystalline-silicon technologies have the largest share of the funding. The amorphous-silicon area is second in size and probably benefitted from the large U.S. research funding of the 1980s in its apparent initial lead in thin-film efforts. But we are now seeing CIS join CdTe as a promising candidate for manufacturing improvements leading to viable products. See Global Solar Energy in Section 3 above for a description of the first CIS subcontract in the problem-solving stage of PVMaT.

TABLE 2. PVMaT FUNDING BY TECHNOLOGY
(through Phase 4)

Technology	Funding (US $K)	Percent by Technology
Amorphous Silicon	17,184	26
Cadmium Telluride	8,206	13
Concentrators	6,162	9
Crystalline Silicon	26,588	41
Generic/Balance of Systems/Systems	7,500	11
TOTALS	**65,640**	**100**

Table 3 shows the relative cost-sharing by phase for the PVMaT project to date. The subcontracts awarded in 3 and 4A1 are generally of the more generic or system component and integration type, with less emphasis on process-specific module manufacture. In addition, these awards were constrained to less effort, both in resources and time. The offerors in these areas have also been smaller companies, generally meeting the "small business" criteria for PVMaT participation. Consequently, they have not been required to cost-share as heavily, and the data show that they have not.

TABLE 3. PVMaT FUNDING AND COST SHARE
(By Phase)

Solicitation	DOE Funds (US $K)	Private Funds (US$K)	Private Cost Share %
PVMaT 2A - Process Specific	30,738	21,316	41
PVMaT 2B - Process Specific	13,384	14,557	52
PVMaT 3 - Generic	2,220	751	25
PVMaT 4A1 - Product Driven BOS and Systems	5,280	1,742	25
PVMaT 4A2 - Product Driven Module Manufacturing	14,017	9,949	42
TOTALS	**65,640**	**48,317**	42

5. CONCLUSIONS

PV manufacturing processes, technology, and cost reduction have been substantially advanced by the U.S. DOE PVMaT project and the U.S. PV industry. PV manufacturing improvements continue in both the more mature crystalline-silicon approaches and the newer thin-film technologies. Finally, based on the response to the most recent PVMaT solicitation, Phase 5A, industry has identified many areas of PV manufacturing which require continued or new R&D, and the responding companies find it useful to share with the government program in supporting these R&D efforts.

6. ACKNOWLEDGMENTS

This work is supported under DOE Contract No. DE-AC36-83CH10093 with NREL, a national laboratory managed by Midwest Research Institute. Many people have contributed to the development and implementation of the Photovoltaic Manufacturing Technology project and to the R&D efforts carried out in this program. The authors thank each of them and recognize this paper represents their work.

REFERENCES

[1] C.E. Witt, L.O. Herwig, R. Mitchell, and G.D. Money, "Status of the Photovoltaic Manufacturing Technology (PVMaT) Project," *Proceedings of the 22nd IEEE Photovoltaic Specialists Conference*, Las Vegas, Nevada, October, 1991.

[2] C.E. Witt, L.O. Herwig, R.L. Mitchell, H.P. Thomas, R. Sellers, and D.S. Ruby, "Recent Progress in the Photovoltaic Manufacturing Technology Project (PVMaT)," *Proceedings of the 1st World Conference on Photovoltaics*, Waikoloa, Hawaii, December, 1994.

[3] R.L. Mitchell, C.E. Witt, H.P. Thomas, D.S. Ruby, R. King, and C.C. Aldrich, "Progress Update on the U.S. Photovoltaic Manufacturing Technology Project," *Proceedings of the 26th IEEE Photovoltaic Specialists Conference*, Anaheim, California, October, 1997.

IV. Cell, Module, and System Testing

PHOTOVOLTAIC SPECTRAL RESPONSIVITY MEASUREMENTS

K. Emery, D. Dunlavy, H. Field, and T. Moriarty
National Renewable Energy Laboratory (NREL)
1617 Cole Blvd., Golden, CO, 80401-3393 USA
phone: 303-384-6632, fax: 303-384-6604, email: keith_emery@nrel.gov

ABSTRACT: This paper discusses the various elemental random and nonrandom error sources in typical spectral responsivity measurement systems. We focus specifically on the filter and grating monochrometer-based spectral responsivity measurement systems used by the Photovoltaic (PV) performance characterization team at NREL. A variety of subtle measurement errors can occur that arise from a finite photo-current response time, bandwidth of the monochromatic light, waveform of the monochromatic light, and spatial uniformity of the monochromatic and bias lights; the errors depend on the light source, PV technology, and measurement system. The quantum efficiency can be a function of the voltage bias, light bias level, and, for some structures, the spectral content of the bias light or location on the PV device. This paper compares the advantages and problems associated with semiconductor-detector-based calibrations and pyroelectric-detector-based calibrations. Different current-to-voltage conversion and ac photo-current detection strategies employed at NREL are compared and contrasted.
Keywords: Experimental Methods - 1: Calibration - 2: Performance - 3

1. INTRODUCTION

The spectral responsivity or quantum efficiency (QE) is essential for understanding current generation, recombination, and diffusion mechanisms in photovoltaic devices. PV cell and module calibrations often require a spectral correction factor that uses the QE. The quantum efficiency in units of electron - hole pairs collected per incident photon is computed from the measured spectral responsivity in units of amps per watt as a function of wavelength.

Typically, the spectral response is measured at short-circuit current. The measured photo-current is often in the μA to mA range with a broadband DC bias light near the devices intended operating point e.g. 1-sun. PV devices normally operate near their maximum power point, This is not normally a problem except in the case of amorphous silicon where the QE is voltage dependant.

The elemental error sources in the determination of the spectral response can be separated into errors in measuring the photo-current and errors in measuring the incident light power. Table I lists error sources in measuring the photo-current for a generic spectral response system. Formal and informal intercomparisons between measurement laboratories have shown significant differences in the relative spectral responsivity because of calibration errors, bias light dependence, light source emission lines, and other unknown sources [1-4]. ASTM Standard E1021 estimates a 0.3% repeatability and 1.7% reproducibility limit in the spectral mismatch parameter calculated using the spectral response data measured by the various participants in an intercomparison [5]. The final reports of the PEP'87 and PEP'93 international intercomparisons show graphically significant wavelength-dependent differences [6,7]. Understanding the various possible random and nonrandom error sources for a given system and minimizing the dominant error sources is essential to reliable absolute or relative quantum-efficiency measurements.

2. NREL MEASUREMENT SYSTEMS

A variety of spectral response measurement systems have been designed by the PV community, including systems based on interference filters, grating monochrometers, and interferometers [2-4,6-8]. Spectral responsivity measurements have been performed by the PV Cell and Module Performance Characterization team at NREL since 1983 on the filter-monochrometer-based system shown in Fig. 1 [3,9]. The system originally used stepping solenoids controlled by digital logic. Modifications are currently underway for a fourth filter wheel and real-time calibrations. An operational amplifier rated at ±40 V, 8 A is used as a current-to-voltage converter with a computer controlled gain of 50 to 10,000. Insertion of a power supply in series with the PV device allows bias voltages up to ±40 V. When an ac amplifier with a gain of 1, 10 or 100 is used the ac signal is typically in the 0.3 to 3 V range, allowing the ac signal to be measured with an ac voltmeter instead of the more traditional lockin amplifier. Modern digital lockin amplifiers have rapid auto-ranging capabilities and will outperform an ac voltmeter for noisy signals. The use of the shutter is essential for the ac voltmeter, but is less important when using a lockin amplifier. The monochromatic beam power is measured with a Laser Probe model 5710 radiometer with a RKP 575 pyroelectric head and a calibrated Si detector.

The grating system shown in Fig. 2 was developed to measure the responsivity of thermophotovoltaic cells from 400 to 2800 nm. This system uses a Laser Probe 5900 elec-

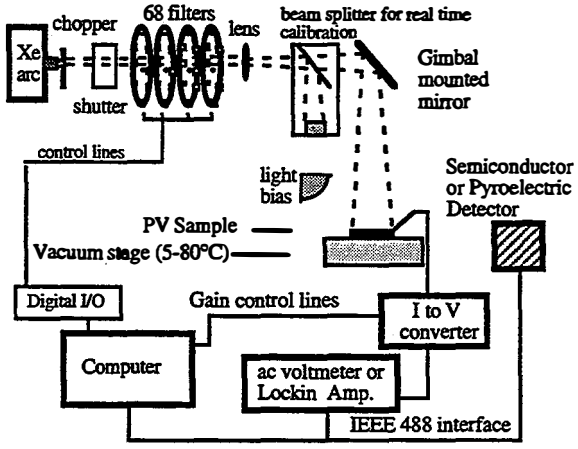

Figure 1: NREL filter QE system with a 280-2000 nm wavelength range.

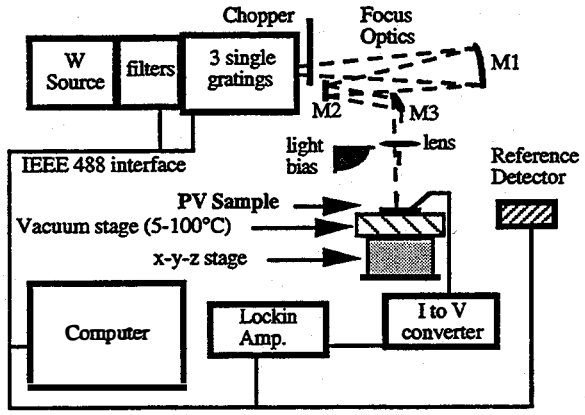

Figure 2: NREL grating monochrometer QE system

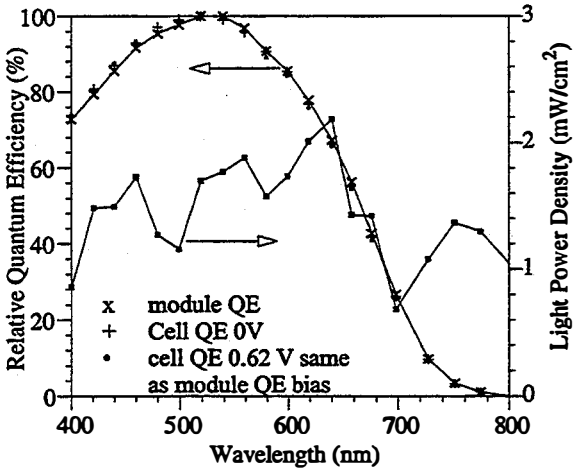

Figure 3: Module *vs.* cell QE measured with the filter system on a Solarex SA5 module.

trically calibrated pyroelectric radiometer (RSP-590/RSV head). Si detectors calibrated by the National Institute of Standards and Technology are also used for calibrations with estimated uncertainties of 0.2% to 2% from 400 to 1150 nm and higher elsewhere [10]. Semiconductor-based calibrations are useful where the photocurrent is known within a multiplicative constant. If the same amplifier is used to measure the reference and unknown PV devices, then uncertainties in the gain drop out. For semiconductor calibrations, the chopper phase is irrelevant, whereas the Laser Precision 5900 pyroelectric radiometer requires that the chopper be manually adjusted until the phase is correct. Semiconductor-based calibrations allow the test and reference signals to be filtered independently to maximize the signal-to-noise ratio.

3. PROCEDURES FOR MODULE QE

It is often desirable to measure the QE of modules consisting of multiple cells in series. The simplest approach would be to illuminate the whole module with ac monochromatic and dc broadband light with the module at 0 V, just as in the case of cells. The NREL filter system shown in Figure 2 is capable of fully illuminating any commercial module. This approach gives reasonable data sometimes. The problem with this method is that different cells may be current limiting at various wavelengths, and the bias point of the current-limiting cell whose QE is being measured is not at 0 V. This problem is similar to the multijunction amorphous silicon QE measurement problem addressed by Burdick and coworkers [11]. The solution to the problem for modules is to:

1. bias the module with light to simulate "1-sun."

2a. forward bias the module to the measured open-circuit voltage (V_{oc}) times (n-1)/n, where n is the number of cells in series.

2b. Another procedure is to set the monochrometer to a wavelength that the cell responds to and to reduce the forward bias voltage from the measured V_{oc} towards 0 V until the ac signal is a maximum.

3. shine the monochromatic light on only one cell.

4. reduce the bias light on the cell that sees the monochromatic light in regions where there is no monochromatic light to ensure that this cell is current limiting.

The region where the monochromatic light strikes the sample does not need light bias if the QE is linear. A custom fixture was made for thin film modules that restricts the beam on the NREL filter system to illuminate just one narrow rectangular cell. Figure 3 shows an example of a module QE measurement on a Solarex SA5 amorphous silicon module where the individual cells have also been contacted. If all the cells in the module were identical, then the bias measured would be 0 V using the method given in step 2a and not 0.62 V. The advantage of method 2b is that the QE is maximized. The light bias level was 3-7% of one-sun as measured with a filtered silicon reference cell depending on where the light was measured. Figure 3 also shows the monochromatic light power density for the approximate 10 cm diameter beam produced by the filter QE system shown in Fig. 1. The monochromatic power density can be increased by focusing the beam to a smaller spot.

4. QE MEASUREMENT ERROR SOURCES

Spectral responsivity measurements involve the measurement of the photo-current produced by light of a given wavelength and power. The quantum efficiency is typically measured with bias light simulating reference conditions, because the device may be nonlinear [1-7]. Typically, the spectral correction factor for efficiency measurements is calculated based on QE measurements near 0 V and is assumed to be the same as at the maximum power point. This assumption is valid for most PV systems and results in a negligible error for amorphous silicon, which has a voltage-dependent spectral responsivity [12].

Error sources related to the measurement of the photocurrent are summarized in Table I. If semiconductor-based calibrations are employed with the same electronics used to measure the test and reference device, then all multiplicative errors drop out. For pyroelectric-radiometer-based calibrations, the absolute photo-current must be measured for absolute QE measurements. Commercial I-to-V converters typically have a limited maximum current of around 10 mA. This limitation is removed for I-to-V converters based on operational amplifiers.

For absolute current measurements, the measured lockin signal must be multiplied by a waveform correction factor that relates the measured RMS signal with the peak signal. This factor is $\sqrt{2}/2$ for a sine wave, $2\sqrt{2}/\pi$ for a square wave, and $2\sqrt{2}\cdot a\cdot\sin(\pi/a)/\pi^2$ for a trapezoid, with the constant π/a

Table I: Error sources for measurement of the photo-current.

- Electrical Instrumentation
  - current-to-voltage (I to V) converter
    - commercial current or custom amplifier
      - gain, linearity, noise, offset
    - shunt resistor
      - calibration, drift, thermovoltages
  - signal from I to V converter measured with
    - lockin amplifier (typically < 1 mA)
      - calibration, resolution, accuracy,
      - waveform to sine wave correction factor,
      - overloading, noise, dynamic range,
      - time-constant,
      - procedures for using lockin amplifier
    - an ac voltmeter
      - gain, offset from noise level,
      - linearity, time-constant
- PV cell or module
  - temperature,
  - response-time to periodic light,
  - linearity of PV device
  - white-light bias spatial uniformity,
  - monochromatic light spatial uniformity,
  - voltage bias of cell being measured,
  - spectral content of bias light,
  - device sensitivity to polarization of light
- Mechanical
  - mechanical movement of optics,
  - mechanical vibration,
  - chopped stray monochromatic light

being the radian angle at the top of the rising edge of the trapezoidal waveform [13].

The response time of PV devices to chopped light can be a problem for electrochemical cells. Similar to results reported elsewhere, chopping frequencies below 4 Hz are required to keep the waveform from changing with frequency [14]. This effect is more pronounced at low light levels and in the infrared.

It is important that light from the bias light source not be allowed to go through the light chopper. A simple procedure to determine if the sample is seeing chopped stray light is to turn off the monochromatic light source and measure the test device's response as a function of bias light intensity.

A variety of error sources associated with measuring the monochromatic light power are listed in Table II. The measurement of the monochromatic light power can be performed with radiometric detectors or semiconductor detectors. When a quartz slide is used as the beam splitter, then errors in the power can arise because of polarization effects. The light off the monochrometer is polarized, and the polarization angle can change with a grating change. The bandgap, photoluminescence, and absorption coefficient for PV devices can be sensitive to the polarization angle. The light reflected off a glass surface will have a different polarization than the light reaching the test plane and will be of much lower intensity. These effects are minimized if a calibration is performed with the detector in the test plane and the file stored to disk. This procedure is required at least once for real-time calibrations. Real-time calibrations account for the change in spectrum with lamp age, current, and time among other things.

Table II: Error sources for measurement of the light power.

- Filament or Xe-arc light source
  - intensity fluctuations,
  - change in spectral irradiance with age and current
- Real-time calibration
  - source-light polarization with a
    - glass beam splitter,
  - signal to noise,
  - detector characteristics,
  - calibration drift with time of monitor detector
- Stored calibration file
  - monochromatic source calibration drift with time
- Stray light
  - detector sees light that cell does not see,
  - area of detector different from device area,
  - different field of views,
  - monochrometer
    - incomplete attenuation of grating orders
  - narrow bandwidth filters
    - pinholes in the filter,
    - degradation of blocking filter,
    - insufficient blocking ($\sim 10^{-4}$)
- Reference detectors and associated electronics in general
  - calibration, resolution, accuracy,
  - gain, phase, offset, linearity,
  - spatial uniformity of detector element,
  - temperature drift,
  - change in the detector's field of view,
  - degradation of detector,
  - spectral response of detector
- Pyroelectric detector
  - different instrumentation used to measure cell and reference
  - time constant of detector,
  - microphonics, signal to noise,
  - phase-angle adjustment,
  - waveform factor (square wave assumed)

If the beam is larger than the sample, then the spatial uniformity of the monochromatic beam is important. For the NREL filter monochrometer system, spatial nonuniformities of ±10% are typical and, more importantly these errors can change with wavelength because of variations in the transmission of the filter and spatial variation in the output of the Xe-arc lamp. Electrically calibrated pyroelectric detectors are spectrally flat from the ultraviolet to far infrared and have a low broadband error of less than ±2%, but are sensitive to microphonics, temperature changes within the detectors field of view, and have noise at the 0.01 μW cm^{-2} level. Semiconductor-based detectors are not sensitive to light outside their relatively narrow response range and can be measured with the same electronics used to measure the test device, eliminating any wavelength-independent multiplicative error sources. Semiconductor-based detectors can drift with age [15] and have temperature coefficients exceeding 1 %/°C near their bandgap. Figure 4 shows the quantum efficiency of a cell measured with a pyroelectric based detector and semiconductor based detector. The light power of the grating monochrometer based system is focussed to a rectangular spot approximately 1 by 3 mm. The monochro-

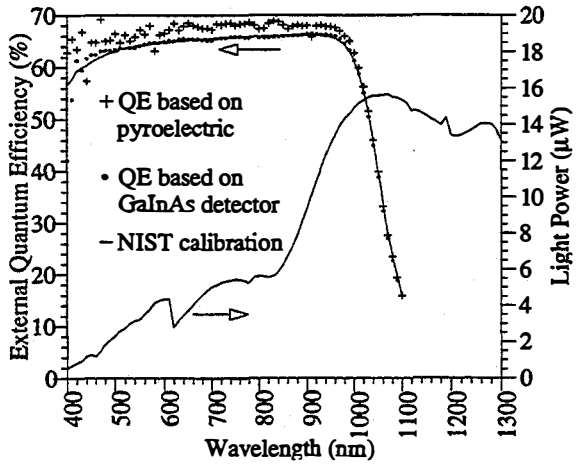

Figure 4: Comparison of semiconductor and pyroelectric based QE measurements on a NIST calibrated Si detector with the NIST calibration.

matic light power for the filter QE system (Fig. 3) is approximately 20,000 times greater than for the grating system (Fig. 4). The random error in the measured QE's in Fig. 4 are summarized in Table III. The Laser Probe 5900 electrically calibrated pyroelectric radiometer in Fig. 2 has a total error of ±0.9% for a 3 mm beam and 95% confidence. Table IV summarizes the error in the QE that can occur because of the monochromatic light. Many of the error sources listed in Tables II and IV are discussed in detail by Kostkowski [16]. The bandwidth of the monochromatic light can contribute to the error near the band gap or when the light transmitted through a bandpass filter is highly asymmetric [13]. These errors have a small effect on the spectral correction factor when the bandwidth is less than 10 nm [13].

5. CONCLUSIONS

A method has been presented to measure the quantum efficiency of modules that is consistent with accepted procedures for measuring the quantum-efficiency of multijunction cells. Various sources of uncertainty for quantum efficiency measurement systems are discussed. Absolute quantum-efficiency measurements with a total uncertainty of less than ±2% are possible, but only with extreme measures to minimize all error sources [3,6].

Table III: Errors in Grating QE Measurements at NREL

Uncertainties	Pyroelectric Calibration File[1,2]	NIST calibrated QE of D205[3]	QE of D205 based on GaInAs Calibration[2]
400-500 nm	15.0%	1.56%	4.0%
500-600 nm	10.0%	0.24%	0.5%
600-900 nm	4.5%	0.24%	0.5%
900-100 nm	3.0%	4.00%	0.5%

[1]Data not available for pyroelectric calibrated QE
[2]Random error, 95% confidence
[3]Relative expanded uncertainty (k=2) extracted from NIST calibration

Table IV: Error sources related to the monochromatic light.

Bandwidth,
Filter defects,
Polarization variation with wavelength,
Wavelength offset,
Wavelength variation with temperature,
Beam wanders with wavelength,
Beam larger than the test device
    detector area versus PV area,
    position of detector and PV different,
    spatial uniformity of beam
Beam smaller than detector and device area
    partially shaded regions,
    spatial variation in responsivity of PV

6. ACKNOWLEDGMENTS

This work is performed under Contract No. DE-AC36-83CH10093 to the U.S. Department of Energy.

7. REFERENCES

[1] C. Jing-Gui, G. Xiong-Jun, Y. Pei-Neo, and W. Yu-Xue, Proc. PVSEC-3, Japan, pp. 743-748, 1987.
[2] H. Ossenbrink et al, "The results of the 1984/1985 round-robin calibration of reference cells for the summit working group on technology growth and employment," Joint Research Center, ISPRA Establishment, EUR 10613 EN, April 1986.
[3] J. Metzdorf et al, "The results of the PEP'87 round robin calibration of reference cells and modules - Final Report," PTB tech rep. PTB-OPT-31, Braunschweig, Germany, Nov. 1990, ISBN 3-89429-067-6.
[4] C. Osterwald et al., "The results of the PEP'93 intercomparison of reference cell calibrations and newer technology performance measurements: final report," NREL Tech. Rep. TP-520-23477, March 1988.
[5] "Standard test methods for measuring spectral response of photovoltaic cells," ASTM Standard E1021, ASTM, 100 Barr Harbor Dr., W. Conshohocken, PA.
[6] J. Metzdorf, Appl. Opt. 26, pp. 1701-1708, 1987.
[7] K. Bücher and A. Schönecker, Proc. 10th EC PV Solar Energy Conf., pp. 107-110, 1991.
[8] J.S. Hartman and M.A. Lind, Solar Cells, 7, pp. 147-157, 1982.
[9] T.J. Coutts and C.R. Osterwald, Solar Cells, 22, pp.195-209, 1987.
[10] National Institute of Standards and Technology, Calibration Program, Building 820, Room 232, Gaithersburg, MD US 20899, e-mail calibrations@nist.gov.
[11] J. Burdick and T. Glatfelter, Solar Cells, 18, pp. 301-314, 1986.
[12] C.R. Wronski, B. Abeles, G.D. Cody, D.L. Morel, and T. Tiedje, Proc. 14th IEEE PVSC, pp. 1057-1061, 1980.
[13] H. Field, Proc. 26th IEEE PVSC, Anaheim, CA, pp. 471-474, 1997.
[14] P.M. Sommeling, H.C. Riefe, J.M. Kroon, J.A.M. Van Roosmalen, A. Schönecker, and W.C. Sinke, Proc. 14th EC PV Solar Energy Conf., pp. 1816-1819, 1997.
[15] K.D. Stock and R. Heine, Optik, **71**, pp. 137-142, 1985.
[16] H.J. Kostkowski, "Reliable Spectroradiometry," ISBN 0-9657713-0-X, 1977.

APPLICATIONS OF "PV OPTICS" FOR SOLAR CELL AND MODULE DESIGN

Bhushan L. Sopori, Jamal Madjdpour, and Wei Chen
National Renewable Energy Laboratory
1617 Cole Boulevard
Golden, CO 80401, U. S. A.

ABSTRACT: This paper describes some applications of a new optics software package, *PV Optics*, developed for the optical design of solar cells and modules. *PV Optics* is suitable for the analysis and design of both thick and thin solar cells. It also includes a feature for calculation of metallic losses related to contacts and back reflectors.
Keywords: Solar Cell Design – 1: Optical Properties – 2

1. INTRODUCTION

High-efficiency solar cells involve a number of features that are difficult to handle by simple optics. An optical design and analysis software package for solar cells and modules must include capabilities to handle: (i) nonplanar interfaces such as those required for optimizing light-trapping; (ii) thick devices such as crystalline silicon solar cells as well as thin cells based on a-Si, CdTe, and CIS; (iii) antireflection and dielectric coatings, (iv) metallic absorption arising from contacts and back reflectors; and (v) thicker materials such as glass and encapsulants used in modules.

We have developed a new, commercial, computer software package, *PV Optics*, for the optical design and analysis of solar cells and modules. This paper describes some applications of this software package.

2. FEATURES OF *PV OPTICS*

PV Optics is an easy-to-use software that accurately models the optics of any solar cell or module, and provides information needed to design a device with maximum-effective light-trapping and optimum photocurrent. *PV Optics*' sophisticated model uses the coherence length of light as a criterion to categorize various regions of a cell as "thin" or "thick" – the former have thicknesses less than the coherence length of light and include interference and polarization effects; the latter are much thicker than the coherence length and are treated on the basis of ray optics. The model separates a multilayer structure into several composite layers each as a "thin" or "thick" group. Each group of layers is analyzed and the entire structure is reassembled. Regions such as glass superstrates or encapsulation layers having thicknesses greater than a few microns, and textured structures, are treated in a noncoherent regime. Thin and specula layers such as those used for antireflection (AR) coatings in a-Si devices are treated as coherent regions.

PV Optics:

Accommodates device design for single and multijunction cells, with as many as three active semiconductor layers plus cover glass, encapsulation, AR coating, buffer, and metal backing.

Calculates the light-trapping impact of nonplanar (textured or intentionally rough) interfaces of any of the device layers.

- Accurately calculates interference effects (caused by coherence of light) of very thin layers such as AR coatings or thin-film semiconductor materials.
- Includes default refractive index and extinction coefficient values for crystalline silicon, amorphous silicon, glass used for encapsulation, encapsulation materials such as EVA, and buffer layer.
- Calculates maximum achievable current density (MACD in mA/cm^2) for each semiconductor layer, providing a benchmark for cell performance.
- For each device, automatically and clearly plots:
  – Reflection, transmission, semiconductor absorbance, and metal absorbance, each as a function of wavelength
  – (For multijunction devices) absorbance for each separate layer plus total absorption
  – Absorbance by wavelength for typical sunlight (AM1.5), predicting actual cell performance
- Photon absorbance as a function of depth within each semiconductor layer—facilitating selection of optimum thickness(es) (this data can be used in an electronic model like AMPS or PC1D for complete cell performance prediction).

PV Optics can be used for optimizing a variety of cell parameters, such as cell absorber thicknesses, the structure of the texture, AR coating parameters, and the back-reflector design. Here, we will demonstrate the capabilities of the package by specific examples. The model is a user-friendly tool using a "Windows" environment. It requires as input the optical constants of each layer as a function of wavelength and the layer thicknesses. Texture is simulated by allowing the user to select appropriate geometric features in addition to co-planar layers. Computing times depend significantly on the conditions chosen and can vary from minutes to hours. The examples we present are intentionally kept simple to demonstrate the capabilities of the package, and show that results are often obtained that would not have been expected intuitively.

3. OPERATING *PV OPTICS*

PV Optics (Version 1) for the PC comes on a single 3.5" floppy disk. The software requires an IBM compatible PC/60 MHz (or a higher speed), a minimum of 8 MB RAM, windows, a VGA monitor, and a color printer (can also operate with a black & white printer).

3.1 Selection of the Device Configuration

PV Optics Version 1, starts with a generalized device configuration as illustrated in Fig. 1. From this, one can select a desired device configuration. The device may include glass, encapsulation, AR coating, three semiconductors, a buffer, and metal. The device-configuration choice is made by simply deleting portions of the device configuration that does not correspond to the desired device, with a click of a mouse.

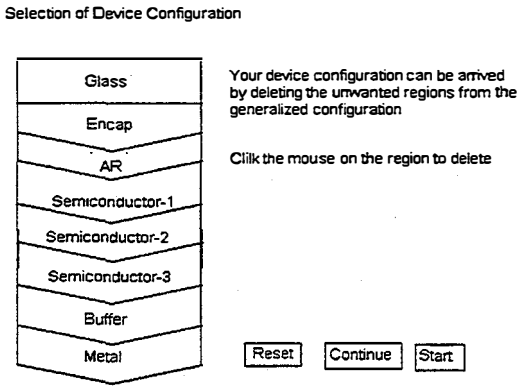

Figure 1: Illustration showing how the device configuration can be selected from the total module configuration.

Once the device configuration is arrived at, the program expects data pertaining to each layer and its interfaces. There is a "page" of each layer. The software provides default values for the interface type, thickness in microns, and n and k of each region. The default values correspond to standard materials used in PV manufacture. One can use the default values or change them simply by a click. The antireflection page provides the default values for the interface type, n1, k1, thickness1, n2, k2, and thickness2 for a two-layer AR Coating (n1, n2 are the refractive indexes and k1, k2 are the extinction coefficient). The selection of semiconductor page provides choices of up to three junction cells, and options to select the material "Silicon" or "Amorphous-Silicon," "Amorphous-Silicon Top," "Amorphous-Silicon Middle," or "Amorphous-Silicon Bottom." Additional semiconductor data can be incorporated at request.

3.2 Results are Displayed as Graphs

There are seven types of graphs: (1) Reflectance / Transmittance, (2) Absorbance, (3) Weighted Absorbance, (4) Photon Flux, (5) Reflectance / Transmittance (Non-Coherent), (6) Reflectance / Transmittance (Coherent), and (7) Weighted Absorbance.

The graphs may be saved as a bit-map (.bmp) file by selecting "Export" from the file menu. This will bring up the files window where you will be able to select drives, directories, and filenames. The files window will also insure that you give the graph a designated extension of ".bmp." Once you have selected or entered the filename that you wish to use, click on the "OK" button. Make sure that you are in the directory that you wish to save the file in. If you click on the "OK" button while the filename still shows "*.bmp," then the window will show you a list of only those files that have been saved as bit-maps.

4. RESULTS

In this section, we present results of calculations, for a number of cell and module structures, as examples of the capabilities of *PV Optics*.

Example 1 is a comparison of the optical characteristics of a silicon solar cell before and after encapsulation. Fig. 2 shows the reflection and absorption of a Si solar cell with the following features: textured front with a two-layer AR coating consisting of 710 Å of Si3N4 (refractive index =1.95) on 100 Å of SiO2 (refractive index=1,45); the texture height is 3 μm, thickness of Si cell is 250 μm, the backside of the cell is also textured with Al metallization. The calculated MACD = 41.02 mA/cm^2. Fig. 3 shows similar plots after the cell is encapsulated. The structures of the cell and the module are illustrated in each figure. The MACD value after the encapsulation is 38.75 mA/cm^2. Thus there is a loss of approximately 2.3 mA/cm^2 associated with encapsulation. From Fig. 3, it can be seen that after encapsulation there is a significant increase in the

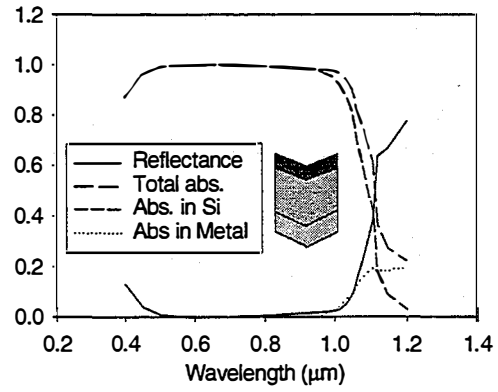

Figure 2: Calculated characteristics of a silicon solar cell (see text for the cell structure).

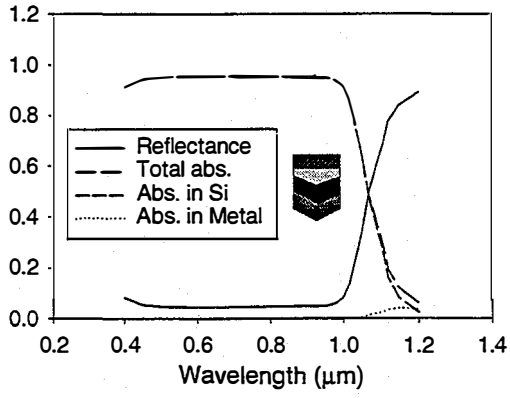

Figure 3: Calculated characteristics of the cell shown in Fig. 2, after encapsulation (see text for the cell structure).

reflection (in the wavelength range of 0.5μm – 1μm). The loss caused by this increase in reflection is offset by a decrease in the reflectance in the wavelength range of 0.4μm – 0.5μm.

From Figs. 2 and 3 we see an expected behavior of the reflectance – the cell reflection has a broad null in the wavelength range of 0.5 μm and 0.9 μm, while the module reflectance is dominated by the glass reflection. These figures also show absorption in the back metal is slightly less in the encapsulated case.

We can now compare the optical characteristics of a frontside textured cell with the double-sided textured cell of Fig. 2. To do this, we consider the cell of Fig. 2 and change the backside of the cell to a planar interface. The calculated results are shown in Fig. 4. Notice that the loss in the metal is lower, yet the MACD decreases to 40.66 mA/cm^2. The lower loss in the back planar surface, compared to the back textured surface can be explained in a rather oversimplified manner as follows. The light that reaches the backside undergoes one reflection at this planar surface, while a textured interface leads to more than one reflection. Because each reflection from the Si-Al interface is accompanied by metallic absorption, the textured interfaces lead to higher metal absorption. Clearly, the metallic loss depends on a number of parameters that include angle of incidence at the Si-Al interface and the intensity of light incident at the interface. Interposing a buffer layer of low refractive index between the semiconductor and the metal can mitigate this loss. This feature is illustrated in Example 3.

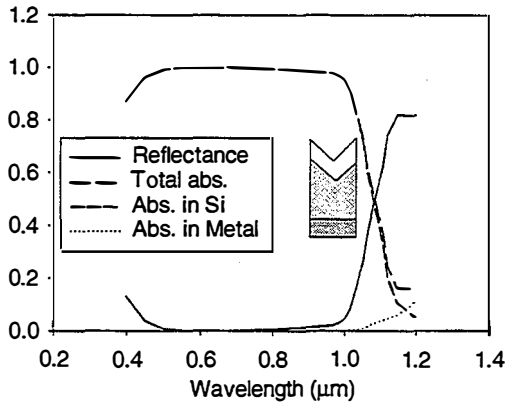

Figure 4: Calculated characteristics of a Si solar cell with frontside textured (see text for cell structure).

The second example demonstrates the ability of *PV Optics* to automatically recognize and deal with structures that are thinner than the coherence length of the incident light. Fig. 5a shows the results of *PV optics* for a structure consisting of a 0.5-μm-thick layer of a-Si on an Al substrate. In this "coherent" mode, the output shows interference fringes. Under this situation, *PV Optics* also performs calculations based on "incoherent" conditions. This result is shown in Fig. 5b.

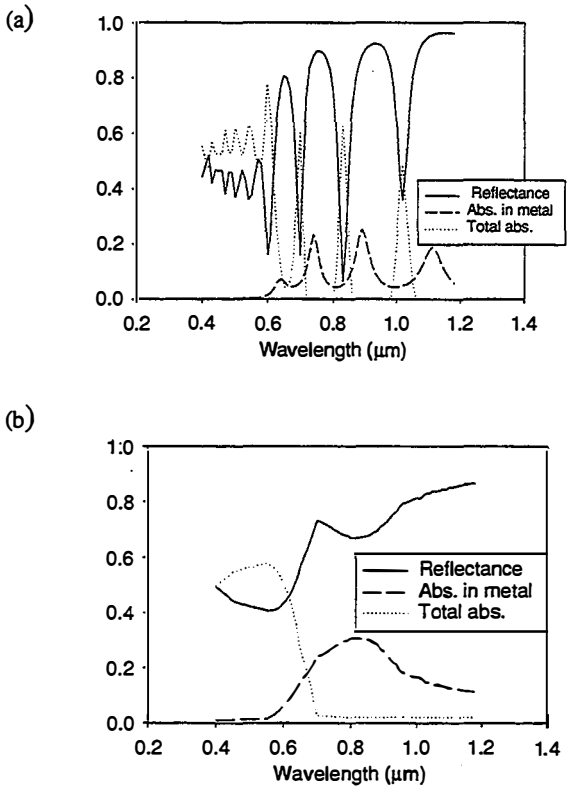

Figure 5: Calculated characteristics of a a-Si solar cell (see text for the cell structure) using *PV Optics* in (a) coherent mode and (b) noncoherent mode.

Example 3 pertains to an assessment of metallic losses in textured a-Si solar cells. Often the losses associated with back reflectors are assumed to be small. This assumption is generally made because reflection coefficients of many metallic reflectors reach close to 0.97 in air. However, this situation is quite different in a solar cell. The reflection at a high-refractive-index semiconductor and a metal can be greatly reduced. The light transmitted into metal is readily absorbed, leading to a significant loss of the optical energy. *PV Optics* can be very effectively used to calculate and gain an understanding of such losses. In particular, it is of interest to determine the effect of a buffer on the back reflection and metallic losses. Figs. 6a and 6b show the results of *PV optics* calculating the absorbance as a function of wavelength in two three-junction cell structures – one without buffer and the other with buffer. The cell structures are illustrated in each figure. The light enters the cell through a nonabsorbing SnO_2. The symbols T, M, B refer to top, middle, and bottom junction layers. The band gaps, Eg_i (i = T, M, B), have values such that $Eg_T > Eg_M > Eg_B$. The thicknesses of the top, middle, and the bottom layers, used in these calculations are assumed to be 0.3, 0.2, and 0.1 μm, respectively. The buffer layer consists of 0.25-μm-thick MgF_2. These modeling cases are simplified optical representations of a-Si "superstrate" cell. Figs. 6a and 6b show absorbance in each semiconductor layer as well as the total absorbance. We see that, for the structure of Fig. 6a without buffer, the MACD values corresponding to each

layer are: 10.3, 7.8, and 5.1 mA/cm^2 in the three a-Si layers and a metal loss of 9.5 mA/cm^2 for the structure without MgF_2. By introducing the buffer layer, the MACD values are 10.3, 8.2, and 6.2 mA/cm^2, with a metal loss of 3 mA/cm^2. It is of interest to note that the MgF_2 "backreflector" affects the current density not only in the semiconductor layer adjacent to it, but also in the a-Si layers further away.

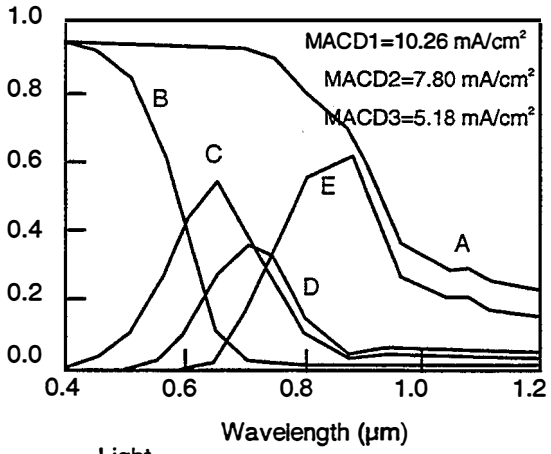

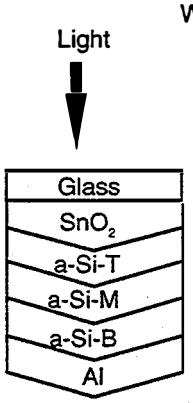

A– Total absorbance
B–Absorbance in semiconductor 1
C–Absorbance in semiconductor 2
D–Absorbance in semiconductor 3
E–Absorbance in metal

Figure 6a. Absorbance in simulated 3-layer a-Si superstrate cell with Al back reflector but no buffer.

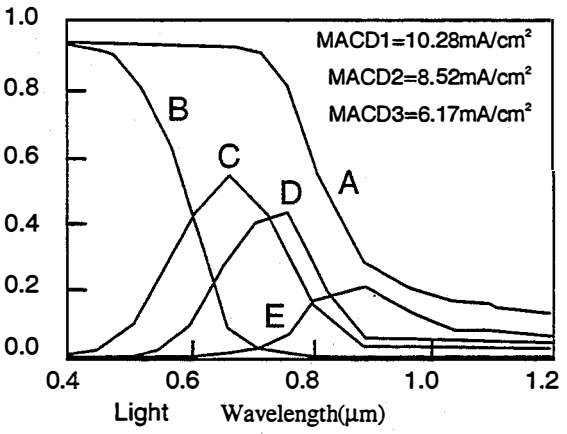

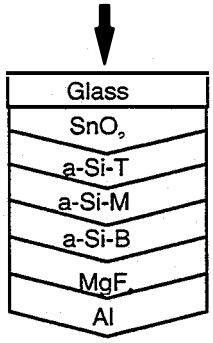

A– Total absorbance
B–Absorbance in semiconductor 1
C–Absorbance in semiconductor 2
D–Absorbance in semiconductor 3
E–Absorbance in metal

Figure 6b. Absorbance in simulated 3-layer a-Si superstrate cell with MgF_2/Al back reflector.

6. CONCLUSIONS

We have presented a brief description of *PV Optics* and discussed its results for a number of solar cells. The cell structures are used only as examples to demonstrate capabilities of this software. This software can be used for analysis of thick as well as thin cells. We have identified why in many instances the current densities observed in actual devices are less than those predicted from simpler analytical considerations. These discrepancies are not due to inadequate texturization or randomization of light, but rather to increased absorption losses in the rear-contact metallization as the light hits the metal from a layer with a refractive index n>1 and at oblique angles.

The present version of *PV Optics* (Version 1) is a two-dimensional model, and the light can be made incident only from the topside. The newer versions will include a number of modifications requested by PV community. *PV Optics* has other applications in modeling and design of display devices.

ACKNOWLEDGMENT

This work was supported by the US Department of Energy under Contract # DE-AC36-83CH10093. The authors are very grateful to Bolko von Roedern in NREL for many valuable discussions.

IMPROVED ACCURACY FOR LOW-COST SOLAR IRRADIANCE SENSORS

David L. King, William E. Boyson, and Barry R. Hansen
Sandia National Laboratories
Albuquerque, New Mexico, USA
http://www.sandia.gov/pv/

ABSTRACT: Accurate measurements of broadband (full spectrum) solar irradiance are fundamental to the successful implementation of solar power systems, both photovoltaic and solar thermal. Historically, acceptable measurement accuracy has been achieved using expensive thermopile-based pyranometers and pyrheliometers. The measurement limitations and sensitivities of these expensive radiometers are a topic that has been addressed elsewhere. This paper demonstrates how to achieve acceptable accuracy (±3%) in irradiance measurements using sensors costing less than one-tenth that of typical thermopile devices. The low-cost devices use either silicon photodiodes or photovoltaic cells as sensors, and in addition to low-cost, have several operational advantages.
Keywords: Pyranometer–1: PV Module-2: Reference Cell-3

1. INTRODUCTION

Thousands of photovoltaic systems, large and small, are now being installed worldwide. As a result, there is a growing demand for inexpensive devices for accurately monitoring the solar irradiance. Most often, the total (global) solar irradiance is the desired measurement. Occasionally, the direct normal (beam) irradiance is required. For most system applications, reasonable accuracy (±5%) at low cost (~200 $US) is usually preferable to high accuracy (±2%) at high cost (~2000 $US). As a result, silicon photodiode pyranometers manufactured by companies such as LI-COR Incorporated [1] and Kipp & Zonen [2] are now commonly used for solar resource measurements and photovoltaic system monitoring. One manufacturer alone (LI-COR) has sold over 31,000 of their low-cost silicon photodiode-based pyranometers. Commercial solar cells have also been packaged in a variety of ways to serve as solar irradiance sensors. Traditional photovoltaic reference cells [3] have been used for many years in test laboratories, occasionally for field applications. Irradiance sensors designed for easy temperature compensation have been produced using two solar cells and standard module lamination procedures by the European Solar Test Installation (ESTI) [4], and by module manufacturers such as AstroPower Incorporated [5]. Small commercial photovoltaic modules have also frequently been used for measuring the solar irradiance.

These photovoltaic-based devices have typically provided a reasonable method for measuring the integrated daily solar irradiance (radiation). However, when used to measure the instantaneous broadband solar irradiance, their accuracy has been less than desired. Their inaccuracy has been due to errors introduced by systematic, time-of-day dependent, variations in the solar spectrum, solar angle-of-incidence, and operating temperature. A method was described in our previous work for obtaining empirical relationships that compensate for these systematic errors [6, 7]. The purpose of this paper is to demonstrate the improvement achieved by applying these corrections.

Sandia is a multiprogram laboratory operated by Sandia Corporation, a Lockheed Martin Company, for the U. S. Department of Energy under contract DE-AC04-94AL85000.

The corrections result in measurement accuracy comparable to more expensive instruments, for both global and direct normal solar irradiance.

2. LOW-COST IRRADIANCE SENSORS

Fig. 1 illustrates a few of the low-cost sensors evaluated in our work. The low-cost devices illustrated include a LI-COR LI-200SA silicon-photodiode pyranometer, a LI-COR LI-200SA fitted with a baffled plastic (PVC) collimator, an ESTI Sensor using two crystalline silicon cells, a two-cell mini-module fabricated by AstroPower using their Silicon-Film™ cell technology, and a common silicon reference cell. For comparison, an Eppley PSP pyranometer [8] is also shown in Fig. 1. For photovoltaic-based devices, empirical "corrections" were developed to compensate for the systematic influences mentioned. Controlled tests were then conducted to compare irradiance measurements, with and without the corrections, to the measurements obtained using carefully calibrated Eppley thermopile-based instruments.

3. SOLAR SPECTRAL INFLUENCE

Compensation for the influence of the time-of-day dependent solar spectrum was achieved by using an empirically determined function [7]. This empirical function, $f_1(AM_a)$, related solar spectral variations to the absolute air mass (AM_a). "Air mass" is the term used to describe the path length that sunlight traverses through the atmosphere before reaching the ground. When adjustment is made for the altitude of the site, it is called the "absolute" air mass. AM_a is readily calculated knowing the zenith angle of the sun and the site altitude [7]. At sea level, AM_a=1 with the sun directly overhead, AM_a=1.5 when the sun's zenith angle is 48 degrees, and AM_a of about 10 at sunrise and sunset. As AM_a increases, the spectrum of the sun shifts to longer wavelengths, becoming more "red."

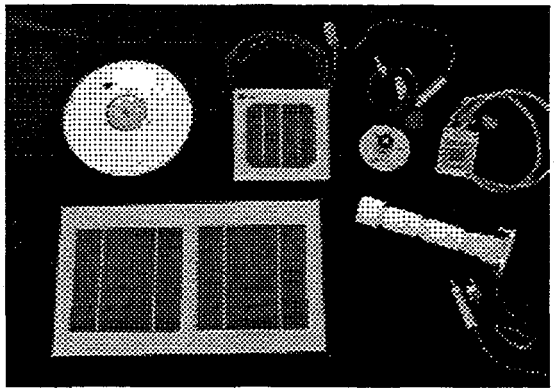

Fig. 1: Solar irradiance sensors, clockwise from upper left: Eppley PSP pyranometer, ESTI Sensor, LI-COR LI-200SA silicon-photodiode pyranometer, silicon reference cell, LI-COR LI-200SA with collimator, and AstroPower mini-module.

The concept of the empirical $f_1(AM_a)$ function can be understood by examining the standard ASTM method for calculating a "spectral mismatch correction" [9]. The test procedure used for determining $f_1(AM_a)$ basically provides a method for measuring a continuously varying spectral correction, referenced to one of two standardized spectra. These two solar spectra have been standardized by ASTM as references for the AM_a=1.5 condition, one for the direct normal spectrum and one for the global spectrum [10, 11]. The $f_1(AM_a)$ function is normalized to a value of one at AM_a=1.5, using one of these two standardized spectra.

Fig. 2 shows the $f_1(AM_a)$ functions measured for the low-cost irradiance sensors, for clear-sky test conditions in Albuquerque, NM. For clear-sky conditions, experience has also shown that these empirically determined relationships have wide applicability to different sites. The solar spectral variation over the day resulted in an effect on the normalized response (short-circuit current) that was characteristic for each device. The magnitude of the spectral effect was directly related to the spectral response characteristics of the device. For instance, the 10% change in response for the LI-COR pyranometer from AM_a=1 to AM_a=5 resulted from a negligible spectral response at "blue" wavelengths (< 400 nm) and good "red" response (> 900 nm). The LI-COR equipped with a collimating tube showed slightly less spectral influence over the day because the spectral distribution of the direct normal irradiance differs from the total (global) normal spectrum.

4. SOLAR ANGLE-OF-INCIDENCE

The irradiance sensor's response to the direct (beam) irradiance component is influenced by the cosine of the solar angle-of-incidence (AOI), and by the optical characteristics of its front surface. The response of the sensor to diffuse irradiance can be assumed to have no dependence on angle-of-incidence. The algorithms for calculating AOI are documented elsewhere [12]. The optical influence of the front surface, which could be a flat- or domed-glass cover or a translucent diffuser, can be described by another empirically determined function, $f_2(AOI)$. An outdoor test procedure for determining the $f_2(AOI)$ function is documented elsewhere [7].

Fig. 3 illustrates the relative response of the irradiance sensors versus the solar angle-of-incidence. For comparison, test results for a well-behaved Eppley PSP pyranometer are also shown. For clarity, measured data points for two of the devices are shown, and in other cases only the polynomial fit to measured values. The sensors with a planar glass front surface have a stronger sensitivity to AOI, for angles greater than 60 degrees. To some degree, the stronger sensitivity is offset by the observation that the planar devices have more repeatable behavior, device to device, than many commercial pyranometers. Users should recognize that all pyranometers are subject to significant measurement errors at high AOI due to mechanical misalignment. For instance at AOI=70 degrees, mounting a pyranometer only 1 degree different from the plane of a photovoltaic array will result in a 5% error in measured irradiance.

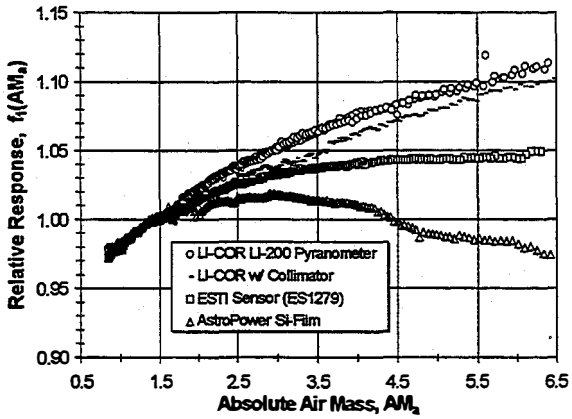

Fig. 2: Influence of solar spectral variation (AM_a) on response (short-circuit current) of irradiance sensors.

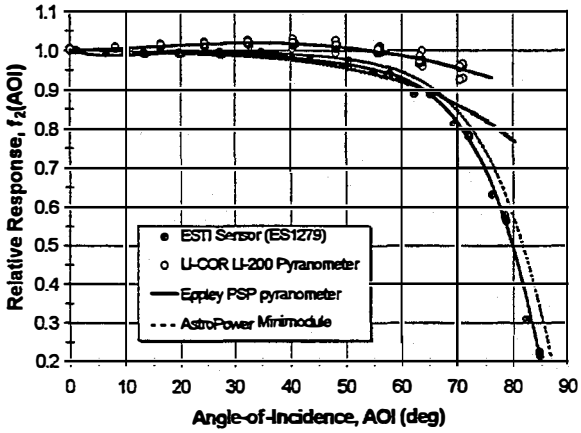

Fig. 3: Influence of solar angle-of-incidence (AOI) on the relative response of irradiance sensors.

5. OPERATING TEMPERATURE

The influence of temperature on a silicon-based irradiance sensor's response is typically small, resulting in less than 0.1 (%/°C) influence. If desired, compensation for the influence of temperature can be

accomplished by determining the device temperature and applying a temperature coefficient, α, which translates the measured response to a reference temperature, T_o. The temperature coefficient can be determined in the same manner routinely used for the calibration of photovoltaic reference cells [13].

Several methods can be used for determining the device temperature during operation, most of which add complexity and cost. Thermocouples can be attached to the device to directly measure the temperature. If two separate photovoltaic cells are used in the device, as in the ESTI Sensor and the AstroPower mini-module, predetermined cell parameters can be used to calculate device temperature by measuring the short-circuit current from one cell and open-circuit voltage from the other [4]. For some sensor designs, the ambient air temperature plus a small offset can be used as a reasonable estimate of the device temperature. For instance, the photodiode inside a LI-COR LI-200 pyranometer typically operates at a temperature about 6 °C above ambient temperature.

6. SENSOR CALIBRATION METHODS

The low-cost irradiance sensors evaluated are fundamentally photovoltaic devices, and as such, standardized test procedures can be applied to calibrate them by using a solar simulator or specific outdoor test conditions [13, 14]. By doing so, a "calibration constant," C_n, is obtained, for one of the two standardized AM_a=1.5 solar spectra, at a reference temperature, T_o. Our previous work indicated that it is also possible to separately address the spectral distribution of both the direct and diffuse components of solar irradiance [7]. However, for most practical applications of low-cost irradiance sensors, attempting to address diffuse spectral influence is probably not necessary. Standardized pyranometer calibration procedures [15, 16] can also be applied to photovoltaic irradiance sensors, as long as the $f_1(AM_a)$ and $f_2(AOI)$ functions are used to compensate for spectral and angle-of-incidence influences.

7. APPLICATION OF CORRECTIONS

Eqn. 1 gives the expression used for correcting the measured response, R, from a photovoltaic irradiance sensor for the influences of solar spectrum, angle-of-incidence, and temperature. Using the corrected response, an improved estimate for the total (broadband) irradiance, E_t, can be obtained.

$$E_t = \frac{R \cdot E_o \cdot [1 - \alpha \cdot (T - T_o)]}{C_n \cdot f_1(AM_a) \cdot f_2(AOI) \cdot} \quad (1)$$

where:

E_t = broadband solar irradiance, (W/m^2)
R = sensor response to irradiance, (mV)
E_o = reference irradiance level, 1000 (W/m^2)
C_n = calibration number for device, (mV)
α = temperature coefficient, (1/°C)
T = device temperature, (°C)
T_o = reference temperature, 25 (°C)
$f_1(AM_a)$ = dimensionless polynomial
$f_2(AOI)$ = dimensionless polynomial

To illustrate the effectiveness of these corrections, broadband irradiance measurements using Eppley thermopile-based instruments were compared directly to the corrected measurements from the low-cost devices. Table I gives the correction parameters required for the sensors addressed in this paper. The A_i coefficients in Table I are simply the constant coefficients associated with a polynomial fit of 4th or 5th order to the $f_1(AM_a)$ data previously shown in Fig. 2. Similarly, the B_i coefficients provide polynomial fits for the $f_2(AOI)$ data in Fig. 3. The temperature coefficient for each device is also in the table.

Table I: Coefficients required for making spectral, AOI, and temperature corrections to measurements using low-cost silicon-based irradiance sensors. Units for α are (1/°C).

Coef	LICOR	LICOR w/ coll.	ESTI Sensor	API minimod
A_o	.932	0.933	.928	.915
A_1	5.401E-2	5.115E-2	6.679E-2	9.282E-2
A_2	-6.319E-3	-6.473E-3	-1.440E-2	-2.819E-2
A_3	2.631E-4	4.918E-4	1.362E-3	3.230E-3
A_4	0	-1.557E-5	-4.855E-5	-1.354E-4
A_5	0	0	0	0
B_o	1	N/A	1	1
B_1	6.074E-5	N/A	-4.849E-3	-4.281E-3
B_2	1.357E-5	N/A	5.447E-4	4.379E-4
B_3	-4.504E-7	N/A	-2.208E-5	-1.657E-5
B_4	0	N/A	3.709E-7	2.703E-7
B_5	0	N/A	-2.289E-9	-1.669E-9
α	.00082	.00082	.00025	.00084

For clear-sky conditions, Fig. 4 graphically illustrates the result of applying the spectral and temperature corrections to global irradiance measurements using the LI-COR LI-200 pyranometer, on several different dates. On these clear days, the agreement between the LI-COR and Eppley PSP was very good, with differences less than ±3%. Without corrections, the LI-COR measurements were 10% high at low irradiance (high AM_a) and 3% low at high irradiance (low AM_a). Similar success has been achieved with corrections to the ESTI Sensor, the AstroPower minimodule, and the silicon reference cell.

For direct normal irradiance measurements, a LI-COR pyranometer was fitted with a plastic collimator tube. The tube was painted black on the inside, was fitted with internal baffles, and sized to provide the same acceptance angle as a typical thermopile pyrheliometer. For clear-sky conditions, the LI-COR with collimator agreed remarkably well with a secondary standard Eppley NIP pyrheliometer, within less than 0.5% over a 3-day test period. Additional testing of this device is in progress.

Overcast sky conditions and intermittent clouds present a larger challenge for all irradiance measuring devices, including thermopile pyranometers. Fig. 5 shows a comparison between the LI-COR and Eppley PSP, for overcast-sky test conditions of four different dates. The majority of corrected data agreed within less than ±5%; but without corrections, differences ranged from 15% high to 15% low. These results indicated that even

though the spectral and optical issues associated with overcast conditions are complex, reasonably accurate irradiance measurements can be achieved with low-cost devices.

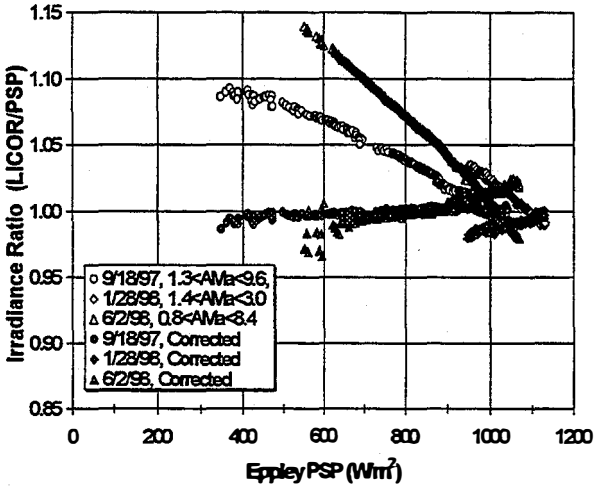

Fig. 4: For clear sky conditions, ratio of corrected irradiance measurements by LI-COR pyranometer to irradiance indicated by Eppley PSP thermopile pyranometer. Instruments mounted on solar tracker to eliminate AOI effects.

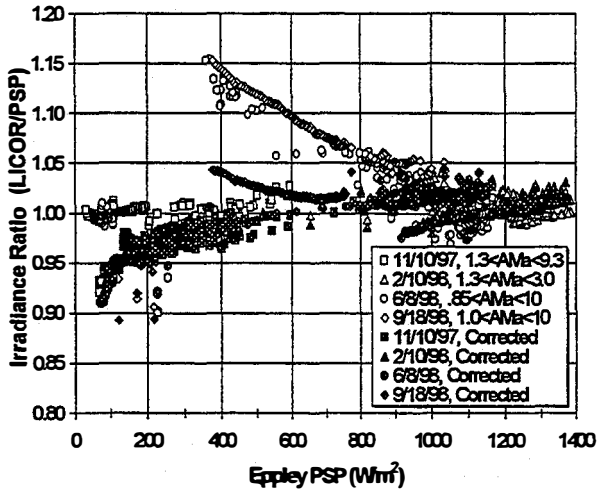

Fig. 5: For overcast sky conditions, ratio of corrected irradiance measurements by LI-COR pyranometer to irradiance indicated by Eppley PSP thermopile pyranometer. Instruments mounted on solar tracker to eliminate AOI effects.

8. CONCLUSIONS

By applying empirically determined corrections for the influences of solar spectrum, angle-of-incidence, and operating temperature, low-cost photovoltaic-based irradiance sensors can be used to provide accurate (±3%) instantaneous measurements of both the global solar irradiance and the direct normal irradiance. The results of this work will enable solar system engineers to more accurately and cost-effectively evaluate the performance of their systems.

Low cost is certainly an advantage. In addition, photodiode pyranometers are small, light weight, provide the opportunity for low-cost redundancy, can be calibrated quickly with a solar simulator, provide rapid response time, and can easily be modified to measure direct normal irradiance. Two-cell sensors with planar glass covers are potentially even lower cost than photodiode pyranometers, but have more sensitivity to angle-of-incidence. If cells and mechanical design match that of a photovoltaic array, two-cell sensors can also provide an estimate of array short-circuit current and operating temperature, as well as solar irradiance.

9. ACKNOWLEDGEMENTS

The authors would like to acknowledge test support from Jay Kratochvil (Sandia), collimator fabrication by Don Ellibee (Sandia), radiometric consultation from Phil Thacher (Sandia), collaborative research with Daryl Myers (NREL), and industrial collaborations with John Wurm (LI-COR) and John Cummings (AstroPower).

10. REFERENCES

[1] LI-COR Incorporated, www.licor.com.
[2] Kipp & Zonen, www.sci-tec.com.
[3] ASTM E 1040, American Society for Testing and Materials Standard.
[4] C. Helmke, W. Zaaiman, and H. Ossenbrink, 25th IEEE PVSC, 1997, pp.1267-1270.
[5] AstroPower Incorporated, www.astropower.com.
[6] D. L. King and D. R. Myers, 26th IEEE PVSC, 1997, pp.1285-1288.
[7] D. L. King, J. A. Kratochvil, and W. E. Boyson, 26th IEEE PVSC, 1997, pp.1113-1116.
[8] The Eppley Laboratory Inc., www.eppleylab.com.
[9] ASTM E 973.
[10] ASTM E 892.
[11] ASTM E 891
[12] J. Duffie and W. Beckman, ***Solar Engineering of Thermal Processes***, 2nd Edition, Wiley & Sons, 1991.
[13] ASTM E 1125.
[14] ASTM E 948.
[15] ASTM E 941.
[16] ASTM E 913.

RESULTS OF SANDIA NATIONAL LABORATORIES GRID-TIED INVERTER TESTING

G. A. Kern
Ascension Technology, Inc.
Boulder, CO, USA, 80301-2305
GKern79725@aol.com

R. H. Bonn, J. Ginn & S. Gonzalez
Sandia National Laboratories
Albuquerque, NM, USA, 87185-0753
rhbonn@sandia.gov

ABSTRACT: This paper proposes a definition for a "Non-Islanding Inverter". This paper also presents methods that can be used to implement such an inverter, along with references to prior work on the subject. Justification for the definition is provided on both a theoretical basis and results from tests conducted at Sandia National Laboratories and Ascension Technology, Inc.

Keywords: Islanding – 1: Grid-Connected – 2: Inverter – 3.

1. PREVIOUS TESTING AT SANDIA

During the summer of 1997 Sandia conducted a series of tests to investigate islanding of multiple inverters on a single 120-V ac circuit. It was found that for $P_{generation}/P_{load}$ ratios in the range of .8 to 1.2 the inverters frequently islanded for more than the minimum 2 seconds (times > 30 seconds were observed) that was required by some utility customers. It was also observed that the presence of a transformer in the islanded circuit resulted in a shorter islanding times (disconnect times of < .5 seconds) because the transformer requires nonlinear magnetizing current that most inverters could not supply.

The conclusions drawn from these tests were

- multiple inverters on a single 120 V ac circuit were not disconnecting quickly enough,
- the presence of a distribution transformer resulted in quicker disconnect,
- future tests should include other than purely resistive loads, so that a worst-case islanding conditions could be determined,
- the use of multiple inverters utilizing different anti-islanding techniques increased islanding times.

Sandia initiated a working group composed of US inverter manufacturers to address these issues, and sponsored the development of a new approach to prevent islanding through Ascension Technology, Inc. The results of this work are discussed below.

2. DEFINITIONS

2.1 Non-Islanding Inverter

A Non-Islanding Inverter is designed for utility interactive operation. In addition to over/under voltage and over/under frequency trip set points, this inverter includes the means to ensure unstable operation when the utility is not present. Under normal operating conditions, these inverters will not maintain an island condition. They should be designed so that their active methods are suitable for large numbers of units installed on utility distribution systems and so that their anti-islanding methods do not interact with each under normal operating conditions. A Non-Islanding Inverter meets the test for Non-Islanding Inverters defined below.

2.2 Normal Operating Conditions (NOC)

A section of a utility distribution system that has been disconnected from the rest of the utility is called an island. That island only consists of non-islanding inverters or other equivalent sources of generation and loads. Voltage source inverters or synchronous generators normally will not meet the definitions of a Non-Islanding Inverter. The total aggregate load present in the islanded section is modeled as a parallel RLC circuit, based upon the fundamental components of voltage and current.

An RLC circuit has a characteristic frequency, sometimes called resonant frequency, f_{res}. An RLC circuit also has a quality factor Q_{res}, or damping factor ζ, which is a measure of whether the circuit is highly resonant or well damped:

$$f_{res} = 1/(2\pi(LC)^{1/2}) \quad (1)$$

$$Q_{res} = 1/(2\zeta) = R(C/L)^{1/2}. \quad (2)$$

The authors propose that normal operating conditions (NOC) be defined as any island, or utility load in which the following is true:

$$Q_{res} < 5 \ (\zeta > 0.10) \text{ when } UF \le f_{res} \le OF \quad (3)$$

Q_{res} = any value when $f_{res} < UF$ or $f_{res} > OF$.

OF and UF are the over and under frequency trip set points. The values of 59.5 and 60.5 Hz are being considered for use in the United States in IEEE P929 [1], compared with the present settings in IEEE 929 of 59 and 61 Hz. Equations (1) and (2) can be rewritten in terms of

real load, P in kW, inductive load $KVAR_L$, and capacitive load $KVAR_C$. The variable, f_m , is the frequency at which $KVAR_L$ and $KVAR_C$ were measured, typically 60.00 Hz.

$$Q_{res} = (KVAR_L * KVAR_C)^{½} / P \quad (4)$$

$$f_{res} = f_m (KVAR_L / KVAR_C)^{½} \quad (5)$$

It takes five times as much reactance versus real power to exceed a Q_{res} of 5.0. In addition, the inductive reactance and capacitive reactance must be matched to within 1.65%. Real power being generated must be roughly matched to the real load in the island as well. It seems impractical that the aggregate load in an island would ever exceed NOC, let alone meet conditions likely for a run-on condition to occur in an island. Therefore inverters that meet the definition of Non-Islanding Inverter, should be considered to provide sufficient islanding protection. Equations (4) and (5) above may be used by utility engineers to determine if any feeder or section of a feeder operates outside of NOC.

2.3 A Non-Islanding Inverter Test

The Tests for Non-Islanding Inverters include all functions required in a Non-Islanding Inverter. They include verification that the over and under voltage and frequency trip set points operate according to national standard requirements or local utility requirements, e.g., IEEE 929. The inverter must be tested with an RLC load where $Q_{res} \approx 5$ when $UF < f_{res} < OF$.

To perform this test, connect an inductive load to the test circuit so that the inductive VARs are equal to five times the real load. Then adjust capacitance so that both the real and reactive power at the point of disconnect is zeroed out to within 1.0 % of the real power of the load in kVA. Under this abnormal loading condition, the average time to trip may not exceed the time specified in the interconnect standard. This test should be conducted ten (10) times to ensure proper operation.

This test may still be conducted if the inverter is designed to operate at a fixed (not variable) power factor other than unity. Voltage source inverters, or inverters which adjust reactive power output to stabilize frequency, such as stand alone 4 quadrant inverters, will probably not pass this test.

3. A NON-ISLANDING INVERTER METHOD

3.1 Sandia Frequency Shift (SFS)

The frequency-shift method, developed for this program, is an accelerated frequency drift with positive feedback. The positive feedback in the frequency control makes the island frequency unstable when there are no other mechanisms present to regulate island frequency. When the utility or other generators that control frequency are connected, the SFS unstable frequency controls do not affect frequency. When the utility is disconnected, the SFS method causes frequency to shift out of the frequency trip set points, causing the inverter to shut down.

When the island frequency starts to move up compared to average frequency, the reference frequency of the inverter moves up at a faster rate. When the island frequency moves down compared to average frequency, the reference frequency of the inverter moves down at a faster rate. In order to prevent out of phase operation between the inverter output and the utility during operation in the normal frequency window, the inverter reference signal is reset at every zero crossing of the voltage waveform. This method was implemented digitally in the inverter firmware.

3.2 Sandia Voltage Shift (SVS)

The voltage shift method is similar to the SFS method. Amplitude of the output current waveform is adjusted in response to utility voltage. When voltage increases, output current is increased. When voltage decreases, output current is decreased. The control signal is based upon the difference between average voltage as measured by an IIR (infinite impulse response) filter and cycle by cycle measurements of voltage. During normal operation, there will be some fluctuation of the utility voltage. If the positive feedback gain is chosen as 2.0, then when the utility voltage fluctuates by 1%, the output current will fluctuate by 2%. This method was suggested by two of the U.S. inverter manufacturers.[2][3].

3.3 Voltage and Frequency Trip Set Points

The voltage and frequency trip set points in Table I were used during all of the tests. In the final implementation tested, these trip set points were the only means for automatic shut down of the inverters.

Table I - Trip Set Points

	Set Point	Time to Operate (cycles)
Frequency	> 63.0 Hz	½
	> 60.5 Hz	5
	< 59.5 Hz	5
	< 57.0 Hz	½
Voltage	> 145 V	1
	> 132 V	100
	< 110 V	100
	< 60 V	5
	< 30 V	1

3.4 Unstable Frequency Trip

Additional means to shut down the inverter may be implemented to supplement the voltage and frequency trip set points. An unstable frequency trip method complements the SFS method. In many but not all tests, the SFS method appears to cause frequency to fluctuate more than normal. These frequency fluctuations occur during the island before the frequency has had time to move outside the frequency limits listed above.

In initial tests a df/dt computation was implemented on a cycle by cycle basis. The absolute value of frequency fluctuation was computed and then filtered with a digital IIR filter. The result was compared with a frequency rate of change of 0.09 Hz/cycle. The initial tests proved very effective, in most cases shutting down the inverter in fewer than 20 cycles. However, there appeared to be nuisance tripping due to the highly sensitive setting.

It is likely that some form of df/dt trip can be successfully implemented to complement the SFS method. Optimization of the IIR filter constants and the trip set point could be performed. This optimization is left for a later time. The present work concentrated on the development and testing of the SFS and SVS methods.

3.5 Prior Inverter Designs

The first inverter to incorporate islanding protection similar to SFS that the authors are aware of, was American Power Conversion Corporation's (APCC) SunSine2000[4]. The APCC inverter used a compensation circuit in the phase response filter portion of the phase lock loop. Far away from 60 Hz, the phase lock loop was stable, and allowed the unit to find and lock onto a 60 Hz voltage. At these frequencies an out-of-frequency trip caused utility disconnect. At frequencies closer to 60 Hz, positive feedback in the frequency control of the phase lock loop makes operation in an island unstable. Other work has been reported that shows excellent results in using similar methods with unstable frequency control [5] [6].

4. TEST RESULTS

4.1 The Significance of Magnetic Components

Before the inverter test results are presented, an important point must be made about magnetic components and their use in islanding testing. Magnetic components such as inductors, transformers and induction motors generally use core materials that are non-linear. In practice, most magnetic components are operated at voltages near their voltage ratings.

Measurements have been made on inductors and transformers to determine the extent to which the measured linearized inductance varied as a function of voltage. The effective inductance of the components tested was found to be highly non-linear in the region of their voltage ratings. The inductors were found to be more ideal (linear) when tested at voltages less than their rated voltage.

The reason this is significant is that in an island, if the voltage increases, then the effective inductance of the magnetic components in the loads will decrease. This will cause the island frequency to increase, so much so that the inverters will shut down on a frequency trip before a voltage trip is reached.

If magnetic components are used in islanding testing at voltages less than their rating, they may behave more like ideal inductors. This may result in longer island times than would occur from operating conditions in the field.

4.2 Defining a Motor Load

A single-phase induction motor with flywheel (grinding wheels) was used in the motor load tests. Capacitance was added to the motor circuit to correct the power-factor to unity. Real power was matched by adding resistance to the motor circuit or by controlling the inverter output power to match the losses in the motor.

The degree to which a motor load will cause an inverter to run-on after disconnect of the utility depends upon one thing: namely, the ratio of rotational kinetic energy stored in the motor to the energy loss per cycle of the motor. The energy losses are due to electrical losses and mechanical losses, such as friction. If there are other resistive loads attached to the same circuit, then they will also help to dissipate the stored energy in the motor.

Measuring the number of cycles (time) it takes for the voltage across the motor to drop by ½ is one means of quantifying the ratio of stored energy to power dissipation. This measurement is made with a power factor corrected motor and no resistive load. The number of cycles is measured with the inverter disabled and is measured from the time the power is disconnected. The authors propose that when motor loads are used in islanding tests, this measurement should be provided, since it is needed to properly specify the test setup. The number is needed so that subsequent test conditions can be reasonably compared. Although the authors do not bound this number, they do identify the numbers used in their tests.

4.3 Worst Case Loads

During the preliminary testing while the anti-islanding methods were being developed, two types of loads were found to result in the longest islanding times. These loads were RLC loads that had a resonant frequency of 60 +/-½ Hz and loads that contained induction motor loads with flywheels and capacitive VAR correction.

Preliminary tests included a wide range of generation to load ratios and load conditions. During the final testing, efforts concentrated on worst case load testing only.

4.4 Single Inverter Tests at Ascension Technology

Tests conducted at Ascension Technology were conducted with a single modified SunSine™300 inverter. A dc power supply was used to provide controlled input power. Since the tests were conducted in the manufacturer's facilities, it was possible to control the inverter through a diagnostics interface. This allowed a much faster test cycle time than is possible in field testing. The firmware installed was version 1.46 of the SunSine™300; it utilized the SFS and SVS methods for anti-islanding.

4.4.1 RLC Loads

The data in the following charts indicates the trip time for a series of tests. For example, in Figure 1, each line shows the change in voltage as a function of cycles (time) with the disconnect time occurring at the point where the line ends. The variable is the P_{gen}.

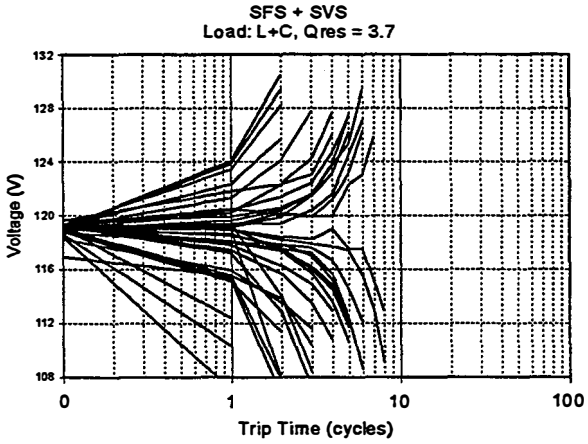

Figure 1. RLC load, voltage trajectories.

The goal of the RLC tests was to achieve the highest possible resonant load. For this set of tests, only inductance and capacitance were used for the load. The resistance in these tests comes from the losses in the inductor. In this case, Q_{res} = 3.7. During the tests, the inverter was operated over a range of power levels to get a range of generation/load ratios. Figure 1 shows the voltage trajectories for the various tests and Figure 2 shows the

frequency trajectories. Note that the voltage and frequency are unstable and not able to sustain an island. In this set of tests the inverter shut down within 10 cycles due to frequency trips.

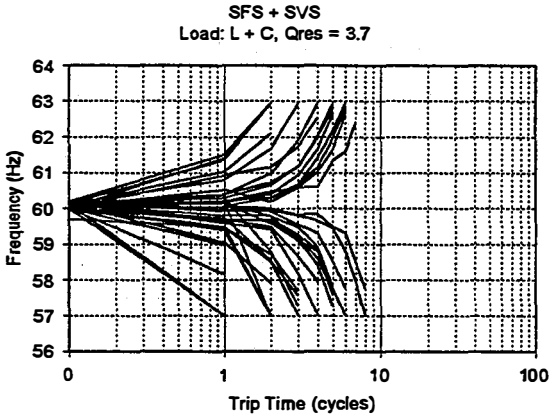

Figure 2. RLC load, frequency trajectories

The tests presented were the worst case tests. Other RLC load combinations were tested, but due to space limitations are not presented here.

4.4.2 Induction Motor Load Test

A ½-hp induction motor with grinding wheels attached was used for the next series of tests. Capacitance, 261 $VARS_C$, was added to correct the power factor of the motor to 1.00. No additional resistance was added to the test circuit, but the no-load losses of the motor were 119 watts.

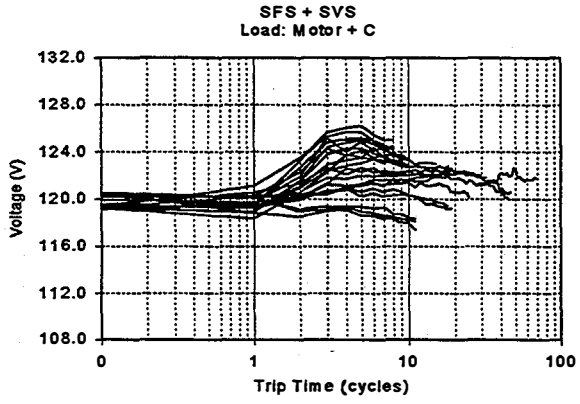

Figure 3. Voltage trajectories for power-factor corrected motor

Again, a range of inverter power levels was used to achieve a range of generation/load ratios. Figures 3 and 4 show the voltage and frequency trajectories of these tests. In these tests, no island exceeded 70 cycles and all anti-island shutdown actions were due to frequency trips. The power-factor corrected motor voltage dropped by ½ in 42 cycles after disconnect of all ac power.

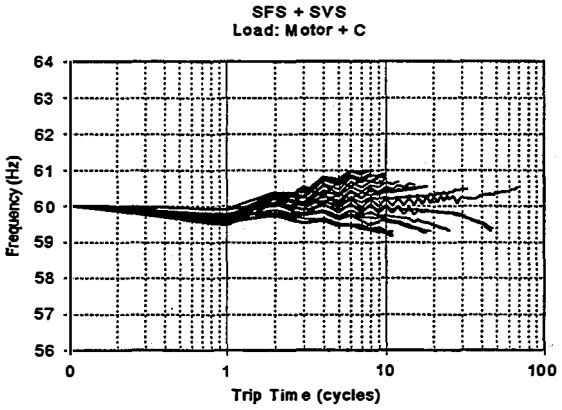

Figure 4. Frequency trajectories for power factor corrected motor

4.5 Test Results from Sandia National Laboratories

4.5.1 Configuration.

Three of the SunSine™ 300 AC Modules were connected in parallel with various loads on an outdoor field array for the evaluation of the SVS/SFS anti-islanding technology. The circuit configuration is shown in Figure 5. The various loads were configured, as required, for each test and included R, RL, RLC, RC, motor, and motors with capacitive VAR compensation. The ½-hp induction motor load included a flywheel, to maximize the back emf. Parameters varied included power factor, $P_{generation}/P_{load}$, and Q_{res}. One of the two contactors shown was used to interrupt the utility power. The location of the contactor used for a test was important because of the nonlinearity of the magnetizing currents in the transformer. When the primary contactor was opened, the distribution transformer remained in the islanded circuit. Since the inverters could not supply harmonics of 60 Hz, the presence of the transformer aided a rapid inverter disconnect.

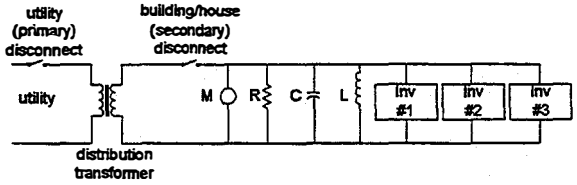

Figure 5: Diagram of circuit configuration

The test loads were selected based on input from previous testing at SNL and input from industry and utility sources. The "distribution used for those tests that included a primary side disconnect was unusually small (2 kVA) for a distribution transformer, however, that size was used to avoid overwhelming the three 300-watt, module-scale inverters. This approach resulted from a belief that two 4-kW inverters connected to a 15-kW distribution transformer would operate in a similar manner.

Initially the value of C in the RLC circuit was fixed at 301 micro-farads and L was selected to provide 60-Hz resonance. The value of R was then sized to dissipate power equal to that produced by the three parallel inverters. Matching inverter power output with the resistance was a necessary condition for islanding. Since the value of R also determines Q_{res}, it follows that in order to obtain high Q_{res}, the inverters were required to operate at

low power (Table II). Thus the circuit could be islanded only for particular combinations of inverter output power and RLC.

Q_{res}	Power (watts)
2	839
5	328
10	164
20	81

Table II: Dissipation power of R that produces Q_{res} for a fixed value of C = 301 μF

4.5.2 Test Results.

Two sets of data are presented. The first data set (Table III, column 2) was the result of extensive testing of the SFS anti-islanding approach. This was an extensive test series that evaluated a full range of load types. The results of the evaluation show that the approach was very successful for all cases with the exception of RLC loads resonant at 60 Hz. The run-on time is related to the circuit Q_{res}, with run-on times exceeding 6 cycles (approximately 100 milliseconds) for a Q_{res} in excess of 1.5. For $1.5 < Q_{res} < 7$, the inverter shut down in less than .5 seconds. For two of the higher Q_{res} cases (Q_{res} of 8 and 11), the circuit islanded until operator intervention

Load	SFS with df/dt	SFS & SVS
R	.068	no data
RL	.028	no data
RC	.036	no data
RLC	Island*, Q=11	.32, Q=7, 301 μF
motor	.228, C=67 μF	.53, C= 67 μF
RLC	no data	.78, Q>8, 641 μF

*operator intervention required

Table III: Islanding times in seconds

The second set of data (Table III, column 3) includes both the SFS and the SVS anti-islanding methods. This series of data was limited to the previously identified worst cases, RLC and a ½-hp induction motor load (with flywheel). The power-factor-corrected motor voltage dropped by ½ in 55 cycles after disconnect of all ac power. This series of tests shows that the islanding associated with RLC resonance has been eliminated; the longest time was .32 seconds for a $Q_{res} = 7$ case.

The last row of data results from doubling the available capacitance and hence increasing the allowable power output from the inverters for a specific value of Q_{res}. While this doubled the islanding time to .78 seconds, the islanding time is still not lengthy and the Q_{res} of 8 is very high.

Recalling the comparison to two 4-kW inverters connected to a 15-kVA transformer, it is clear that power matching any significant power output of these larger inverters would require a low value of resistance and thus a very low Q_{res} circuit. The conditions for which the inverters were found to island for the SVS/SFS anti-islanding approach are unlikely to occur in normal distribution circuits where Q_{res} is generally less than 5.

5. CONCLUSIONS

The combination of SVS and SFS were shown to be sufficient to achieve a Non-Islanding Inverter.

SVS and SFS are likely to work with high penetrations of distributed generators. They do not require synchronization between inverters to operate. They do not perform active perturbations on the utility system that can be undesirable or unworkable in high penetrations. Other active methods that try to perturb the utility and measure a coincident change in voltage or frequency will not work in high penetrations unless the perturbations are synchronized.

The SVS and SFS methods have been easy to implement. The only modifications necessary to implement them were changes in firmware in an existing inverter design. No changes to the hardware were required. This may not be true for all inverter designs.

Additional utility input is needed to determine an appropriate value of Q_{res} in the definition of normal operating conditions (NOC). The results presented here are far superior to results of other anti-islanding tests conducted over the last 18 months both at Ascension Technology, Inc. and at Sandia National Labs.

This work was supported by a consensus of U.S. inverter manufacturers. Although not guaranteed, it is likely that the results of this work will move the industry toward a defacto standard for anti-islanding in the United States. It is hoped that by sharing these results, similar methods would be considered in the international community.

6. REFERENCES

[1] ANSI/IEEE Draft Standard P929-1998, Draft 5, Recommended Practice for Utility Interface of Photovoltaic (PV) Systems.

[2] R. Wills, Advanced Energy Systems, discussions at Soltech 1998 with R. Bonn and G Kern.

[3] C. Freitas, Trace Engineering, discussions at Soltech 1998 with R. Bonn and G Kern.

[4] O. Wasynczuk, P.C. Krause, *Computer Modeling of the American Power Conversion Corporation Photovoltaic Power Conditioning System*, Sandia National Labs Contractor Report SAND87-7006, March 1987.

[5] T. Ambo, "Islanding prevention by Slip Mode Frequency Shift," IEA-PVPS-Task V, *Proceedings of the Grid Interconnection of Photovoltaic Systems Workshop*, Zurich, September 1997.

[6] Chihiro Okado, *Protection Device for Stopping Operation of an Inverter*, assignee K.K. Toshiba, U.S. Patent No. 5,493,485 Feb 20, 1996.

Sandia is a multiprogram laboratory operated by Sandia Corporation, a Lockheed Martin Company, for the United States Department of Energy under contract DE-AC04-94L85000.

FIELD EXPERIENCE WITH A NEW PERFORMANCE CHARACTERIZATION PROCEDURE FOR PHOTOVOLTAIC ARRAYS

David L. King, Jay A. Kratochvil, and William E. Boyson
Sandia National Laboratories
Albuquerque, New Mexico, 87185, USA
http://www.sandia.gov/pv/

ABSTRACT: As photovoltaic systems become larger and more numerous, improved methods are needed for testing and modeling their performance. Test methods that successfully separate the interacting, time-of-day dependent influences of solar irradiance, operating temperature, solar spectrum, and solar angle-of-incidence have now been developed. These test methods have resulted in a new array performance model that is reasonably simple, yet accurately predicts performance for all operating conditions. This paper describes the new model, outdoor tests required to implement it, results of field tests for five arrays of different technologies, and the evolution of the model into a numerical tool for designing and sizing photovoltaic arrays based on annual energy production.
Keywords: PV Array-1: Performance-2: Sizing-3

1. INTRODUCTION

The maturity of the photovoltaic industry can be gauged by its ability to design and size arrays for different applications and sites, and then to accurately and cost-effectively verify array performance in the field. These abilities will be fully manifested when they can be equitably applied to crystalline silicon, thin-film, and concentrator photovoltaic technologies, with array sizing based on either power or energy production. Current practices are not yet adequate to meet the needs of a growing PV industry.

Outdoor measurement procedures and photovoltaic performance models have evolved over many years in laboratories all over the world, and considerable effort has been spent by agencies such as ASTM, IEEE, and IEC toward standardizing test methods. Sandia has been conducting outdoor tests of module and array performance since 1976. Our work has recently led to new outdoor module testing procedures that effectively address the interacting influences mentioned in the abstract, thus providing the context for a performance model that works well for a wide range of outdoor operating conditions. Over the last three years, our module testing procedures and models have been adapted and applied with a high degree of success to a variety of large photovoltaic arrays.

Collaborative efforts are now in progress by Sandia, NREL, PVUSA, NIST, module manufacturers, system integrators, and developers of system design software to combine the best elements of different approaches. The goal of this collaboration is to arrive at consensus-based standards for testing and modeling of array performance.

2. ARRAY RATING CONDITIONS

Historically, the performance of photovoltaic (PV) cells and modules has been determined at a test condition called the "Standard Reporting Condition (SRC)," or commonly the "Standard Test Condition (STC)" [1, 2].

The SRC test condition was originally intended to mimic actual outdoor conditions, but was also modified to facilitate indoor testing procedures. As a result, the irradiance level, 1000 W/m^2, and the two "standard" solar spectral distributions [3, 4] are representative of typical clear-sky operating conditions, but the 25°C cell temperature is not. Outdoor operating conditions commonly result in cell temperatures closer to 50°C. Unfortunately, the difference between actual operating temperatures and the SRC temperature has often been a source of array design errors, marketing difficulties, and dissatisfied customers.

In lieu of a new standard, system engineers have attempted in different ways to determine array or system performance for "actual operating conditions" [5, 6].

2.1 PVUSA Test Conditions (PTC)

A government and utility sponsored activity called "Photovoltaics for Utility Scale Applications (PVUSA)" has developed and implemented a test method that relates photovoltaic system performance to the prevailing environmental conditions; solar irradiance, ambient temperature, and wind speed [5]. This method has been applied to a variety of PV technologies, can be used to determine either dc or ac performance, and uses a simple regression model. The limitations of the method include the requirement for continuous data acquisition over an extended period of time, relatively poor accuracy of the model for low irradiance levels, and it does not explicitly address the systematic influences of solar spectral and angle-of-incidence variation [7].

2.2 New Array Rating Methodology

At the risk of introducing additional confusion, the authors would like to propose an array rating methodology that combines a specific "array rating condition" (ARC) with a method for calculating performance at other "specified operating conditions" (SOC). This approach should meet the needs of the system owner who may have a variety of specific operating conditions of importance. In addition, the specific array rating condition chosen

Sandia is a multiprogram laboratory operated by Sandia Corporation, a Lockheed Martin Company, for the U. S. Department of Energy under contract DE-AC04-94AL85000.

should be consistent with traditional PV testing standards and meets the needs of the metrologist tasked with field performance verification. The ARC is the same as the traditional standard reporting condition (SRC) with the exception that the cell temperature used as a reference, T_o, is raised to a value more representative of actual operating conditions for the module being evaluated.

Ideally, the array rating methodology should not only provide a rating at the ARC and performance estimates at a variety of SOC, but also provide the information required to accurately estimate the annual energy production from the PV system. The results in this paper describe our progress toward this ideal goal.

3. NEW PV PERFORMANCE MODEL

Photovoltaic array performance parameters, for an arbitrary operating condition, can be described using Eqns. (1-5). The variables defining the operating condition are irradiance, cell temperature, absolute air mass, and solar angle-of-incidence on the array. The equations for short-circuit current (I_{sc}), maximum-power current (I_{mp}), open-circuit voltage (V_{oc}), and maximum-power voltage (V_{mp}) provide the four primary parameters from which others (fill factor, maximum power, efficiency) can be calculated. Eqns. (1, 3, and 4) result in linear relationships closely related to the fundamental electrical characteristics of cells in the module. Eqn. (5) uses a second order relationship for V_{mp} that implicitly contains the influence of factors such as series resistance (R_s) and non-ideal shunting behavior (R_{sh}, n_2) of cells at low irradiance levels. Two additional empirical relationships, $f_1(AM_a)$ and $f_2(AOI)$, are used to compensate for the influences of the solar spectrum and solar angle-of-incidence (AOI) on the short-circuit current.

A fundamental premise of this performance model is that the I_{mp}, V_{mp}, and V_{oc} of a cell, module, or array are predictable parameters when described as functions of I_{sc} and cell temperature (T_c) only. In other words, for a given I_{sc} and T_c, the shape of the current-voltage (I-V) curve will be the same for any solar spectrum and angle-of-incidence. When this premise is valid, the performance characterization of an array becomes simply a matter of first determining the short-circuit current, I_{sco}, at the array rating condition. Then the other three performance parameters are measured and related to I_{sco} using the "effective irradiance" term (E_e) in Eqn. (2). The concept of "effective irradiance" is used in ASTM methods [8] to account for the fact that photovoltaic devices do not respond to all wavelengths of light contained in the solar spectrum. As used in this paper, the term is expanded to include not only the solar spectral influence, but also the optical effects related to solar angle-of-incidence. Thus, the effective irradiance, E_e, in Eqn. (2) depends on both the solar spectrum and the solar angle-of-incidence.

One advantage of this approach is that compensating for the effects of solar spectrum and solar angle-of-incidence can be accomplished by adjusting only the I_{sc} parameter in Eqn. (1). In addition, the model is easily adapted, if necessary, to special cases. For instance, if a module requires a second spectral correction function to more closely model I_{mp} at low irradiance (high AM_a) conditions, it can be applied to E_e in Eqn. (3).

$$I_{sc}(E, T_c, AM_a, AOI) = (E/E_o)\, f_1(AM_a)\, f_2(AOI)\, \{I_{sco} + \alpha_{Isc}(T_c - T_o)\} \quad (1)$$

$$E_e = I_{sc}(E, T_c = T_o, AM_a, AOI) / I_{sco} \quad (2)$$

$$I_{mp}(E_e, T_c) = C_0 + E_e \{C_1 + \alpha_{Imp}(T_c - T_o)\} \quad (3)$$

$$V_{oc}(E_e, T_c) = V_{oco} + C_2 \ln(E_e) + \beta_{Voc}(T_c - T_o) \quad (4)$$

$$V_{mp}(E_e, T_c) = V_{mpo} + C_3 \ln(E_e) + C_4\{\ln(E_e)\}^2 + \beta_{Vmp}(T_c - T_o) \quad (5)$$

Where:
E = plane-of-array (POA) solar irradiance using broadband (thermopile) pyranometer measurement corrected for angle-of-incidence sensitivity, W/m^2
E_e = "effective" irradiance, dimensionless, or "suns"
$\ln(E_e)$ = natural logarithm of E_e
E_o = reference "one sun" irradiance on array, 1000 W/m^2
AM_a = absolute air mass, dimensionless
AOI = solar angle-of-incidence on module, degrees
T_c = temperature of cells inside module, °C
T_o = reference temperature for cells in module, e.g. 50 °C
$f_1(AM_a)$ = empirically determined "AM_a-Function" describing solar spectral influence on I_{sc}
$f_2(AOI)$ = empirically determined "AOI-Function" describing angle-of-incidence influence on I_{sc}
$I_{sco} = I_{sc}(E = 1000$ W/m^2, $AM_a = 1.5$, $T_c = T_o$ °C, AOI = 0°)
$I_{mpo} = I_{mp}(E_e = 1, T_c = T_o$ °C)
$V_{oco} = V_{oc}(E_e = 1, T_c = T_o$ °C)
$V_{mpo} = V_{mp}(E_e = 1, T_c = T_o$ °C)
$\alpha_{Isc} = I_{sc}$ temperature coefficient, A/°C
$\alpha_{Imp} = I_{mp}$ temperature coefficient, A/°C
$\beta_{Voc} = V_{oc}$ temperature coefficient, V/°C
$\beta_{Vmp} = V_{mp}$ temperature coefficient, V/°C
C_0, C_1 = empirical coefficients relating I_{mp} to irradiance
C_2 = empirical coefficient relating V_{oc} to irradiance
C_3, C_4 = empirical coefficients relating V_{mp} to irradiance

4. MODULE PERFORMANCE

The first step toward achieving a comprehensive array performance characterization is to accurately determine the performance characteristics of the modules used in the array. This section summarizes outdoor test procedures that can be used for this process.

4.1 Solar Irradiance Measurements

Historically, one of the largest contributors to the uncertainty in field measurements of array performance has been error in measurements of the solar irradiance. The irradiance measurements are used to translate array performance data to a reference irradiance level. So, errors in irradiance measurements translate directly into errors in array performance ratings. Particular attention must be paid to the angle-of-incidence sensitivity of the pyranometer being used, and if silicon-based pyranometers are used, then solar spectral influence must

be addressed [9]. With appropriate correction for these systematic influences, solar irradiance measurements with a total uncertainty of less than 3% should be achievable using typical instruments.

4.2 Temperature Coefficients

Two temperature coefficients, one for current and one for voltage, are currently used in ASTM standard methods for translating measured current-voltage (I-V) curves from one temperature to another [2]. Our experience has indicated that improved accuracy in performance modeling can be achieved by recognizing that the temperature coefficients for current and voltage at the maximum-power point can differ significantly from those obtained at short-circuit and open-circuit conditions [10]. As a result, the performance model previously presented uses four separate temperature coefficients. The common practice of using a single temperature coefficient for power, or efficiency, should also be avoided.

4.3 Solar Spectral Influence

Compensation for the influence of time-of-day dependent solar spectral variation was achieved by using an empirically determined function. The method for determining this function was documented elsewhere [11]. This empirical function, $f_1(AM_a)$, related solar spectral influence on I_{sc} to the absolute air mass (AM_a). Fig. 1 illustrates the empirical relationships measured for several commercial PV modules, including crystalline and multi-crystalline silicon (c-Si and mc-Si), amorphous silicon (a-Si), silicon film, and cadmium telluride (CdTe). Experience has indicated that, for clear sky conditions, the $f_1(AM_a)$ function is widely applicable to different sites. The coefficients, A_i, in Table I provide polynomial fits to the measured data shown in Fig. 1.

For further clarification, "air mass" is the term used to describe the path length that sunlight traverses through the atmosphere before reaching the ground. When air mass is adjusted for the altitude of the site, it is called the "absolute" air mass (AM_a). AM_a is readily calculated knowing the zenith angle of the sun and the site altitude [12], as indicated in Eqns. (6-8). At sea level, AM_a=1 when the sun is directly overhead, AM_a=1.5 when the sun's zenith angle is 48 degrees, and AM_a of about 10 is achieved at sunrise and sunset. As AM_a increases, the spectral distribution of sunlight shifts to longer wavelengths, becoming more "red."

$$AM = \left[\cos(Z_s) + 0.5057 \cdot (96.080 - Z_s)^{-1.634}\right]^{-1} \quad (6)$$

$$AM_a = \frac{P}{P_o} \cdot AM \quad (7)$$

$$\frac{P}{P_o} \approx e^{(-.0001184 \cdot h)} \quad (8)$$

Where:

AM = atmospheric optical air mass

AM_a = absolute (pressure corrected) air mass

Z_s = zenith angle of the sun, degrees

P = local atmospheric pressure, mmHg

P_o = standard pressure at sea level, 760 mmHg

h = site altitude, m

The concept of the empirical $f_1(AM_a)$ function can be understood by examining the standard ASTM method [13] for calculating the "spectral mismatch correction" parameter, M, shown mathematically in Eqn. (9).]. When a thermopile (broadband) pyranometer is used as the reference irradiance sensor, the simpler Eqn. (10) results. Our outdoor test procedure for determining $f_1(AM_a)$ provided the method used for directly measuring the spectral correction parameter as it continuously varied over the course of a day [11]. Thus, $f_1(AM_a)$ was determined by directly measuring broadband irradiance and module short-circuit current over the a day, without the need for numerical integration or spectral irradiance measurements. The $f_1(AM_a)$ function was normalized to a value of one at the time of day when AM_a=1.5 occurred.

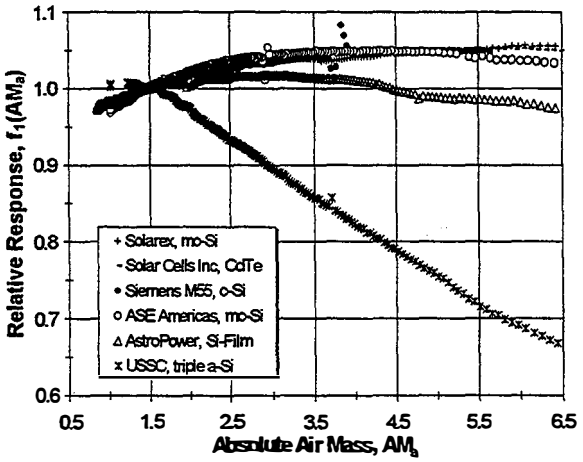

Fig. 1: Measured effect of solar spectral variation (AM_a) on the relative response (short-circuit current) of different commercial modules, for clear sky conditions.

Table I: Polynomial coefficients required for modeling spectral and AOI influence on module performance.

Cof	ASE300 (EFG-Si)	SM55 & MSX120	AP8225 (Si-Film)	SCI (CdTe)	US64 (a-Si)
A_o	.875	.928	.915	.891	.976
A_1	1.221E-1	6.796E-2	9.282E-2	9.907E-2	8.250E-2
A_2	-3.019E-2	-1.507E-2	-2.819E-2	-2.239E-2	-5.707E-2
A_3	3.104E-3	1.587E-3	3.230E-3	2.238E-3	8.242E-3
A_4	-1.187E-4	-6.377E-5	-1.354E-4	-8.868E-5	-3.919E-4
B_o	1	1	1	1	1
B_1	-2.438E-3	-2.438E-3	-2.438E-3	-2.438E-3	-5.020E-3
B_2	3.103E-4	3.103E-4	3.103E-4	3.103E-4	5.842E-4
B_3	-1.246E-5	-1.246E-5	-1.246E-5	-1.246E-5	-2.300E-5
B_4	2.112E-7	2.112E-7	2.112E-7	2.112E-7	3.826E-7
B_5	-1.359E-9	-1.359E-9	-1.359E-9	-1.359E-9	-2.310E-9

$$M = \frac{\int_a^b E(\lambda)R_t(\lambda)\cdot d\lambda}{\int_c^d E(\lambda)R_r(\lambda)\cdot d\lambda} \cdot \frac{\int_c^d E_o(\lambda)R_r(\lambda)\cdot d\lambda}{\int_a^b E_o(\lambda)R_t(\lambda)\cdot d\lambda} \quad (9)$$

$$M \approx \frac{Isc_t}{E^*} \cdot \frac{E_o^*}{Isc_{to}} = f_1(AM_a) \quad (10)$$

Where:

M = spectral correction parameter

λ = wavelength (nm)
$E(\lambda)$ = solar spectral irradiance present during test,
$E_o(\lambda)$ = reference solar spectral irradiance at prevailing AM_a=1.5 condition,
$R_t(\lambda)$ = spectral response of test module at reference temperature,
$R_r(\lambda)$ = spectral response of reference thermopile pyranometer,
a,b = integration limits defined by photovoltaic module,
c,d = integration limits defined by reference pyranometer,
E_o^* = total irradiance indicated by thermopile (broadband) pyranometer for normal incidence, AM_a=1.5 condition,
E^* = total irradiance indicated by thermopile pyranometer for prevailing test spectrum, normal incidence,
Isc_o = short-circuit current from test module at reference temperature, normal incidence, AM_a=1.5 condition,
Isc_t = measured short-circuit current at reference temperature, normal incidence, prevailing test spectrum.

4.4 Angle-of-Incidence Influence

A module's response to the direct (beam) irradiance component is influenced by the cosine of the solar angle-of-incidence, AOI, and by the optical characteristics of its front surface. The response of the module to uniformly diffuse irradiance can be assumed to have no dependence on angle-of-incidence. Algorithms for calculating the solar angle-of-incidence for both fixed and solar-tracking modules are documented elsewhere [14]. The optical influence of the module's front surface, which is typically glass, sometimes a polymer sheet, can be described by another empirically determined function, $f_2(AOI)$. The outdoor test procedure for determining the $f_2(AOI)$ function was also documented elsewhere [11]. Basically, the test procedure involves measuring the I_{sc} while moving the module through a range of AOI. Simultaneous measurements of diffuse solar irradiance (E_{diff}) in the plane of the module and direct normal irradiance (E_{dni}) provide $f_2(AOI)$, as given by Eqn. (11).

$$f_2(AOI) = \frac{\frac{E_o}{I_{sc\,o}} \cdot I_{sc}(AM_a = 1.5, T = T_o) - E_{diff}}{E_{dni} \cdot \cos(AOI)} \qquad (11)$$

Fig. 2 illustrates the relative response of several commercial flat-plate PV modules versus the solar angle-of-incidence. With the exception of the amorphous silicon module from United Solar Systems Corporation (USSC), all the modules had a glass front surface. The front surface of the USSC module was a stippled sheet of Tefzel™ polymer, and its AOI characteristics differed somewhat from the glass modules. It appears that a single $f_2(AOI)$ function may be applicable for most modules with glass front surfaces. The coefficients, B_i, for the polynomial fits shown in Fig. 2 are given in Table I.

4.5 Module Operating Temperature

Often during PV system design and array sizing, it is necessary to estimate module operating temperature from tabulated environmental parameters; ambient temperature, wind speed, and POA irradiance. The thermal environment that dictates module operating temperature is complex, also being influenced by wind direction and module design, orientation, and mounting structure. However, a simple model has been found to provide reasonably accurate estimates (±5°C) of module back surface temperature for typical flat-plate modules, near thermal equilibrium, mounted in an open rack structure. Eqn. (12) gives the simple relationship used. Roof-integrated modules with minimal convective cooling from the rear surface may operate at temperatures 10 to 20 °C above those in open racks.

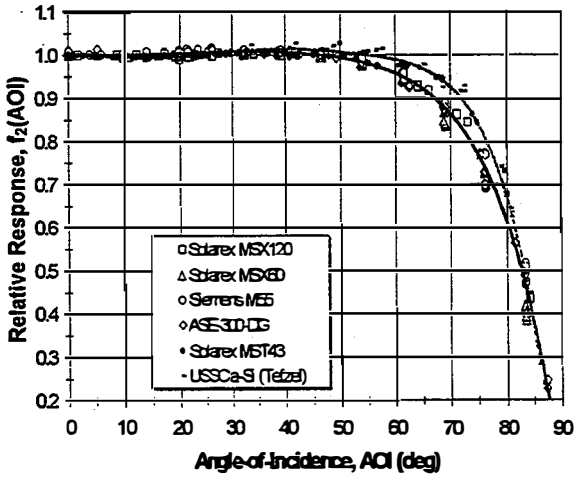

Fig. 2: Measured effect of angle-of-incidence (AOI) variation on the response (short-circuit current) of different commercial photovoltaic modules.

Module performance should actually be related to cell temperature inside the module, which is typically warmer than the back surface. The temperature difference between the cell and the back surface (ΔT) depends on the solar irradiance level and the type and thickness of the materials used for the substrate of the module. Eqn. (13) gives a simple relationship between module back-surface temperature and cell temperature. Table II gives the parameters found to give good agreement with measured temperatures for two different module types.

$$T_m = \frac{E}{E_o} \cdot \left\{ T_1 \cdot e^{b \cdot WS} + T_2 \right\} + T_a \qquad (12)$$

Where:
T_m = back-surface module temperature, °C
T_a = ambient temperature, °C
E = solar irradiance on module, W/m^2
E_o = reference irradiance, 1000 W/m^2
WS = wind speed measured at standard 10-m height, m/s
T_1= empirical coefficient determining upper temperature limit at low wind speeds
T_2 = empirical coefficient determining lower temperature limit at high wind speeds
b = empirical coefficient determining the rate that module temperature drops as wind speed increases

$$T_c = T_m + \frac{E}{E_o} \cdot \Delta T \qquad (13)$$

Table II: Empirical coefficients for module and cell temperature estimation, for two typical module designs.

Type	T_1 (°C)	T_2 (°C)	b	ΔT (°C)
Glass/cell/glass	25.0	8.2	-.112	2
Glass/cell/Tedlar	19.6	11.6	-.223	3

1. ARRAY TEST PROCEDURE

Once performance characteristics of individual modules have been determined, array performance characterization becomes relatively straight forward. The spectral and angle-of-incidence characteristics can be applied directly for an array of modules. Module temperature coefficients are simply scaled in a manner consistent with the series/parallel configuration of modules in the array. Field tests are conducted by measuring current-voltage (I-V) curves for the array at intervals during one clear day from sunrise until sunset. Simultaneous measurements of module temperature and plane-of-array solar irradiance using an AOI-corrected thermopile pyranometer are also recorded. Analysis of the field measurements results in the coefficients (C_0, C_1, C_2, C_3, C_4) required to implement the performance model in Eqns. (1-5). When the model is applied to array data, the coefficients implicitly contain the influences of module mismatch, wiring losses, bypass diodes, and blocking diodes.

5.1 Test Results for Arrays

To illustrate the accuracy and versatility of our new performance model, the results of field measurements and analysis for five arrays of different technologies will be presented. These systems included a 25-kW ASE Americas array with EFG-silicon cells, a 1.3-kW United Solar Systems array with triple-junction a-Si cells, a 17-kW AstroPower array with Si-Film™ cells, a 11-kW Solar Cells Inc. array with CdTe cells, and a 75-kW Solarex array with mc-Si cells. Figs. 3-7 graphically illustrate the results from our field measurements, after application of $f_1(AM_a)$, $f_2(AOI)$, and temperature coefficients determined at the individual module level. In order to illustrate all the arrays in the same figures, the measured data for each parameter was "normalized" by dividing by its value at the array rating condition (ARC). In general, the new method has worked quite well, giving good agreement between measured and modeled performance over a wide range of operating conditions. For the five arrays presented, agreement between measured and modeled power was typically within less than 3%, as illustrated in Fig. 7.

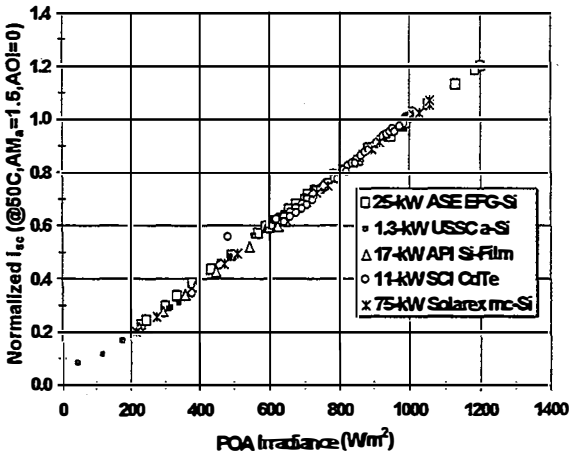

Fig. 3: Normalized I_{sc} versus solar irradiance for five PV arrays of different technologies, new performance model.

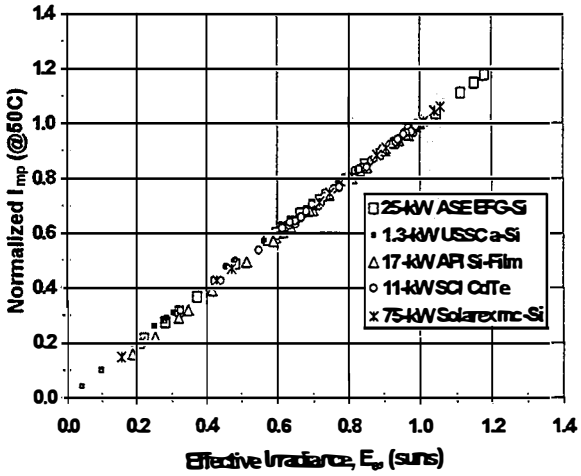

Fig. 4: Normalized I_{mp} versus effective irradiance for five arrays of different technologies, new performance model.

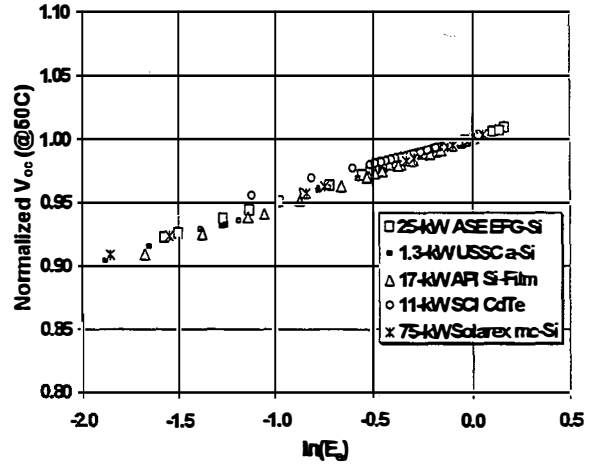

Fig. 5: Normalized V_{oc} versus logarithm of effective irradiance for five arrays, using new performance model.

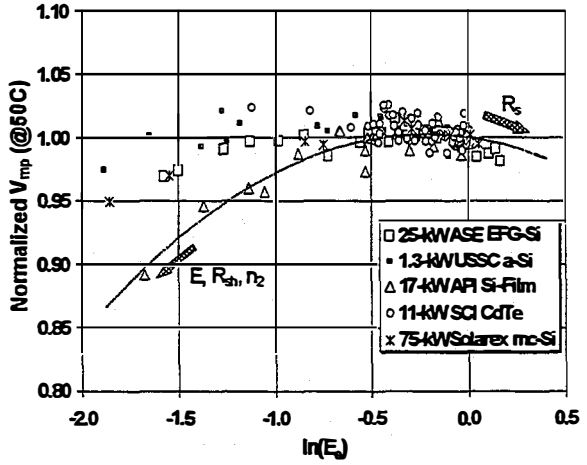

Fig. 6: Normalized V_{mp} versus logarithm of effective irradiance for five arrays, using new performance model.

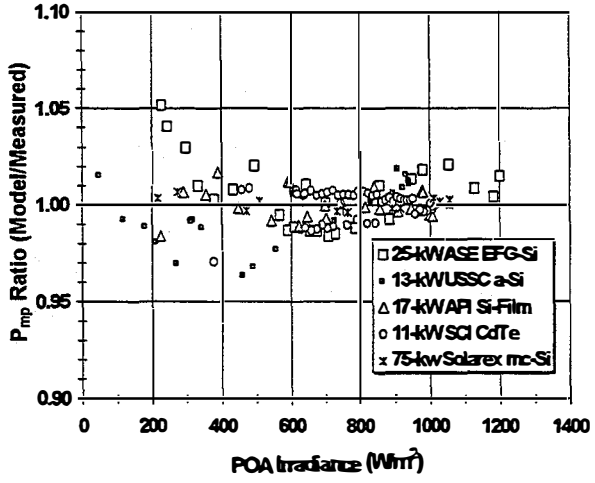

Fig. 7: Modeled P_{mp} divided by measured P_{mp} versus solar irradiance for five arrays, using new performance model.

5.2 Array Sizing for Energy Production

As a final illustration of the application of our array performance modeling methodology, Fig. 8 illustrates the predicted daily energy production (dc and ac) by month for a horizontal, roof-mounted, 100-kW array of ASE Americas modules, located in Hawaii. The array was connected to the local utility through a Trace Technologies inverter. Prior to operation, "Typical Meteorological Year (TMY2)" data were used to define the hourly average solar resource and ambient conditions, and our performance prediction accounted for the influences of irradiance, solar spectrum, AOI, calculated operating temperature, inverter efficiency, and other balance-of-system losses. After the system is operational, measured power production will be compared to predicted power providing a continuous assessment of array performance.

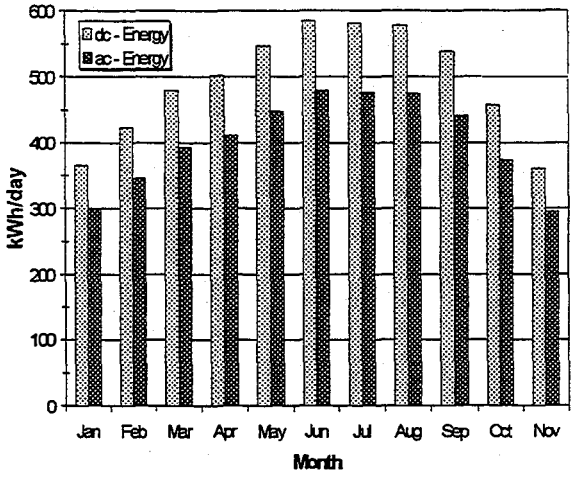

Fig. 8: Calculated daily energy production (dc and ac) for a 100-kw, roof mounted, ASE Americas array in Hawaii.

6. CONCLUSIONS

Our work has provided a significant improvement in the field testing methods and modeling procedures currently used for characterizing photovoltaic module and array performance. The array testing and modeling procedures have now been validated through field tests of 17 different arrays of nine different technologies. The new methods will improve industry's abilities to optimize system designs, to rate or specify array performance, and to monitor system performance. With industry involvement, the new modeling techniques are evolving into numerical tools for sizing systems based on either power at a specific operating condition or annual energy production.

7. ACKNOWLEDGEMENTS

The authors would like to acknowledge valuable technical interactions with Chuck Whitaker and Tim Townsend (Endecon), Tim Ball (APC), Steven Durand (FSEC), Andy Rosenthal (SWTDI), John Wohlgemuth and Jean Posbic (Solarex), Moneer Azzam (ASE Americas), Bob Hammond (ASU), Alain Chuzel (Photocomm), Dan Shugar (PowerLight), Doug Danley (Orion), Howard Wenger (Pacific Energy), and Bill Caszeta (PVRI).

8. REFERENCES

[1] ASTM E 1125, "Calibration of Silicon Non-Concentrator Terrestrial Photovoltaic Reference Cells Using a Tabular Spectrum."
[2] ASTM E 1036, "Testing Electrical Performance of Nonconcentrator Photovoltaic Modules and Arrays Using Reference Cells."
[3] ASTM E892, "Terrestrial Solar Spectral Irradiance at Air Mass 1.5 for a 37° Tilted Surface."
[4] ASTM E891, "Terrestrial Direct Normal Solar Spectral Irradiance for Air Mass 1.5."

[5] R. N. Dows, et.al., "PVUSA Procurement, Acceptance, and Rating Practices for Photovoltaic Power Plants," PG & E Co. Report #95-30910000.1, Sept. 1995.
[6] K. Bucher, et. al., "RRC Module Energy Rating: A Module Strategy," 26th IEEE PVSC, 1997, pp.1187-1191.
[7] C. M. Whitaker, et. al., "Application and Validation of a New PV Performance Characaterization Method," *26th IEEE PVSC*, 1997, pp. 1253-1256.
[8] ASTM E 1039-85, "Calibration on Non-Concentrator Terrestrial PV Reference Cells Under Global Irradiation."
[9] D. King, W. Boyson, and B. Hansen, "Improved Accuracy for Low-Cost Irradiance Sensors," this conf.
[10] D. L. King, J. A. Kratochvil, and W. E. Boyson, "Temperature Coefficients for PV Modules and Arrays: Measurement Methods, Difficulties, and Results," *26th IEEE PVSC*, 1997, pp.1183-1186.
[11] D. L. King, J. A. Kratochvil, and W. E. Boyson, "Measuring Solar Spectral and Angle-of-Incidence Effects on PV Modules and Solar Irradiance Sensors," *26th IEEE PVSC*, 1997, pp.1113-1116.
[12] F. Kasten and A. Young, *Applied Optics*, 28, pp.4735-4738 (1989).
[13] ASTM E973, "Determination of the Spectral Mismatch Parameter Between a Photovoltaic Device and a Photovoltaic Reference Cell."
[14] J. A. Duffie and W. A. Beckman, ***Solar Engineering of Thermal Processes***, 2nd Edition, Wiley & Sons, 1991.

DEVELOPMENT OF INTERIM TEST METHODS AND PROCEDURES FOR DETERMINING THE PERFORMANCE OF SMALL PHOTOVOLTAIC SYSTEMS

P. McNutt, B. Kroposki, R. Hansen, K. Algra, R. DeBlasio
National Renewable Energy Laboratory
1617 Cole Boulevard
Golden, Colorado 80401 USA

ABSTRACT: The National Renewable Energy Laboratory (NREL) is developing tests and procedures that will determine if the configuration of a small photovoltaic (PV) system is suitable for its intended use, and if the system will perform as specified. An overview of these procedures is presented in this paper. Development of standard test procedures will allow designers, manufacturers, system integrators, users, and independent laboratories to assess the performance of PV systems under outdoor prevailing conditions. An NREL Technical Report detailing the procedures is under way, and the IEEE Standards Coordinating Committee 21 (SCC21) has established a project on this subject. The work will be submitted to the IEEE SCC21 and International Electrotechnical Commission Technical Committee 82 (IEC TC82) for consideration as a consensus standard. Certification bodies such as PowerMark and PV Global Approval Program (PVGAP) may adopt the IEC and IEEE documents when testing systems. Developing standardized test methods and procedures at NREL to evaluate the outdoor performance of PV systems will encourage product quality and promote PV standards development. Standardized tests will assure people that PV systems will perform as specified for their intended applications. As confidence in PV systems increases, the successful commercialization of PV will grow internationally.
Keywords: Photovoltaic Systems – 1: Test Procedures – 2: System Performance - 3

1. BACKGROUND

Selection and validation, through type testing, of the appropriate design and construction of a PV system and its subsystems is a critical area of concern with regard to meeting and optimizing performance, operation and maintenance (O&M), reliability, and safety. Over- or undersizing a system, inadequate subsystem and component selections, and improper interface matching have been concerns over the years with regard to meeting performance requirements and cost. Failure or reduced performance of systems due to exceeding the operational limits of subsystems and components within the system has led to misunderstandings regarding why the system failed to meet its application load requirements. Exaggerated performance expectations and marginal design limits have also led to failure in parts of the system and have increased O&M system cost. Users must feel assured that a system will meet its intended design and application load requirements. This barrier to acceptance of PV systems can be reduced and eliminated with the proper tools one can reference for design and performance verification.

The test document will fill a testing void and provides the catalyst and focus for establishing the technical foundation and bridging the institutional barriers needed to reduce uncertainty that a system's performance will be what its designers and builders claim. The need for a document was recently made more apparent with the initiation of a PVGAP at the international level and is in response to concerns that PV systems being fielded must meet performance standards and that these standards include system-level performance type tests. The title of the test procedure is prefaced with the word "interim" because experience in using the procedures is needed before a consensus standard is developed and accepted by the PV community through its activities with the IEEE SCC21 and IEC TC82 national and international standards-making bodies. Both entities have initiated projects to develop test standards and will need the technical basis and validation of test procedures such as those presented in this document before a consensus is achieved by the PV community.

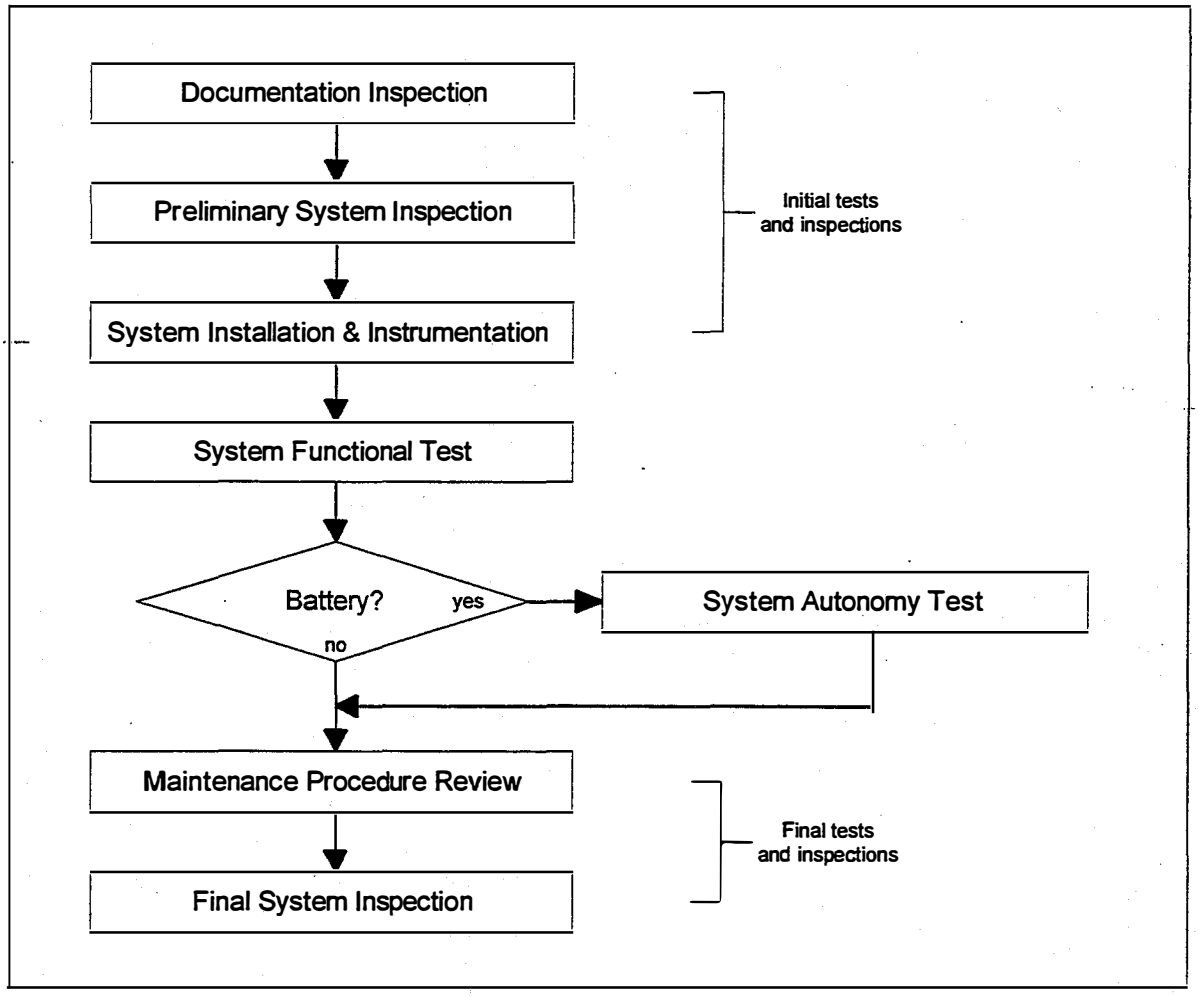

Figure 1: Small PV systems test sequence

2. OVERVIEW OF THE TEST PROCEDURES

The test procedures NREL is developing are intended to evaluate the performance of stand-alone and utility-tied PV systems up to 5 kW. One complete system is required for testing. The test sequence is shown in Figure 1. The test system should include documentation and all parts for installation. All measurements, notes, and comments are compiled into a test report. The procedures can be broken down into four areas: initial system tests and inspections; system functional test; system autonomy test; and final system tests and inspections. The procedures do not address component or system reliability, safety, or compliance to mechanical or electrical codes.

2.1 Initial Tests and Inspections

Documentation inspection, preliminary system inspection, and system installation and instrumentation comprise the initial tests and inspections. Before the performance of a PV system can be tested, the system must have been shipped in its entirety, undamaged, and the documentation should include instructions on the proper installation, operation, and maintenance of the system.

The documentation inspection consists of making an inventory of the documentation shipped with the PV system; recording all given specifications for the system, load, and components; and reviewing the documentation to verify that system installation, operation, and maintenance can be performed.

The preliminary system inspection consists of checking all electrical and mechanical system components against the parts list to verify the system has been shipped in its entirety and that nothing is damaged.

Using the system installation instructions, the system is assembled. Any problems with the installation instructions or assembly process are noted. The instrumentation to monitor the performance of the PV system is installed at this time.

2.2 System Functional Test

The system functional test is performed by monitoring the PV system during several weeks of normal outdoor operation: Initiate system operation according to the manufacturer's instructions. Cycle the load according to its designed load profile, and verify it starts and operates properly. If a load and load profile are not provided with the system, one or several realistic loads and profiles will need to be selected. During normal system operation, measure and record the voltage drops throughout the system. From the data collected during this test, and depending on the system configuration, determine the power output of the array, the charge and discharge setpoints of the charge controller, and the operating characteristics of the inverter.

2.3 System Autonomy Test

The system autonomy test determines how long a fully charged battery can satisfy the system load with no contribution from the PV array. This test should only be run after the system functional test and should only be run on systems with a battery protected by low-voltage disconnect (LVD) circuitry.

With the PV array disconnected, use the load to discharge the battery until it reaches LVD. Disconnect the load, reconnect the array, and while monitoring the ampere-hours (Ah) into the battery, charge the battery until the charge controller begins regulating and the battery has accepted a predetermined number of Ah. (During tests conducted at NREL, 125% of the rated Ah battery capacity was used as the target yielding favorable results.) Again, disconnect the array, reconnect the load, and while monitoring the Ah withdrawn from the battery, discharge the battery until it reaches LVD. The system autonomy, often referred to as "days of autonomy," is calculated as the amp-hours withdrawn from the battery divided by the daily load amp-hours.

2.4 Final Tests and Inspection

As part of the final system tests, the system maintenance procedures are reviewed to verify that maintenance can be performed without undue difficulty. An example of a difficult procedure would involve having to disassemble a system in order to inspect the water level of flooded batteries. At the conclusion of all tests, a final inspection is conducted on the system. Any damage or problems with the system components are noted.

The results of all tests, having been compiled in the test report, are compared against the system specifications to determine if the system meets its performance specifications.

3. NREL TEST VALIDATION AND FUTURE WORK

To date, these procedures have been tested on two small PV indoor lighting systems consisting of one module, a fluorescent lighting load, a charge controller, and a 12 volt battery. The functional test procedures were conducted over a 3-week period, followed by a 2-week system autonomy test. In the process of using these tests, improvements have been incorporated into the procedures.

Future work at NREL will involve validating the procedures on other types of PV systems. Some examples include outdoor area lighting systems; water-pumping systems with no battery storage; and grid-tied systems with and without battery storage. The NREL procedures will be submitted to the IEEE SCC21 and IEC TC82 for consideration as a consensus standard.

As work progresses with the NREL procedures, we expect that the tests will evolve into accepted practice in small PV system performance testing.

4. CONCLUSION

Developing standardized test methods and procedures at NREL to evaluate the outdoor performance of PV systems will encourage product quality and promote PV standards development. Standardized tests will assure users that PV systems will perform as specified for their intended applications. As confidence in PV systems increases, the successful commercialization of PV will grow internationally.

ACKNOWLEDGEMENTS

The authors wish to thank Mike Thomas (Sandia National Laboratories) for his detailed reviews of the test procedures. This work was performed under U.S. DOE Contract No. DE-AC36-83CH10093.

REFERENCES

"Maintenance and Operation of Stand-Alone Photovoltaic Systems," Photovoltaic Design Assistance Center, Sandia National Laboratories, December 1991.

"Photovoltaic System Design," Course Manual, Florida Solar Energy Center, 1991.

"Stand-Alone Photovoltaic Systems: A Handbook of Recommended Design Practices," Photovoltaic Design Assistance Center, Sandia National Laboratories, March 1995.

Perez, Richard, "The Complete Battery Book," Tab Books, Blue Ridge Summit, PA, 1985.

LARGE-AREA, HIGH-INTENSITY PV ARRAYS FOR SYSTEMS USING DISH CONCENTRATING OPTICS

J. S. Ward, A. Duda, K. Zweibel, and T. J. Coutts
National Renewable Energy Laboratory
1617 Cole Blvd., Golden CO, 80401 USA

ABSTRACT: In this paper, we report on our efforts to fabricate monolithic interconnected modules (MIMs) using III-V semiconductors with bandgaps appropriate for the terrestrial solar spectrum. The small size of the component cells comprising the MIM allows for operation at extremely high flux densities and relaxes the requirement for a small spot -size to be generated by the optics. This makes possible a PV option for the large dish concentrator systems that have been developed by the solar thermal community for use with Stirling engines. Additionally, the highly effective back - surface reflector integrated into the MIM design is an effective tool for thermal management of the array. Development of this technology would radically alter the projections for PV manufacturing capacity because of the potential for extremely high power generation per unit area of semiconductor material.

Keywords: Concentrator - 1: High-Efficiency - 2: III-V - 3

INTRODUCTION

Most attempts to utilize photovoltaics for solar energy conversion using highly concentrated sunlight have involved very small devices and Fresnel lenses. The last decade has seen impressive progress in the state of the art for high efficiency III-V devices. GaAs-based multijunction devices are now entering production for space power applications. These devices have demonstrated efficiencies in excess of 30% under the simulated direct solar spectrum ASTM E 891 [1]. This level of performance makes them attractive candidates for terrestrial concentrator systems. Unfortunately, similar progress in the design, implementation, and reliability of the high-intensity tracking concentrator module has apparently not been demonstrated. A study comparing flat-plate and concentrator systems conducted by Arizona Public Service Company concluded that "concentrators have the potential to be the lowest-cost PV technology in sunny regions, but that potential has still not been realized [2]". The primary reason given for this statement was the lack of reliability of the systems under consideration. So, for concentrator PV technology, we have a situation where progress on the module, including the optics and the tracking mechanisms, has not kept pace with the development of the energy-conversion technology (high-efficiency PV devices).

Conversely, in the solar-thermal community, impressive progress has been made, over the past decade, in developing cost-effective, reliable means of concentrating sunlight. Dishes composed of single and multiple facets have been developed. Light weight stretched-membrane facets have been introduced. All of this innovation is being put into the service of a conversion technology that was patented by a Scottish minister (Stirling) in 1816. Clearly, a marriage between the concentrator technology developed by the solar-thermal community and the latest generation of high-efficiency photovoltaic energy converters would be of great interest for utility-scale solar-to-electric energy conversion. Several technological challenges have prevented photovoltaics from being used in this capacity in the past. The large spot size of the concentrated light (between 750 and 2000 cm^2) implies the need to fabricate a module composed of many tiny cells. The heat generated by the infrared component of the incident flux will degrade the performance of conventional PV devices. Creating a module of primarily series-connected devices could render it highly susceptible to non-uniform flux. This paper discusses a device design originally developed for thermophotovoltaic (TPV) energy conversion that could overcome the problems identified above and which has the potential to make PV a viable option for dish concentrator systems.

MONOLITHIC INTERCONNECTED MODULES (MIMS)

Thermophotovoltaic systems employ solid state photovoltaic devices to convert radiant energy from a heat source to electricity. Recent advances in low-bandgap PV devices have led to a resurgence of interest in this field. The elements of a typical TPV system are illustrated in Figure 1.

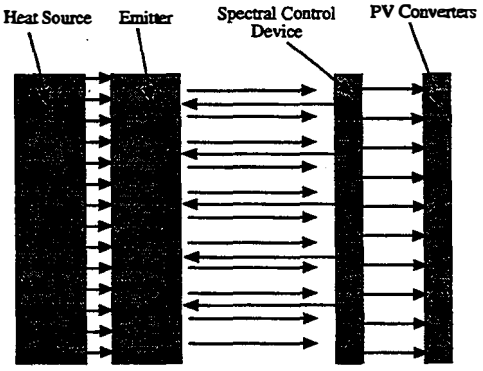

Figure 1: Block diagram illustrating key components of a TPV system.

They include a heat source, a radiator, the PV converters, and an element referred to as a "spectral control" device. This element of the system is necessary because, despite the advances in low-bandgap semiconductors, the bulk of the spectrum generated by the heat source has energy below the response range of the PV devices. To achieve high system efficiency, some means of returning this portion of the flux back to the heat source is required. Spectral control may be

achieved with a high-pass filter that is placed in front of the converters and reflects sub-bandgap photons back to the heat source while transmitting higher-energy photons for conversion. Spectral control may also be achieved by the use of a selective emitter that radiates within a narrow band, convertible by the PV devices. An alternative method of achieving spectral control is the use of a back-surface reflector (BSR) [3]. Another challenge associated with the design of TPV converters is that most systems are expected to be of a relatively large area illuminated with high flux. This results in very high current densities generated within the TPV converter. Parasitic I^2R power losses are a concern when dealing with high current densities and are exacerbated by the low voltage generated by the low-bandgap devices.

As a response to these challenges, monolithic interconnected modules (MIMs) are being developed for this application [4]. These devices use GaInAs with bandgaps as low as 0.5 eV and are currently being epitaxially grown by metalorganic vapor phase deposition (MOCVD) on semi-insulating Fe-doped InP substrates. They are comprised of a number of small devices, series-connected during the fabrication process. In this way, the voltage is increased, while the current generated by the MIM is limited to that which is generated within one of the component cells. Additionally, the use of a semi-insulating substrate facilitates the incorporation of an extremely efficient BSR as a spectral control device. Therefore, this single solid-state device incorporates two of the essential elements of a TPV system. It limits I^2R power losses by reducing the current while increasing the voltage, and it returns the sub-bandgap photons to the heat source very efficiently. The MIM employs interdigitated front and back contacts and a novel interconnect scheme that uses the grid fingers of the component cells as the interconnect structure [4]. This approach results in a high degree of flexibility in terms of current handling capacity and the output parameters of the device. Figure 2 is a simplified plan view of this design. It includes just two sub-cells for clarity. Most MIM designs are composed of many more. Indeed, the number of sub-cells per unit length is an adjustable parameter that allows one to determine the output voltage of the device because, in series, the voltages are additive. Figure 3 is a scanning electron micrograph (SEM) image of the grid finger interconnect structure.

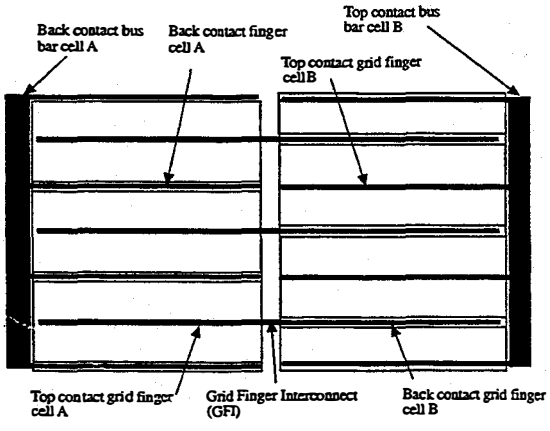

Figure 2: Simplified plan view of interdigitated MIM. This illustration shows only two cells. Actual MIMs typically have 4 to 24 cells.

Figure 3: 500X SEM image of TPV MIM illustrating the grid-finger interconnect.

PROTOTYPE GaAs MIMs

The characteristics that make the MIM an attractive solution to the challenges presented by TPV power conversion have the potential to overcome the obstacles to using PV converters with solar dish concentrator systems. Traditionally, one of the difficulties associated with using PV in these systems is the relatively large, high-intensity spot size of the illuminated area at the receiver. Monolithic integration offers a solution to that problem. I^2R power losses are minimized by fabricating high-voltage, low-current MIM devices. Additionally, the highly efficient BSR that was the spectral control element in the TPV system, becomes an effective tool for thermal management in the high-intensity solar PV application. The sub-bandgap photons that would have been converted to heat are now reflected out of the power conversion unit in an almost specular fashion . This offers the opportunity for clever engineering to use this portion of the spectrum efficiently. Finally, the effects of non-uniform illumination may be minimized by choosing a size for the MIM over which the illumination is relatively uniform. The flexibility in the output parameters of the MIM means that the required output voltage may be achieved by a single device that fits within this area of uniform illumination. The fabrication technology developed for the GaInAs on InP-based material system, can be readily transferred to the GaAs-based material system, which has bandgaps more appropriate for the terrestrial solar spectrum.

We have fabricated small (0.25-cm^2) prototype MIMs from GaAs device structures grown on double-side polished Cr-doped semi-insulating GaAs substrates. Figure 4 shows a cross-sectional schematic of the device structure. It is, in most respects, a typical GaAs double-heterostructure employing GaInP as both the window and back-surface field layers. The exception is the inclusion of a GaAs back contact layer that provides for lateral current flow between the back contact grid fingers. These initial efforts were attempted using an n/p structure. Future efforts will include fabrication of p/n devices because of an asymmetry in the absorption properties of the n and p type material. Free-carrier absorption is more severe in the p-type material due to the larger effective mass of the holes. Therefore, to optimize the performance of the BSR, the p-type layer needs to have minimal thickness. The back-contact layer needs to be thicker than the emitter.

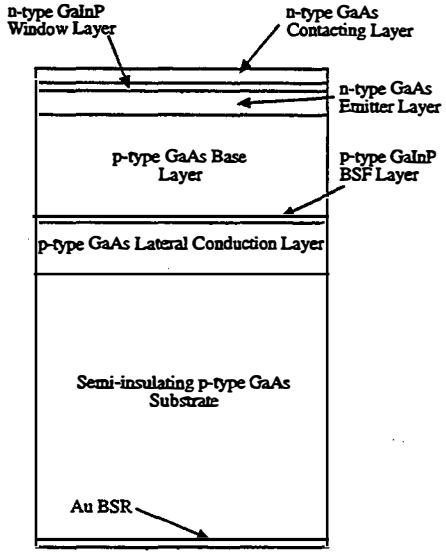

Figure 4: Cross-sectional schematic of GaAs double-hetero structure used for MIM fabrication.

because the distance between back-contact fingers is typically greater than the distance between front-contact fingers. Common MIM grid designs use multiple front-contact fingers for each back-contact finger. Therefore a p/n configuration is preferred. The prototype GaAs MIM is composed of four component cells, using the interconnect structure described above. No attempt has yet been made to optimize the grid design for the anticipated operating conditions in the system.

Figure 5 is a reflectance curve for a Au BSR on a semi-insulating Cr-doped GaAs substrate. Addition of the thin, active device layers will marginally impact this performance. It is seen that very good performance is obtained for this BSR. For the terrestrial application, 41% of the incident flux in the direct-normal spectrum has a wavelength greater than 867 nm (the band edge of GaAs), which may then be used for co-generation purposes.

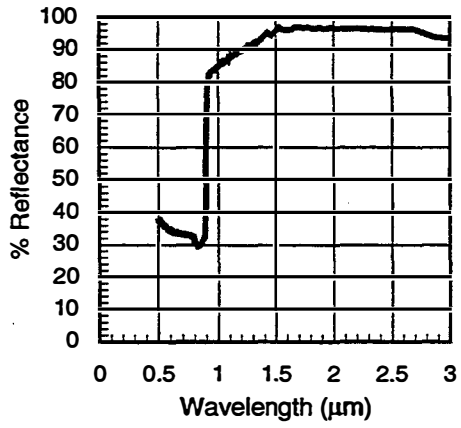

Figure 5: Reflectance curve for Au BSR on semi-insulating GaAs substrate.

A typical dish concentrator system may afford between a 400X and 2000X geometric concentration ratio. At a nominal direct-normal insolation of 0.08 watts/cm² and a concentration ratio of 2000X, there will be 65.6 watts/cm² of incident energy below the response range of the device. This BSR will do an effective job of removing most of this energy from the power conversion unit and reflecting it to an area where it may be usefully employed.

Figure 6 illustrates the current-voltage characteristics of a prototype GaAs MIM under an arbitrarily intense illumination from a flash simulator. Evidence of series resistance due to the non-optimized grid structure, as well as some shunting, is apparent in the fill-factor of 71.8%. A high-quality GaAs device may be expected to generate roughly 24 mA/cm² at 1 sun and 1000 watts/ m² and 19.2 mA/cm² at 800 watts/m². The individual cells in the 4-cell, 0.25-cm² MIM have an area of 0.0625 cm². Allowing for a 15% loss of active area associated with the grid structure and interconnects, the Isc of 0.395 A represents a current density within the active area of the component cells of 7.45 A/cm². This is what one would expect from a geometric concentration ratio of approximately 387X. The power output density of 5.2 watts/ cm² would represent an efficiency of 16.8%. It should be stressed that no efficiency claim is made here. Rather, it is an indication of how this device would perform under these conditions were the current optimized. There is clearly room for improvement in the fill factors of these devices, and it is reasonable to expect real, measured, efficiencies to exceed 20% after further development.

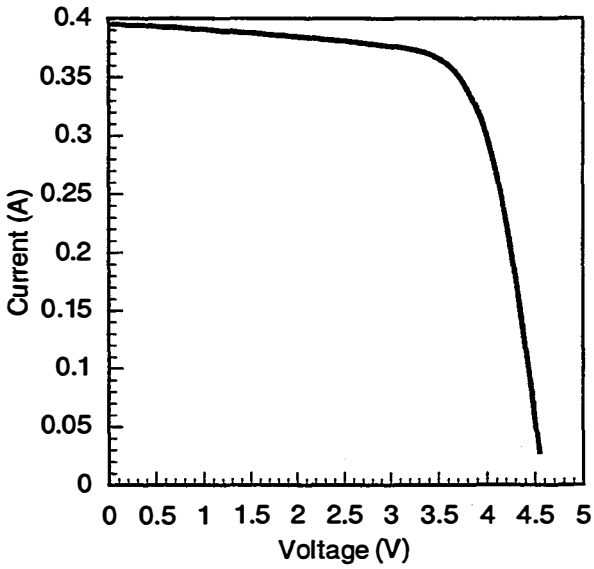

Voc = 4.585 V
Isc = 0.3954 A
Fill Factor = 71.85%
Area = 0.25 cm²

Vmax = 3.686 V
Imax = 0.3535 A
Pmax = 1.303 W

Figure 6: Current-voltage characteristics of a prototype 4-cell 0.25-cm² GaAs MIM under a flash simulator with arbitrary intensity.

MULTIJUNCTION APPROACHES

The real promise of this technology, however, will be realized with the use of advanced multi-junction devices. GaInP/GaAs, two-terminal, two-junction solar cells, invented and developed at the National Renewable Energy Laboratory, are being produced commercially by several manufacturers for space power applications. These devices have demonstrated efficiencies in excess of 30% under the direct-normal spectrum, although they have yet to be fully optimized for use in concentrator systems [5].

The advantage of using a GaInP/GaAs tandem device for this application is not limited to increased efficiency, and hence, power density output. It also offers an advantage related to thermal management. The response range of the tandem device is the same as a single-junction GaAs device because GaAs is the bottom (low-bandgap) component of the tandem. The BSR on a tandem MIM will still reflect back out most of the light with a wavelength above 867 nm. This represents 41% of the incident spectrum. The enhanced efficiency over the remaining 59% of the spectrum means that there will be less energy converted to heat, reducing the load on the cooling system required for high intensity operation. Additionally, because the spectrum is split between the two component cells, the current density as a function of geometric concentration ratio is effectively halved.

Because I^2R power losses and thermal management are the key restraints to high-intensity operation, the tandem device may be expect to operate at significantly higher concentration ratios. Work is continuing on adding a third, and ultimately, a fourth junction to the GaInP/GaAs tandem cell. Efficiencies in excess of 44% have been projected for a three-junction device using a third junction with a bandgap of 1.10 eV. These efficiencies increase to over 50% when a low-bandgap (around 0.7 eV) fourth junction is added [5].

Although a 50%-efficient power conversion unit composed of ultra-efficient future PV devices would be clearly superior to the mechanical alternative, the 30%-efficient GaInP/GaAs devices that are entering production today would rival the output of the current Stirling engines being used in these systems, while offering a number of advantages. The primary advantage is the potential for high reliability and low maintenance costs that are characteristic of PV systems when compared to mechanical devices. Another advantage is the significantly reduced mass of the power conversion unit. This has implications for increasing the tracking reliability of the dish and reducing its costs. Added to these advantages is the fact that, in this configuration, fully 41% of the incident energy is still available for conversion by other means.

ECONOMIC CONSIDERATIONS

A study done by Research Triangle Institute (RTI) comparing the cost of energy produced by various concentrator systems identified a required price of $\$10/cm^2$ for tandem-junction GaInP/GaAs devices grown on GaAs substrates [6]. This price includes the profit for the manufacturer. The MIM fabrication process is not significantly more complicated than that of a high-quality concentrator cell. There is, however, a requirement for an extra photolithographic step, as well as the deposition of an insulating layer. For this reason, we are conservatively using an estimated price of double that of a standard concentrator cell, or $\$20/cm^2$. A 30% efficient device operating at 1000X geometric concentration ratio with a direct-normal insolation of 800 watts/m^2 will have an output power density of 24 watts/cm^2. At a selling price of $\$20/cm^2$, this amounts to \$0.83/watt. This works out to \$20,750 for tandem PV devices with the potential to generate 25 kW of electricity. As a point of comparison, the price of a 25 kW Stirling-engine-based power conversion unit (PCU) is currently around \$180,000.

The Stirling engine's PCU includes an inverter and power conditioning, as well as any required cooling system. Still, it is clear that within the \$159,250 difference between the two approaches, adequate funds should be available to pay for these elements of a PV-based PCU. Even the most optimistic projections of future cost reductions for the Stirling-engine-based PCU has them priced at over \$30,000. It is clear that the dual-junction GaInP/GaAs tandem MIM approach would make PV competitive with these cost projections for Stirling engines. When weight, reliability, and maintenance considerations are factored into the calculations, PV offers a clearly superior conversion technology. Add to these considerations that 41% of the incident power is still available for co-generation in the PV approach and the PV-based PCU seems even more advantageous.

SUMMARY

Recent advances in high-efficiency III-V solar cells, particularly the GaInP/GaAs tandem cell, combined with a new device configuration developed for TPV applications, make PV a viable alternative to the Stirling-engine-based PCUs used in large dish concentrator systems. Potential advantages to using PV for this application include reduced price, reduced mass, reduced maintenance costs, increased reliability, and the ability to use 41% of the incident radiation for cogeneration purposes. The economics of this application, with its focus on efficiency, becomes a strong motivation for continued development of high-efficiency multijunction device technology.

Prototype monolithic interconnected modules, using GaAs device structures, have been fabricated and characterized. The performance of a back-surface reflector on a semi-insulating GaAs substrate has been investigated. Future work will include the fabrication of larger-area MIMs using GaInP/GaAs tandem devices and optimized grid structures, as well as on-sun testing of these devices using NREL's solar furnace.

ACKNOWLEDGMENTS

The authors wish to thank Dan Friedman, Sarah Kurtz, and Charlene Kramer of NREL's High-Efficiency III-V team for supplying the GaAs device structures. They would also like to thank Mark Wanlass and Jeff Carapella of NREL's TPV team and Chris Murray of Westinghouse Electric Power Company for their efforts in developing the MIM technology. The efforts of Keith Emery and Tom Moriarty of NREL's Characterization team are also gratefully acknowledged.

REFERENCES

[1] Annual Book of ASTM Standards, Voulume **14.02** (1987) 470.

[2] T. Lepley, B. Hammond, A. Harris, Proceedings 26th Photovoltaic Specialists Conference, (1997) 1257.

[3] G. W. Charache, D. M. DePoy, P. F. Baldasaro, and B. C. Campbell, Proceedings The Second NREL Conference on Thermophotovoltaic Generation of Electricity, (1995) 339.

[4] J. S. Ward, A. Duda, M. W. Wanlass, J. J. Carapella, X. Wu, R. J. Matsun, T. J. Coutts, T. Moriarty, C. S. Murray, and D. R. Riley, Proceedings The Third NREL Conference on Thermophotovoltaic Generation of Electricity, (1997) 227.

[5] S. R. Kurtz, D. Myers, and J. M. Olson, Proceedings 26th Photovoltaic Specialists Conference, (1997) 875.

[6] R. A. Whisnant, J. A. Hutchby, M. L. Timmons, R. Venkatasubramanian, J. S. Hills, First World Conference on Photovoltaic Energy Conversion, (1994) 1103.

V. Market Development

THE RAMAKRISHNA MISSION ECONOMIC PV DEVELOPMENT INITIATIVE

J. L. Stone and H. S. Ullal
National Renewable Energy Laboratory
1617 Cole Boulevard
Golden, CO 80401 USA
Tel: 303-384-6470 Fax: 303-384-6481 E-mail: stonej@tcplink.nrel.gov
Tel: 303-384-6486 Fax: 303-384-6430 E-mail: ullalh@tcplink.nrel.gov

C. Sherring
Sherring Energy Associates
3 Bellaire Drive
Princeton, NJ 08540 USA
Tel: 609-799-8889 Fax: 609-799-5258 E-mail: csherring@home.com

Abstract: India is the world's second most populous country, quickly approaching one billion persons. Although it has a well-developed electricity grid, many of the people have little or no access to electricity and all of the benefits associated with it. There are areas that are isolated from the grid and will not be connected for many years, if ever. One such area is the Sundarbans located in the delta region of the two great rivers, the Ganges and Brahmaputra, partially in India and partially in Bangladesh. It is estimated that 1.5 million people live in this area, crisscrossed by many islands and rivers, who have only marginal supplies of electricity generated primarily from diesel generators and batteries. Working with the regional non-governmental organization (NGO), the Ramakrishna Mission, and the West Bengal Renewable Energy Development Agency, the governments of India and the United States initiated a rural electrification initiative to demonstrate the economic and technical feasibility of photovoltaics to provide limited supplies of electricity for such applications as solar home lighting systems (SHS), water pumping, vaccine refrigeration, communications, and economic development activities. This paper details initial results from approximately 30 kilowatts of PV systems installed in the area, including socio-economic impacts and technical performance.
Key Words: Stand-alone PV Systems - 1: Developing Countries - 2: Sustainable - 3

1.0 INTRODUCTION

With some two billion people worldwide without access to electricity, the developed countries are challenged to deploy their technologies to meet this large need. The many attributes of photovoltaics (PV) make it ideal in many respects to confront the challenge. The availability of even as few as 20-50 watts of power can have major impacts on the lives of villagers living in isolated communities. PV has already been demonstrated to be technically feasible; the challenge is more economic. Can the end users afford to spend their limited disposable income on PV systems at the expense of not having other needs met? Many can, but the reality is that subsidies may be required, and in many cases, outright gifting may be the reality. Thus, governments will be faced with difficult choices amongst their funding priorities.

The U.S. Department of Energy (DOE) with its National Renewable Energy Laboratory (NREL), agreed in 1993 to cooperate on a 50-50 cost shared initiative with India's Ministry of Non-Conventional Energy Sources (MNES). This demonstration was to demonstrate the economic viability and sustainability of PV systems to provide the basic needs of villagers in the isolated region of southern West Bengal known as the Sundarbans [1].

1.1 The Sundarbans

The vast swampy delta of the two great rivers, Brahmaputra and Ganges, extends over areas comprising mangrove forests, swamps, forests, and islands, all interwoven in a network of small rivers and streams that flow into the Bay of Bengal. The area is about 10,000 square kilometers, renowned for its abundant wildlife including the royal Bengal tiger. Transportation into the area and between its countless villages is by boat and on the land areas by foot or bicycle rickshaw.

Snake bites represent one of the largest contributors to death in the area, primarily because refrigeration for snake bite serum is not available. Home lighting is provided by candles, kerosene lights, dry-cell batteries, and rechargeable car batteries. Battery recharging is difficult because of the distances that batteries must be transported to be recharged and the unpredictable quality of the available charging service.

The Sundarbans is served by the Ramakrishna Mission (RKM), which provides education, agriculture, training, and medical services. The RKM is a well-respected humanitarian organization principally known for their slum-relief activities in the Calcutta area.

1.2 The Ramakrishna Mission

Ramakrishna Mission Ashrama, Narendrapur, is a branch center of the Ramakrishna Mission headquartered at Belur Math, Howrah, West Bengal. Through its integrated development wing, the Ramakrishna Mission Lokasiksha Parishad, this Ashrama is actively engaged in various rural and urban development programs. Its training wing offers several development programs such as literacy, child and mother care, integrated rural development, agriculture programs, intensive sanitation programs, environmental restoration, participatory forest management, employment and entrepreneurship, and most recently, renewable energy systems. The Mission's work is carried out at the village level through a number of youth clubs that are coordinated and monitored by local cluster organizations. Today, the Ramakrishna Mission Lokasiksha Parishad is working with about 40 affiliated cluster organizations, with 1500 youth clubs spread over 4000 villages in 12 districts of West Bengal.

The renewable energy programs are an important part of the Lokasiksha Parishad. The RKM was recommended as the working NGO to implement the

cooperative program between India's Ministry of Non-Conventional Energy Sources and the DOE's National Renewable Energy Laboratory. The Mission has been responsible to identify the beneficiaries of the PV systems, provide trained personnel to install and maintain the systems, collect the loan repayments, and work with other funding organizations to expand the program.

2.0 THE U.S.-INDIA SUSTAINABLE ENERGY PROGRAM

High-level meetings were held in 1994 between MNES's Minister Krishna Kumar and DOE's Secretary Hazel O'Leary. An agreement was reached to implement a 50-50 cost-shared program to supply PV energy systems to eight villages in the Sundarbans region of West Bengal. A number of participants were identified with various responsibilities for the project. The organizational structure is shown in Figure 1.

The Sustainable Rural Economic Development Ramakrishna Mission PV Initiative was conceived as a small-scale demonstration project that would show the economic viability of photovoltaic systems in the Sundarbans region of West Bengal. The viability was to be predicated on the systems being economical without substantial subsidies, and eventually, without any subsidy at all. The operation and maintenance of the systems was to be the responsibility of the chosen NGO [2].

2.1 Project Responsibilities

NREL was assigned the responsibility to manage the U.S. side of the cooperative agreement. PV hardware was procured under a competitive solicitation. Modules and charge controllers were delivered dockside to Calcutta, where MNES had contracted with Exide Industries to receive the materials and deliver them to the Sundarbans under the auspices of the West Bengal Renewable energy Development Agency (WBREDA). System hardware provided by the Indian side was joined and installed by Exide and WBREDA. The trained Mission installers carried out much of the system installation and worked with the end-users to educate them in the correct use of their new power systems.

2.2 Project Financing

The Government of India (GOI) provides about a 40% subsidy to qualified beneficiaries (the unit costs Rs. 14,000 for which the GOI provides Rs. 6,000). The remaining 60% (Rs. 8,000) was either in the form of cash or through low-interest loans of Rs. 4,500 repayable over an extended period of time (a down payment of Rs. 3,500 was required at the time of system delivery). Typically the Mission has limited the loan period to less than 3 years, which they have found to be a more effective period to achieve total repayment. The experience to date is that they have achieved in excess of 95% repayment rates due largely to the prior establishment by the Mission of good borrowing and banking habits in the communities. Most of the villages that have taken part in the program have already established village-level banking.

The Indian Renewable Energy Development Agency (IREDA) is charged with the responsibility of dispersing World Bank funds for qualified renewable

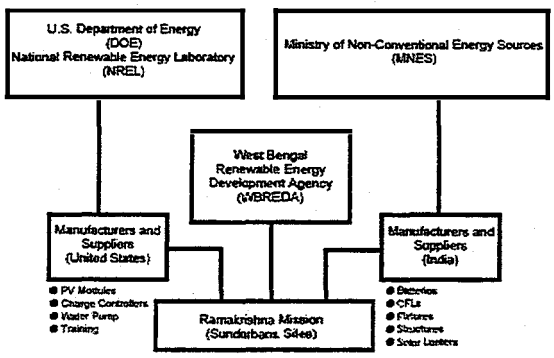

Figure 1. Project Organization

energy projects. To aggregate larger numbers of systems sales, a leasing arrangement has been established that removes all subsidies while allowing end-users access to low-interest money to purchase solar home lighting systems. IREDA has contracted with a private organization to purchase the solar systems and to lease them to the end-users. The organization treats this arrangement strictly as a business deal. They buy the PV systems directly from a dealer and receive 85% of the purchase price from IREDA as a low-interest loan (2.5% over 10 years). The company is then eligible to receive the full depreciation and tax benefits available from the Government of India. They then lease the equipment to the Rural Energy Service Company (RESCO). RESCO then provides the systems to the end-users with a repayment schedule of 1 or 2 years. This arrangement has been approved for a trial of 3000 SHS. If successful, the approach could be replicated to much larger projects.

2.3 Project Details

The Sundarbans region was chosen for its remoteness and the reality that the electrical grid will be long time coming, if ever. The seven villages chosen to receive the PV systems were provided 300 home lighting systems (one VLX-53 Solarex polycrystalline silicon module and one SunSaver 6LVD charge controller per each home lighting system) that furnish 50 watts dc for 2-9- watt compact fluorescent lamps (CFLs) and one electrical outlet of about 30 watts for a black-and-white television or other appliance; 15 street lights; electrification for a clinic, the training center, and a youth club; and two battery-charging stations of 4 kW each, capable of charging 10-100-amp-hour car batteries from complete discharge to full charge within one day at full sunlight.

A typical installation in Figure 2 shows the PV module mounted on the thatched roof. The addition of about four hours of light each night allows the young students to study at home at night, allows additional productivity such as found at the weaving center, and provides health care at the local clinic where the vaccine refrigerator makes snake bite serum available. The street lights will be deployed in the village gathering places.

3.0 EXPERIENCE AND LESSONS LEARNED

NREL has contracted with the Tata Energy Research Institute (TERI) to perform a before-and-after impact study in the region. The study will include both

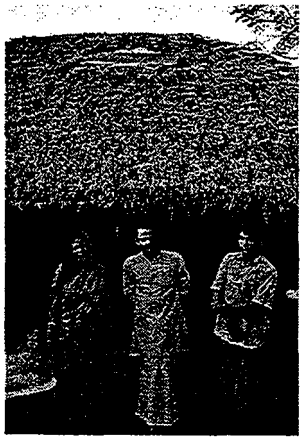

Figure 2. Solar home lighting system mounted on home owner's thatched roof

social and economic impacts. It is hoped that the experiences in the Sundarbans can be replicated in other regions of the world experiencing a similar lack of access to electricity.

3.1 Technical Issues

In addition to the 300 home lighting systems, lighting has been installed at youth cubs in Katakhali, Satjlia, and Shantigachi. The clinic at Satyanarayan is completed, but the vaccine refrigerator still remains to be delivered by WBREDA. The weaving center at Pakhiralya is also completed, with the Gosaba Rupayan Lighting system remaining to be installed.

One minor problem with the home lighting systems has been the flush mounting of the PV modules on the thatched roofs. This hinders air circulation behind the panels which prevents cooling that would improve the performance. Flush mounting also leaves the panels tilted at the pitch of the roof, of about 40 degrees. The slight penalty by not having the panels at an optimum 30 degrees is minor. Because the panels are facing south, they catch the cooling breezes from that direction.

The battery-charging stations have not been installed because the locations have not been settled on. The RKM plans to charge 15 rupees per charge initially. Once everything is operational, they plan to increase the fee to 25 to 30 rupees. The RKM has provided the following information for charging a 60-amp-hour battery 3 times per month. The battery, with an expected lifetime of two years, costs of 3500 rupees, or about 150 rupees per month. A battery charge is estimated at 30 rupees, or 90 rupees per month. The boat trip required to transport the battery to the charging station is 20 rupees or 60 rupees per month. This totals 300 rupees per month.

3.2 Customer Satisfaction and Infrastructure Development

During a recent visit to the region, it was clear that customer satisfaction was high. No systems have hit their low voltage discharge, indicating that the batteries are operating at a high state of charge (SOC). This was confirmed by taking specific gravity measurements, all of which were at or above 80% SOC. This indicates that the PV systems are underutilized. Most home owners do not have a televison and are only powering 2 or 3 9-watt CFLs for 3 to 4 hours per night. Those with TV (14 watt) will operate it 2 to 3 hours per night. Thus, the 50-watt systems are more than adequate to provide additional power beyond this.

The RKM is very committed to PV for SHS. Since the NREL systems have been installed, more than 1100 systems have been sold and installed in the region. Up to now, the RKM has focused their attention on four districts, South 24 Parjanas, Modnapur, Bankura, and Gosaba. A senior PV technician is responsible for each district. Under him are four or more village-level technicians who work on solar energy systems, taking care of installation, maintenance, and inspections. The RKM plans to expand into three other districts, Burdwan, Hoogly, and Birbhum. The have selected 10 new technicians who will undergo training in basic electronics with a PV emphasis. All electronic students at the Mission get solar in their courses.

In other areas of the Sundarbans, the RKM has begun to sell PV systems through shopkeepers. The Mission does not install or maintain these systems, but does send a technician out to inspect the installation once it is completed. The shopkeeper performs any follow-on service. The shopkeeper gets a 600-rupee commission on the sale for making the contact and setting it up. Shopkeepers are responsible for approximately 10% of the follow-on sales. Another indication of the success of their infrastructure is the attention to record keeping. The NREL systems are inspected once a month, and the technician fills out an inspection report. Each homeowner is provided a simple homeowners's guide for his system.

Homeowners were asked what they used for lighting before PV. The majority used hurricane lamps that use kerosene. Their fuel charges were 60 to 80 rupees per month. This provided two lamps for 4 hours per night.

Figure 3. Where there was once darkness, there is now light.

4.0 Retrospective

This collaborative project has successfully brought the benefits of electricity to a region formerly with little or no electrical power. Figure 3 is a powerful picture showing mother and child enjoying quality light for the first time. PV system sales are now continuing without

government subsidy. Evaluations are ongoing to determine the economics of PV and the real benefits to the end-users. From this information a definitive statement can be made as to how sustainable these projects can be. The Ramakrishna Mission continues to interact with other funding agencies to expand the electrification effort to other areas in their sphere of influence. Their efforts have led to one of the largest and most successful rural electrification efforts in Asia [3].

5.0 Conclusions

The impact of the initiative will only be known after the passage of time. Very clearly, the major influence will be on the young. Figure 4 shows a young man in the village studying under PV-powered light. Before, he would most likely have used candles or kerosene-fueled lanterns. The project will be sustained by the number of trained personnel, shown receiving their initial training in Figure 5, responsible for maintaining the systems. The quality of health care in the region will be improved with PV power for lighting and vaccine refrigeration (Figure 6 illustrates the involvement of the locals in installing the PV modules on the clinic roof). The project will continue to be monitored, and lessons learned will be applied to similar projects, both in this region and in other countries around the world.

Acknowledgments

The authors would like to thank the many people involved in the success of this Program. Special thanks go to Dr. E.V.R. Sastry of MNES and Mr. Jim Welch of Remote Power International. Thanks also to the personnel of the Ramakrishna Mission and the West Bengal Renewable Energy Development Agency.

This work was supported under contract DE-AC36-83CH10093 with the U. S. Department of Energy.

References.

[1] J.L. Stone and H. S. Ulal, "PV Opportunities in India," 13th NREL Photovoltaics Program Review, Lakewood, CO 1995, pp. 275-280, *AIP Conference Proceedings 353.*

[2] J.L. Stone and H.S. Ullal, "The Ramakrishna Mission PV Project — a Cooperation between India and the United States," NREL/SNL Photovoltaics Program Review, Proceedings of the 14th Conference—A Joint Meeting, Lakewood, CO, 1966, pp. 521-527, *AIP Conference Proceedings 394.*

[3] J. L. Stone, H. S. Ullal, and E.V.R. Sastry, "The Indo-U.S. Cooperative Photovoltaic Project," 26th IEEE Photovoltaics Specialists Conference, Sept.30-Oct.3, 1997, Anaheim, CA, pp. 1273-1275.

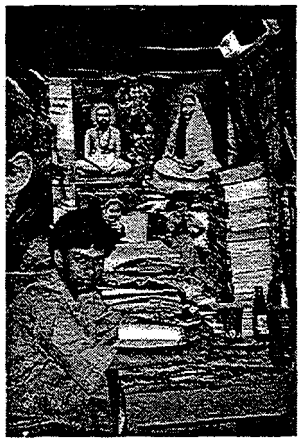

Figure 4. Where there is light there will be knowledge—a student studies under light powered by photovoltaics

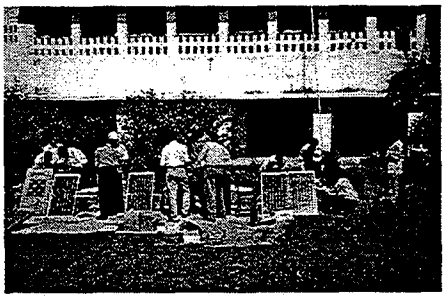

Figure 5. Hands-on training offered to RKM personnel

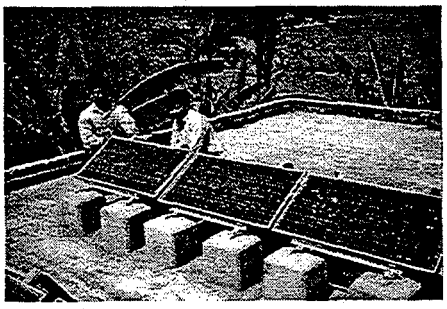

Figure 6. Installing PV modules on the village clinic

LESSONS LEARNED FROM THE NREL VILLAGE POWER PROGRAM

R. W. Taylor
National Renewable Energy Laboratory
1617 Cole Blvd., Golden, CO, USA

ABSTRACT: Renewable energy solutions for village power applications can be economical, functional, and sustainable. Pilot projects are an appropriate step in the development of a commercially viable market for rural renewable energy solutions. Moreover, there are a significant number of rural electrification projects under way that employ various technologies, delivery mechanisms, and financing arrangements. These projects, if properly evaluated, communicated, and their lessons incorporated in future projects and programs, can lead the way to a future that includes a robust opportunity for cost-effective, renewable-based village power systems. This paper summarizes some of NREL's recent experiences and lessons learned.
Keywords: Sustainable – 1: Developing Countries – 2: Villages – 3

1. BACKGROUND

Following the Earth Summit in June 1992, held in Rio de Janeiro, Brazil, the U.S. Department of Energy's National Renewable Energy Laboratory (NREL) became seriously engaged in assisting with the introduction and integration of renewable technologies in developing countries. In 1993, a workshop was convened at NREL with 33 representatives from the private sector, government agencies, development organizations, nongovernment organizations, and research institutions to discuss the issues of applying renewable energy in a sustainable manner to international rural development. A summary recommendation was that NREL could assist in renewable energy-based rural electrification (RERE) by developing and supporting six related activities: resource assessment, comparative analysis and modeling, performance monitoring and analysis, pilot project development, Internet-based project data communications, and training. Thus was born the NREL Village Power Program consisting of activities that cut across several renewable technologies and have grown to include a wide range of technical, economic, and social disciplines.

Currently, NREL is active in 20 countries, and is supporting pilot projects in 12 of those countries. Technologies presently include photovoltics, wind, biomass, and hybrids; increasing emphasis on small geothermal and small hydro are on the horizon. The remote rural applications include home, communications, water pumping, school and health clinic, battery charging, ecotourism, and village minigrid hybrid power systems.

While considerable effort has been devoted to developing new computer models for economic analysis, training and working with in-country partners, and gathering and documenting not only NREL experiences, but also experiences of others, it is the facilitation of pilot projects that counts most. Pilot projects are more than mere technical demonstrations—they are central to renewable energy-based village power development. By and large, it has been shown that renewable technologies work. The most important aspects of pilot projects are their inherent ability to engage in-country partners in hands-on experience that can lead to not only technical, but economic and institutional sustainability as well.

It is important to note that many of the pilot projects from which NREL's experience has been gained were funded, and in many cases developed, by other organizations and agencies. NREL has provided a variety of services including technical, economic, regulatory, and project management assistance to a wide range of projects.

The purpose of this paper is to describe the lessons NREL staff have gleaned from their participation in the various pilot projects. We hope that these lessons will help the RERE community to implement increasingly more-sustainable projects that lead to widespread replication.

2. APPROACH

The approach used to document the lessons was to poll eight key NREL Village Power team members who have been involved in the development, implementation, and evaluation of renewable-based pilot projects. Consolidating this information, an attempt has been made to look for common themes, while maintaining the variety of experiences. The following four categories were chosen as a way to capture our experiences: institutional aspects, pilot project characteristics, implementation processes, and technology development needs.

3. LESSONS LEARNED

3.1 Institutional Aspects

Reliable, well-designed, and integrated technology is important, but it is the institutional aspects of a project that make or break long term sustainability.

Partnering. Establishing an effective working relationship with a capable, credible in-country champion is critical to project success. In-country partners understand the local legal, political and social context. However, recognize that partner capabilities and interests may change over time. State-owned electric utilities that are sold to private sector, for profit institutions can undergo a dramatic swing in interest and support.

Maintenance. Nothing is maintenance-free, therefore, a maintenance support infrastructure needs to be established and nurtured. This issue must be addressed from the very conception of a project. It need not be complex, but it does need to be functional and appropriate for the size, complexity, and sophistication of the systems deployed. A training program with documentation that is matched to the local capabilities, regular refreshers, personnel turnover, a spare parts' inventory and supply information, and funds for preventive and problem maintenance must all be addressed.

Tariff design (grid systems). Developing world rural tariffs for grid-connected systems are often heavily subsidized and send the wrong price signals. While rural subsidies may be appropriate in some cases, the tariff design needs to reflect both the actual cost and quality of service. Multilevel or stepped tariff designs are particularly important in cases where 24 hour, ac service with renewable hybrids is subsidized due to the large swings in short-run marginal cost. The technical (metering) and institutional (meter reading and billing) costs of grid connected line extension or minigrids need to be evaluated when considering the tradeoffs between grid power and small stand-alone systems.

Tariff design (stand-alone systems). In small stand-alone systems for homes, schools, health clinics, water pumping, and other applications, strong efforts need to be made to decouple the concepts of electricity sales measured in ¢/kWh from fee-for-service monthly payments. Many rural customers are already paying US$5-15/month for basic energy services that can be better met with stand-alone renewable energy systems (and without subsidies). It is often difficult to convince electric utilities and other local officials to think about an energy-services approach.

Development coordination. Most countries have significant rural development programs including education, health, communications, economic development, agriculture, water, and electricity. The links among these programs and the supporting agencies are potentially substantial, and currently underutilized. Rural electrification, does not, in and of itself, create rural economic development. Linking programs is important for overall success.

Planning tools. Rural electrification planning methodologies and policies generally do not integrate and evaluate renewable energy solutions fairly, if they are recognized at all. While pilot projects seldom need to be formally evaluated, up front, by the planning agencies, pilot projects can provide important input to these agencies to further enhance their adoption of renewables as a viable option. There needs to be a conscious effort to work with planning agencies to modify their evaluation methods to fairly accommodate renewable energy solutions.

Economics. Because rural electrification generally consists of line extension or diesel minigrids based on an annual budget for installations, the concept of life-cycle cost analysis, which fairly compares capital intensive and operating-expense intensive technologies, is uncommon. The concept of life-cycle costing needs to be integrated into the training of planning officials.

Language. Many expectations have not been met because of misunderstanding resulting from language and culture differences rather than nonperformance. It is particularly important in pilot projects to emphasize open and complete communications.

3.2 Pilot Project Characteristics

Pilot projects are more than just technical demonstrations. The most successful pilot projects seek to create an environment that can lead to future replication.

Performance. First and foremost, the project must perform well technically. To this end, extra care and expense should be devoted to the design, construction, commissioning, robustness, and reliability of the pilot system. In pilot projects, robustness and reliability are more important than energy-conversion efficiency. Resist the temptation to field the "latest and greatest" until it has been thoroughly tested under controlled conditions. Repairing equipment in remote locations is difficult and expensive.

Energy efficiency. Energy-efficient end-use applications/appliances are critical to economically sized renewable energy systems. Investments in energy efficiency have much more economic value than adding generation capacity to meet the demand of inefficient appliances. It is important that a complete systems engineering approach be maintained, attempting to deliver the best end-use service for the least overall system cost. Retrofitting expensive hybrid power systems in a village without first addressing end-use appliances is a mistake.

Quality of service. Along with the issue of energy efficiency comes the issue of quality of service. Examples include: electric lighting provides better light than from kerosene wick lamps; 24-hour service is preferred to 4-6 hour service; reliable, available electricity is more valued than an unreliable supply. These differences in quality of service should be reflected in comparing alternative solutions.

Replication mind-set. Pilot projects need to be designed technically and conceptually, with the commercial replication path in mind. Pilot projects that cannot be replicated in the region commercially serve only as technology demonstrations with far less value to the existing electrification program than those designed to feed into a national rural electrification plan. It is important to ask the question: "If the pilot project is successful, what is the likelihood that a commercial solution will follow?" If the answer is "none," rethink the rational for the project.

One-of-a-kind demonstrations. Single projects in remote locations are not sustainable. While it is tempting from a budgetary perspective to do single projects, they quickly become operation and maintenance (O&M) nightmares. Multiple systems in a region are required to develop and sustain the necessary support infrastructure. Single-unit technical demonstrations do have their place. Make sure they are in a place that they can be maintained, or removed, when the demonstration is over.

Loads. Estimating electric loads for newly electrified villages is difficult, often resulting in overdesign, wasted energy, and poor economics. Estimating load growth in villages receiving ac power for the first time is equally difficult. Integrating deferrable and discretionary loads helps system economics, but is difficult in practice. Designing modular systems that can be incrementally grown as village loads increase needs more attention. Incorporating these issues into planning models is equally challenging.

Diesel retrofits. It is often more economical (from a life-cycle cost perspective) to install a new, appropriately sized diesel than to use the existing, oversized, poorly maintained one. However, local authorities and renewable energy equipment suppliers resist scrapping the existing diesel because the new diesel reduces the capital available for the nonconventional equipment.

Performance monitoring. Pilot projects, unlike commercial projects, are explicitly intended, based on their performance, to lead to larger scale replication. To this end, they need to be instrumented to confirm energy and operational performance. They also need to be evaluated for institutional response and effectiveness. The results of these evaluations need to be communicated to both the

local and international development communities so that technical and nontechnical lessons can be adapted in the replication process.

Buy-down. Because pilots generally introduce new technical solutions to regional authorities, it is often necessary to cost-share the initial project. However, it is important to require significant cost-sharing by the implementing/operating organization to assure partner commitment and capture management attention.

3.3 Implementation Process

Pilot projects help country programs obtain firsthand experience that may lead to widespread adoption of renewable energy technology in the rural electrification process.

Political will. The most important factor for successful implementation is a supportive, positive attitude by the rural electrification officials. The existence of a champion for renewables for rural services who is in a position of authority keeps up the momentum during the extended process of resource assessment, site selection, project design implementation, evaluation, and replication. There is no substitute to a dedicated, influential, local champion.

Duration. The time from initial interest in renewables to commercial replication takes 4-6 years, in a positive climate. The pilot phase usually takes 2-3 years from site selection through initial evaluation. Pilot projects are part of a long-term process of change. Initial commitments should be coupled with the realization that long-term collaborations are a key to successful programs.

Commercial replication. The transition from the pilot phase to commercial replication can be difficult. The transition is greatly aided by a well-funded pilot phase that includes multiple, regional projects; local capacity building; strong engagement and commitment by a commercial partner; and substantial technical assistance. The transition usually means a change from primarily sponsor-driven activities to business-driven activities. The more the pilot project can be set up to look and act like a business, the easier the transition.

Needs-driven approach. Renewable energy solutions to rural electrification should be resource- and need-driven, rather than based on a specific technology/application. The available renewable resources, the village electrical demand and applications, villager willingness and ability to pay for electrical service, and the economics of alternatives should determine the appropriate solutions. It is important to be objective and neutral in evaluating and presenting options. It is important to let the locals participate, and select, appropriate solutions.

Administration. In order to sustain a newly implemented rural electricity system, an administrative system needs to be developed and sustained. Many rural villages have formed cooperatives for fishing, agriculture, and other economic development activities. The specific electricity administrative solution will be regional or village dependent or both. While a number of models have been successful, care is needed in matching the administrative system to the village social dynamics.

3.4 Technology and Development Needs

While it is essential to deploy only commercial technology in pilot projects, it is fair to say that there are opportunities for technological improvement in components, systems, ancillary equipment, and supporting processes.

Hybrid systems. While wind, PV, and micro-hydro have been commercial technologies for a number of years, their hybridization with fossil fuel generators for rural applications are an emerging technology. Renewable energy-fossil hybrids have their roots in telecommunications applications in remote sites; however, the extremely high-value electricity for telecommunications applications has resulted in expensive, extreme reliability designs that are inappropriate for rural electricity service. While there are tens of thousands of isolated diesel generators deployed throughout the world, village hybrid system sales are infinitesimal at this stage because the design, manufacturing, integration, implementation, and distribution segments of the industry are very sparse and immature. This results in high prices, costly implementation and support, and rapidly evolving designs. Hybrid systems are a potentially significant solution to rural ac electricity needs, but further technology development and industry expansion will be required.

Controls. Electronic controls and converters are the least robust component in the reliability/robustness chain. While there have been significant improvements in the quality and functionality of these components over the last 5-years, they remain the chief cause of system problems. Complicating the issue is the lack of maintenance support capacity for these components in rural areas. Robustness and modular electronics need to be the focus of controls development; in addition, spare parts and development of electronic service capacity need to be part of any pilot project.

Lightning/corrosion. Many developing countries' rural applications are exposed to severe corrosion and electrical storm conditions. While much is known about lightning and corrosion protection of electrical components, in many cases conventional solutions for high-value electrical systems are neither cost-effective nor appropriate for rural systems. Cost-effective application engineering is required for corrosive and electrical storm-sensitive environments.

Meters. Metering and billing are often a problem. Prepayment meters may greatly increase the sustainability of mini-grid systems. While several prepayment meter designs are commercial, they need to be less expensive in order to receive serious international attention.

Resource data. Wind resource data for rural areas are either nonexistent or of marginal quality, yet are critically important for comparing wind-based systems to other options. Wind mapping, using various existing meteorological and geographic databases and customized computer models, has enhanced the ability to evaluate wind as an option. Existing solar databases are sufficient for estimating PV as an option. There is an increasing use of GIS-based census and demographic data in the developing world for grid extension planning. There is an opportunity to combine resource mapping and GIS-based rural planning models for determining the opportunity and the best locations for renewable village electrification.

Integrators/packaged systems. Because the market for rural renewables is just emerging, the role of system integration is underdeveloped. There are a number of component and system suppliers, but the function of system integration (comparing and packaging alternative architectures and solutions, along with due attention to load

efficiency and demand-side options) is very limited, especially as an in-country capability. While integrated, packaged systems have certain commercial and functional benefits, they (and their supply) are premature; therefore, the market will need to develop further to attract/enhance the integration function.

4. SUMMARY

Renewable energy solutions for village power applications can be economical, functional, and sustainable. Pilot projects are an appropriate step in the development of a commercially viable market for renewable rural solutions. Moreover, there are a significant number of rural electrification projects under way that employ various technologies, delivery mechanisms, and financing arrangements. These projects, if properly evaluated, communicated, and their lessons incorporated in future projects and programs, can lead the way to a future that includes a robust opportunity for cost-effective, renewables-based village power systems.

ACKNOWLEDGEMENTS

This paper was made possible by generous contributions from key members of NREL's Village Power team. Led by Larry Flowers, team leader, other members include Ian Baring-Gould, David Corbus, Steve Drouilhet, Vahan Gevorgian, Rick Holz, Peter Lilienthal, and the author.

THE USE OF PHOTOVOLTAICS FOR RURAL ELECTRIFICATION IN NORTHWESTERN CHINA

William L. Wallace
National Renewable Energy Laboratory
1617 Cole Boulevard
Golden, CO 80401 USA
Tel: 303-384-6476 Fax: 303-384-6490 E-mail: wallaceb@tcplink.nrel.gov

Li Jingming and Gao Shangbin
Chinese Ministry of Agriculture
11, Nongzhanguan Nanli
Beijing 100026 P.R.C.
Tel: 010-6419-2612 Fax: 010-6500-2448 E-mail: gaoshb@mail.ied.ac.cn

Abstract: The use of renewable energy technologies in China is becoming increasingly important to meet the needs of a large rural population. Solar and wind renewable resources in particular are available in regions of China that at present have no access to conventional grid power. Two regions in China that have an acute lack of electricity are a large region in northern and western China and the coastal island region of China. These regions have attracted the attention of the Chinese government in terms of increasing the quality of life and standard of living conditions of the rural population. These regions have also attracted the attention of domestic Chinese companies and of international companies, governments, and multilateral development organizations as a potential market for renewable energy rural electrification systems. This paper focuses on the bilateral cooperation between the United States Department of Energy and China in providing assistance for the use of renewable technologies for rural electrification in northwestern China.
Key Words: Stand-alone PV Systems - 1: Developing Countries - 2: Sustainable - 3

1. INTRODUCTION

Approximately 70% of China's 1.2 billion population live in rural areas. Of this rural population, Chinese agencies have reported that 70 to 100 million people have no access to electricity in terms of proximity to an electrical grid [1]. A large number of these people also do not have near-term prospects of obtaining electricity through grid extension because of the high costs of building transmission lines to remote locations. There is also a large rural population throughout China, which is difficult to quantify, that live in electrified regions near local transmission lines, but who are not connected to the grid because of electricity shortages or other access problems.

A large region in northern and western China contains a rural population with characteristics that include: i) low population density and dispersion over a large land area, ii) high percentage of minority populations, iii) lack of access to an electric grid, and iv) variable income levels, with a large number of people living at or below the national poverty level. This area generally includes the provinces of Xinjiang, Qinghai, Gansu, Ningxia, and Shaanxi, and the autonomous regions of Inner Mongolia and Tibet. In most of this region, the existing electrical generating capacity is based on hydropower and coal-fired plants that provide grid power primarily to the larger urban centers.

The U.S. Department of Energy (DOE) initiated bilateral cooperation with China in 1995 in the field of renewable energy under the Energy Efficiency and Renewable Energy Protocol agreement signed with the Chinese State Science and Technology Commission (now the Ministry of Science and Technology). Within the scope of this protocol, DOE and its National Renewable Energy Laboratory (NREL) have been working under a project annex with the Chinese Ministry of Agriculture (MOA) associated with rural energy development using solar photovoltaics (PV), wind, biomass and other technologies. This paper describes joint projects that are being pursued with the MOA and other agencies to promote rural electrification in northwestern China.

2. SCOPE OF CURRENT EXPERIENCE IN CHINA

2.1 Market in Northwestern China

The inhabited rural areas of northwestern China consist of farmland and grasslands. Annual incomes are generated mainly by farming and ranching, with ranching dominated by raising sheep. Annual household incomes fall in the range of 800 to several thousand RMB per year (8.2 RMB = $1 US), but annual incomes can be 30,000 RMB and higher for the wealthier segment of the rural population. The rural population of Gansu has among the lowest annual incomes in China, and the rural population in Inner Mongolia has among the highest annual incomes in China.

Table I: Estimate of unelectrified towns, villages, and remote households in selected provinces in northwestern China.

Province	Towns	Villages	Households
Gansu	20	1300	603,000
Qinghai	94	770	100,000
Xinjiang	51	1180	408,000
Inner	47*	1450	350,000
Total	212	4700	1,461,000

Source: 1) Ministry of Agriculture for Gansu, Qinghai, and

Xinjiang and ii) Inner Mongolia Planning Commission for Inner Mongolia; based on provincial statistics for end of 1997. *Aggressive electrification program in progress.

2.2 Photovoltaic Development in China

The development of PV in China is still in an early stage. In 1997 the annual production of PV modules in seven domestic manufacturing plants was approximately 2 MWp. The cumulative installed capacity of PV in China at the end of 1997 was approximately 11 MWp. Major applications included telecommunications, household electrification, agricultural and industrial uses, and consumer applications. Power for telecommunication stations is presently the largest market for PV, but PV for solar home systems is the most rapidly growing market sector. At the end of 1997 there were about 70,000 installed PV remote household systems with a total capacity of 1.3 MWp in China [2]. A typical small solar home system installation is shown in Figure 1.

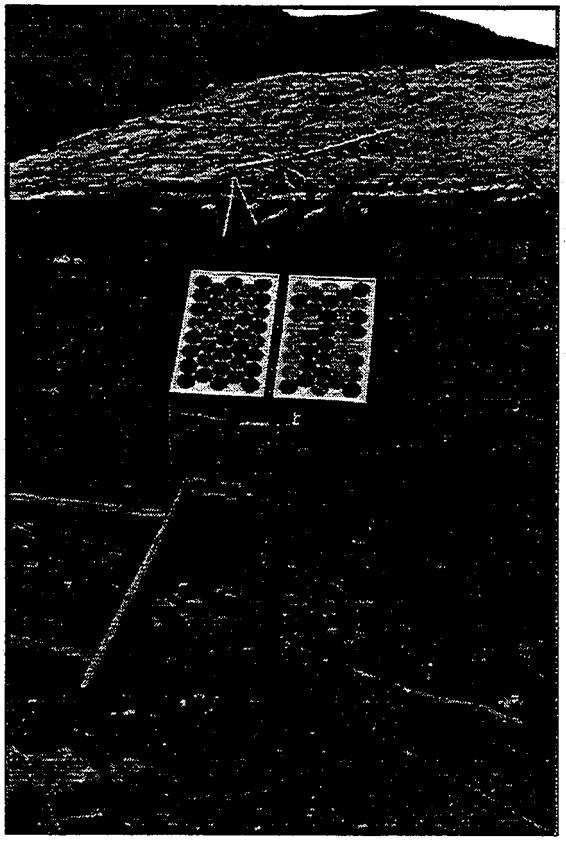

Figure 1. Solar home system installation in Xinjiang Province, typical of such installations in China.

2.3 System and Application Experience

There is a growing and broad experience base in China for the use of PV for rural electrification applications. Small solar home systems for individual household applications are sold in a variety of sizes from 8 watts to 300 watts. Twelve- volt, 20-watt dc systems are common, consisting of a PV module, charge controller, and battery to provide power for two fluorescent lights and a black-and-white television set. Larger dc and ac systems provide power progressively for a color television set, appliances, and satellite receiver.

Central village power systems using PV and battery storage are also being developed in China. Table II contains selected examples of installed systems in several provinces in China. Such village systems typically supply power for lighting, television and consumer electronic loads, and increasingly washing machines, refrigeration, and small electric motor loads.

The Bureau of Electric Power in Tibet plans to add 300 kW of additional village power systems during 1997-2000. During 1998, PV village power systems at the level of 100 kW will be installed in Tibet and Inner Mongolia. A number of wind/diesel hybrid village power systems in the 10-40 kW size range have been operating in Inner Mongolia and the coastal island region of China. The largest PV/wind hybrid system currently in China (30 kW) is installed on Xiaoguan island in Shandong Province. Household PV/wind hybrid systems in the 150-500 watt range are currently being developed in Inner Mongolia. More than 140,000 small wind turbines in the 100-200 watt size range have been cumulatively installed over the past decade, 80% of which are in Inner Mongolia.

Table II: Selected examples of PV village systems in China.

Location	Date	Power
Zhiherna, Qinghai	9/90	400 W
Qiuzhi, Qinghai	5/93	544 W
Shinaihai, Qinghai	9/93	4010 W
Shege, Qinghai	7/96	7000 W
Geji, Tibet	6/90	10 kW
Gaize, Tibet	92	20 kW
Cuoqin, Tibet	94	20 kW
Shuanghu, Tibet	12/94	25 kW
Inner Mongolia (17)	90-97	0.6-10 kW
Xiaoguan, Shandong (PV/Wind Hybrid)	1/95	25 kW Wind, 5 kW PV

Source: Discussions with provincial officials and electric power administrations.

Although significant numbers of field installations of a broad range of PV, wind, and various hybrid systems at the village and household levels have accumulated in China, surveys of the long-term performance of this technology base are incomplete. It is known that the quality of components and of complete systems is an issue in China. Some systems are no longer operating and some have experienced maintenance problems resulting in expensive repairs. Some systems that have been monitored over time have exhibited a satisfactory long-term performance record. There is especially a continuing issue in China with the variable quality of small household system components, particularly batteries and charge controllers.

3. RURAL ELECTRIFICATION IN GANSU

3.1 Project Description

The U.S. DOE and the Chinese MOA have been jointly supporting a solar home system project in Gansu

Province in western China [3,4]. The project objective is to support the installation of up to 600 solar home systems and a number of small school systems in remote rural areas of Gansu. Integral components of the project include: i) a training program to provide village technicians and qualified system installers, ii) a component and system testing program to ensure that systems meet minimum quality control standards and to provide performance information, and iii) use of a revolving account to provide project leverage by using sales receipts to finance the purchase of new systems.

Solar home systems consist of a 20-watt PV module, charge controller, 70-Ah battery, and two 8-watt fluorescent lights. System purchasers also buy a black-and-white television set. In the project, the U.S. side is supplying Solarex VLX-20 modules, 38-Ah sealed lead-acid batteries from SEC Industrial Battery Corporation, and some complete USSC Unikit solar lighting systems. These small systems are used for basic lighting services and television viewing.

Ten 53-watt school systems, consisting of Solarex VLX-53 PV modules, Ananda Power charge controllers, and 65-AH batteries, are also supplied. Chinese companies supply charge controllers and lights for the project and installation and warranty services. The school systems and 300 household systems have been installed to date, of which 40% have been acquired by using the revolving account for the project. In July, 1998 a survey is being conducted for these systems after several months of operation.

3.2 Project Participants

The U.S. and China cost-shared the Gansu project on a 50/50 basis with each side contributing $220 K. On the U.S. side, project participants include DOE, NREL, and the Solar Electric Light Fund in Washington, D.C. (SELF). On the China side, project participants include the Gansu Solar Electric Light Fund (GSELF), the Gansu Poverty Alleviation Office, Gansu Planning Commission, and Gansu Economic and Trade Commission. Project implementation is conducted by SELF and GSELF. Marketing support is provided by the rural energy office network of the Ministry of Agriculture in Gansu.

Table III: Companies in China Involved in Gansu Project

Company	Type
Gansu PV Company	Private Entrepreneur
Zhong Xing Electronic Instrument Company	State-Owned Military Conversion
Gansu Zi Neng Automation Engineering Company	Research Institute For-Profit Company
SEC Industrial Battery Company (U.S.)	Joint Venture Mfg. Facility in Shenzhen

Four types of companies are involved in Gansu as shown in Table III. These types of companies are commonly encountered in China. Private companies started by entrepreneurs can be aggressive and innovative, as demonstrated by the Gansu PV Company, which has pioneered very successful advertising techniques in Gansu and has promoted marketing approaches aimed at solving the affordability problem for low-income customers. State-owned companies such as Zhong Xing can be better financed and have critical connections, especially in the government, providing an advantage in government-supported projects. Zhong Xing is a military conversion company now making consumer electronic products, but maintaining its prior business network. For-profit companies affiliated with research institutes are now very common in China and tend to be resource limited. However, these companies can possess valuable technical expertise. Foreign joint-venture companies with Chinese partners are becoming important in the development of renewable energy in China and can provide a critical pathway for the entree of foreign companies into Chinese markets.

3.3 Expansion of the Gansu Project

Based on the experience gained with the solar home system project in Gansu, the Chinese MOA has developed a 10,000-household project in northwestern China. The project will be conducted in 3 years in the provinces of Xinjiang, Qinghai, Ningxia, Gansu, and Shaanxi, and the autonomous region of Inner Mongolia. In 1998 the project is being initiated with 3000 installations in Gansu, Qinghai, and Xinjiang. An integral component of the project is the support of testing and training activities and the development of standards for solar home systems, for which a regional center will be established at facilities of the Gansu Natural Energy Resources Institute in Lanzhou. This facility will provide services for the northwestern region of China. Key objectives of the MOA project include: i) improving the quality of solar home systems through the development of standards and testing protocols and ii) promoting new mechanisms for market development for PV solar home systems in China.

3.4 Applications for Solar Home Systems

Solar home systems are most frequently used to provide energy for basic lighting, television, and radio services. Interviews with owners of these systems indicate that individuals place a high value on the quality of lighting available with fluorescent lights and on the use of TV and radios as an "information window." Information of value includes not only entertainment, but local, national, and international news and cultural information impossible to obtain by other means in remote locations. Solar home systems can also contribute to household income by supporting light home industry, such as sewing and use of small appliances in farm and ranch activities.

Particular interests of the Chinese government in promoting the distribution of solar home systems include: i) education value for school-age children with improved lighting quality and TV/radio information that complements school curricula, ii) language instruction, especially in minority regions, to promote fluency in Mandarin, and iii) transmission of agricultural information, such as weather reports, crop prices, and instruction programs, to support income-producing activities for farming and ranching. These activities contribute to poverty alleviation in rural China, which is a national priority. It should be noted that the State Council Office

for Poverty Alleviation in Beijing, which is a cost-sharing partner in the Gansu project, spends over 1 billion $US per year in rural development projects in China.

4. HOUSEHOLD PV/WIND HYBRID SYSTEMS

4.1 Background

Inner Mongolia has been aggressive in developing wind and PV for rural electrification. Support includes: i) use of declining subsidies to support technology and market development, ii) assistance to renewable energy companies, and iii) formation of a network of new energy service stations at the county level to install and maintain wind and PV household systems. Because of the higher level of annual incomes of the rural population, larger household PV and wind systems are affordable. DOE and NREL have been pursuing joint cooperation for the development of PV/wind hybrid household systems in Inner Mongolia with the New Energy Office of the Science and Technology Commission in Hohhot. Other partners include the Inner Mongolia Polytechnic Institute, the University of Inner Mongolia, the Chinese Academy of Sciences in Beijing, the Shangdu Machinery Company in Inner Mongolia, and the JiKe Company in Beijing. In the first phase of the cooperation, the University of Delaware, NREL, and the Inner Mongolia team completed a levelized cost analysis of rural electrification options for several counties. The analysis compared renewable energy options with conventional gas gen sets based on local renewable resources and costs [5].

An attractive option for household systems resulting from the analysis and prior research in Inner Mongolia are PV/wind hybrid systems with battery storage. These systems are more reliable than PV or wind systems alone because of the seasonal complementarity of the wind and solar resources (with wind relatively more available in winter months and solar relatively more available in summer months). Analyses show that wind, PV, and PV/wind hybrid systems are lower- cost options for rural energy systems than fossil-fuel based generators [4,5].

4.2 Current Cooperation

Current cooperation with Inner Mongolia is focused on PV/wind systems consisting of: i) a 100-watt wind turbine combined with 50-70 watts of PV and ii) a 300-watt wind turbine combined with 150-200 watts of PV, with battery storage. These systems are capable of delivering 0.6 kWh/day and 1.6 kWh/day, respectively, with high reliability as a function of local resources at a given site. The systems provide energy for lighting, color television, consumer electronics, and some discretionary load. Systems of 450-500 Watts (Figure 2) can also maintain a freezer load, which is a major driving force for system development.

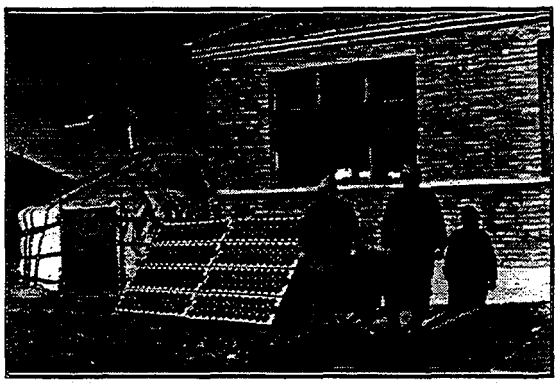

Figure 2. 500-Watt PV/wind hybrid household system in Inner Mongolia. Courtesy of Wang Sicheng, JiKe Company.

In 1998, the New Energy Office in Inner Mongolia will initiate a household PV/wind pilot project consisting of 240 installations to evaluate the technical and economic performance of these systems. The pilot project is part of long-term program to facilitate 80,000 PV, wind, and hybrid household installations. U.S. cooperation in this project will consist of supplying PV modules and some complete PV/wind hybrid systems manufactured in the United States. A system monitoring component of the project will place data acquisition systems on several households to collect system performance data and solar and wind resource data.

5. MARKET DEVELOPMENT ISSUES IN CHINA

5.1 Classification

Based on the experience to date with several rural electrification projects in China, several issues can be identified as challenges to the continued development of these markets. Some of the key challenges can be classified as technical, financial, and institutional.

5.2 Technical

Technical challenges include: i) variable and poor quality of component and system hardware, ii) poor system installation and maintenance, and iii) lack of availability of some domestic components. General recognition of these issues has resulted in a effort by several Chinese agencies to develop certification standards and testing for solar home systems in China. There is also an effort to upgrade the test capabilities of selected institutes to provide certification testing. Multiple agency efforts directed at system certification are not yet well coordinated at the national level.

Distributors of small household rural electrification systems in China frequently express the desire to acquire foreign equipment because of higher quality, particularly PV modules and batteries. For larger PV or PV hybrid systems installed in villages, and for other remote applications requiring more power, some domestic equipment is not available (e.g., most inverters of 5 kW and over are imported). PV module manufacturers in China are also developing plans for expansion, and new entrepreneurs are interested in building new module

production or module assembly plants. These areas of need are examples of potential business opportunities in China for foreign companies.

5.3 Financial

Financial challenges include developing financing and marketing approaches to accommodate the ability of low-income populations to buy rural electrification systems. Because of the emphasis on poverty alleviation, subsidies are heavily used in China to buy down the system cost to the end user. This use of subsidy funding can restrict the ability of the market to expand in a sustainable fashion, suppress business development, and discourage investment. Innovative use of subsidy funding to support business development, provide loan pools, or build capacity for training and infrastructure development can overcome some of these problems.

There is also a general lack of installment-credit experience in the rural sector in China, and some experiments with credit have resulted in high default rates. Nevertheless, consumer interviews indicate that continued experimentation with credit terms and infrastructures has the potential to greatly expand the market for rural electrification systems in China. Discussions with local banks in China also indicate an interest in this loan market, if suitable mechanisms, such as energy service companies, can be developed to aggregate large numbers of small loans.

5.4 Institutional

Institutional challenges include: i) developing distribution infrastructures to provide service to remote dispersed populations, ii) developing the capacity to support improvements in system quality and quality control in manufacturing, and iii) creating conditions to attract investment; for example, policy initiatives and tariff and value added tax (VAT) reform. Targets of international and multilateral development assistance to China include policy reform, business development (assistance in creating business plans, technical, and financial assistance), training, education, and technology transfer.

Local solar home system distributors in the provinces of northwestern China have been aggressive and innovative in developing distribution networks. For example, distributors train and employ village technicians to sell, service, and repair equipment.. Many distributors have established local village outlets or have contracted with village retail shops that sell consumer electronics. These outlets provide sales and maintenance services, including stockpiling spare parts and battery fluid. Entrepreneurs in the agricultural service station network of the Ministry of Agriculture, which regularly deal with farmers and ranchers in extreme remote locations, are beginning to sell solar home systems.

6. NEAR TERM RURAL ELECTRIFICATION ACTIVITIES

In the near term, the development of renewable energy projects for rural electrification in China will increase. For example, the World Bank and the Global Environmental Facility (GEF) is currently developing a renewable energy project in China in cooperation with the Chinese State Economic and Trade Commission. This project will include two components. One component will support commercial wind farm development and a second component will support PV and PV/wind hybrid stand-alone systems for rural electrification. The rural electrification component will provide business development assistance to commercial companies in China and will install approximately 10 MWp of systems in households, businesses, and community facilities [6].

The United Nations Development Programme (UNDP) and the GEF are also developing a program to fund capacity-building projects to increase the rate of commercialization of renewable energy in China. The program focuses on such activities as training, removing financing barriers, building institutional capacity for resource assessment, developing technology standards, and supporting pilot projects [7].

A number of provinces in China are increasing support for renewable energy for rural electrification. For example, Inner Mongolia is one of the leaders in promoting renewable energy, with more than 10 years of experience in supporting small-scale PV and wind technologies for household and village power applications. The New Energy Office of Inner Mongolia has developed a strategic plan for facilitating the installation of 80,000 household systems during the next five years. The Inner Mongolia Planning Commission is also supporting village power systems under the State Development Planning Commission's Brightness Program. The Chinese Ministry of Agriculture will implement a 10,000 solar home system project through its rural energy office network in six provinces in northwestern China.

The electric power utility industry in China is also becoming aware of the value of renewable energy options for meeting national rural electrification objectives in remote regions. Electric Power Administrations in Inner Mongolia, Qinghai, Xinjiang, Quangdong, and Shandong have actively supported renewable energy rural projects involving PV and wind technologies by cost-sharing the financing of projects or by providing management support for projects, primarily at the village power scale.

International assistance to China for renewable energy rural electrification projects is also increasing. The United States, Germany, Netherlands, and Japan are implementing or have discussed specific rural electrification projects in northwestern China and other provinces. These projects collectively could involve a large number of household installations using PV and wind technologies and an increase in village power projects using hybrid systems.

ACKNOWLEDGMENTS

Grateful support is acknowledged for several persons and organizations associated with the projects discussed in this paper. For the Gansu project, the support of Robert Freling of the Solar Electric Light Fund and personnel at the GSELF organization and participating companies is

acknowledged. For the Inner Mongolia project, special acknowledgement is made to Lin Li in the New Energy Office of Inner Mongolia, Wang Sicheng in the JiKe Company, and Li Xiuguo in the Chinese Academy of Science. Grateful acknowledgement is also made to John Byrne and Bo Shen in the Center for Energy and Environmental Policy at the University of Delaware and to the Village Power Group at NREL. This work was supported under contract DE-AC36-83CH10093 with the U. S. Department of Energy.

REFERENCES

[1] Lu Weide, Proceedings World Energy Council Asia Pacific Regional Forum, (April, 1997) 249.
[2] S.Wang, Solar Energy in China, Beijing, China (1995) 105, updated with private communications.
[3] W. L. Wallace and Y.S. Tsuo, Proceedings 26th IEEE Photovoltaic Specialists Conference, (1997) 1277.
[4] W. L. Wallace and Y. S. Tsuo, Proceedings ASES Solar 97 Conference, Washington, D.C. (1997).
[5] J. Byrne, B. Shen, and W. Wallace, Energy Policy, Vol. 26, No. 1, (1998) 45.
[6] Project Information Document, available from S. Bogache, World Bank, 1818 H Street, NW, Washington, D.C. 20433.
[7] Private communication with Dennis Fenton, UNDP, 2 Dong Qi Jie, Beijing, P.R.C.

REPORT DOCUMENTATION PAGE

Form Approved
OMB NO. 0704-0188

1. AGENCY USE ONLY (Leave blank)	2. REPORT DATE	3. REPORT TYPE AND DATES COVERED
	September 1998	Technical Report

4. TITLE AND SUBTITLE

NCPV Preprints for the 2nd World Conference on Photovoltaic Solar Energy Conversion; 6–10 July 1998; Vienna, Austria

5. FUNDING NUMBERS

TA: PV801702

6. AUTHOR(S)

7. PERFORMING ORGANIZATION NAME(S) AND ADDRESS(ES)

8. PERFORMING ORGANIZATION REPORT NUMBER

8. SPONSORING/MONITORING AGENCY NAME(S) AND ADDRESS(ES)

National Renewable Energy Laboratory
1617 Cole Blvd.
Golden, CO 80401-3393

10. SPONSORING/MONITORING AGENCY REPORT NUMBER

TP-520-25101

11. SUPPLEMENTARY NOTES

12a. DISTRIBUTION/AVAILABILITY STATEMENT

National Technical Information Service
U.S. Department of Commerce
5285 Port Royal Road
Springfield, VA 22161

12b. DISTRIBUTION CODE

13. ABSTRACT *(Maximum 200 words)*

This document consists of 26 papers prepared by scientists working in photovoltaics at the National Renewable Energy Laboratory and Sandia National Laboratories. The papers were presented at the 2nd World Conference on Photovoltaic Solar Energy Conversion, held on July 6–10, 1998, in Vienna, Austria. The work described here was performed under the auspices of the U.S. Department of Energy's National Center for Photovoltaics.

14. SUBJECT TERMS

photovoltaics ; silicon ; thin-film PV technologies ; amorphous silicon ; cadmium telluride ; copper indium diselenide ; high-efficiency devices ; solar cells ; solar modules ; solar systems

15. NUMBER OF PAGES
144

16. PRICE CODE

17. SECURITY CLASSIFICATION OF REPORT	18. SECURITY CLASSIFICATION OF THIS PAGE	19. SECURITY CLASSIFICATION OF ABSTRACT	20. LIMITATION OF ABSTRACT
Unclassified	Unclassified	Unclassified	UL